Howard University

Structure and Evolution of Developing and Non-developing African Easterly Waves During National Aeronautics and Space Administration African Monsoon Multidisciplinary Analyses (NAMMA)

A Dissertation
Submitted to the Faculty of the
Graduate School

of

HOWARD UNIVERSITY

in partial fulfillment of
the requirements for the
degree of

DOCTOR OF PHILOSOPHY

Department of Atmospheric Sciences

by

Nelsie A. Ramos

Washington, D.C.
December 2012

HOWARD UNIVERSITY
GRADUATE SCHOOL
DEPARTMENT OF ATMOSPHERIC SCIENCES

DISSERTATION COMMITTEE

Tsann-Wang Yu, Ph.D.
Chairperson

Sim D. Aberson, Ph.D.

Belay Demoz, Ph.D.

Vernon R. Morris, Ph.D.

Daniel Melendez, Ph.D.
Meteorologist
National Oceanic and Atmospheric Administration

Sim D. Aberson, Ph.D.
Dissertation Advisor

Candidate: Nelsie A. Ramos
Date of Defense: November 2, 2012

DEDICATION

This work is dedicated to my family and mentee students, which encouragement and motivation was essential for the achievement of this great personal and professional goal.

ACKNOWLEDGMENTS

First, infinite thanks to the greatest advisers I could ever had: Dr. Sim Aberson and Dr. Vernon Morris. Without your guidance, support and general encouragement this work would not be possible. I also want to extend my gratitude to key people in the success of this project: Dr. Altug Aksoy for his assistance with HEDAS, Kathryn Sellwood for help with the quality control and pre-processing of dropwindsondes, Lisa Bucci for initial HWRFx training, Dr. Thiago Quirino for assistance with the HWRFx postprocessor, Jason Dunion for providing with the satellite imagery data, Mike Black for help with the dropwindsonde data and Dr. Gopalakrishnan for HWRFx and GrADS support. Special thanks to Dr. Sim Aberson, Dr. Frank Marks and Howard Friedman for making the National Oceanic and Atmospheric Administration (NOAA) Atlantic Oceanographic and Meteorological Laboratory (AOML)/Hurricane Research Division (HRD) my second home while completing my graduate studies and the Educational Partnership Program (EPP) Graduate Sciences Program (GSP). My career would not be the same without the knowledge and work experience I gained there. From the NOAA National Hurricane Center (NHC), I am thankful to Dr. Ed Rappaport and Hugh Cobb for the support and flexibility provided that allowed the fast completion of my degree. My appreciation also to the NHC Tropical Analysis and Forecasting Branch staff for valuable training provided that improved the direction of my research. Last but not least, I would like to thanks the NOAA EPP staff for the funding provided to conclude this work and the opportunity of a lifetime.

ABSTRACT

A modeling and data impact study was performed using the NOAA AOML/HRD experimental Hurricane Weather Research and Forecasting (HWRFx) model with the aim to find distinguishing factors to better discriminate between possible developing and non-developing African Easterly Waves (AEWs) into tropical cyclones (TCs). Two AEWs from the 2006 hurricane season were examined. One AEW was the precursor of Hurricane Helene (HAEW). The second AEW preceded Helene (NDAEW), however it failed to intensify into a TC.

The effect of convection, nesting and initial conditions in the forecast of the AEWs were evaluated. New initial conditions were produced by the Hurricane Ensemble Data Assimilation System (HEDAS) and had assimilated dropwindsonde data gathered in NAMMA not ingested into NOAA/NCEP models in real time. Nested simulations had a static parent domain with grid spacing of 9 km and higher resolution-moving nest of 3 km. Un-nested simulations were run with the 9-km static parent domain. Physics options applied to the model were semi-operational or aligned as close as possible to the operational HWRF.

The HWRFx implicit convection in the 9-km domain and the 3-km domain nesting capability had a strengthening effect on the AEWs. Assimilation of additional dropwindsondes data for the NDAEW case greatly improved the initial state of the model and produced a more accurate forecast while the HAEW case demonstrated that additional data sometimes could result in intensity forecast degradation. A detailed analysis of the dynamic-thermodynamic evolution of the environments and structures of the two AEWs provided favorable and un-favorable conditions for TC development and

showed that the cyclogenesis process occurs from approximately 700 hPa to the surface or the lower troposphere. A distinctive signal for a developing system consisted on the formation of a relative vorticity (RVORT) core at the mean of the locations of wind speed minima (MLWSM) and extending from the surface to at least 850 hPa. The core of RVORT did not coincided with the location of the RVORT maximum during cyclogenesis. This emphasizes the importance of evaluating the RVORT structure horizontally and vertically in order to accurately predict cyclogenesis.

TABLE OF CONTENTS

LIST OF TABLES

Tables **Page**

LIST OF FIGURES

Figures **Page**

LIST OF ACRONYMS

AEJ = African Easterly Jet

AEW = African Easterly Wave

AMMA = African Monsoon Multidisciplinary Analyses

AOML = Atlantic Oceanographic and Meteorological Laboratory

BC = Boundary Conditions

BT = Best Track

CIMSS = Cooperative Institute for Meteorological Satellite Studies

CNTRL = Control

CUP = Cumulus Parameterization

D = Dropwindsonde

DA = Data Assimilation

ECMWF = European Centre for Medium-Range Weather Forecasts

EnKF = Ensemble Kalman Filter

EPP = Educational Partnership Program

EXP = Experimental

GEFS = Global Ensemble Forecast System

GFDL = Geophysical Fluid Dynamics Laboratory

GFS = Global Forecast System

GPS = Global Positioning System

GrADS = Grid Analysis and Display System

GRIP = Genesis and Rapid Intensification Processes

GSI = Gridpoint Statistical Interpolation

HAEW = AEW associated with Helene

HCS = Horizontal Cross Section

HEDAS = Hurricane EnKF Data Assimilation System

HFIP = Hurricane Forecast Improvement Program

HWRF = Hurricane Weather Research and Forecasting

HWRFx = Experimental Hurricane Weather Research and Forecasting

HRD = Hurricane Research Division

IC = Initial Conditions

IFEX = Intensity Forecasting Experiment

IR = Infrared

JAS = July, August, and September

LHN = Latent Heat Nudging

MCS = Mesoscale Convective Systems

MLWSM = Mean of the Locations of Wind Speed Minima

MSLP = Mean Sea Level Pressure

MSW = Maximum Sustained Winds

NAMMA = National Aeronautics and Space Administration African Monsoon Multidisciplinary Analyses

N = North

NASA = National Aeronautics and Space Administration

NCAR = National Center for Atmospheric Research

NCEP = National Center for Environmental Prediction

NCU = Cumulus Parameterization Off

NDA = No DA

NDAEW = Non-developing AEW

NHC = National Hurricane Center

NMM = Non-hydrostatic Mesoscale Model

NOAA = National Oceanic and Atmospheric Administration

NWS = National Weather Service

NWP = Numerical Weather Prediction

OI = Optimal Interpolation

PBL = Planetary Boundary Layer

PDF = Probability Density Function

PI = Physical Initialization

PREDICT = PRE-Depression Investigation of Cloud-systems in the Tropics

RAINEX = Rainband and Intensity Experiment

RH = Relative Humidity

RVORT = Relative Vorticity

SAL = Saharan Air Layer

SAS = Simplified Arakawa-Schubert

SCM = Successive Correction Method

TAFB = Tropical Analyses and Forecasting Branch

TC = Tropical Cyclone

TD = Tropical Depression

TEXMEX = Tropical Experiment in Mexico

TS = Tropical Storm

TCSP = Tropical Cloud Systems and Processes

UTC = Universal Time Coordinated

VCS = Vertical Cross Section

W = West

WRF = Weather Research and Forecasting

3DVAR = 3-Dimensional Variational

4DVAR = 4-Dimensional Variational

1. INTRODUCTION

The topic of this research was developed during an internship with the NOAA AOML/HRD under the advice of Dr. Sim D. Aberson, and made possible by the NOAA EPP.

1.1 Motivation

Tropical cyclones (TCs) are mesoscale-rotating storms that form over warm ocean waters in tropical regions, and their circulations can extend more than 1000 km from the storm center (Montgomery and Farrell 1993). The strongest TCs (called hurricanes in the Atlantic and in the Pacific east of the dateline and typhoons in the Pacific west of the dateline) have sustained surface wind speeds of 64 kt or higher. Its extremely high wind speeds, heavy rainfall, and storm surge make the hurricane one of the most life-threatening and destructive natural phenomena that exist. The less severe TCs are called tropical depressions (TD; with maximum sustained wind speeds up to 33 kt) and tropical storms (TS; with wind speeds from 34 to 63 kt); however they also carry destructive potential and are frequently associated with heavy precipitation.

A lot is unknown about how TCs form (e.g., Frank 1987; Aiyyer and Molinari 2008; McTaggart-Cowan et al. 2008; Pratt and Evans 2009; Schreck III and Molinari 2009; Shaman et al. 2009). Predicting the time and location of TC formation has proven to be difficult due to the lack of understanding of the physics behind their initiation. Improvement of cyclogenesis forecasts is critical, especially if development represents a potential threat for landfall in a short period of time. Operationally, some global forecasting models over-predict the chances of cyclogenesis while others under-predict it.

A major factor limiting the accuracy of forecast of TC formation is the lack of an accurate description of the initial conditions (ICs) in numerical simulations due to the deficiency of observational data over tropical oceans. Besides the need for a better atmospheric and oceanic observing network, other factors that may contribute to increased model accuracy and reliability are the development of new data assimilation (DA) techniques and the improvement of model resolution and physics (e.g., Aberson and DeMaria 1994).

Assimilation of dropwindsonde data into the National Center for Environmental Prediction (NCEP) operational global model that have been gathered in the environments of mature TCs has shown to improve forecasts significantly (Aberson 2003). However, there exist very few observations of both African Easterly Waves (AEWs) as the precursors to cyclogenesis and the subsequent TC formation process itself. During the 2006 NAMMA campaign, major AEWs were sampled over the eastern Atlantic, thus generating a very unique dataset. Nevertheless, this data were not assimilated into NOAA/NCEP models in real time.

This research takes advantage of such a dataset to investigate if the assimilation of additional dropwindsonde data into a high-resolution regional model may aid in finding distinguishing factors between developing and non-developing AEWs in order to aid in the creation of new approaches and tools that would facilitate the forecast of cyclogenesis.

1.2 Science and research objectives

The forecast of tropical cyclogenesis remains as a challenging problem these days due to the involvement of multiple time and space scales and the required interaction of many different processes. Frequently, the operational global forecasting models tend to over-predict or under-predict cyclogenesis. Reasons for this are mainly attributed to the lack of adequate ICs and resolution to resolve atmospheric processes at small scales as well as inadequate physics parameterizations in the model.

In this investigation, a modeling and data impact study is performed using the experimental NOAA/AOML/HRD Hurricane Weather Research and Forecasting (HWRFx) high-resolution regional model to find distinguishing factors to better discriminate between possible developing and non-developing AEWs. To achieve this purpose, a detailed analysis of the dynamic-thermodynamic evolution of the environments and structures of two AEWs from the 2006 hurricane season is executed. In addition, this study seeks to assess the HWRFx model for the study of weak tropical disturbances (i.e. AEWs) as opposed to its exclusive use for mature TCs and to determine if early sampling of these tropical systems has the potential to improve the forecast of cyclogenesis.

The first objective of the research was the execution of HWRFx control (CNTRL) simulations. Within this set of simulations two tests were performed. One test investigated the model sensitivity to cumulus parameterization (CUP). A second test evaluated the model sensitivity to nesting or improved resolution. The second objective of the investigation consisted of a data impact analysis. For this stage of the investigation, experimental (EXP) simulations were generated using the Hurricane

Ensemble DA System (HEDAS) to assimilate into HWRFx dropwindsonde data and determine if this additional dataset provides further details that may increase the understanding of cyclogenesis predictability. To examine the environment evolution and structure of the AEWs under study, results from the CNTRL and EXP simulations were presented as horizontal cross sections (HCS) and vertical cross sections (VCS) of moisture, wind, wind shear, relative vorticity (RVORT) and mean sea level pressure (MSLP). The standard terms for tropical disturbance, TD, TS and the Saffir-Simpson Hurricane Wind Scale were used to categorize the intensity of the AEWs or AEWs spawned system. Particularly, for the developing AEW (HAEW), the NHC best track (BT) and analyses of maximum sustained winds (MSW) and MSLP were employed to validate the intensification stages.

The third and final objective of the study was the validation of the HWRFx ICs dynamic-thermodynamic structure against the NAMMA dropwindsonde data to determine if its assimilation improves upon the analysis of the AEWs, hence the predictability of tropical cyclogenesis.

2. SCIENTIFIC BACKGROUND

2.1 Theories of Tropical Cyclones Genesis

Successful interaction of many different processes, each acting on a different spatial and temporal scale than the others, characterizes the story of TCs development. Ooyama (1982) suggested that the probabilistic nature of tropical cyclogenesis is rooted in the scale-dependent dynamics of the atmosphere that include the climatological and synoptic conditions as well as the mesoscale dynamics of organized convection. Bracken and Bosart (2000) suggest that the details of the interactions between synoptic-scale processes and the mesoscale flow will ultimately determine where, when, and how a warm core vortex is formed. From the earliest studies (Riehl 1948), it has been recognized that all TCs originate in some independent disturbances. Emanuel (2003) states that TCs always develop from pre-existing atmospheric disturbances; especially waves of 1000–3000 km in scale and that generally intensify, principally by heat transfer from the tropical ocean water whose surface temperature exceeds 26º C and in regions where the absolute vorticity of the airflow has a positive value. He also suggests that a necessary condition for cyclogenesis is the establishment of an order of 100-km-wide column of nearly saturated air in the core of the system, so that cumulus convection rising into this air cannot produce low-entropy downdrafts driven by evaporating rain, and that any environmental influence that disrupts the formation of such a saturated column will prevent cyclogenesis and weaken any existing system.

Gray (1968) demonstrated that cyclogenesis only occurs in environments characterized by small vertical shear of the horizontal wind, and also favors regions of relatively large cyclonic low-level vorticity. Additionally to the two aforementioned

factors, Gray (1968) argued that larger values of the Coriolis parameter, the heat content of the upper ocean (reflecting the depth of the ocean mixed layer), and the relative humidity (RH) of the middle troposphere all favor cyclogenesis. On the other hand, Ritchie and Holland (1993) put forward the idea that cyclogenesis involves the fusion of several small vortices associated with individual convective systems that can, under certain circumstances, merge to form a well-built initial cyclone. Retention of the heat released via cumulus convection by means of an inertially stable atmosphere (when the background vorticity is strong) seems to be one of these circumstances as several studies (Ooyama 1982, Schubert 1980) have shown. If strong convection is present, the released latent heat is trapped within the cyclone and a warm core may accumulate. Consequently, this will increase the rotational wind and, as a result, the inertial stability, creating an even more effective retention of the cloud-released heat. A case study of the cyclogenesis of Hurricane Danielle in 2004 using the Advanced Research Weather Research and Forecasting model shows that the simulation of persistent, deep, moist convection at an early stage of the AEW development is important for cyclogenesis to occur (Ramos 2007). Moreover, Ramos (2007) observed that the merger and amplification of strong convection in the AEW greatly influenced the merger and strengthening of vorticity at 850 hPa, allowing Hurricane Danielle to form.

The most recent cyclogenesis hypotheses are the ones developed in 2008 by Wang, Montgomery and Dunkerton, which were tested during the PRE-Depression Investigation of Cloud-systems in the Tropics (PREDICT) 2010 field experiments aimed at understanding the dynamics of TC formation (Montgomery et al. 2012). These theories are known as the marsupial paradigm of tropical cyclogenesis and argue that TC

formation proceeds through essentially the same mesoscale and cloud processes regardless of the variety of precursor disturbances (i.e. tropical waves, monsoon troughs, upper-tropospheric PV features, etc.). The marsupial theory suggests that dynamical isolation would protect a given region and provide a " sweet spot" where a favorable mesoscale condition could exist for several days, dramatically increasing the chances of a tropical depression forming. Once generated in the lower troposphere, this "sweet spot" is protected from hostile influences such as vertical wind shear and low column-humidity, favoring sustained column moistening and vortex-tube stretching by deep cumulus convection.

2.2 African Easterly Waves

Since at least the 1930s, it has been acknowledged that AEWs often serve as the seedling circulations or precursors for a large proportion of TCs over the north Atlantic Ocean and also the eastern Pacific Ocean (e.g. Avila and Pasch 1992). Affirmation of this assumption is made in a study by Thorncroft and Hodges (2001), which showed that a notable positive correlation exists between the AEW activity and Atlantic TC activity. In addition, a study (Berry et al. 2007) showed that, during the months of July, August, and September (JAS) of 2004, 45% of the AEWs leaving the West African coast developed into a TC in either the Atlantic or Pacific Ocean basins.

AEWs are defined formally as westward-traveling synoptic scale disturbances that exist over Africa and propagate out into the tropical North Atlantic during northern summer (Burpee 1972), acting as a disruption of normal tropical easterly flow. Normally, the waves have a period of about 5 days over land before they propagate to the

Atlantic at an approximate speed of 5º to 7º of longitude per day. AEWs have wavelengths of 2000 to 2500 km (Burpee 1974), are mostly centered between latitudes 10º and 15º N, are strongest near the 700-hPa level, and generally are accompanied with areas of disturbed weather. These waves are first seen usually in April or May and continue until October or November, the months of August and September being their most active period. This means that they are active during the West African wet season and therefore play an important role in modulating precipitation (Payne and McGarry, 1977).

There are different theories about the origin of the AEWs, though the most popular consider the African Easterly Jet (AEJ) baroclinic-barotropic instability being a very important ingredient that gives birth of these waves (e.g. Reed et al. 1977, Thompson et al. 1979). The AEJ arises due to the reversed lower-tropospheric temperature gradient caused by the warm temperatures from the desert in North Africa and the cooler temperatures along the Gulf of Guinea coast (Cook 1999). When these two air masses meet, the atmosphere become very unstable and very heavy thunderstorms with areas of low pressure develop, giving rise to the AEWs. Another theory (Berry et al. 2007) suggests that AEWs have a multiscale nature and originate as discrete entities (typically mesoscale convective systems (MCSs) over central and eastern Africa) that couple with the unstable basic state over the African continent and amplify. Identification and tracking of all the 2004 AEWs over tropical North Africa during the months of JAS in the latter study showed that most AEWs were first identified (by the first appearance of the 700 hPa trough axis in the Global Forecast System (GFS) analysis) east of the Greenwich meridian and developed as they moved westward. The study also

suggested that the most probable starting position of AEW trough axes seems to progress further and further east as the season progresses.

2.3 The 2006 NAMMA field program

In 2006, the National Aeronautics and Space Administration (NASA) led an important field campaign known as NAMMA based in the Cape Verde Islands. It was designed to study tropical convective systems and cyclogenesis. Its mission was intended to characterize the evolution and structure of AEWs and MCSs over the West African continent, the formation and evolution of hurricanes in the eastern and central Atlantic, the composition and structure of the Saharan Air Layer (SAL), and the possible effect of aerosols in cloud precipitation and TC development. With the African Monsoon Multidisciplinary Analyses (AMMA) campaign providing data over a vast area of west Africa, NASA was able to extend the data westward over the Atlantic during the field program, while NOAA further extended that east-west coverage with research aircraft operating out of Barbados (Zipser et al. 2009). NAMMA utilized the NASA DC-8 research aircraft, with a total of 10 instruments and nearly 100 scientists in the field to sample tropical storm systems and provide valuable data to validate NASA's earth science satellites (Gaunce 2006). Thirteen science flights sampled seven major AEWs, including the cyclogenesis of tropical systems Debby, Ernesto, Gordon, and Helene, from mid-August to mid-September of 2006. In addition, NASA flew a number of dedicated missions studying cloud microphysics and the SAL. NAMMA's data are being employed in an attempt to determine the reasons for which some AEWs developed into hurricanes and some failed to intensify.

The NAMMA field campaign possibly represents the best AEW validation database ever obtained in the eastern North Atlantic (Zipser et al. 2009), hence an opportunity to evaluate remote sensing retrieval algorithms, and the dynamics and microphysics parameterizations of numerical models used in an effort to unlock the mystery of tropical cyclogenesis.

The NAMMA mission was collaboration between NASA, NOAA AOML/HRD, several universities, the U.S. Air Force, and the Cape Verdean National Institute of Meteorology and Geophysics.

3. METHODOLOGY

3.1 HWRFx configuration, physics and initial conditions

The AOML/HRD HWRFx is a version of the NCEP operational HWRF model, developed jointly at AOML and Earth System Research Laboratory to study the hurricane intensity change problem at a model grid resolution of about 3 km (Gopalakrishnan et al. 2010, Zhang et al. 2010). The HWRFx model is a regional high-resolution hurricane prediction system designed to forecast the intensity, structure, and rainfall of TCs. HWRFx slightly differs from the operational version in terms of the physics, domain size, methods to generate ICs and lack of coupling to the ocean component.

Results from idealized HWRFx experiments in Gopalakrishnan et al. (2010) have shown that the model is able to produce vortex intensification consistent with other theoretical and numerical studies, and the importance of high resolution in the fundamental understanding of the dynamics behind the TC rapid intensification. In another study of Gopalakrishnan et al. (2012), two configurations of HWRFx were used (27:9 km, 9:3 km) to study the influence of model grid resolution, ICs (from GFDL and HWRF), and physics for 87 cases of Atlantic TCs during the 2005, 2007, and 2009 hurricane seasons. Besides improved structure predictions, the 9:3-km configuration using GFDL ICs and a system of physics similar to the operational HWRF provided better results in terms of both track and intensity prediction. Zhang et al. (2010) conducted another study on the impact of increased HWRFx resolution on TC forecast performance for a sample of 69 cases from two hurricane seasons. Again, the high-resolution forecasts (9:3 km) demonstrated a better performance in reducing the track and intensity errors and in generating a more realistic structural evolution, such as eyewall replacement cycles. Moreover, HWRFx has shown to be generally comparable to the

NOAA operational models, in terms of the accuracy of both track and intensity forecasts per results from real-time experiments during the 2008 hurricane season (Yeh et al. 2011). The current work tests HWRFx for the study of weak tropical disturbances (as opposed to its usual use for mature TCs) and is applied with the aim to provide further insights about how TCs form.

The HWRFx model utilizes the Non-hydrostatic Mesoscale Model (NMM) dynamic core, whose system of equations is formulated on a rotated latitude-longitude projection with the Arakawa-E grid. This atmospheric model uses a pressure-sigma hybrid coordinate with 42 vertical levels with the top level set to 50 hPa and is integrated with a time step of 18 seconds. The outer domain was set approximately to 55 x 55 degrees with a moving inner nest of about 6 X 6 degrees. In terms of horizontal resolution, the static parent domain has grid spacing of 9 km with the higher resolution-moving nest of 3 km. For the un-nested model configuration, the 9-km static parent domain was used. The physics options applied for the current work were semi-operational, meaning aligned as close as possible to the operational HWRF. The NCEP GFS surface and planetary boundary layer (PBL) options were used to calculate surface fluxes and their subsequent incorporation into the atmosphere. To explicitly resolve condensation or clouds elements such as water vapor, cloud, and precipitation processes, the Ferrier microphysics scheme was employed. Since cumulus parameterizations are theoretically only valid for coarser grid sizes (e.g., greater than 10 km), due to the nature of the current investigation in studying weak tropical disturbances with a model designed for mature storms, initial control model runs were made using the Simplified Arakawa Schubert (SAS) scheme to represent the subgrid-scale effects of convective and/or

shallow clouds (or vertical fluxes due to unresolved updrafts and downdrafts). Land-surface and radiation physics were evaluated by the Geophysical Fluid Dynamics Laboratory (GFDL) scheme, which are also used operationally at NCEP.

The NCEP 6-hourly GFS final operational analyses on 1.0 x 1.0 degree grids were used to provide the initial and lateral boundary conditions (BCs) for the CNTRL nested and un-nested runs as well as the BCs of the EXP runs. The ICs for the HWRFx EXP runs were generated by HEDAS using Global Ensemble Forecast System (GEFS) data as the first guess.

3.2 Data Assimilation

Numerical Weather Prediction (NWP) is an initial/boundary value problem: given an estimate of the present state of the atmosphere (ICs), and appropriate surface and lateral BCs, the model simulates (forecasts) the atmospheric evolution. In theory, the more accurate the estimate of the ICs, the better the quality of the forecast. However, this is not always the case since models usually contain many errors arising from horizontal, vertical and time-differencing schemes, parameterized processes, boundary conditions and the incorporation of inadequate terrain (Krishnamurti et al. 1980). Currently, operational NWP centers produce ICs through a statistical combination of observations and short-range forecasts. This approach has become known as DA, whose purpose is defined by Talagrand (1997) as "using all available information, to determine as accurately as possible the state of the atmospheric (or oceanic) flow" (Kalnay 2003).

DA is a way to objectively correct the modeled state of the atmosphere by using measurements, such that the model could be effectively used to analyze and predict it (Vukicevic 2010). DA aims at accurate analysis, estimation and prediction of an

unknown, true state by merging observed information into a model. It finds some way to blend a model "first guess" (i.e a short-range forecast) with observations to best estimate the truth. The first guess (also known as the background field or prior information) should be the best estimate of the state of the atmosphere prior to the use of the observations. With the improvement of forecasts over time, the use of short-range forecasts as a first guess was universally adopted in operational systems in what is called an "analysis cycle".

The analysis cycle is an intermittent DA system that continues to be used in most global operational systems, which typically use a 6-h cycle performed four times per day. The model forecast plays a very important role. Over data-rich regions, the analysis is dominated by the information contained in the observations. In data-poor regions, the forecast benefits from the information upstream, meaning that the forecast is able to transport information from data-rich to data-poor regions.

The existing assimilation algorithms can be described as either sequential or variational (Kalnay 2003). The most common DA methods are the empirical, statistical and the advanced methods. The Successive Correction Method (SCM), Nudging, Physical Initialization (PI), and Latent Heat Nudging (LHN) are examples of empirical methods. Statistical methods include the Optimal Interpolation (OI), 3-Dimensional Variational (3DVAR), and 4-Dimensional Variational (4DVAR) DA. The Extended Kalman Filter and the Ensemble Kalman Filter (EnKF) are the advanced methods. In all of the mentioned methods above, except for the advanced methods, the forecast error covariance matrix is estimated once, as if the forecast errors were statistically stationary. However, the more advanced schemes include, at least implicitly, the evolution of the

forecast error covariance. Starting with the 2014 hurricane season, a new "hybrid" DA system will be employed operationally by the NCEP. This new hybrid system consists on the utilization of the Gridpoint Statistical Interpolation (GSI) 3DVAR system and the EnKF DA technique for the NCEP GFS global model.

HEDAS, which is the DA system from HRD employed in the current study, contains an HWRFx forecast/analysis cycle in which a six-hour GEFS (at 1-degree resolution) forecast from the previous cycle provides the first guess to an EnKF DA system. Once the DA cycling process is completed, a mean final analysis containing the new storm structure is produced and added back onto the GFS final environmental analysis fields in order to generate an HWRFx deterministic run.

Figure 3.1 shows a flow diagram of the HWRFx DA process for a retrospective run using HEDAS.

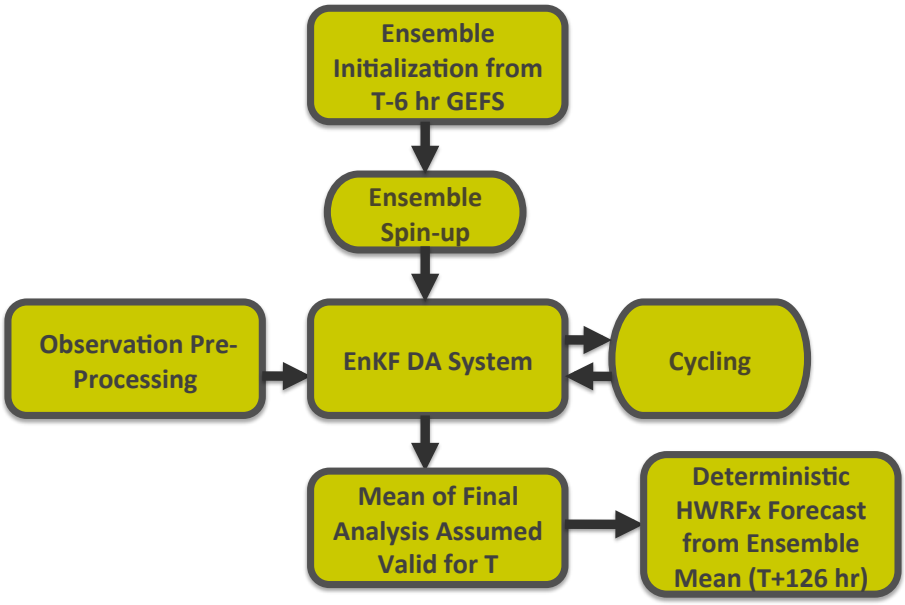

Figure 3.1 HEDAS sequencing on HWRFx for a retrospective run.

3.3 Ensemble Kalman Filter Technique

The EnKF is a sophisticated sequential DA method, which means that the model is integrated forward in time and, whenever measurements are available, these are used to reinitialize the model before the integration continues. It applies an ensemble of model states to represent the error statistics of the model estimate as well as ensemble integrations to predict the error statistics forward in time, and uses an analysis scheme, which operates directly on the ensemble of model states when observations are assimilated. The EnKF has proven to efficiently handle strongly nonlinear dynamics and large state spaces and is now used in realistic applications with primitive equation models for the ocean and atmosphere (http://enkf.nersc.no/). It represents the distribution of the system state using a collection of state vectors, called an ensemble, and replaces the covariance matrix by the sample covariance computed from the ensemble. The ensemble is operated with as if it is a random sample, but the ensemble members are really not independent (they are all the same model). One advantage of the EnKF is that advancing the probability density function (PDF) in time is achieved by simply advancing all members of the ensemble.

Originally proposed by Evensen (1994), the EnKF later has been further developed and examined in a large number of published papers. A recent review and overview of the EnKF is given by Evensen (2003), which provides detailed information on the formulation, interpretation and implementation of the EnKF, and now serves as a reference document for the basic methodology.

A critical component of successful numerical modeling of TCs is the assimilation of available observations to minimize the errors in initial model states (Aksoy et al.

2010). The NOAA AOML/HRD routinely conducts flight missions into hurricanes to collect synoptic-scale surveillance (by the Gulfstream-IV aircraft) and high-resolution inner-core (by the P-3 Orion aircraft) data. These data include flight level, dropwindsonde, surface wind speed, and Doppler radar observations. Presently, the synoptic-scale surveillance data are assimilated by most operational centers. Contrarily, due to lack of sufficient resolution and sophisticated DA tools, use of the high-resolution data for the initialization of hurricane prediction models is limited.

HRD has been developing a state-of-the-art EnKF DA system to utilize the high-resolution inner-core data obtained from flight missions, as part of NOAA's Hurricane Intensity Improvement Program (HFIP). Within this development effort, assimilation of dropwindsonde observations is considered as one of the higher-priority tasks, as dropwindsondes provide very valuable information on overall TC structure throughout the depth of the troposphere (Aksoy et al. 2010).

In 2012, NCEP started running operationally a 3-domain configuration (27:9:3) of HWRF, which includes the 3-km nest where assimilation of high-resolution inner-core data will be possible in the near future. Scientists at HRD are working to make this capability possible. For this research, the HRD HEDAS is used in an effort to assimilate into HWRFx dropwindsonde data obtained during NAMMA.

3.4 Dropwindsondes data assimilation impact on tropical cyclones

In 1997, the NOAA NHC and HRD began operational synoptic surveillance missions with the Gulfstream IV-SP jet aircraft aiming to improve the numerical guidance for hurricanes that threaten the continental United States, Puerto Rico, the U. S.

Virgin Islands, and Hawaii (Aberson 2009). Since then, numerous missions have sampled the inner core and surrounding environment of TCs utilizing the Global Positioning System (GPS) dropwindsondes (Hock and Franklin 1999). The GPS dropwindsonde (also known as dropsonde) is a cylindrical instrument package deployed from the aircraft at 150-200-km intervals along the flight track that transmits vertical profiles of wind velocity, temperature, pressure, and humidity every half-second while descending through the TC environment from flight level (about 150 hPa) to the surface. Once gathered, these observations are processed and formatted aboard the aircraft and then are sent to NCEP and the Global Telecommunications System to be ingested into the GFS, which serves as IC and BC for regional numerical models that also forecast TC track and intensity (Aberson 2009).

As many studies indicate, these observations have revolutionized the understanding of mature TC structure, dynamics, thermodynamics, and intensity change (e.g. Franklin et al. 2003; Powell et al. 2003; Uhlhorn and Black 2003; Eastin et al. 2005a, b; Halverson et al. 2006; Montgomery et al. 2006; Aberson et al. 2006; Kepert 2006a, b). The combination of optimal observing strategies and the assimilation of the dropwindsonde observations from the hurricane missions have produced large improvements in dynamical TC track forecast models (Aberson 2009) as well. However, scarce airborne measurements exist in tropical disturbances mainly because of the difficulty in forecasting such events, and the high costs associated with a complete flight including the required dropwindsondes (Aberson et al. 2006). Even though satellite data has revolutionized weather forecasters' ability to detect early signs of TCs before they form there are still many important tasks they are not suited for. Satellites cannot

determine the interior barometric pressure of a TC nor provide accurate wind velocity information. Thus, one of the major factors limiting the accuracy of forecasts of tropical cyclogenesis is the lack of an accurate description of the ICs in numerical simulations due to the deficiency of observational data over tropical oceans. Besides the need of a better observing network, other factors that may contribute to increased model accuracy and reliability, and produce improved operational forecasts are the development of new DA techniques and the improvement of model resolution and physics (e.g., Aberson and DeMaria 1994).

In an effort to better understand the dynamics of tropical cyclogenesis, several field campaigns have been conducted in recent years. The NOAA multi-year Intensity Forecasting Experiment (IFEX) that started in 2005, the Tropical Cloud Systems and Processes (TCSP) also in 2005, and the NAMMA project in 2006 are examples of these campaigns. Other earlier efforts include the Tropical Experiment in Mexico (TEXMEX; Bister and Emanuel 1997), and the Rainband and Intensity Experiment (RAINEX; Houze et al. 2006, 2009). The most recent field experiments are the PREDICT and the NASA Genesis and Rapid Intensification Processes (GRIP), which started in the 2010 hurricane season.

Limited observations of both the precursors and the subsequent tropical cyclogenesis process exist. Dropwindsonde data gathered during NAMMA and NOAA IFEX in 2006 constitute a very unique dataset since it sampled major AEWs over the eastern Atlantic, including the two AEWs cases presented in this study. Given the fact that this data was not assimilated into the NOAA/NCEP models in real time, it provides an opportunity to evaluate its impact in the interpretation of the structure and evolution of

some AEWs into TCs. Besides that, it represents an opportunity to validate HWRFx's dynamics and thermodynamics and to determine if early sampling of tropical disturbances has the potential to improve the cyclogenesis forecasts.

4. EXPERIMENTAL DESIGN

4.1 Cases Selection

Two AEWs from the 2006 Hurricane Season have been selected for this study. One AEW is the precursor of Hurricane Helene, hereinafter to be called HAEW (where H refers to Helene). Helene was a long-lived Cape Verde hurricane that remained at sea and attained category 3 on the Saffir-Simpson Hurricane Scale. Its cyclogenesis was reasonably well anticipated as it was just moving off the African coast about 24-h prior to TC formation, and many of the global forecast models accurately predicted it (Brown 2006). The high predictability of Helene makes it ideal to study how cyclogenesis occurred, which might provide insight on less predictable cases. Helene is the only case of tropical cyclogenesis that was sampled off the coast of Africa (by NAMMA) and after genesis (by NOAA). Furthermore, the NAMMA airborne data gathered were not assimilated into NOAA/NCEP models in real time, which provides the opportunity to study the impact of this additional data for the prediction of cyclogenesis. The second AEW preceded the HAEW. Particular interest in studying this wave came from the fact that intensification into a TC did not occur and due to dropwindsonde data availability from NAMMA for its further examination. Further in this document, the non-developing AEW will be referred as NDAEW (where ND mean non-developing).

Figure 4.1 is a Hovmöller diagram of Meteosat-8 Infrared (IR) imagery during the period of September 7 2330 UTC to September 13 1130 UTC showing the evolution of these AEWs. The red circles in the image follow the NDAEW and the yellow circles the HAEW. Satellite imagery, NHC text products, and the NAMMA dropwindsonde

observations were utilized in the following two sections to describe the AEWs initial environment and further evolution.

4.1.1 Pre-Helene non-developing AEW

The NDAEW came off the West African coast on September 8 0000 UTC. At that time, the Meteosat-8 SAL tracking product showed dry air proximity north and west of the elongated cloud cluster associated with the NDAEW (Fig. 4.2). The SAL is a dry, well-mixed layer that often extends to 500-hPa over Africa during the summer months (Carlson and Prospero 1972) and is associated with AEWs that advance westward from the North African coast. According to Dunion et al. (2004), when the Saharan dry air engulfs either a TC or an AEW, much of their deep convection dissipates, thus weakening these tropical systems while still over the warm tropical Atlantic.

Although the wave was not yet identified in the NHC Tropical Analyses and Forecasting Branch (TAFB) surface analysis on September 8 1200 UTC, the first NAMMA flight to investigate this system commenced almost immediately after this time. A total of fifteen dropwindsondes were launched from the aircraft at approximately 200-km intervals starting at 1337 UTC (first dropwindsonde release) and ending at 1830 UTC (last dropwindsonde release). The blue numbers in Figs. 4.4-4.7 indicate the order in which the dropwindsondes were released in the NDAEW environment. These figures portray dropwindsonde data of temperature (Celsius degree), RH (%), geopotential height (meters), wind magnitude (kt), and wind direction at the mandatory levels 300, 400, 500, 700, 850, 925, and 1000 hPa. To refer to each particular dropwindsonde, the letter D followed by a number was used. Both the dynamic and thermodynamic data from the

dropwindsondes was used to verify the environment at the AEW and thus validate the HWRFx CNTRL and EXP IC on September 8 at 1800 UTC.

Dynamically, the dropwindsondes sampled a weak wind structure that appeared unfavorable for development at that time. Figures 4.4-4.6a showed that starting from 1000 hPa up to 500 hPa the dropwindsondes sampled two cyclonic circulations each one north and south of 13°N, however neither definitively closed. The axis of the NDAEW was located approximately at 19°W where wind shifts from southeasterly to northeasterly in the northern part of the wave. Maximum wind speed at 1000, 925, 850, 700, and 500 hPa was 15, 20, 15, 35, and 25 kt, respectively. At 400 hPa, there were mixed wind patterns where the northern cyclonic circulation prevailed, however below 13°N winds were anticyclonic west of 19°W but cyclonic eastward (Fig. 4.6b). At 300 hPa, there were also mixed wind patterns but anticyclonic wind dominated, especially west of the wave axis (Fig. 4.7). Maximum wind speed at 400 and 300 hPa was 30 kt and 20 kt, respectively.

Thermodynamically, the dropwindsondes sampled SAL dry air engulfing the northern part of the NDAEW axis, which represents in part an unfavorable environment for development. The plots at the mandatory levels 1000 hPa to 500 hPa (Figs. 4.4-4.6a) indicated that in general D1, and D9-D15 reported lowest RH percentages. From this group of eight dropwindsondes and from 1000 hPa to 700 hPa, D12-15 showed to have the highest temperatures. D12, D13, and D14 were located in Senegal where air temperature is expected to be warmer due to the heating of land. These dropwindsondes were released during 1734 UTC-1808 UTC (sunset to dusk) when the land was still warm from the daylight solar incoming radiation. Conversely, D15 was off the coast in the

eastern Atlantic (17.5°N 18.7°W) but nearby the strongest SAL signal that was engulfing the NDAEW around 1800 UTC (Fig. 4.3). According to Dunion et al. (2004), the SAL characterizes by being intensely dry and warm. Skew-T diagrams of the dropwindsondes confirmed a much overall drier environment west-northwest of 19°W north of 12°N for D1, D9 and D10 (Figs. 4.8-4.9a) where D9 showed the strongest SAL signal. D13, D14 and D15 to the north-northeast of 19°W north of 14°N also captured a dry environment, though D15 in a lesser extent (Figs. 4.9b-4.10). Conversely, the vertical profiles of D11 and D12 showed a largely moister environment with limited slightly drier regions (Fig. 4.11). The Meteosat-8 true color imagery, which provides a better detection and tracking of suspended aerosols and their source, showed that during September 8 1800 UTC Saharan dust (brown haze) was spread over the location of D1, D9-10 and D15 (Fig. 4.12). It also showed that D13 and D14 were located over the Saharan Desert, which explains its stronger SAL signal. The remainder seven dropwindsondes of the flight track (D2-D8) showed generally a quasi-saturated to saturated environment (Figs. 4.13-4.16). The Meteosat-8 true color imagery showed none to minimal signal of brown haze associated with Saharan dust over the region sampled by these dropwindsondes (Fig. 4.12).

Starting September 9 0000 UTC, the SAL tracking imagery evidenced dry air intrusion at the NDAEW (Fig. 4.17), which acted to dissipate most of its convection by September 9 1200 UTC (Figs. 4.18-4.19). The Hovmöller of Meteosat-8 IR imagery (Fig. 4.1) illustrated that after September 9 the cloud coverage associated with the NDAEW (red circles) significantly reduced and that by September 12 1130 UTC its

signal started to vanish. Both an unfavorable wind structure and a dry environment appeared to be major factors on the development hindrance of the NDAEW.

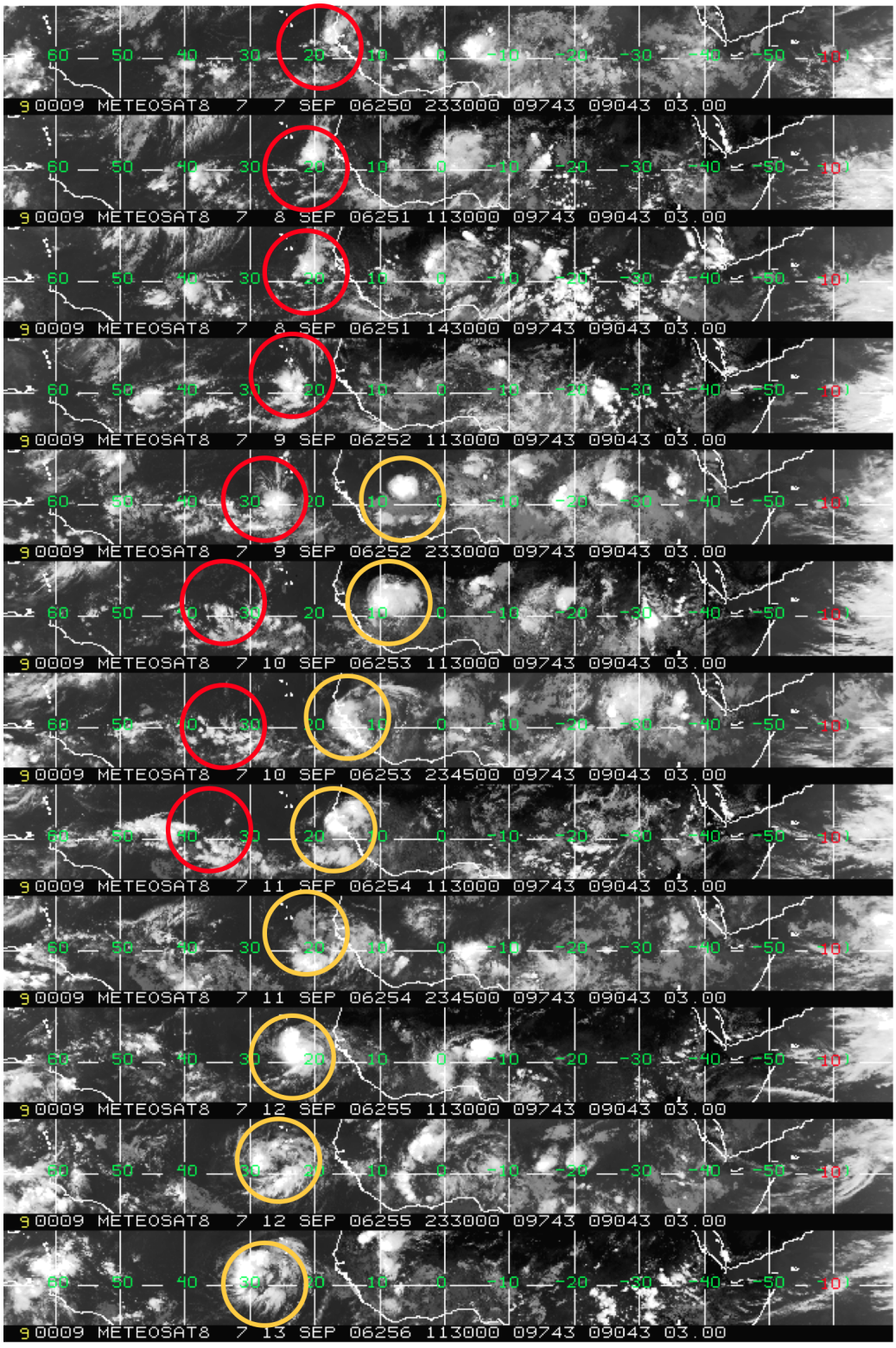

Figure 4.1 Hovmöller of Meteosat-8 IR imagery (Sep 7 2330 UTC – Sep 13 1130 UTC) depicting the NDAEW (red circles) and the HAEW (yellow circles).

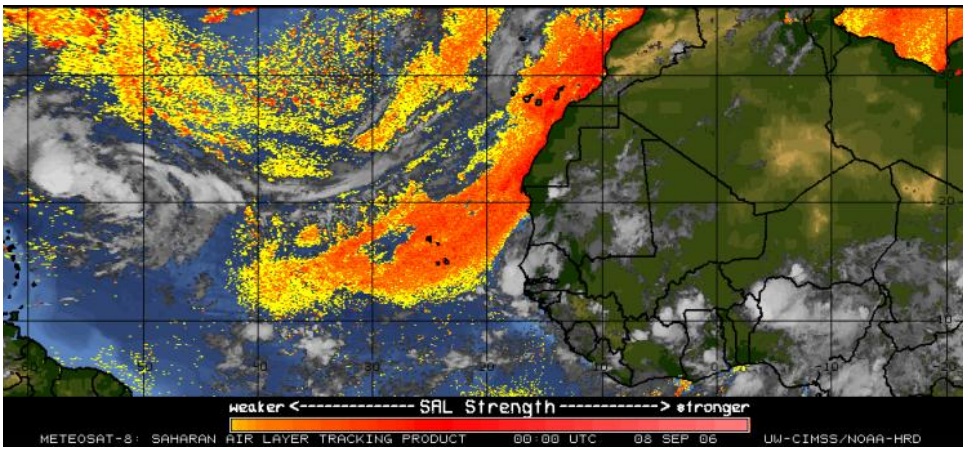

Figure 4.2 SAL tracking imagery showing the NDAEW coming off the African coast on September 8 0000 UTC.

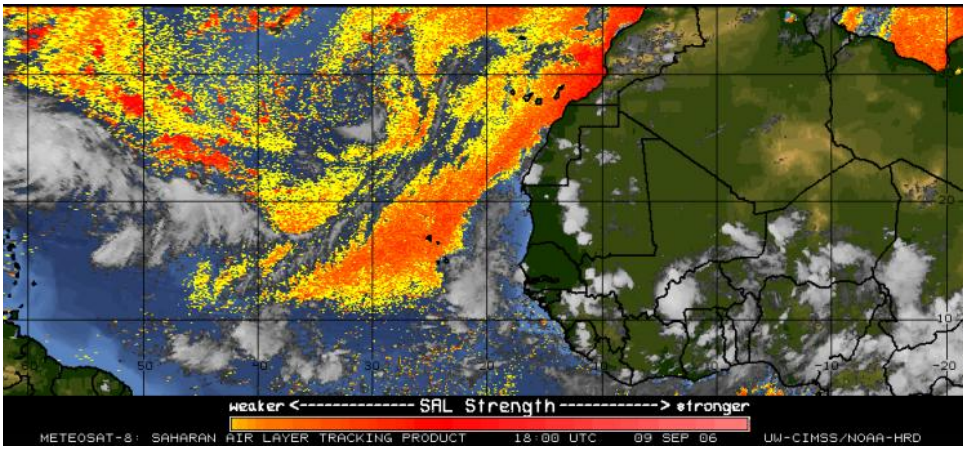

Figure 4.3 SAL tracking imagery showing the NDAEW being engulfed by dry air on September 8 1800 UTC.

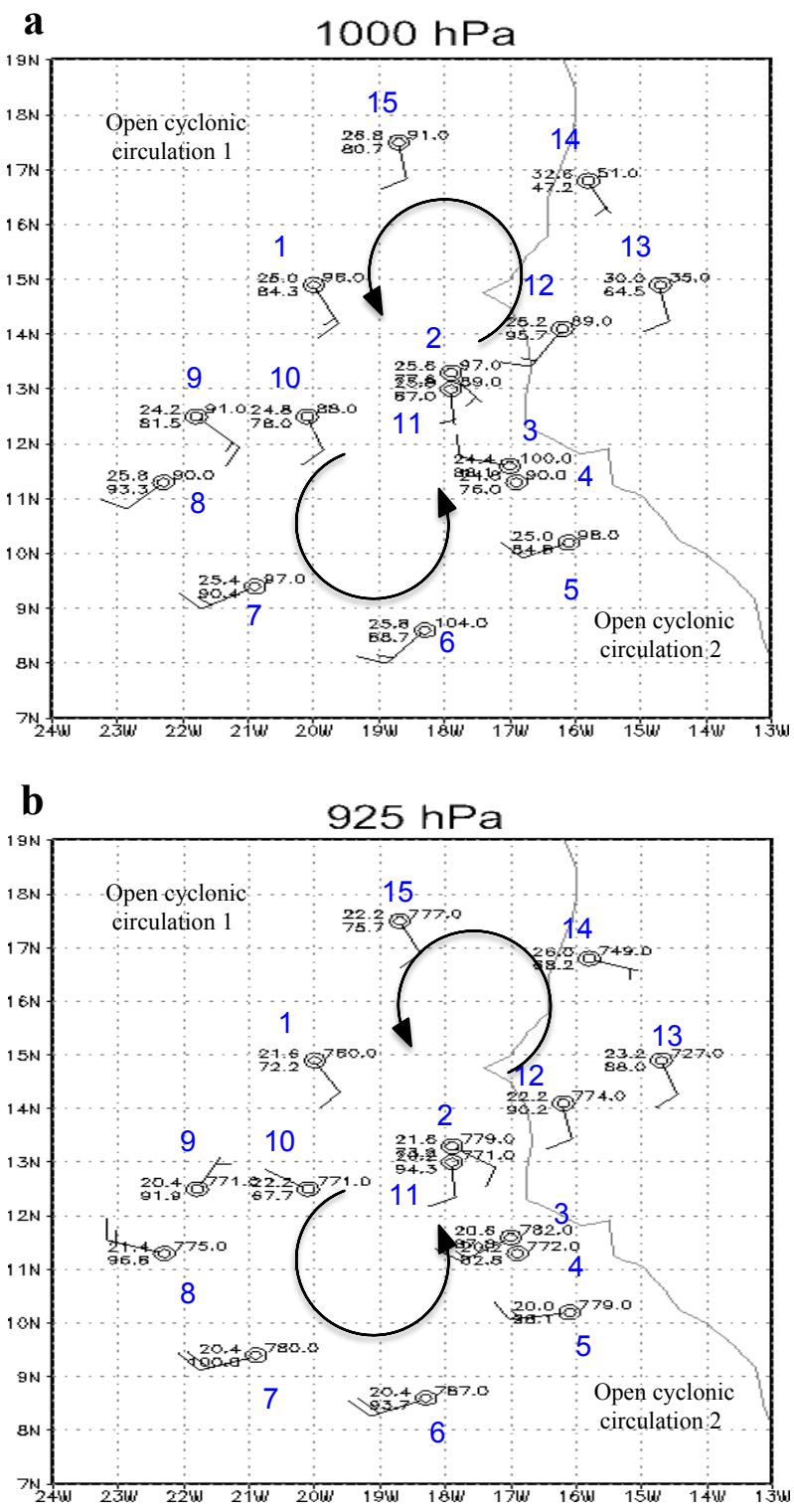

Figure 4.4 NDAEW dropwindsonde data at mandatory levels 1000 hPa (a) and 925 hPa (b).

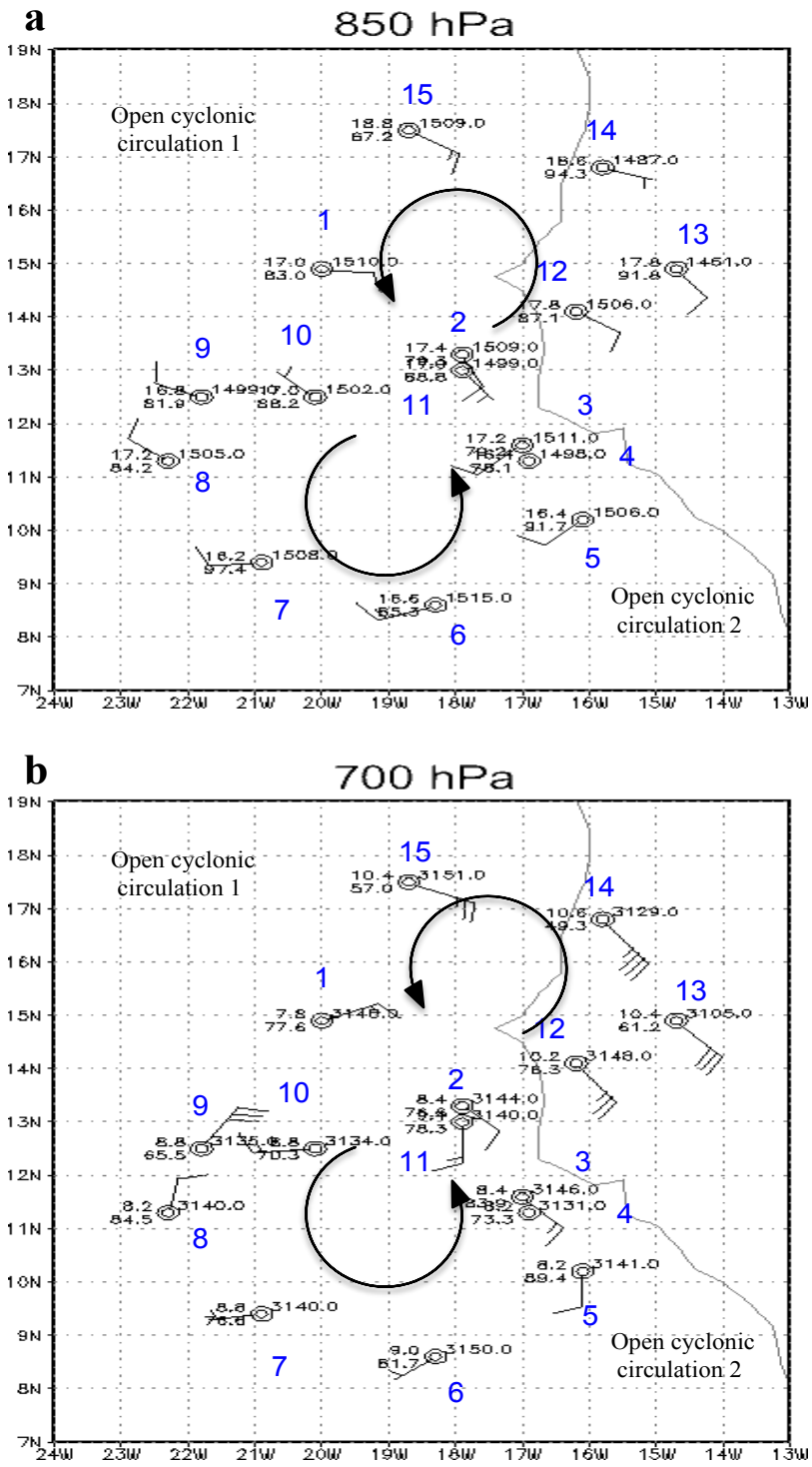

Figure 4.5 NDAEW dropwindsonde data at mandatory levels 850 hPa (a) and 700 hPa (b).

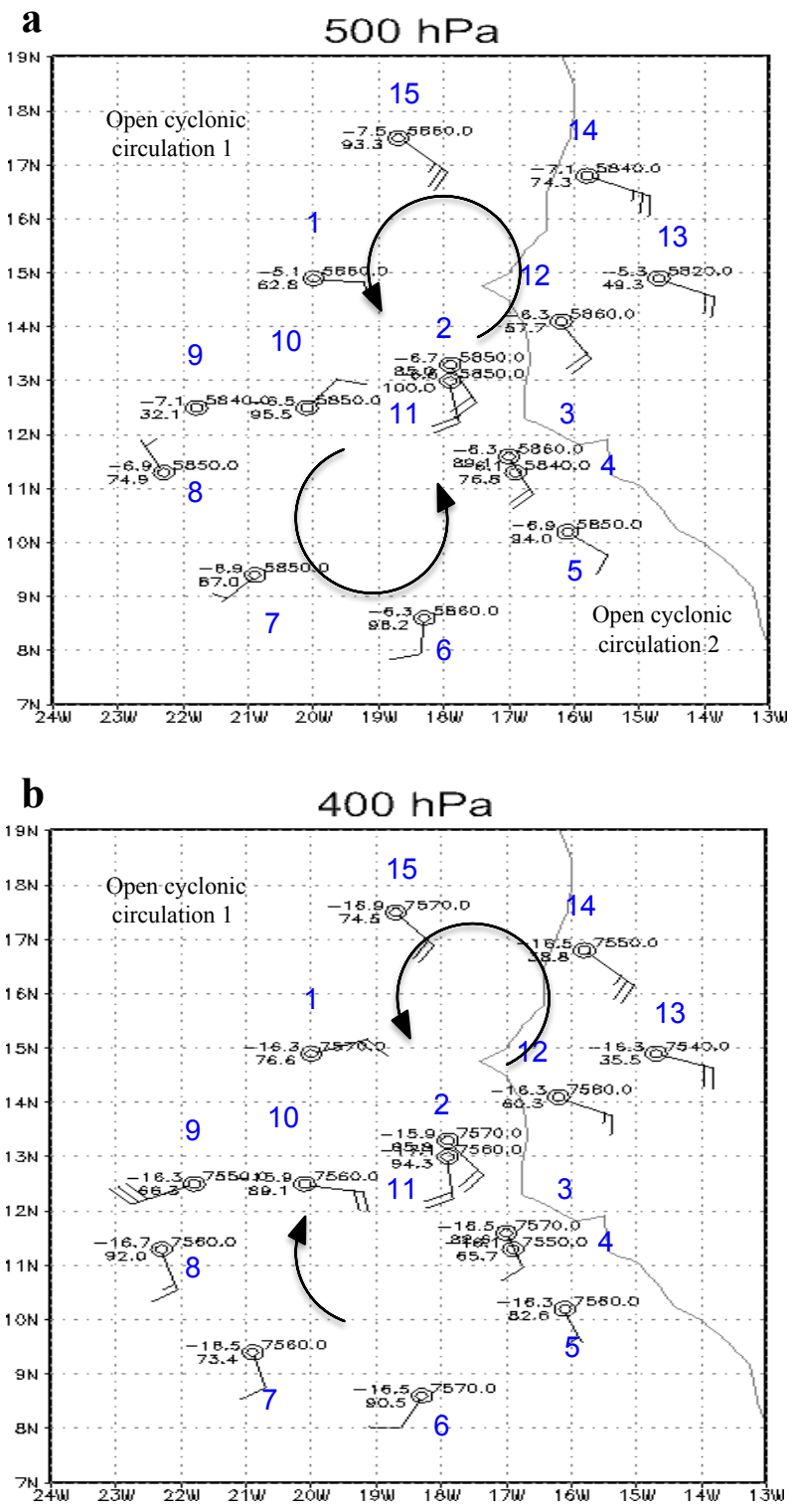

Figure 4.6 NDAEW dropwindsonde data at mandatory levels 500 hPa (a) and 400 hPa (b).

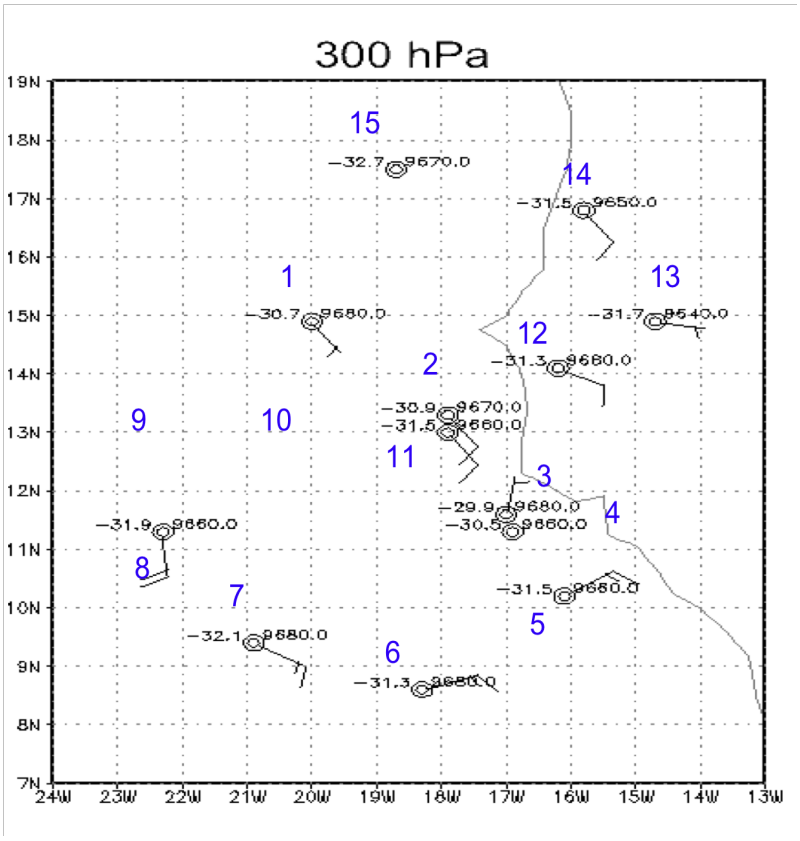

Figure 4.7 NDAEW dropwindsonde data at mandatory level 300 hPa.

a

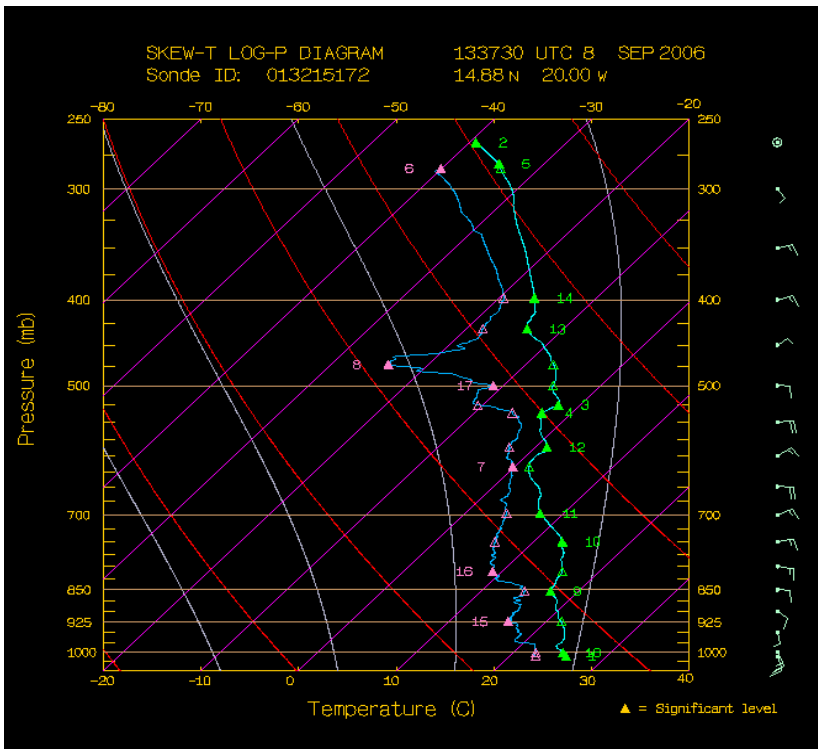

b

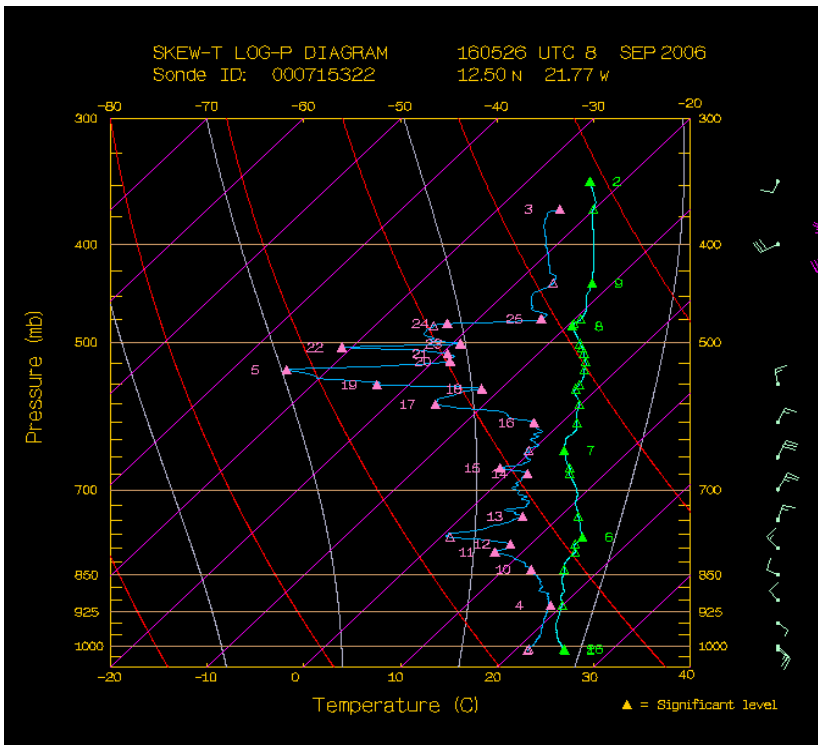

Figure 4.8 NDAEW sounding data from dropwindsondes (a) 1 and (b) 9.

a

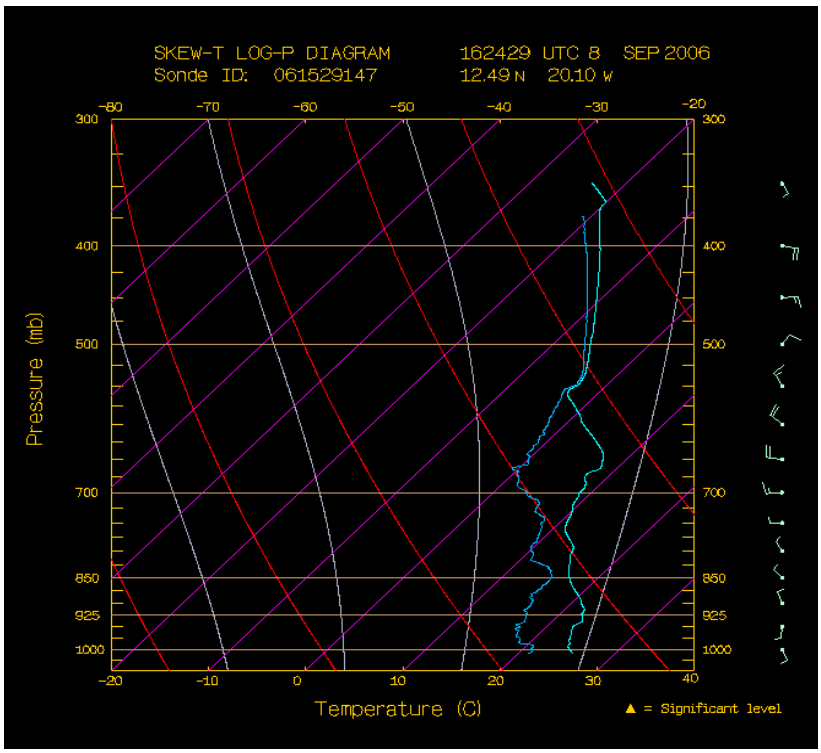

b

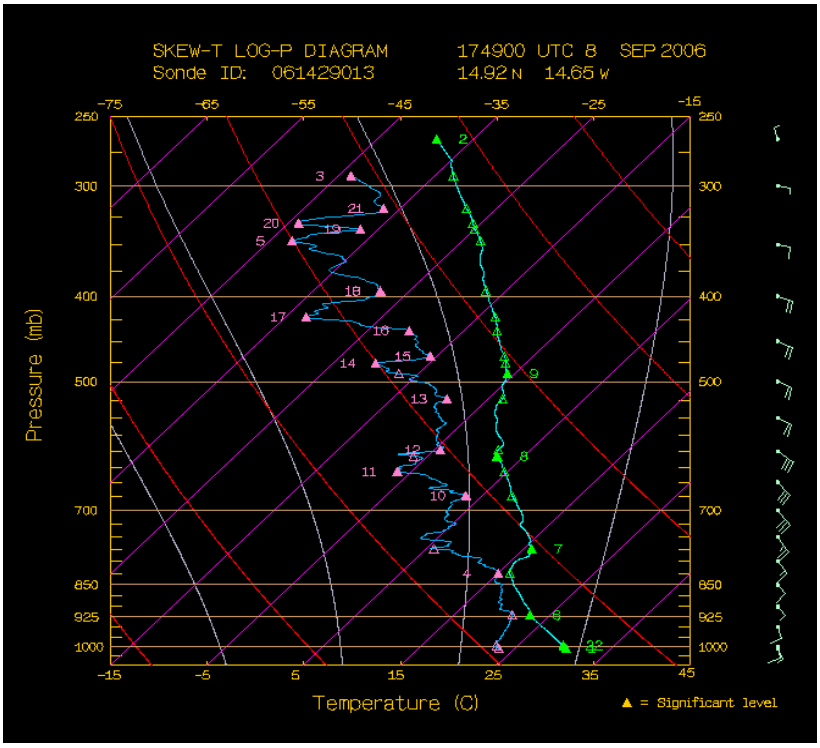

Figure 4.9 NDAEW sounding data from dropwindsondes (a) 10 and (b) 13.

a

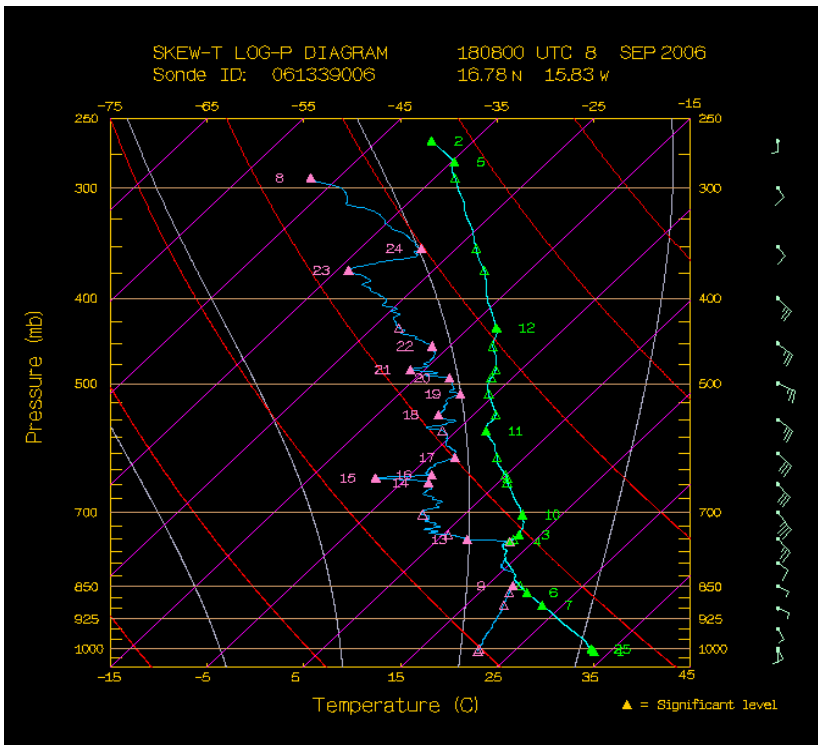

b

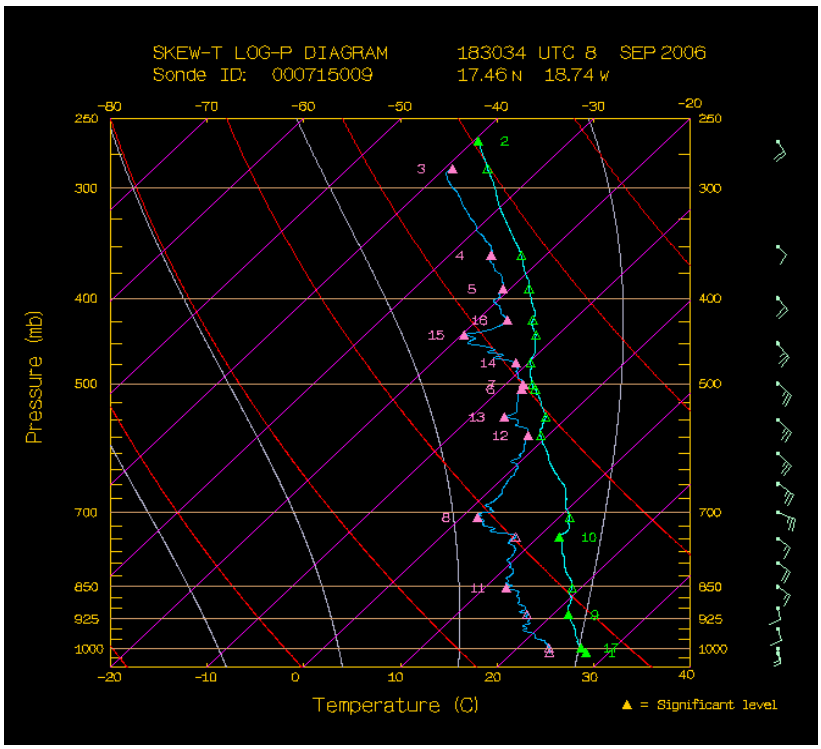

Figure 4.10 NDAEW sounding data from dropwindsondes (a) 14 and (b) 15.

a

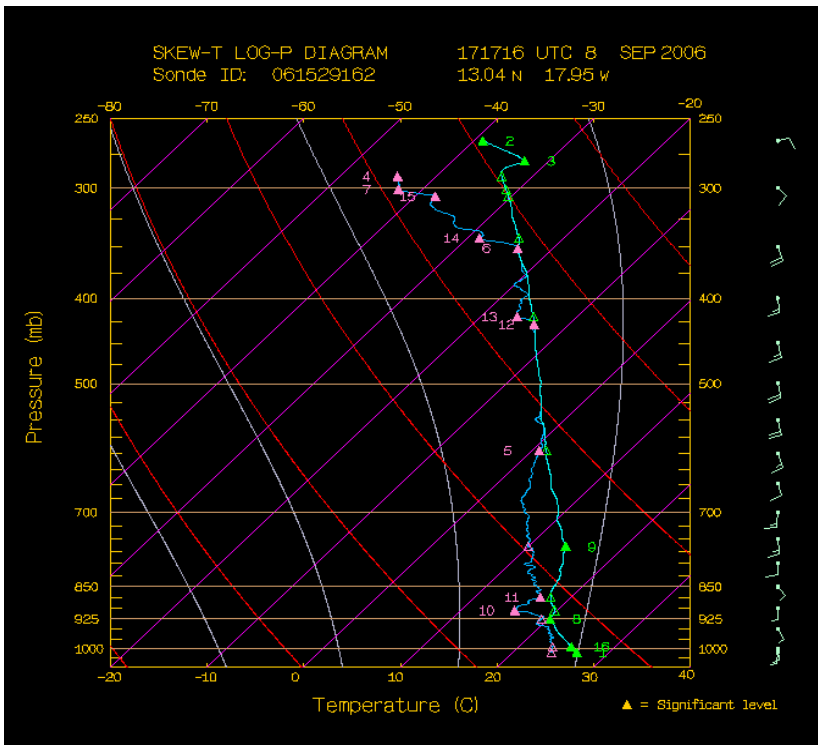

b

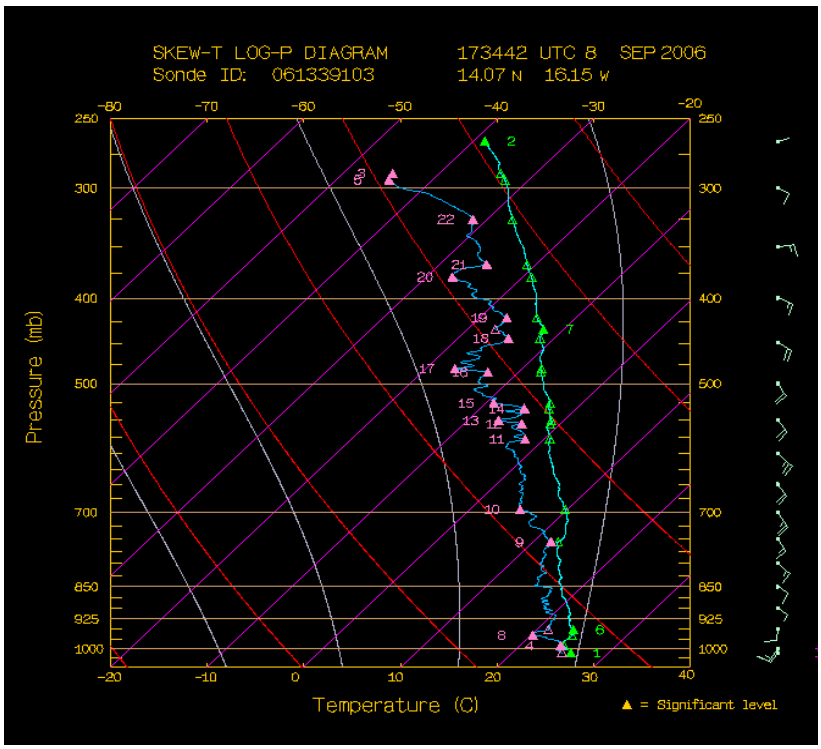

Figure 4.11 NDAEW sounding data from dropwindsondes (a) 11 and (b) 12.

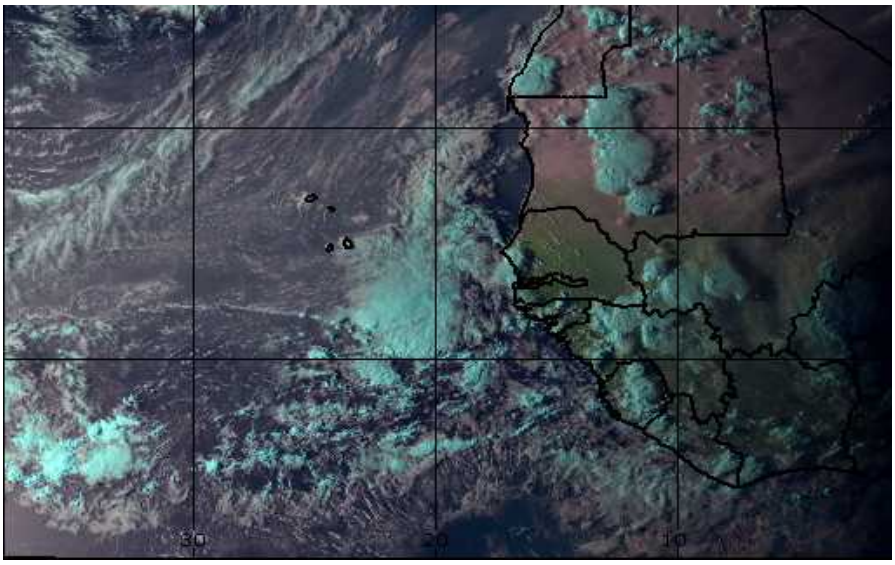

Figure 4.12 Meteosat-8 true color imagery on September 8 18 UTC depicts a Saharan dust storm affecting the NDAEW. Image courtesy of University of Wisconsin – CIMSS.

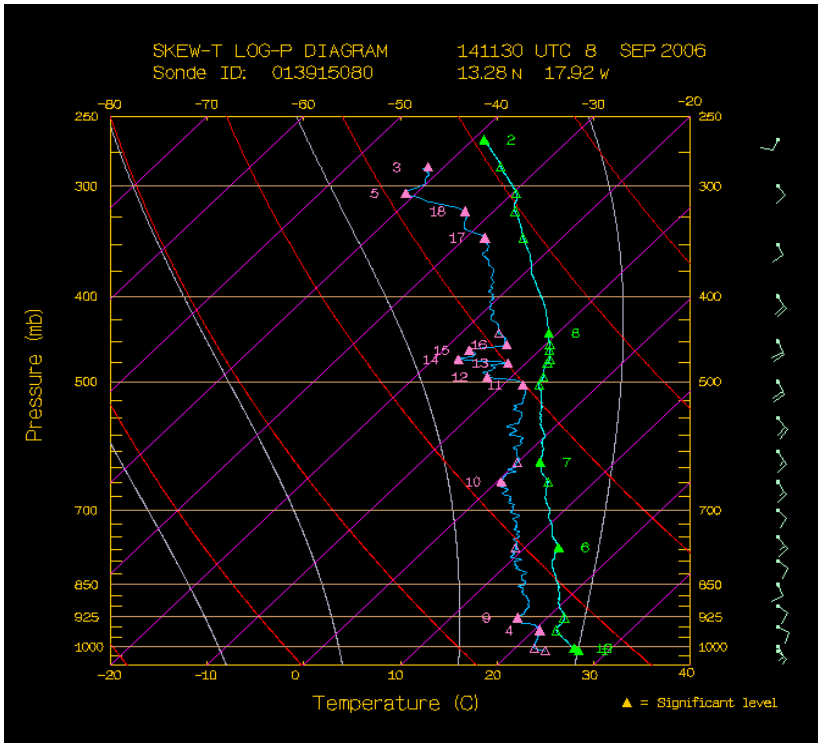

Figure 4.13 NDAEW sounding data from dropwindsonde 2.

a

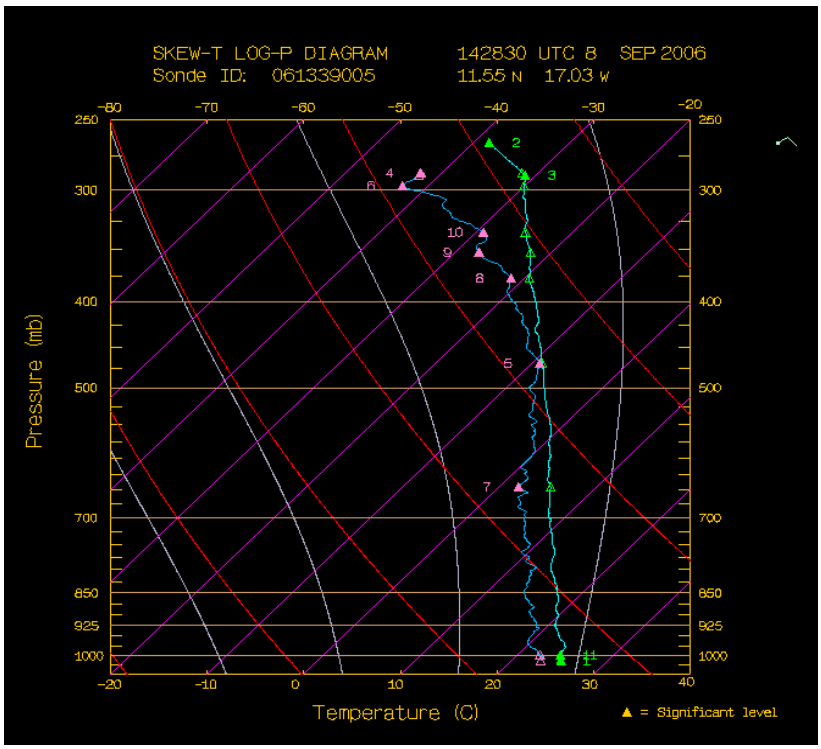

b

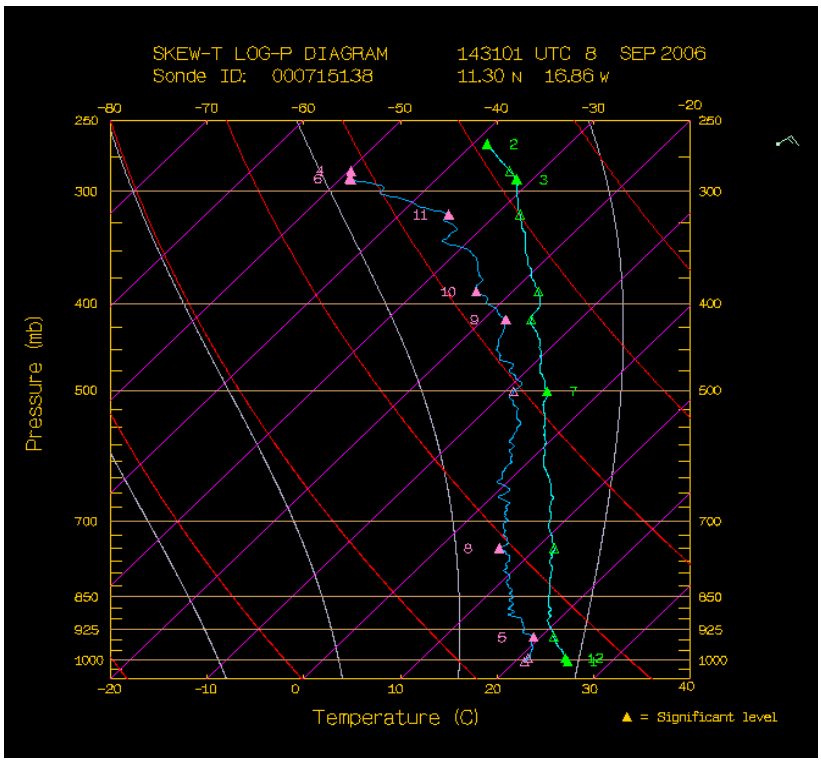

Figure 4.14 NDAEW sounding data from dropwindsondes (a) 3 and (b) 4.

a

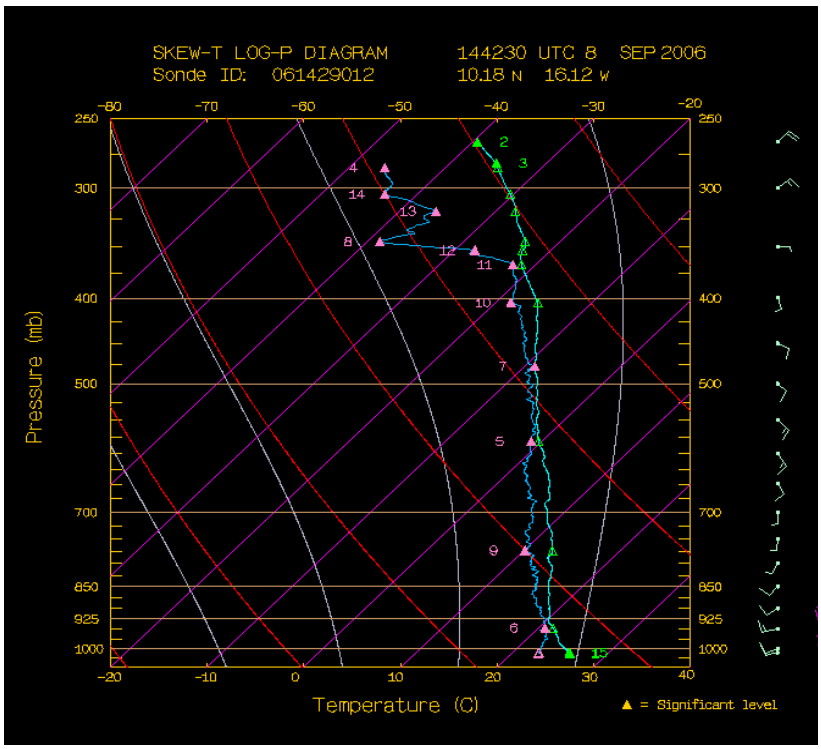

b

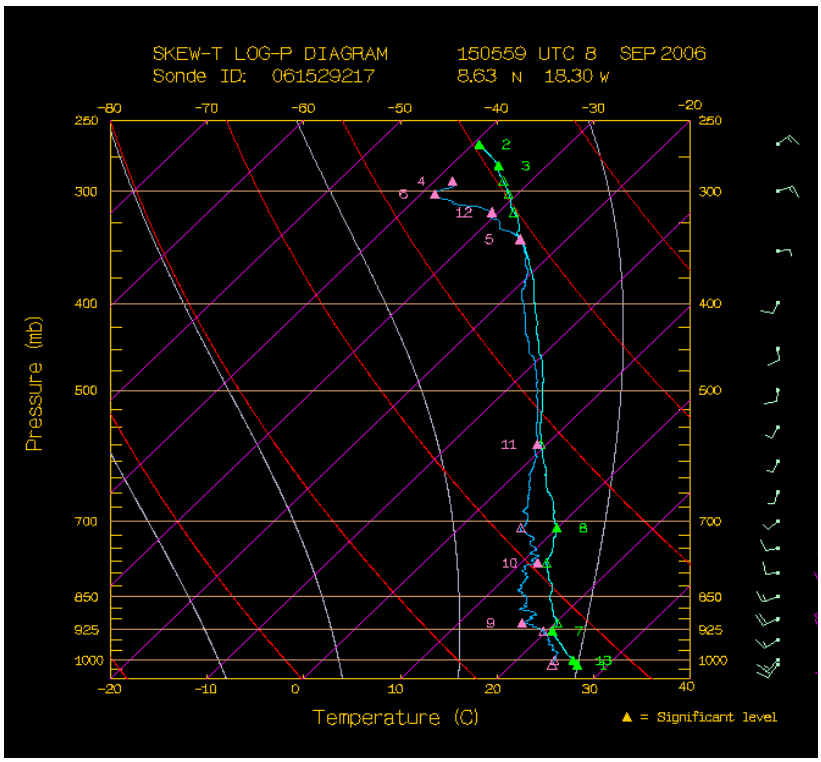

Figure 4.15 NDAEW sounding data from dropwindsondes (a) 5 and (b) 6.

a

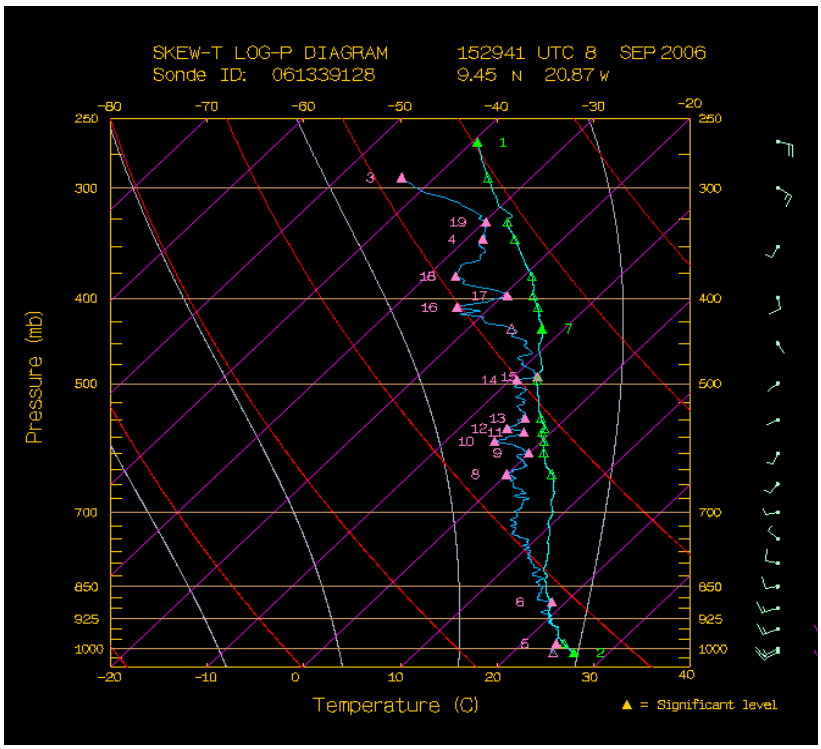

b

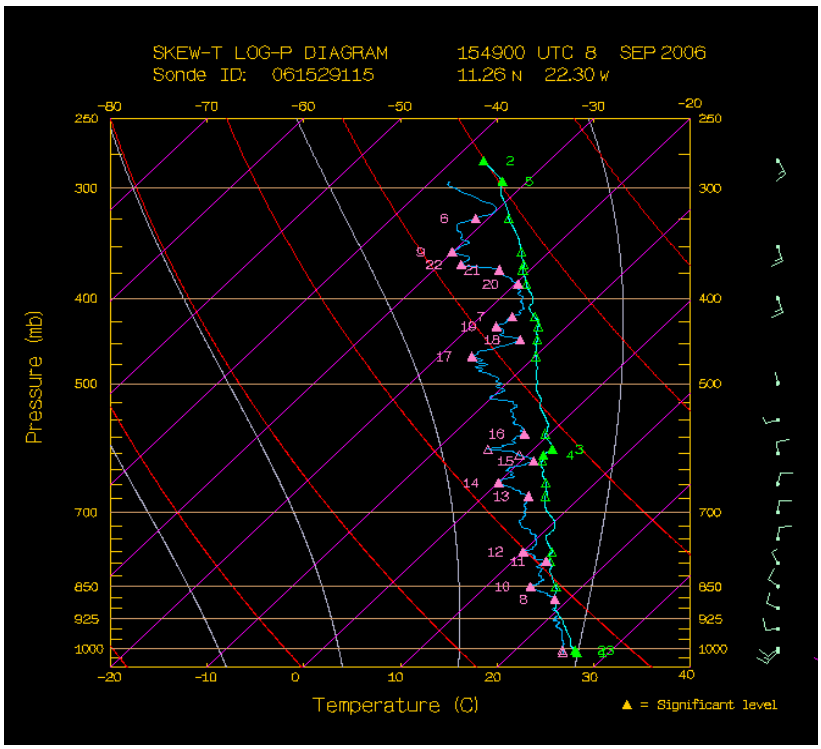

Figure 4.16 NDAEW sounding data from dropwindsondes (a) 7 and (b) 8.

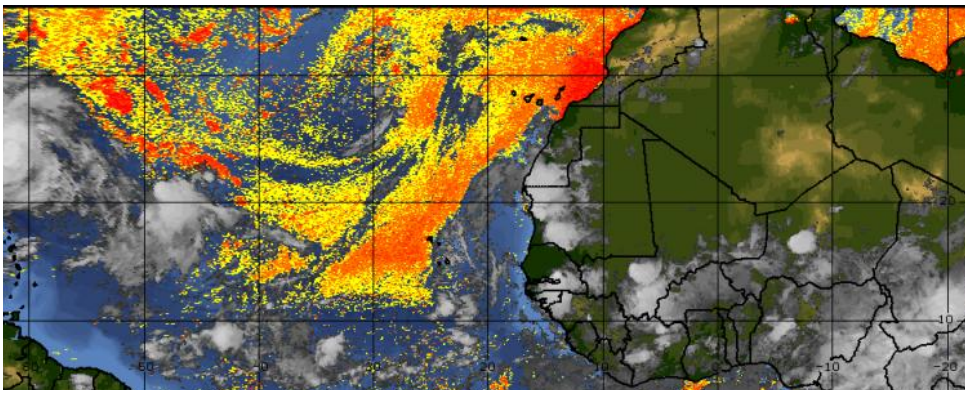

Figure 4.17 SAL dry air intrusion to the NDAEW on September 9 0000 UTC.

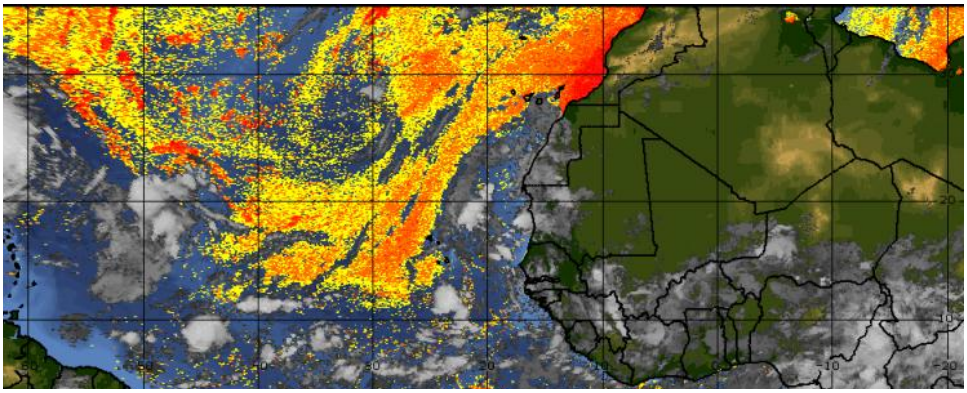

Figure 4.18 SAL dry air intrusion to the NDAEW on September 9 0600 UTC.

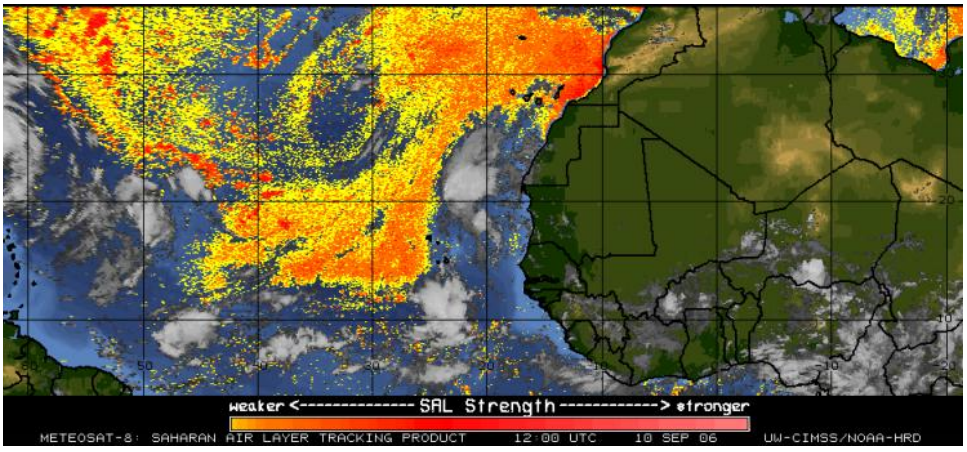

Figure 4.19 Remnants of the cloudiness associated with the NDAEW during September 9 1200 UTC.

4.1.2 2006 Hurricane Helene

The 2006 Hurricane Helene developed from an AEW associated with a broad area of low pressure that emerged from the coast of Africa on September 11 around 1130 UTC (Fig. 4.1). After the HAEW moved out the coast, showers and thunderstorms associated with the broad area of low pressure assisted in the organization of the system and a TD formed on September 12 1200 UTC. The SAL imagery at the time of cyclogenesis (Fig. 4.20) showed that similar to the NDAEW the HAEW was engulfed by dry air, however it was more distant from the system.

The first NAMMA flight to investigate the TD released its first dropwindsonde on September 12 1220 UTC and concluded the sampling at 1557 UTC. Contrary to the NDAEW flight mission, only seven dropwindsondes were utilized to sample the TD associated with the HAEW. Similarly to the NDAEW, Figs. 4.21-4.24 depict the flight track locations where dropwindsondes were released for the TD mission as well as their dynamic and thermodynamic data at the mandatory levels. Unlike the NDAEW, data at mandatory level 250 hPa were available for this case. Dynamic and thermodynamic data from the dropwindsondes was used to verify the environment of the TD and thus validate the HWRFx CNTRL and EXP IC on September 12 1800 UTC.

Regarding the wind dynamics, the TD cyclonic circulation was observed from 1000 hPa to 400 hPa (Figs. 4.21-4.23). At 300 hPa, winds were anticyclonic westward from 24°W and remained cyclonic eastward of that longitude (Fig. 4.24a). At 250 hPa, winds were anticyclonic westward from 23°W whereas cyclonic wind was sampled eastward by D4 and D5 (Fig. 4.24b). Maximum wind speed at 1000, 925, 850, 700, 500, and 400 hPa was 20, 30 (D6), 30 (D1), 50 (D2), 35, and 40 (D1) kt, respectively. At the

time of cyclogenesis, NHC reported maximum sustained winds of 25 kt and 30 kt during 1800 UTC, which matches pretty well the observed values from 1000 hPa to 850 hPa during that period. Maximum wind speed at the upper-levels 300 hPa and 250 hPa was 20 kt.

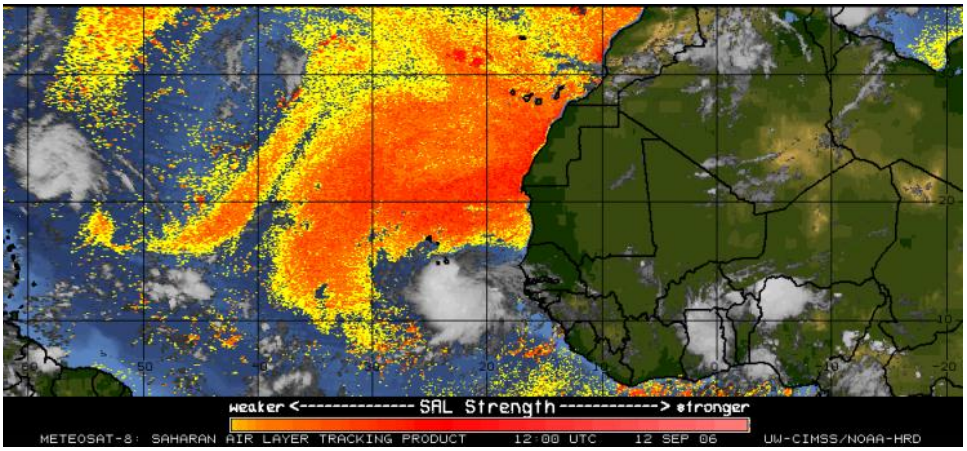

Figure 4.20 HAEW engulfed by dry air at the time of cyclogenesis on September 12 1200 UTC.

In terms of the thermodynamics, the RH observations at the mandatory levels 1000 hPa to 400 hPa showed that a moister environment existed at the D3, D4, D5 and D7 (Figs. 4.21-4.23). These dropwindsondes also generally reported lower temperatures from 1000 hPa to 700 hPa when compared to D1, D2 and D6, which reported warmer temperatures at these levels. However, the RH of D1, D2 and D6 indicated a drier environment west of the TD center for most of the mandatory levels. The drowindsondes vertical profiles of D1, D2 and D6 proved an overall drier environment at these locations west of the TD center, however more markedly at D1 and D6 (Figs. 4.25 and 4.26a). On the other hand, the skew-T diagram of D4 and D5 showed a quasi-saturated environment

(Figs. 4.26b and 4.27a) whereas the D3 and D7 depicted saturation through a great portion of the troposphere (Figs. 4.27b and 4.28). Although the SAL imagery on September 12 1800 UTC (Fig. 4.29) do not depicted dry air intrusion near 25°W-26°W (dry air was considerable distant from the system), the Meteosat-8 true color imagery showed Saharan dust (brown haze) spread over the TD (Fig. 4.30). The location of D1, D2 and D6 coincided with the region where the Saharan dust brownish haze looked denser (along the leading cyclonic clouds band).

During September 13, convective banding began to increase over the northwestern semicircle of the circulation and the TD slowly strengthened (Brown 2006), becoming TS Helene at September 14 0000 UTC. Moving in a west-northwestward direction over the tropical Atlantic Ocean, Helene progressively intensified and became a hurricane on September 16 1200 UTC. Further strengthening continued and Helene attained category 3 status on September 18 0000 UTC. Six hours later Helene reached its peak intensity of 105 kt. By September 24 1800 UTC, Helene became an extra-tropical cyclone about 275 n mi northwest of the Azores Islands.

Besides a favorable wind structure and moist environment at the core of the TD, the HAEW was associated with a broad area of low pressure since it emerged from Africa. These three factors combined might have acted to increase the low-level convergence as well as the moist convection, thus intensifying Helene.

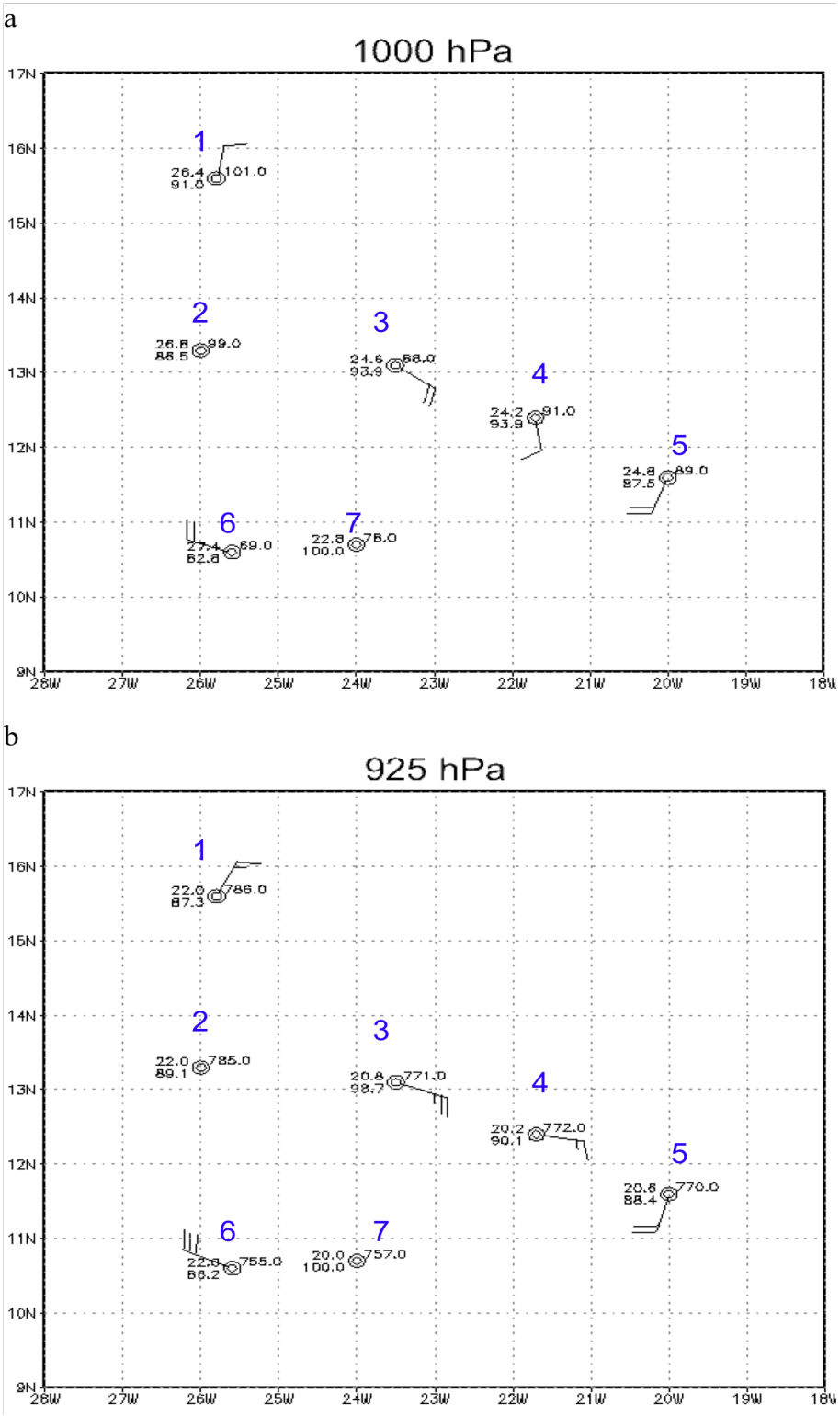

Figure 4.21 HAEW dropwindsonde data at mandatory levels 1000 hPa (a) and 925 hPa (b).

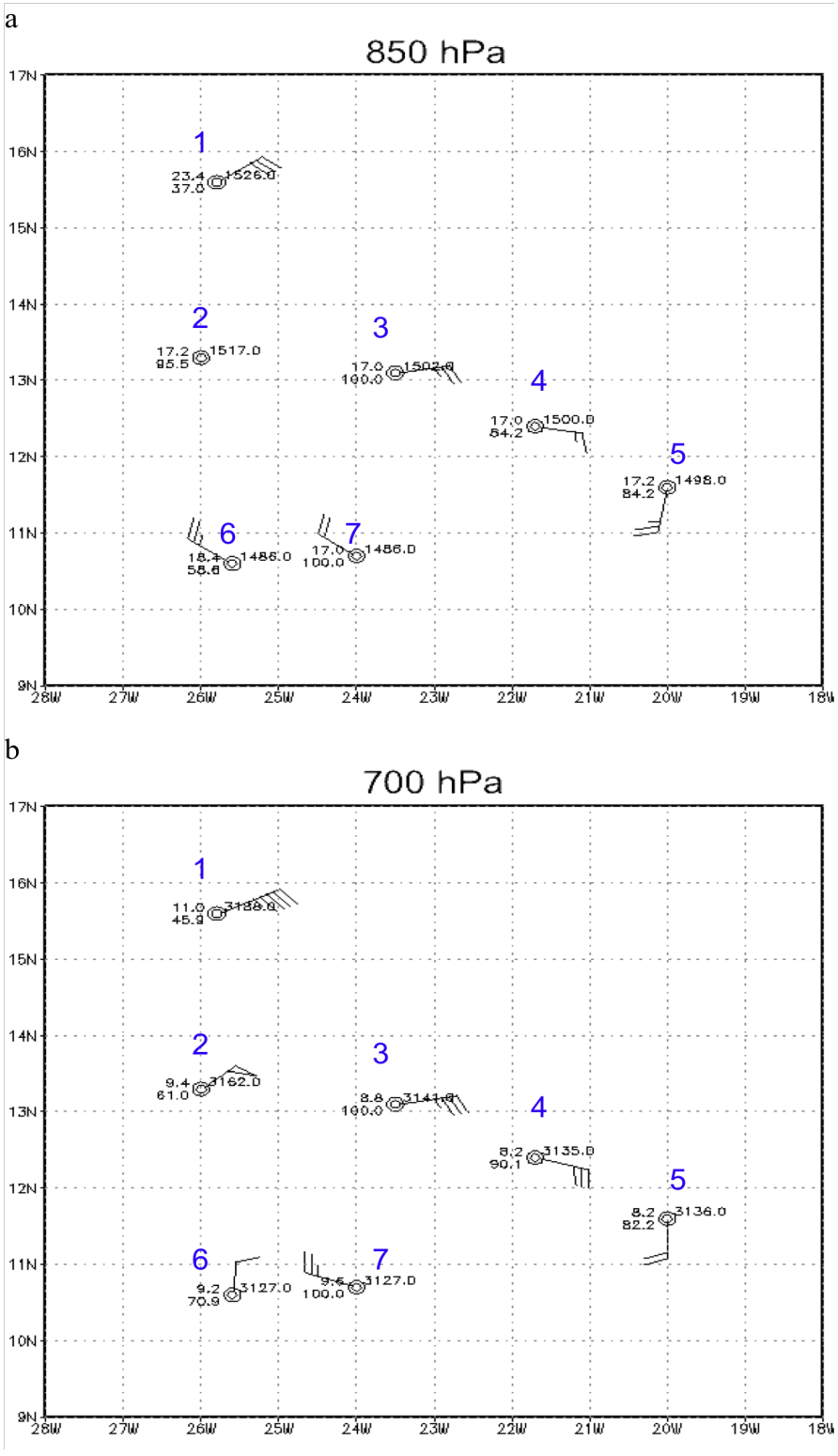

Figure 4.22 HAEW dropwindsonde data at mandatory levels 850 hPa (a) and 700 hPa (b).

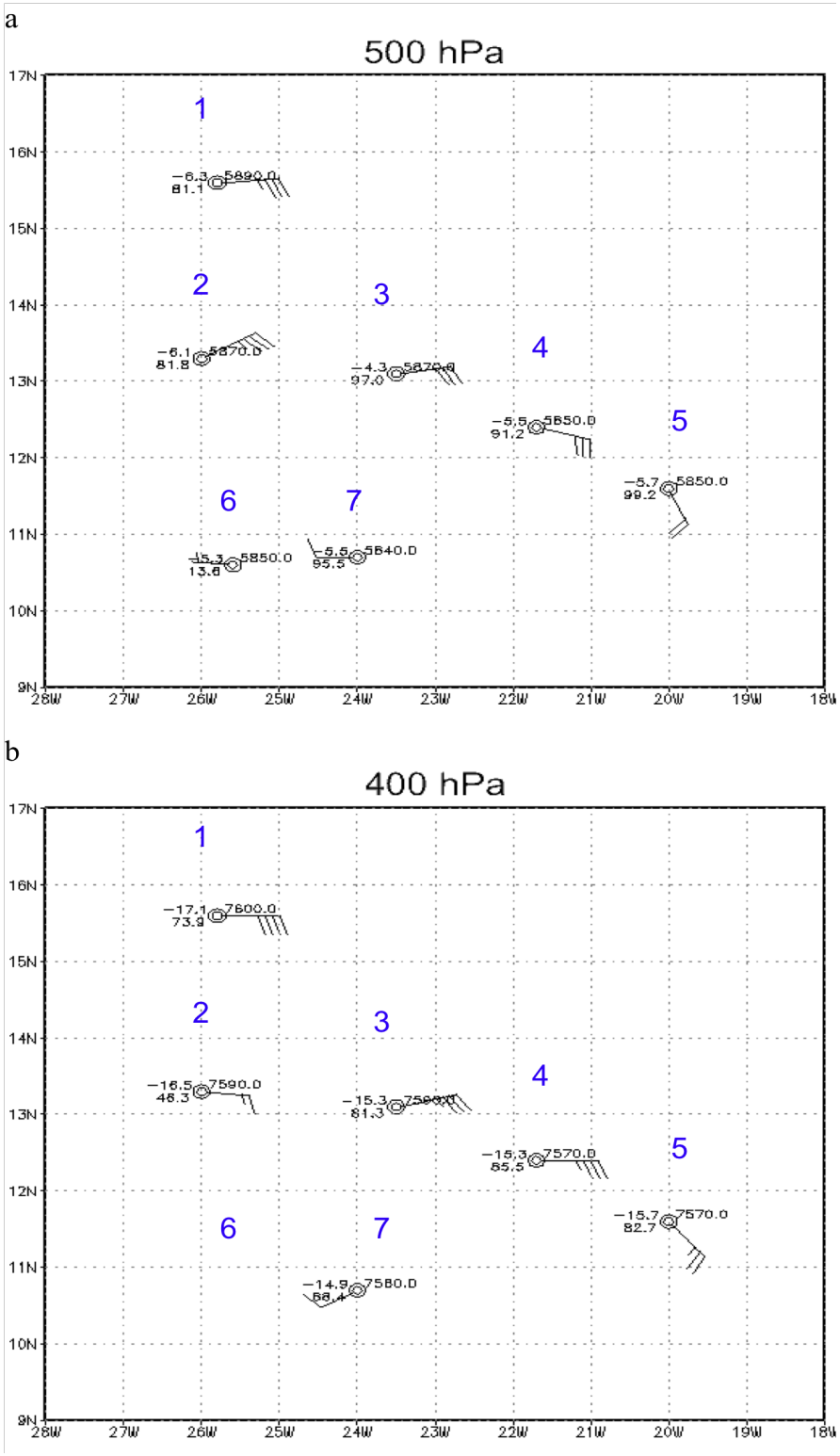

Figure 4.23 HAEW dropwindsonde data at mandatory levels 500 hPa (a) and 400 hPa (b).

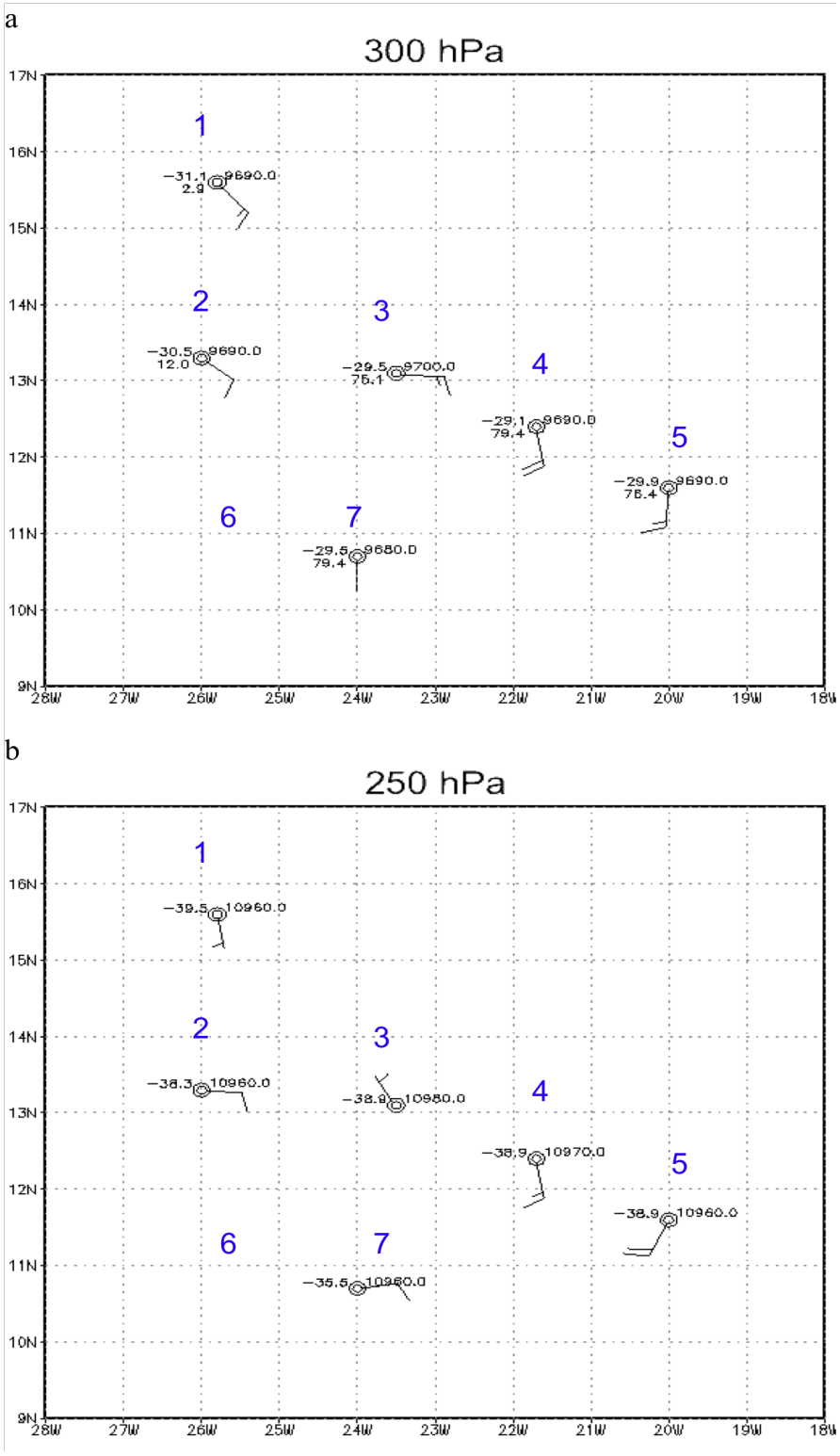

Figure 4.24 HAEW dropwindsonde data at mandatory levels 300 hPa (a) and 250 hPa (b).

a

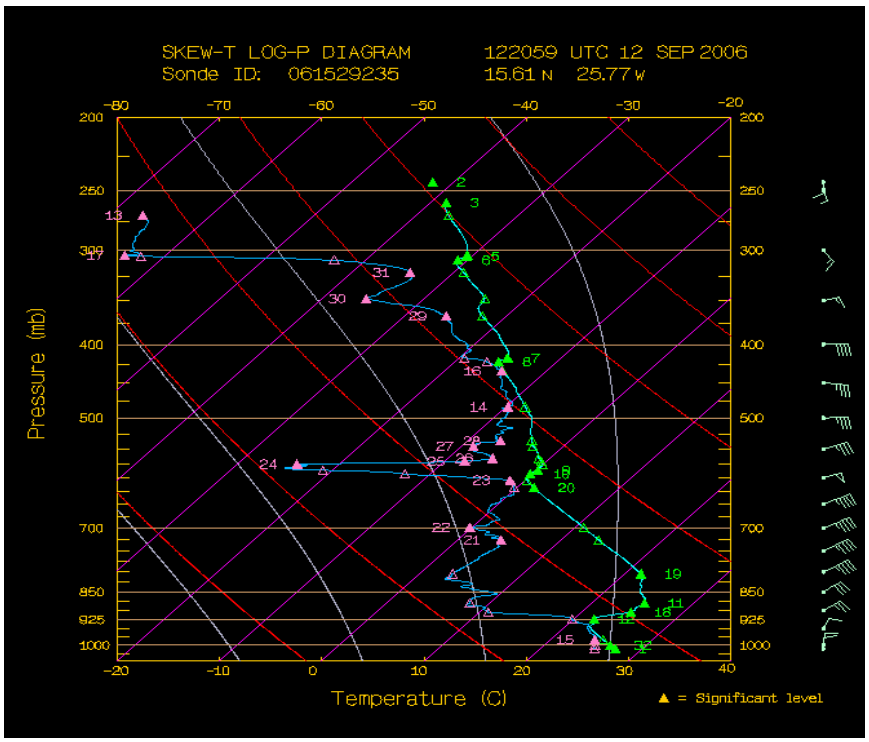

b

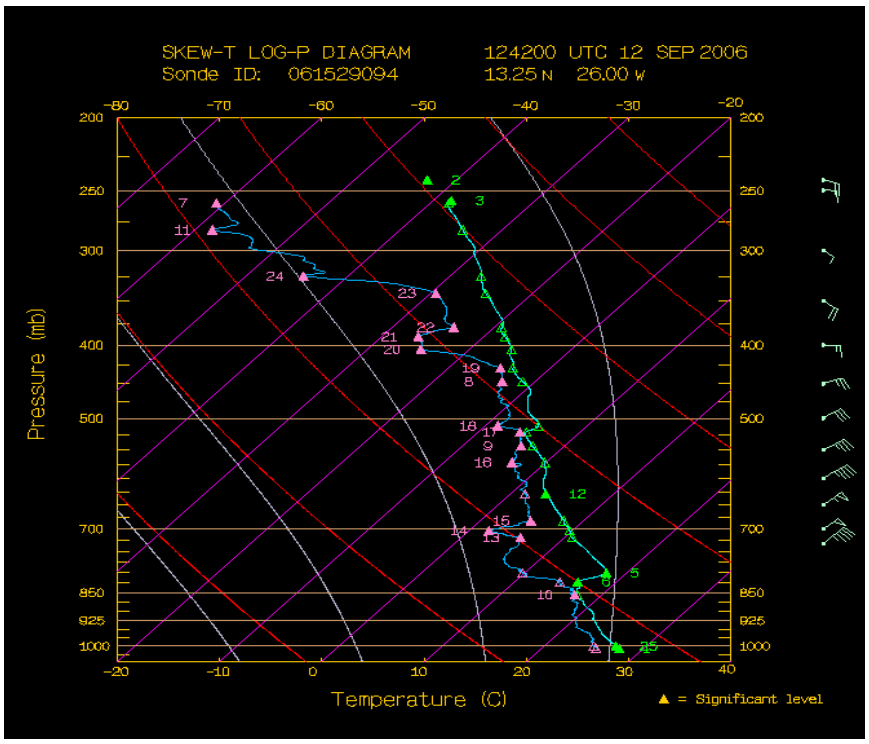

Figure 4.25 HAEW sounding data corresponding to dropwindsondes 1 and 2 in the flight track.

a

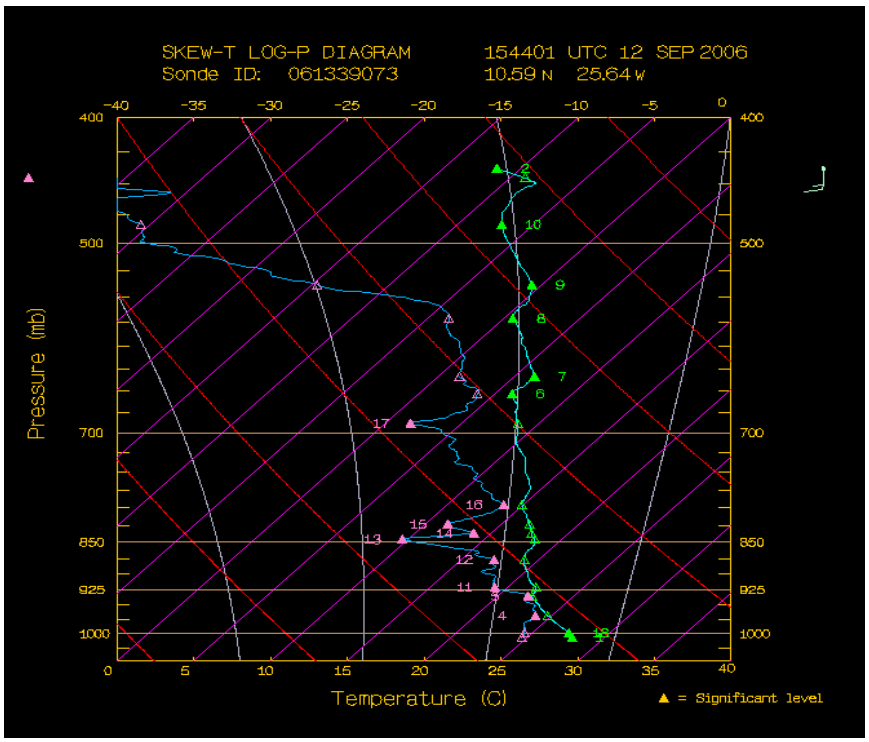

b

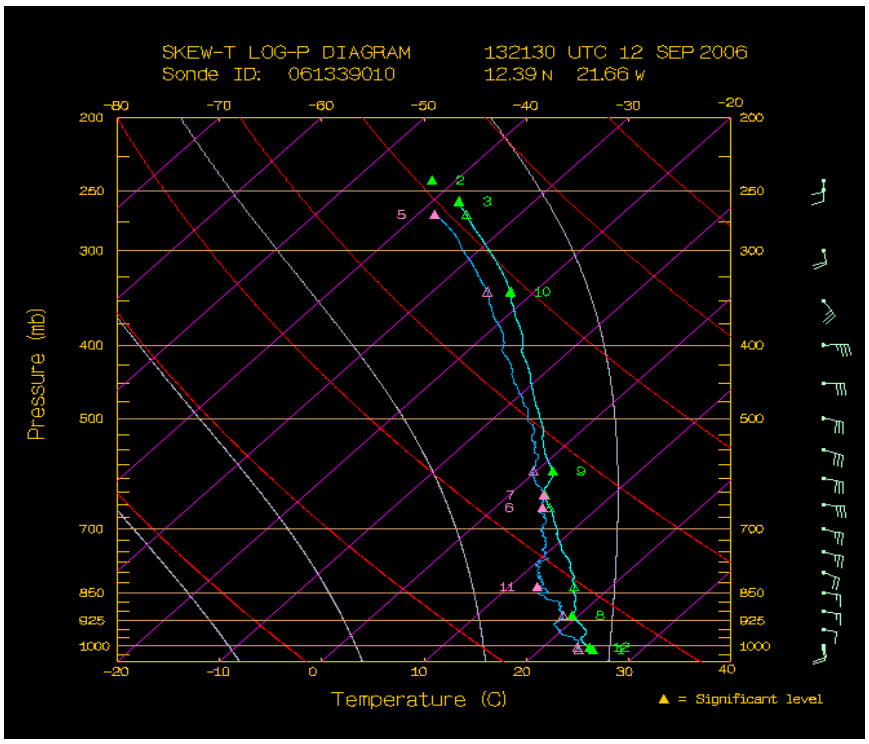

Figure 4.26 HAEW sounding data corresponding to dropwindsondes 6 and 4 in the flight track.

a

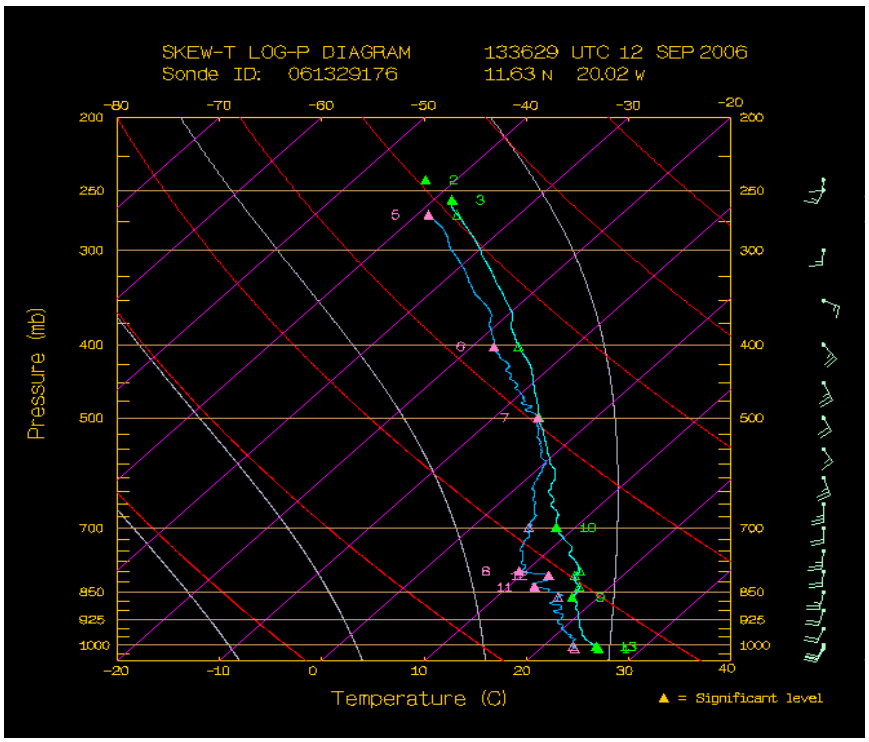

b

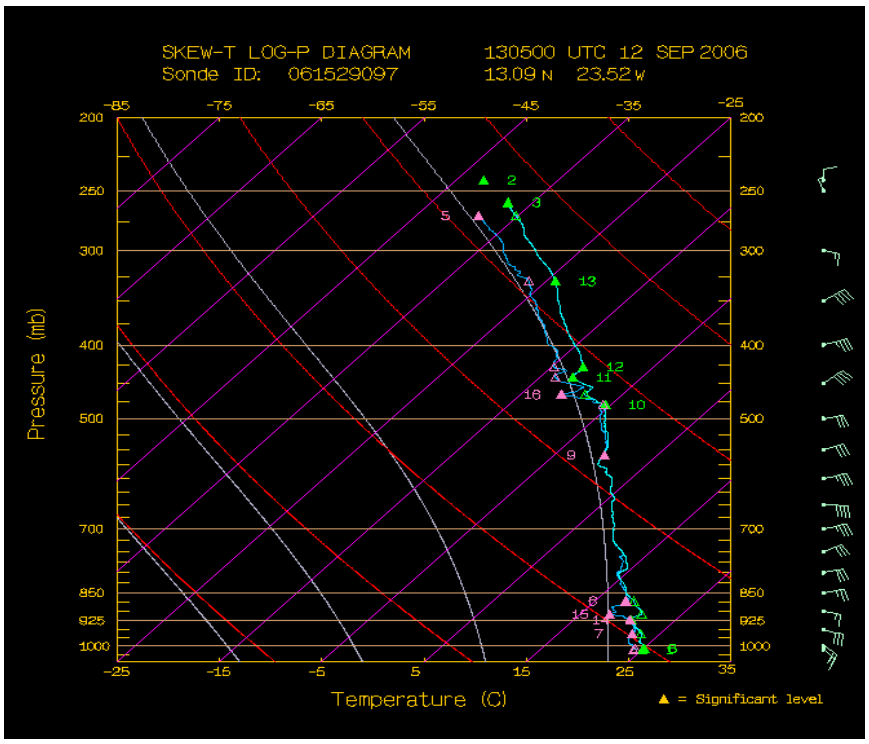

Figure 4.27 HAEW sounding data corresponding to dropwindsondes 5 and 3 in the flight track.

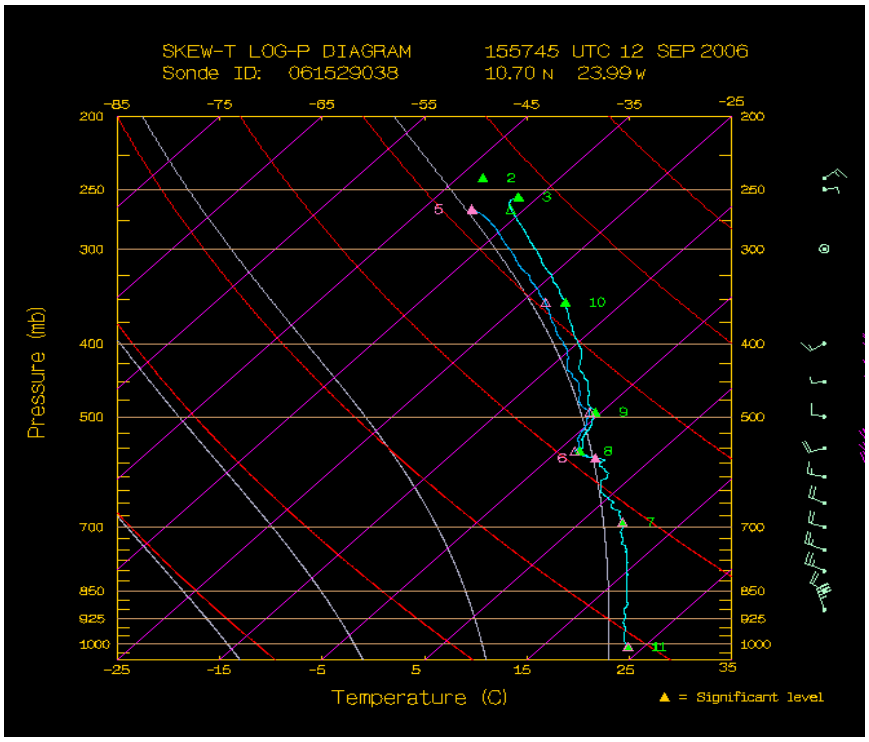

Figure 4.28 HAEW sounding data corresponding to dropwindsonde 7 in the flight track.

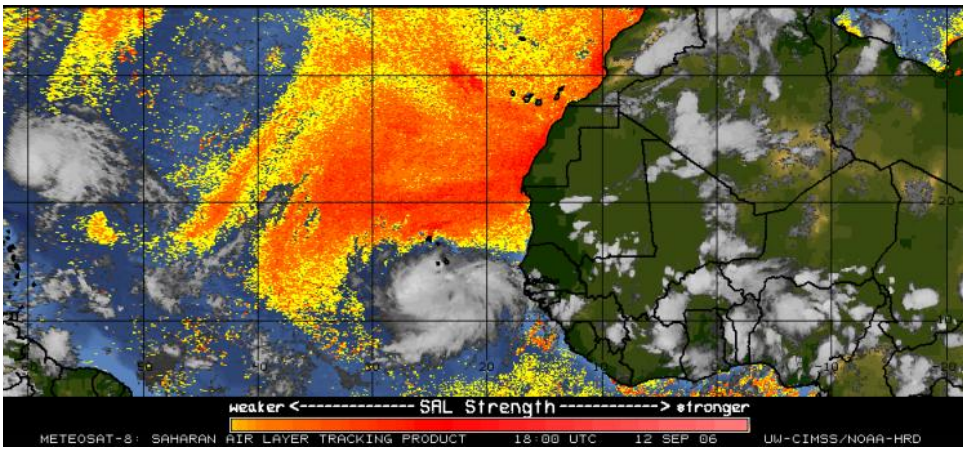

Figure 4.29 TD eight associated with the HAEW being engulfed by Saharan dry air on September 12 1800 UTC.

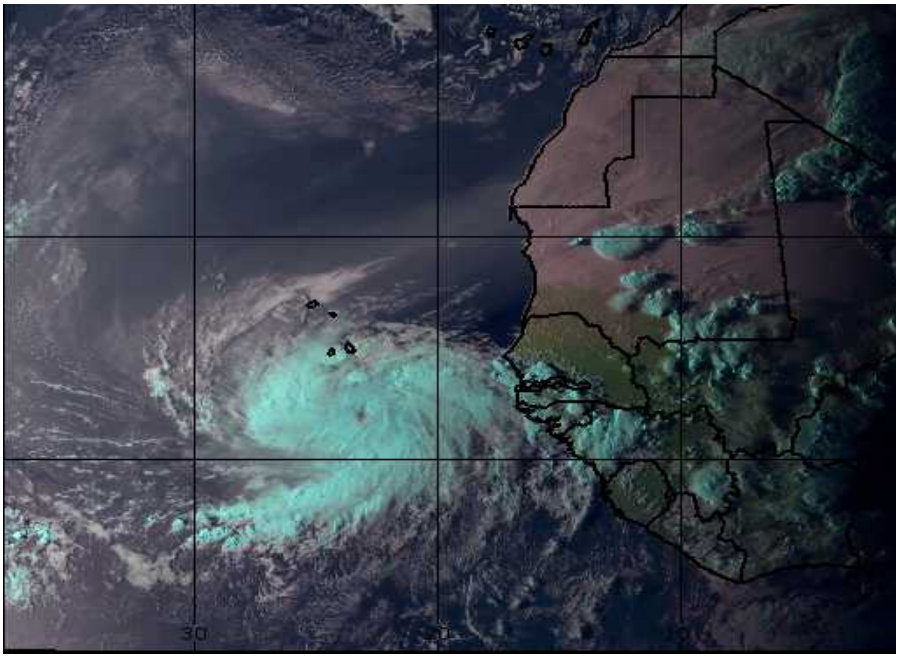

Figure 4.30 Meteosat-8 true color imagery on September 12 1800 UTC depicts a Saharan dust storm spread over the TD associated with the HAEW. Image courtesy of University of Wisconsin – CIMSS.

4.2 Simulations specifications

The first objective of the investigation was the completion of a series of HWRFx CNTRL simulations (hereinafter NDA which stands for non-DA) for both the NDAEW and the HAEW. Within this first set of runs, the first test performed investigated the effect of cumulus parameterization (CUP) in the forecast of tropical disturbances with a high-resolution (9-km) domain and a model designed for TCs. Each type of model runs was described with a three-digit number where the first two digits represent the short- and long-wave radiation schemes used. For all type of model run the first two digits that identify it is the number 99, which mean that the GFDL radiation scheme was applied. The third digit stands for the CUP option applied. The number four indicates that the SAS CUP was used and zero denotes that the CUP scheme was removed. Alternatively, the letters NCU (CUP is off) were utilized to indicate a 990 run type. To discriminate between the non-developing and developing AEWs, R1 is assigned to the NDAEW runs and R3 for the HAEW cases. Table 4.1 summarizes these runs specifications. The second test evaluated the effect of nesting for the NCU NDA simulations. To specify nested or un-nested runs, figure caption and/or labels within the figures are utilized.

A data impact study was the second objective of this research where additional deterministic simulations were generated having new ICs produced by HEDAS. These new ICs test runs were denominated EXP (experimental) as they were designed to evaluate the impact of the NAMMA dropwindsonde data assimilated. The assimilated data from the dropwindsondes include temperature, specific humidity and wind from the flight level down to the surface. The same CNTRL runs naming convention was applied to the EXP simulations. However, evaluation of the NDA runs results determined the

choice of removing the CUP and the nesting for this second phase of the investigation where DA was performed.

In summary, a designation such as NDA/DA R1/R3 994/990 denotes a CNTRL/EXP run for either the NDAEW or HAEW using/removing the SAS CUP. Table 4.2 shows the settings of all the experiments conducted for the current investigation. Finally, all the simulations run for 5 days with initialization dates specified in Table 4.3.

Table 4.1

HWRFx runs specifications

AEW	Run Identifier	Radiation Scheme	CUP Option
NDAEW	R1	99 (GFDL)	4 (SAS)
			0 (CUP off)
HAEW	R3	99 (GFDL)	4 (SAS)
			0 (CUP off)

Table 4.2

HWRFx experiments settings

HWRFx Run	Test	Run Identifier	Telescoping Option		CUP Option	
			Nested	Un-Nested	SAS	Off
CNTRL/NDA	CUP	R1	X (9:3 km)		X	X
		R3				
	Nesting	R1	X (9:3 km)	X (9 km)		X
		R3				
EXP/DA	IC	R1		X (9 km)		X
		R3				

Table 4.3

HWRFx runs initialization times

AEW Case	Start Date	End Date	Run Length (h)
NDAEW	Sep 8 1800 UTC	Sep 13 1800 UTC	120 (5 days)
HAEW	Sep 12 1800 UTC	Sep 17 1800 UTC	120 (5 days)

4.3 Tracking of AEWs

Various methods have been employed to identify and track AEWs. One of the widely used techniques consists in locating the wave axis on streamlines at 600–700 hPa where they are considered to have maximum amplitude (Carlson 1969a-b, Burpee 1972, Reed et al. 1977, Fink et al. 2004, Chen 2006). Other approaches include designation of the AEW center by the maximum of RVORT from 600-850 hPa or lower troposphere (Reed 1988, Thorncroft and Hodges 2001, Hopsch et al. 2007, Kerns et al. 2008, Serra et al. 2010), by winds and cloud pattern analyses, identifying inverted-V structures, cloud clusters, and squall lines (Frank 1969, Martin and Sikdar 1979, Hennon and Hobgood 2003) or combinations of any of these methods. Several ways of applying these techniques involve manual methods (Carlson 1969a-b, Reed et al. 1977, Reed et al. 1988, Fink et al. 2004), statistical methods (Burpee 1972, Albignat and Reed 1980, Duvel 1990, Fyfe 1999), and automatic tracking (Thorncroft and Hodges 2001, Hopsch et al. 2007, Serra et al. 2010). The latter method by Thorncroft and Hodges (2001) is an objective procedure that traces RVORT maxima at 600 and 850 hPa using particular amplitude, lifetime and zonal propagation thresholds. However, due to the complex nature of the AEWs these tracking schemes are subject to ambiguities. Tropical disturbances such as

AEWs can have multiple individual embedded RVORT maxima that eventually can merge and intensify the system (Simpson et al. 1997, Berry and Thorncroft 2005, Ramos 2007). Therefore, uncertainty arises for both manual and automated techniques due to the assumption that a single RVORT maximum represents the entire wave or that this mesoscale feature is representative of the parent synoptic-scale wave (Shelton 2011). Furthermore, manual analyses tend to be subjective. In 2007, Berry et al. suggested an alternative automated objective method to identify the AEW trough based on the 700-hPa streamfunction, which captures the synoptic scale of the AEWs.

The current investigation utilizes a multivariate automated objective technique to track the AEWs under study. This technique consists of a Grid Analysis and Display System (GrADS) script designed to work interactively with the user to get the position of the core of the system. To identify the easterly wave trough of interest, the user is presented with a composite plot of the 700-hPa streamlines superimposed to the RH shaded field at the same pressure level for the whole domain of the simulation at every available run time. Figure 4.31 shows an example of this type of plot.

Selection of the 700 hPa to locate the easterly wave trough was based on previous studies (e.g. Burpee 1974 and Erickson 1963), which have demonstrated that AEWs are stronger or have their maximum amplitude near the AEJ level. RH at 700 hPa was chosen to examine the role of a humid or drier environment on the structure and intensification of the AEWs. To properly identify the AEWs throughout the entire run, the user must take into consideration characteristics of these systems, such as an inverted-V wind flow, approximate speed of 5º to 7º longitude per day, wavelengths, latitude

range where they are mostly centered (Burpee 1972 and 1974), and possible through shape changes from one time to the next.

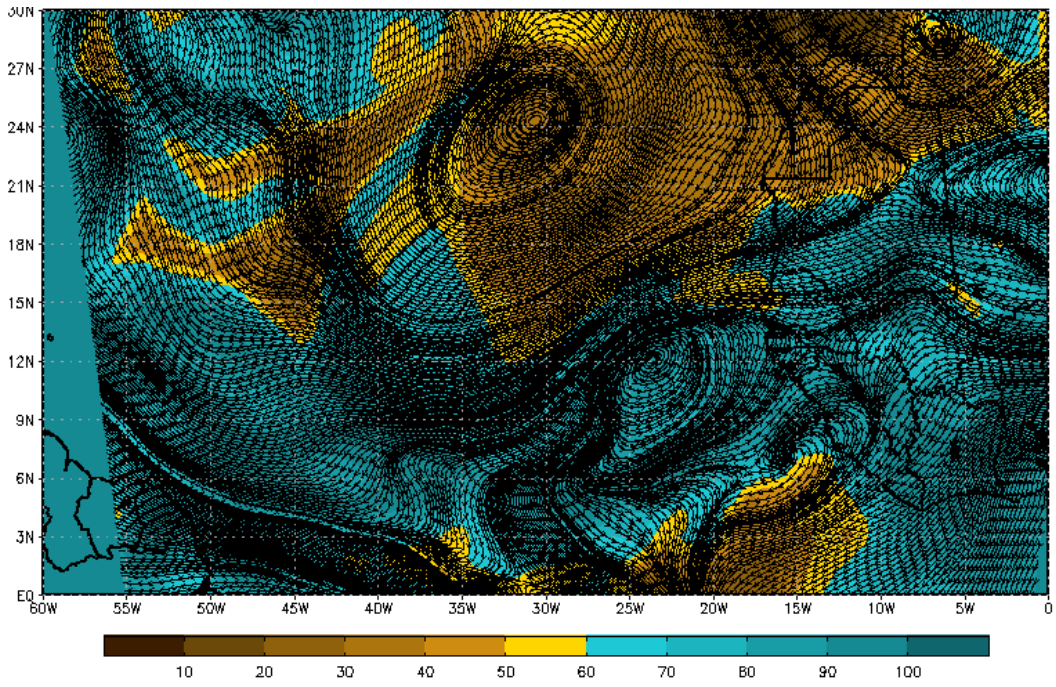

Figure 4.31 Example of composite plot used in the multivariate automated objective technique to identify and track the AEWs under study.

Following the composite plot, the user is asked to select the boundaries of a box that will frame the AEW trough. Subsequently, an algorithm scans the selected area to define the core of the AEW where it determines the mean of the locations of wind speed minima (hereinafter MLWSM) at 700, 750, 800, 850 and 900 hPa. The resulting geographic location is then stored in a file for every available time of a specific run. In order to investigate the AEWs environment, the generated coordinate is used as the input of multiple GrADS scripts that generate HCS and VCS plots of RH, wind, wind shear, RVORT and MSLP.

The MLWSM is located at the center of both the HCS (e.g. 10° x 10°) and VCS plots. In the HCS plots, a black "X" or "+" symbol marks the MLWSM coordinate. However, in the VCS plots, the MLWSM is represented by the central longitude of the plot. The latitude and longitude of the MLWSM is also used to make track plots.

Utilization of the MLWSM coordinate to track the AEWs allows the objective investigation of a larger-scale feature rather than a passing small-scale one (i.e. RVORT). The multivariate automated objective technique to get the MLWSM has disadvantages though. This method requires the identification of the AEW trough throughout the run, which can be extremely time-consuming depending on the length of the run. Therefore its application can be limited to short research periods. Another limitation is that it can be subjected to the constraint that the AEW under study must be identifiable at 700 hPa in order for the user to properly select the initial boundaries that will be used to determine the location of the AEW core.

5. HWRFx RESULTS AND ANALYSES

In this chapter, HWRFx sensitivity results due to CUP, nesting and ICs are discussed for each AEW under study. The final section of this chapter compares the environment and structure of the NDAEW and the HAEW with the aim to determine the factors that were conducive to development versus the ones that hindered intensification.

The simulated structure and intensity of tropical cyclones in numerical models have shown to be highly sensitive to details in the physics parameterizations (Bao et al. 2012, Hausman 2001, Gopalakrishnan et al. 2012, Pattanayak et al. 2012). However, knowledge on which model parameterization has the greatest impact on the structure and intensity is still uncertain. Particularly, weak tropical systems (below hurricane strength) pose special challenges for the models, as the impact of model physics on these systems is not well understood. As a result, a consensus on whether current operational physics parameterizations are suitable for weak and sheared storms has not been reached (Gopalakrishnan et al. 2012).

Understanding the sensitivity to variations in model physics is essential in order to evaluate accurately the quality of a numerical model's prediction using observations (Bao et al. 2012). The exclusive use of operational metrics as a way of quantifying the sensitivity of the intensification process to variations in physics parameterization schemes is a non-optimal approach since it cannot represent the structure of the model-simulated cyclones (Bao et al. 2012, Gopalakrishnan et al. 2012). Bao suggests that in order to provide useful recommendations for models improvement, structure metrics that evaluate the dynamical impacts associated with the change in model physics should be used in addition to the operational metrics.

A moving (based on the concept of dynamic pressure), two-way interactive nested grid for the WRF-NMM dynamical core started being evaluated and tested at NCEP in 2002 with the aim to improve the hurricane predictions. The moving nested grid method transfers meteorological information from a fine to a coarser mesh and vice versa over the region of coinciding grid points. In order to deal with the multi-scale nature of hurricanes, a horizontal mesh refinement capability (or telescopic mesh) was developed for this dynamical core, which supports one and two way interaction between a lower-resolution parent domain and one or more higher-resolution nests (Gopalakrishnan et al. 2002). The two higher resolution domains (9:3 km) of the current operational HWRF include the two-way interactive nesting capability, which has demonstrated to produce the structure of the hurricanes quite well (Gopalakrishnan et al. 2006). To the best knowledge of the author, the HWRFx sensitivity to nesting for the simulation of the intensity and structure of weak tropical systems is tested for the first time in the current investigation.

Besides sensitivity to physics parameterizations and improved resolution, model forecast are sensitive to ICs (Aberson et al. 1994, Gopalakrishnan et al. 2012). For example, in Gopalakrishnan et al. (2012), the performance of HWRFx was evaluated for 87 cases of Atlantic TCs during three different hurricane seasons and at two horizontal resolutions (27-km parent domain with 9-km moving nest and 9-km parent domain with a 3-km moving nest). For each horizontal resolution, GFDL and operational HWRF ICs were used with a semi-operational and National Center for Atmospheric Research (NCAR) suite of physics. Results showed that the higher resolution HWRFx system using the GFDL initial conditions and a system of physics similar to the operational

version (HWRF) provided the best results in terms of both track and intensity prediction. HWRF initial conditions in the HWRFx model provided reasonable skill, particularly for hurricane strength storms. However, for weaker storm cases, none of the predictions provided any consistent improvement. In general, HWRFx appeared to rapidly spin down the initial vortex for strong storms when using GFDL initial conditions. On the other hand, for both model resolutions with HWRF initialization, the runs illustrated an overly cyclogenic behavior (spin up) of HWRFx for initially weaker storms.

5.1 Cumulus Physics test

Even though it includes phenomena other than cumulus clouds, the problem of parameterizing convective processes in a conditionally unstable atmosphere is referred to as CUP (Frank 1983). The employment of parameterization procedures in prognostic models provides opportunity for further observational verification of the effects of convection on the evolution of the vertical profiles of momentum, temperature, and humidity, rainfall rates and pressure (Krishnamurti et al. 1980). During the last decades, many CUP schemes have been constructed, however nowadays it is still considered a very young subject (Arakawa 2004). As acknowledged by Arakawa (2004), besides the basic question of how to pose the CUP problem, a number of uncertainties in modeling clouds and their associated processes remain. He also states that the severity of the problem goes beyond that since there is a lack of a sufficiently general framework, such as a unified cloud system model for implementing detailed formulations of these processes. Besides the CUP problem itself, there is a limitation in the use of prognostic models for testing a parameterization of a physical process. The downside consists in

that models usually contain many errors arising from horizontal, vertical and time-differencing schemes, as well as additional parameterized processes (i.e. PBL), the incorporation of inadequate terrain, and errors in the initialization and boundary conditions (Krishnamurti et al. 1980).

The operational HWRF utilizes the SAS CUP scheme for the 27-km parent domain as well as the 9-km moving nest while the 3-km higher resolution nest has this option off since convection is explicit (http://www.emc.ncep.noaa.gov).

The SAS is a CUP scheme designed by Grell (1993) based on Arakawa and Schubert (1974), which consider only one cloud top at a specified time and location and not the spectrum of cloud sizes, as in the computationally expensive original scheme (http://www.emc.ncep.noaa.gov/HWRF/HWRFScientificDocumentation2011.pdf). The SAS CUP convection depends on the cloud work function that is a quantity derived from the temperature and moisture in each air column of the model, which is similar to the convective available potential energy. If the cloud work function exceeds a certain critical threshold, the parameterizations are triggered and the mass flux of the cloud is determined using a quasi-equilibrium assumption. As the large-scale rising motion becomes strong, the cloud work function is allowed to approach neutral stability.

The SAS scheme was revised in 2011 to make cumulus convection stronger and deeper by increasing the maximum allowable cloud base mass flux and having convective overshooting from a single cloud top. The revised SAS contributed to reductions in the root mean squared errors of tropical winds and improved hurricane tracks (Han et al. 2011). A CUP sensitivity study using the WRF-NMM for major TC Nargis (2008) determined that the SAS CUP best represented the intensification and

forecast a better track (Pattanayak et al. 2012). The current work investigated the HWRFx 9-km static parent domain SAS CUP scheme effect in the structure and intensity forecast of two AEWs. Similar to the operational settings, the SAS CUP is not applied to the higher resolution-moving nest of 3 km. Nested simulations were conducted for each of the NDAEW and HAEW as well as two CNTRL simulations. One simulation included the SAS CUP option (994); the other simulation removed it to have explicit convection (990). See Table 4.1 for details on the number convention.

The SAS is applied to represent and verify the resulting effect of convection on the intensification of AEWs though the 9-km domain grid size is within the horizontal scale of individual cumulus clouds (0.1 to 10 km) and can directly resolve the cumulus clouds without the need of a CUP.

5.1.1 NDAEW CUP sensitivity

The NDAEW CUP sensitivity results showed that the wave developed into TS with and without the inclusion of the SAS. However, it developed earlier and stronger when the SAS CUP was utilized. The operational metrics in both runs indicated similar surface intensity during the period of 6-60 h (Figs. 5.1a-b). Afterwards, the surface intensity of the runs started to diverge greatly. The MSW of R1 994 and R1 990 suggested TS intensification starting on 66 h and 96 h, respectively (Fig. 5.1a). However, the AEWs structure and environment determined that TS cyclogenesis happened at 75 h in R1 994 whereas it occurred at 114 h in R1 990. Figures 5.2-5.3 and Figs. 5.4-5.8 shows the R1 994 and R1 990 NDAEW environment and structure at the time of TS cyclogenesis, respectively. After cyclogenesis both runs sustained TS status to the end of the simulations. Stronger TS in R1 994 was attributed in part to the constant deepening

in MSLP after 60 h since for the R1 990 it slightly deepens toward the end of the run (Fig. 5.1b). Removal of the SAS CUP assisted delaying the cyclogenesis by 39 hours.

Besides more intense operational metrics, R1 994 showed radical structural differences when compared to the R1 990, which resulted in stronger TS when the CUP was added. The addition of the SAS CUP to the model supported the early generation and further intensification of minimum MSLP closed contours. These contours were superimposed the lower-levels cyclonic circulation and MLWSM, which greatly enhanced moist convection resulting in greater surface convergence. Both the merger of smaller vortices facilitated by increased convergence and the vertical advection of vorticity in convective updrafts assisted in the generation of a RVORT core centered at the lower-levels cyclonic circulation, which Tory el al. (2006) indicated to be a necessary condition for cyclogenesis. Formation of a mid-to-upper levels anticyclone with center aligned or closely aligned to the lower-levels MLWSM was also identified at the time of cyclogenesis. Less than 10 kt of shear was observed at the anticyclone center while shear values close to the center were in the range of 10-29 kt. After cyclogenesis, stronger anticyclonic outflow (revealed by the deep layer environmental shear) indicated further intensification. Conversely, the removal of the SAS CUP kept closed minimum MSLP contours superimposed the NDAEW, and predicted a drier environment due to prolonged periods of major multi-level dry air entrainment to the core of the system (i.e. Figs. 5.6a-b). Both factors delayed moist convection and the formation of a RVORT core (i.e. Fig. 5.6c), thus the TS cyclogenesis.

Thermodynamically, the R1 990 was able to capture the SAL dry air weakening the AEW. However, the model managed to maintain the initial cyclonic circulation,

which later on intensified. This suggests that the cyclogenesis has a dynamic-thermodynamic nature. It also suggests that besides the removal of implicit convection, there are other aspects and factors in the model that could be driving to the development of a non-developing AEW. Lack of accurate ICs and influence of other parameterizations schemes (i.e. PBL scheme) could be some of those factors. Besides the aforementioned, results from this section confirmed that the exclusive use of operational metrics as a way of quantifying the sensitivity of the intensification process to variations in physics parameterization schemes is a non-optimal approach since it cannot represent the structure of the model-simulated cyclones (Bao et al. 2012, Gopalakrishnan et al. 2012).

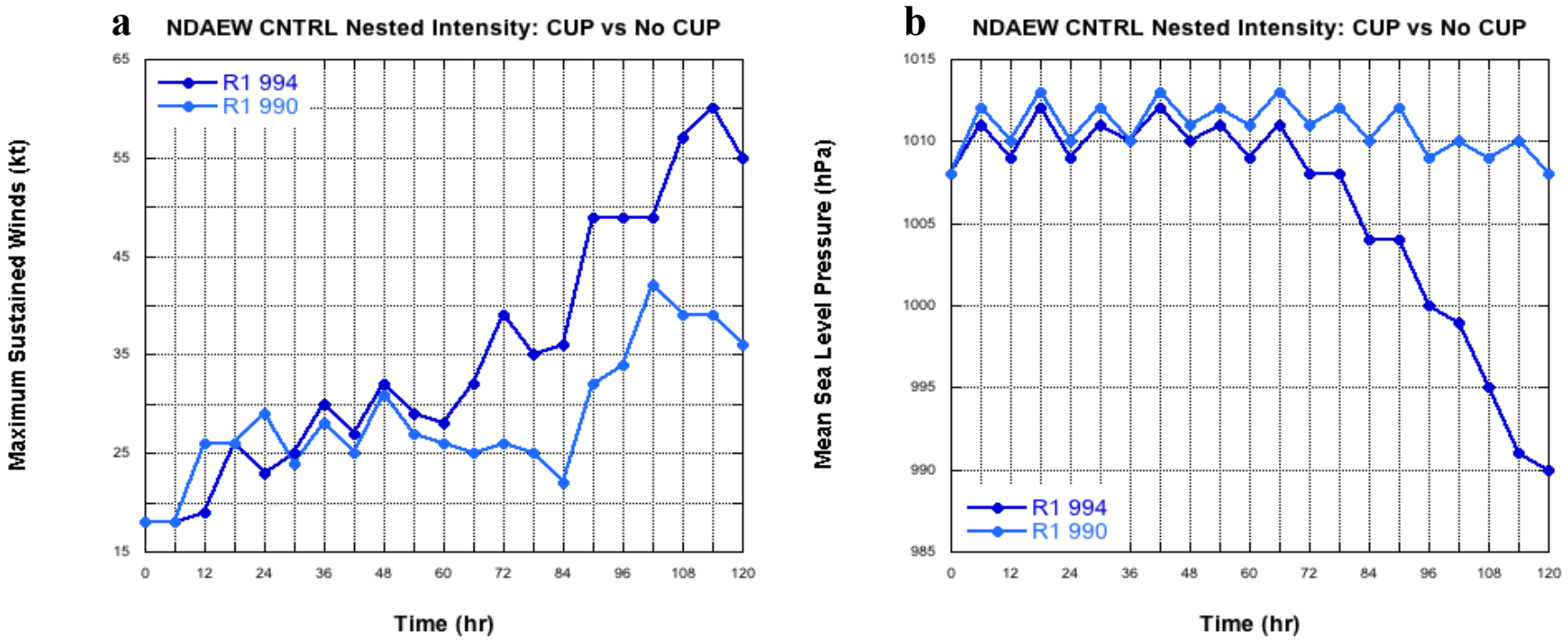

Figure 5.1 NDAEW surface intensity evolution from CNTRL CUP sensitivity runs: (a) maximum sustained winds (kt) and (b) MSLP (hPa). The dark blue line represents the simulation that included the SAS CUP (R1 994). The light blue line corresponds to the run that removed the SAS CUP (R1 990).

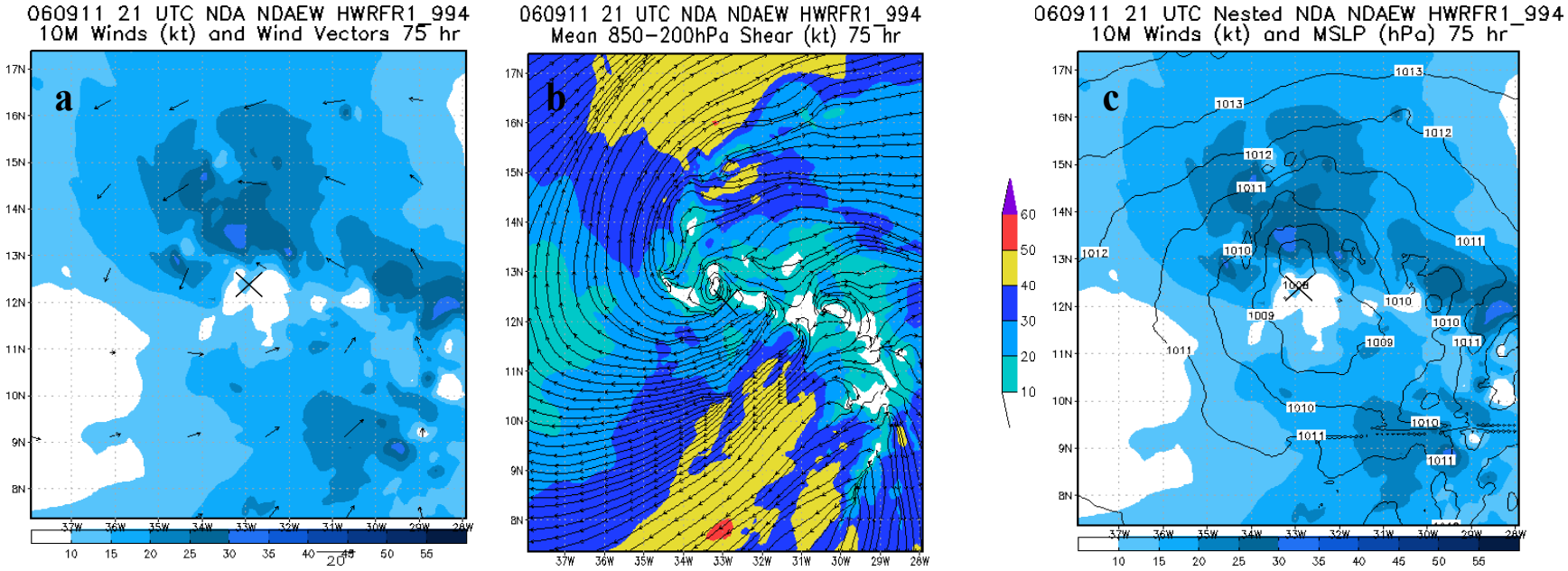

Figure 5.2 CNTRL Nested R1 994 NDAEW structure at the time of TS cyclogenesis: (a) 10 m wind speed and vectors (b) deep layer environmental shear and (c) 10 m wind speed and MSLP. At 75 h, the MSW was 34 kt and the minimum of MSLP was 1008 hPa.

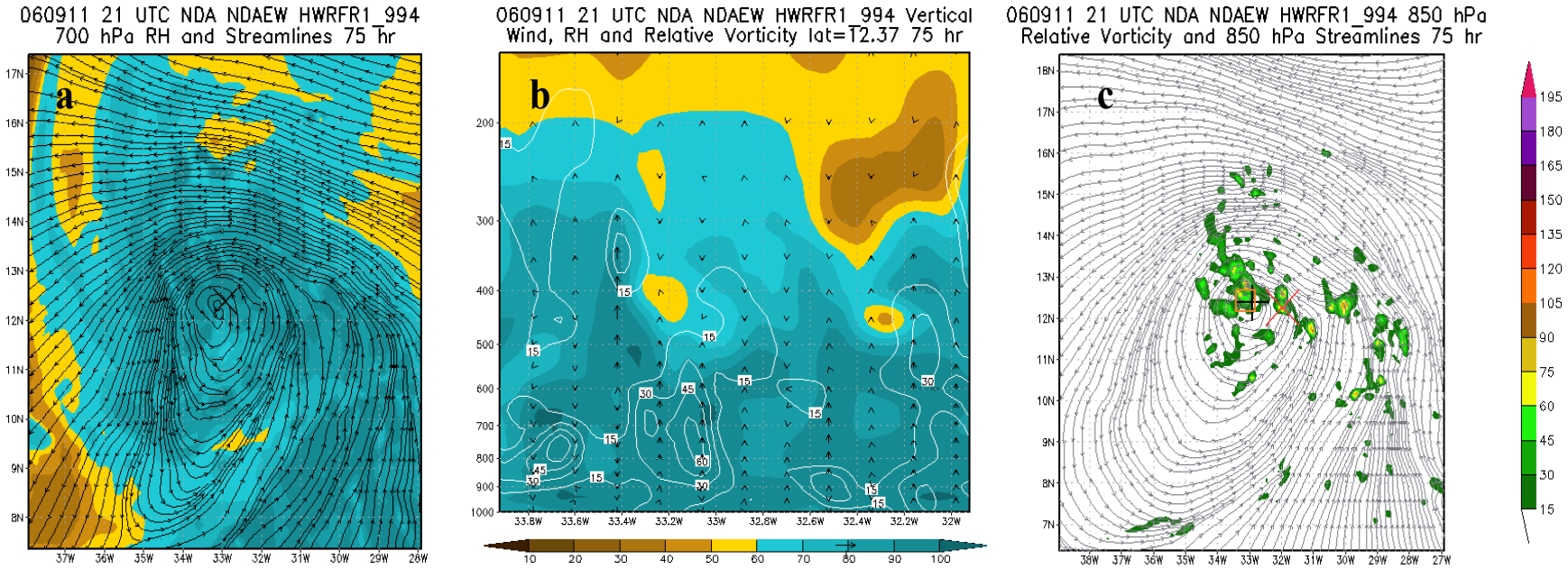

Figure 5.3 CNTRL Nested R1 994 NDAEW structure at the time of TS cyclogenesis (continued): (a) 700-hPa RH and streamlines (b) east-west zonal VCS of RH (shaded), vertical wind (arrows) and RVORT (white contours) centered at the MLWSM, and (c) 850-hPa RVORT and streamlines.

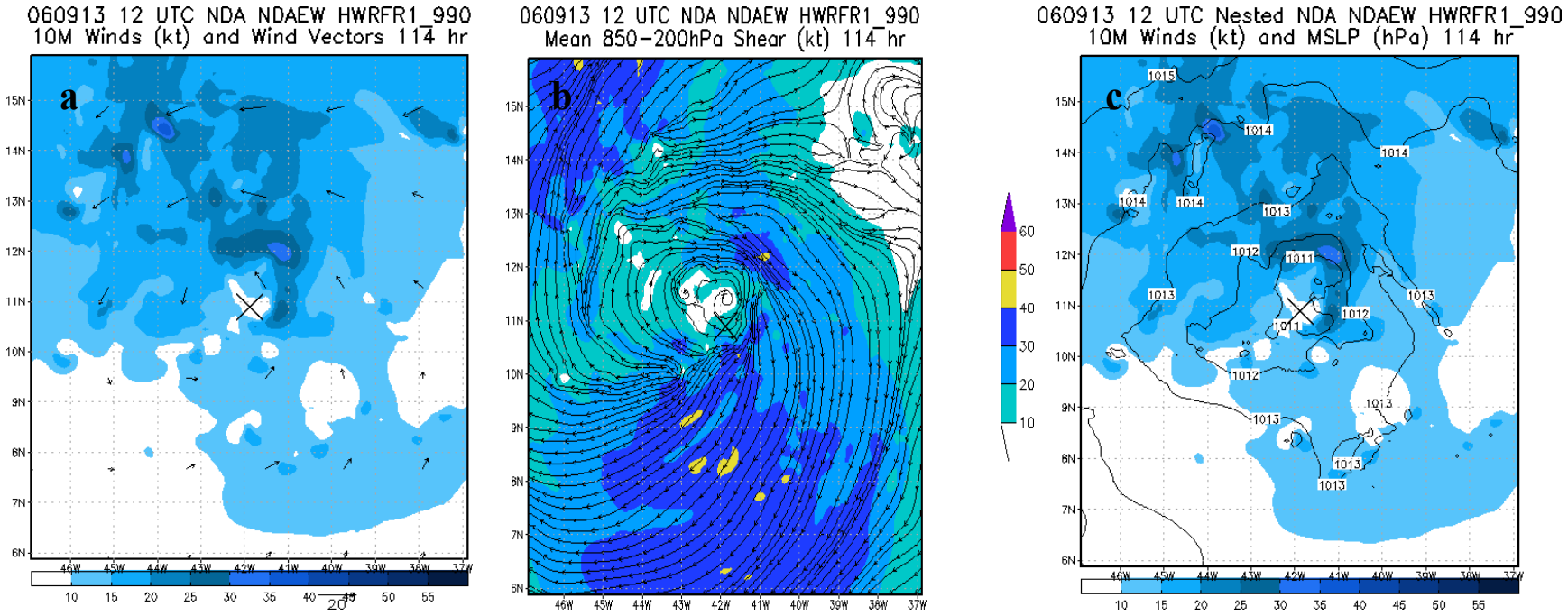

Figure 5.4 CNTRL Nested R1 990 NDAEW structure at the time of TS cyclogenesis: (a) 10 m wind speed and vectors (b) deep layer environmental shear and (c) 10 m wind speed and MSLP. At 114 h, the MSW was 39 kt and the minimum of MSLP was 1010 hPa.

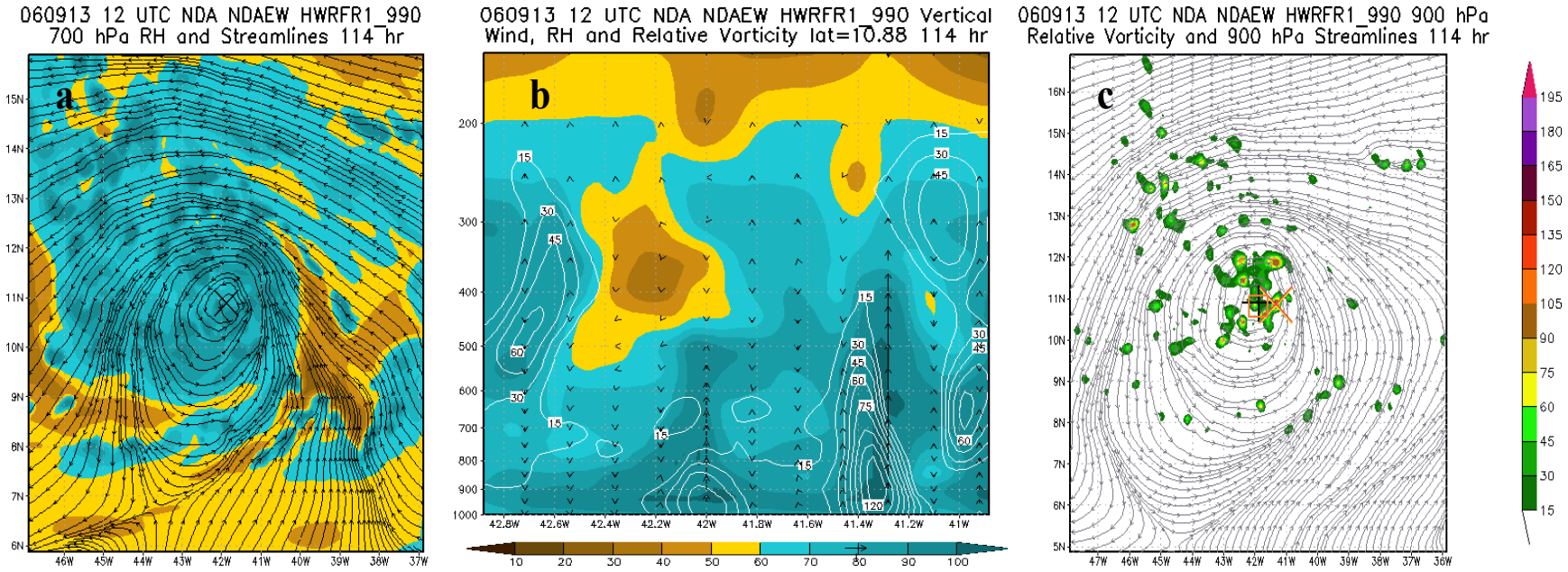

Figure 5.5 CNTRL Nested R1 990 NDAEW structure at the time of TS cyclogenesis (continued): (a) 700-hPa RH and streamlines (b) east-west zonal VCS of RH (shaded), vertical wind (arrows) and RVORT (white contours) centered at the MLWSM, and (c) 900-hPa RVORT and streamlines.

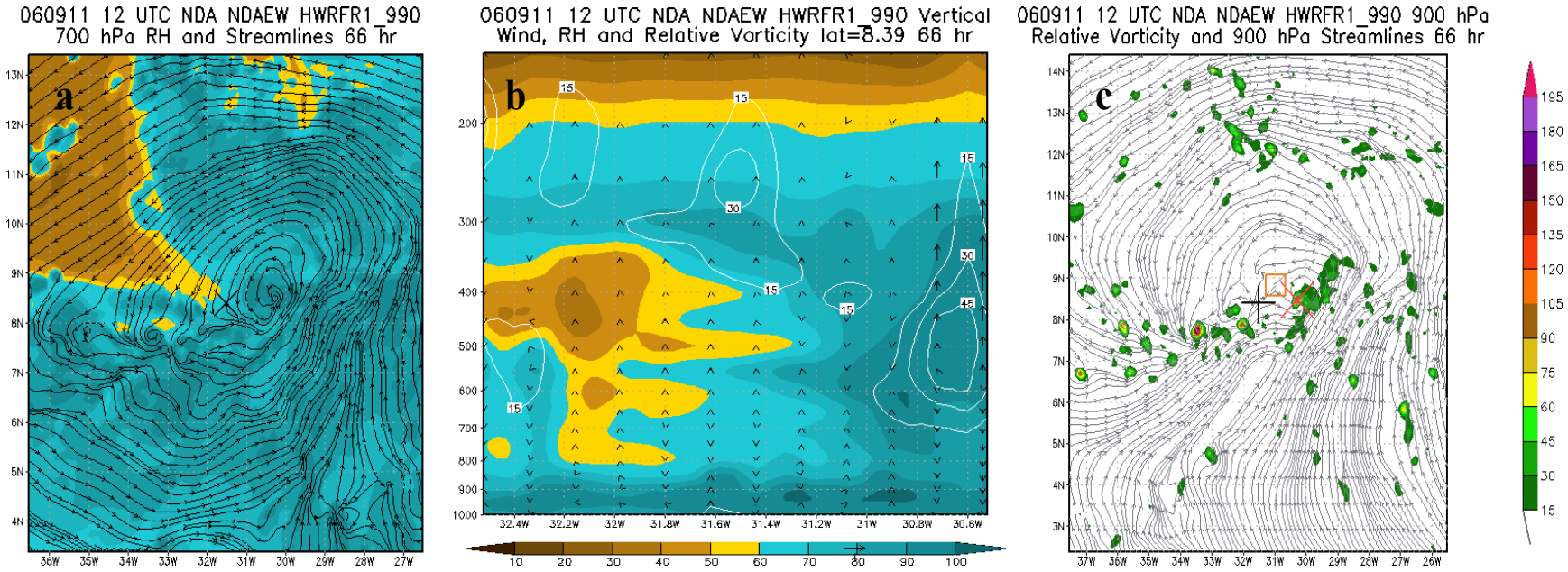

Figure 5.6 CNTRL Nested R1 990 NDAEW structure during a dry air entrainment period at 66 h: (a) 700-hPa RH and streamlines (b) east-west zonal VCS of RH (shaded), vertical wind (arrows) and RVORT (white contours) centered at the MLWSM, and (c) 900-hPa RVORT and streamlines. Major multi-level dry air intrusion occurred at the MLWSM as well as in the NDAEW environment at 700 hPa. The lack of a closed minimum MSLP (not shown) hindered the formation of a surface closed cyclonic circulation. This factor combined to dehumidification due to dry air at the NDAEW core hindered moist convection and the formation of a RVORT core.

5.1.2 HAEW CUP sensitivity

Similarly to the NDAEW case, the HAEW CUP sensitivity results showed that inclusion of the SAS had a strengthening effect. The SAS CUP assisted in predicting stronger TS and earlier than when the CUP was removed. Conversely, the removal of the CUP prolonged a sheared environment in R3 990 and also predicted a period of dry air intrusion, which hindered the earlier organization and intensification of the HAEW. HAEW runs with and without the inclusion of the SAS were also able to predict the TD stage of Helene, however just during the first six hours of the simulations and weaker than the NHC BT analyses. According to the AEW environment and structure, TD intensity is predicted for a second time at 42 h in the R3 994. Both simulations predicted TS Helene, however posterior to the NHC BT analyses. R3 994 predicted it at 48 h whereas R3 990 at 63 h, which represents 18 h and 33 h delay when compared to NHC (BT at 30 h). Figures 5.8-5.9 and Figs. 5.10-5.11 show the R3 994 and R3 990 HAEW structure at the time of TS prediction, respectively. However, none of the R3 simulations were able to predict strengthening to hurricane category one (BT at 90 h) or two (BT at 120 h). Instead, both runs sustained TS intensity until the end of the simulations. Throughout the TS stage, the inclusion of the SAS results in a stronger storm forecast in R3 994 as revealed by both the wave structure and the operational metrics (Fig. 5.7). Figures 5.12-5.13 and Figs. 5.14-5.15 show the R3 994 and R3 990 Helene structure at 120 h, respectively.

After the 6-h forecast until prior to TD intensification in R3 994 and TS genesis in R3 990, both simulations showed a highly sheared (30-60 kt) environment that acted to disrupt the surface and lower-levels center of the cyclonic circulation as well as the mid-

to-upper levels anticyclone. In addition to a prolonged sheared environment that elongated the HAEW, from 30-60 h the R3 990 experienced frequent dry air intrusion to the AEW core. During that thirty hours period, air with RH less than 60 % was observed to extend periodically between 500-700 hPa. Besides these two factors, a weaker MSLP than R3 994 assisted in hindering moist convection, which delayed the formation of a RVORT core. Despite the environmental shear that affected both runs, the model was able to preserve multiple closed contours of MSLP around the system, which assisted in maintaining the low-level convergence.

At the time of TD or TS cyclogenesis, these observations were common for both R3 simulations: surface and lower-levels closed cyclonic circulation with a well-defined center, environmental shear less than 30 kt at the TC center by the establishment of a mid-to-upper levels anticyclone center nearly or completely aligned to the MLWSM, the continuity of a highly moisturized environment, and the formation of a RVORT core at the lower-levels cyclonic circulation center. However, besides stronger operational metrics, these features were observed during TS genesis, especially in the R3 994 run: stronger and amplified RVORT core, stronger outflow, and a much moist environment.

Beyond TS genesis, Helene intensified in both runs due to increased convergence, which further assisted the strengthening of the RVORT core via merger of smaller vortices that concentrated at the center of the storm. Continued MSLP deepening increased the area of maximum winds, and the RVORT core amplified through vertical advection due to augmented moist convection. The VCS of RH at 120 h showed that the RVORT advection reached lower in the troposphere for the R3 990 (Fig. 5.15b), which was associated with weaker MSLP (Fig. 5.7b) and a second period of dry air entrainment

from 96-114 h that hampered the moist convection. During this period the MSW also weakened (Fig. 5.7a). Figure 5.16 shows dry air intrusion at 102 h at both 700-hPa TS environment and above 600 hPa. Past the 114 h, there is a slight increase in the MSW (Fig. 5.7b) that coincided with dry air retreat from the TS center and its immediate surroundings. After the dry air retreat, a column of quasi to super saturated air established and the RVORT amplified both horizontally and vertically through advection (Fig. 5.15b). Apparently, besides the prolonged period of shear, the proximity and intrusion of dry air to the R3 990 HAEW had an effect in forecasting smaller TS at 120 h (Fig. 5.14c) than R3 994 (Fig. 5.12c). Other intensification signs posterior to the TS genesis included the contraction of the cyclone and mid-to-upper levels anticyclone centers, and the broadening of stronger outflow.

Results for this case confirmed the dynamic-thermodynamic nature of TC genesis. The inclusion of the SAS CUP had a strengthening effect in the HAEW. However, the unrealistic periods of strong shear and frequent dry air entrainment to the HAEW core in both runs suggest that besides the CUP there were other factors in the model that could have inhibited the further intensification of the HAEW. As was mentioned in section 5.1.1, possible factors include the lack of accurate ICs and the influence of other parameterizations schemes such as the PBL scheme.

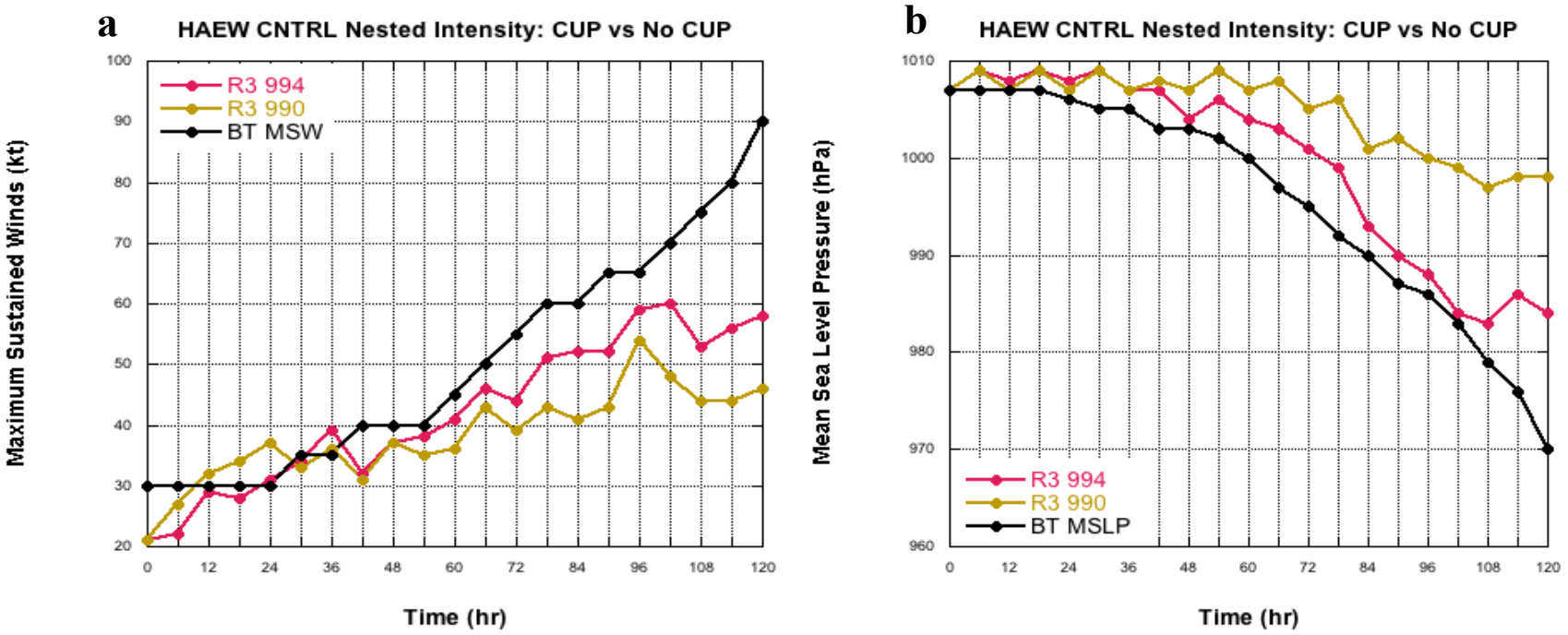

Figure 5.7 HAEW surface intensity evolution from CNTRL CUP sensitivity runs: (a) maximum sustained winds (kt) and (b) MSLP (hPa). The magenta line represents the simulation that included the SAS CUP (R3 994). The dark yellow line corresponds to the run that removed the SAS CUP (R3 990). The black line is the NHC BT of Helene. Like for the R1 case, these graphs show that the intensification of the HAEW was sensitive to differences in convective processes (i.e. implicit versus explicit).

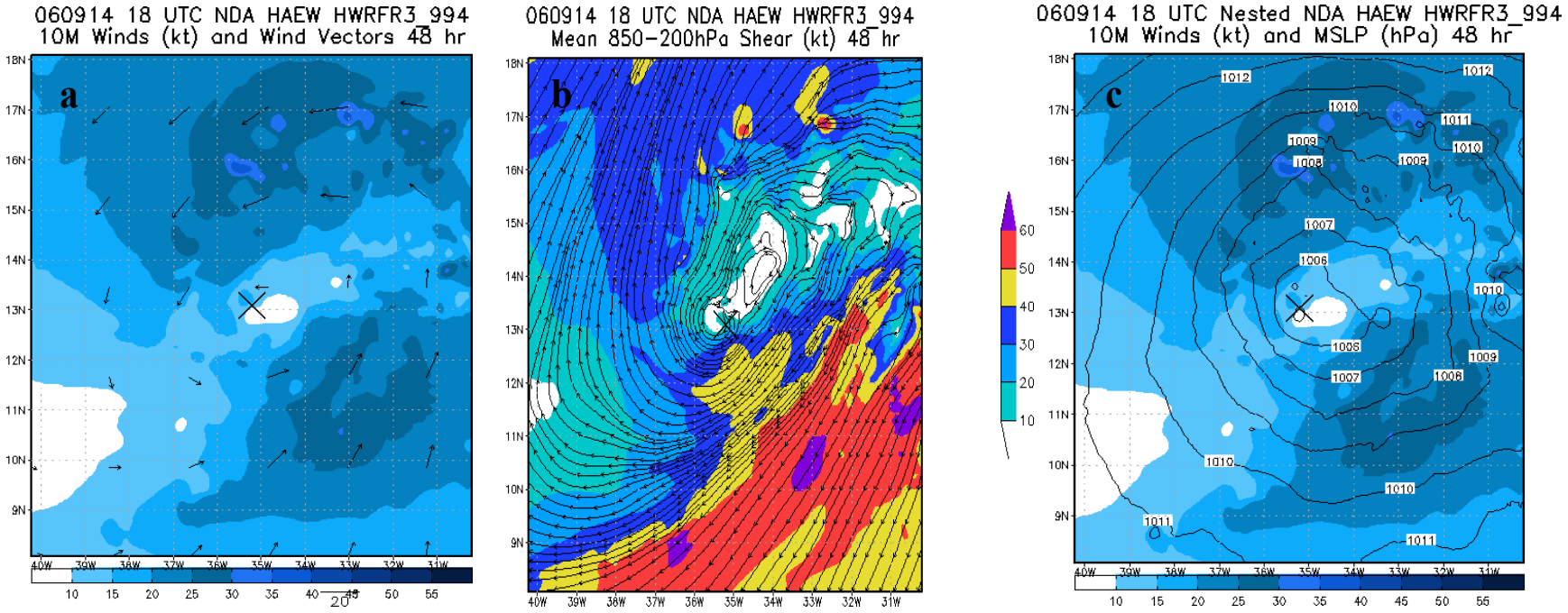

Figure 5.8 CNTRL Nested R3 994 HAEW structure at the time of TS cyclogenesis: (a) 10 m wind speed and vectors (b) deep layer environmental shear and (c) 10 m wind speed and MSLP. At 48 h, the MSW was 38 kt and the minimum of MSLP was 1005 hPa.

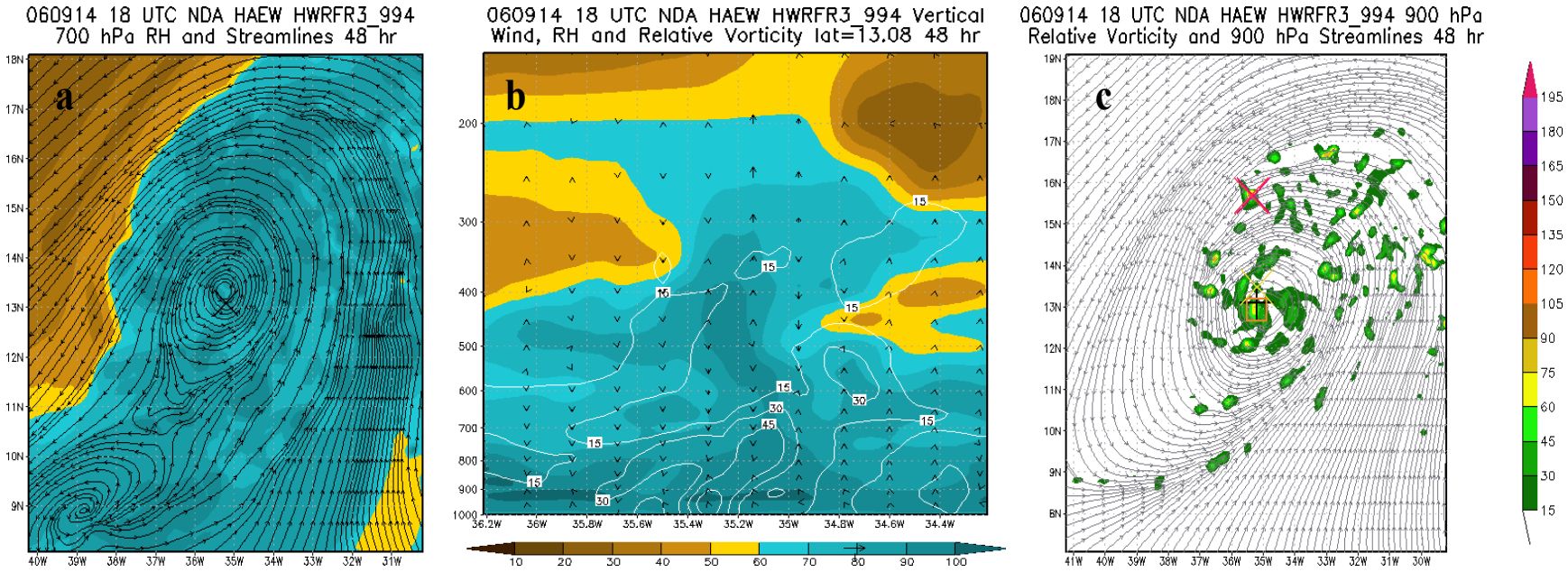

Figure 5.9 CNTRL Nested R3 994 HAEW structure at the time of TS cyclogenesis (continued): (a) 700-hPa RH and streamlines (b) east-west zonal VCS of RH (shaded), vertical wind (arrows) and RVORT (white contours) centered at the MLWSM, and (c) 900-hPa RVORT and streamlines.

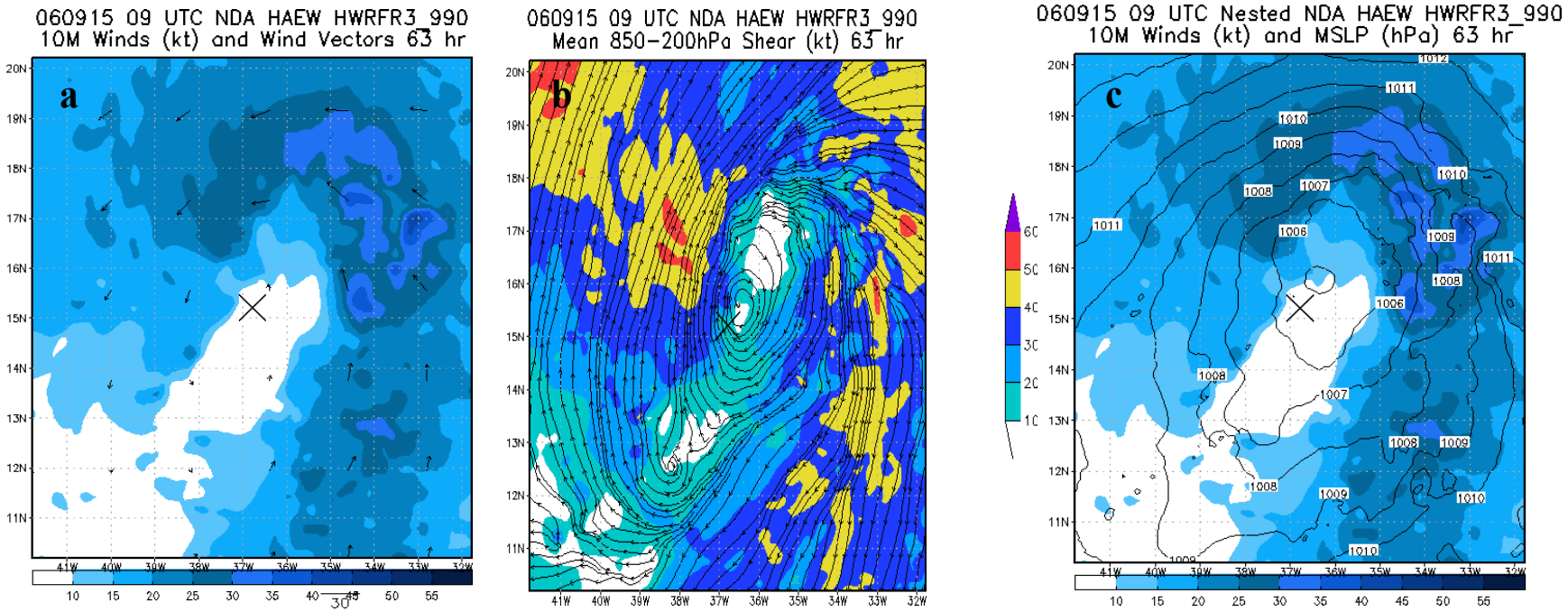

Figure 5.10 CNTRL Nested R3 990 HAEW structure at the time of TS cyclogenesis: (a) 10 m wind speed and vectors (b) deep layer environmental shear and (c) 10 m wind speed and MSLP. At 63 h, the MSW was 44 kt and the minimum of MSLP was 1005 hPa.

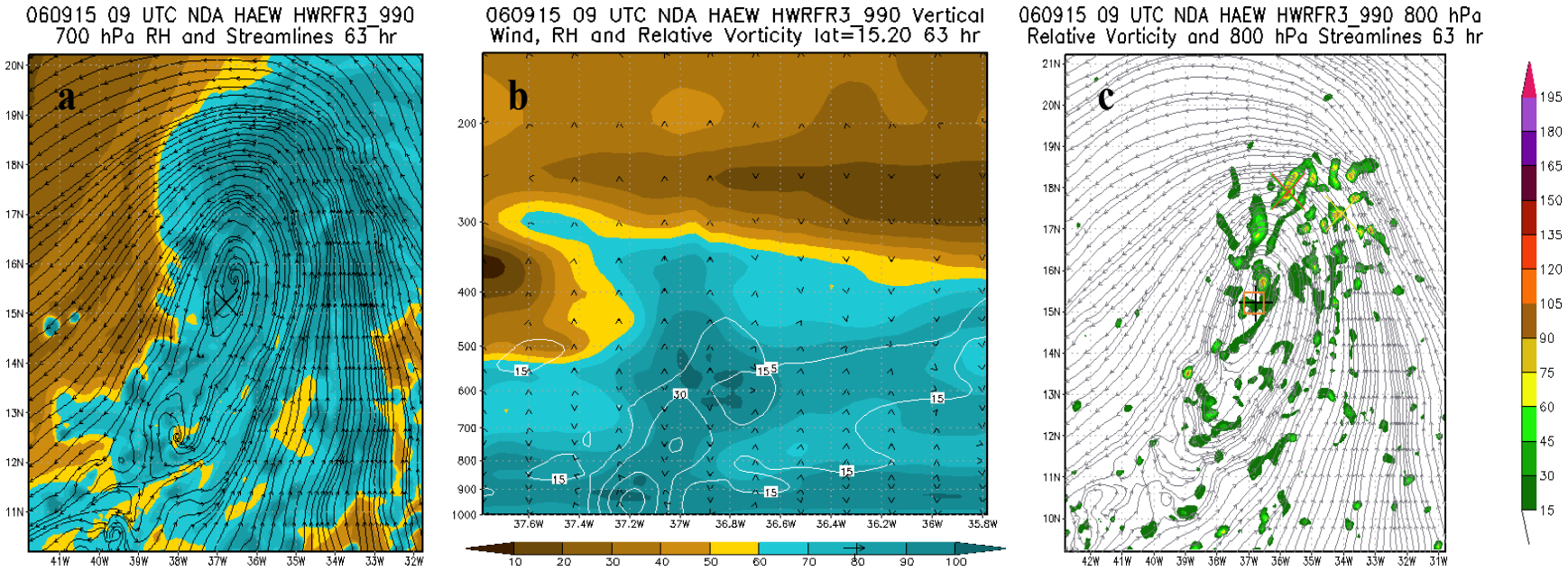

Figure 5.11 CNTRL Nested R3 990 HAEW structure at the time of TS cyclogenesis (continued): (a) 700-hPa RH and streamlines (b) east-west zonal VCS of RH (shaded), vertical wind (arrows) and RVORT (white contours) centered at the MLWSM, and (c) 900-hPa RVORT and streamlines.

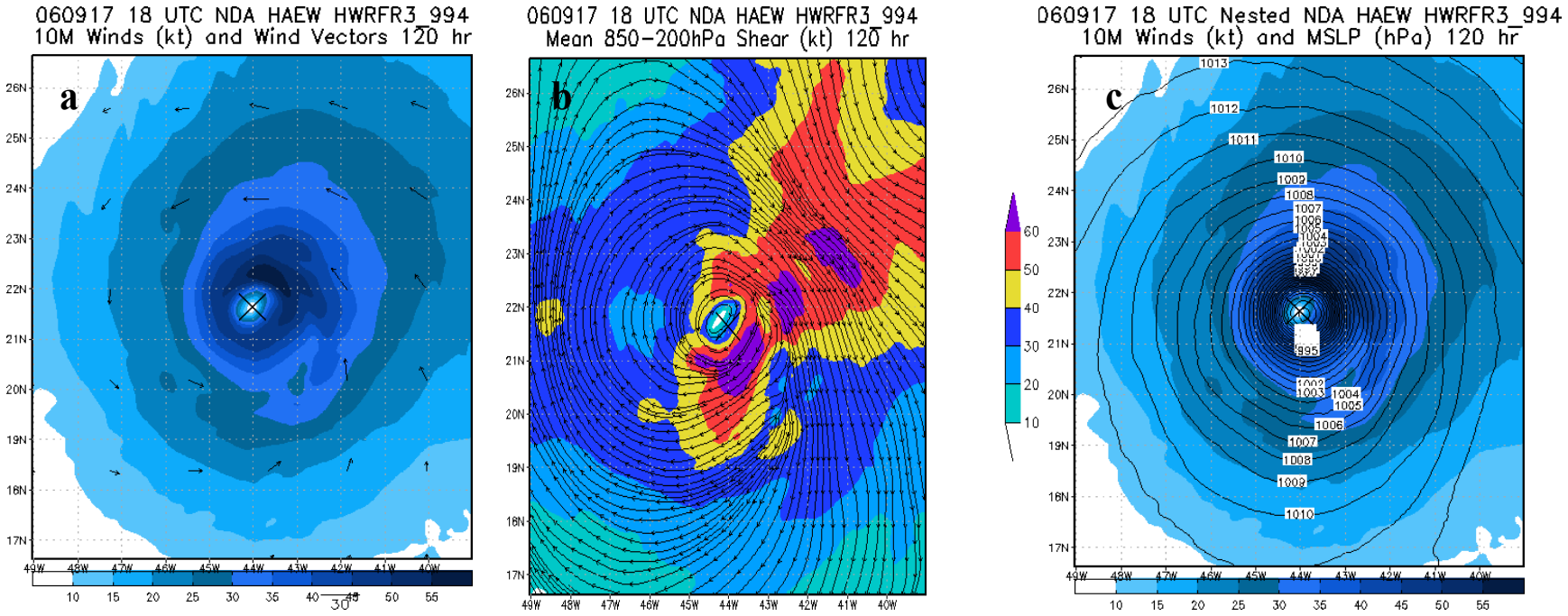

Figure 5.12 CNTRL Nested R3 994 structure of Helene at 120 h: (a) 10 m wind speed and vectors (b) deep layer environmental shear and (c) 10 m wind speed and MSLP. The MSW at this time was 58 kt and the minimum of MSLP was 984 hPa.

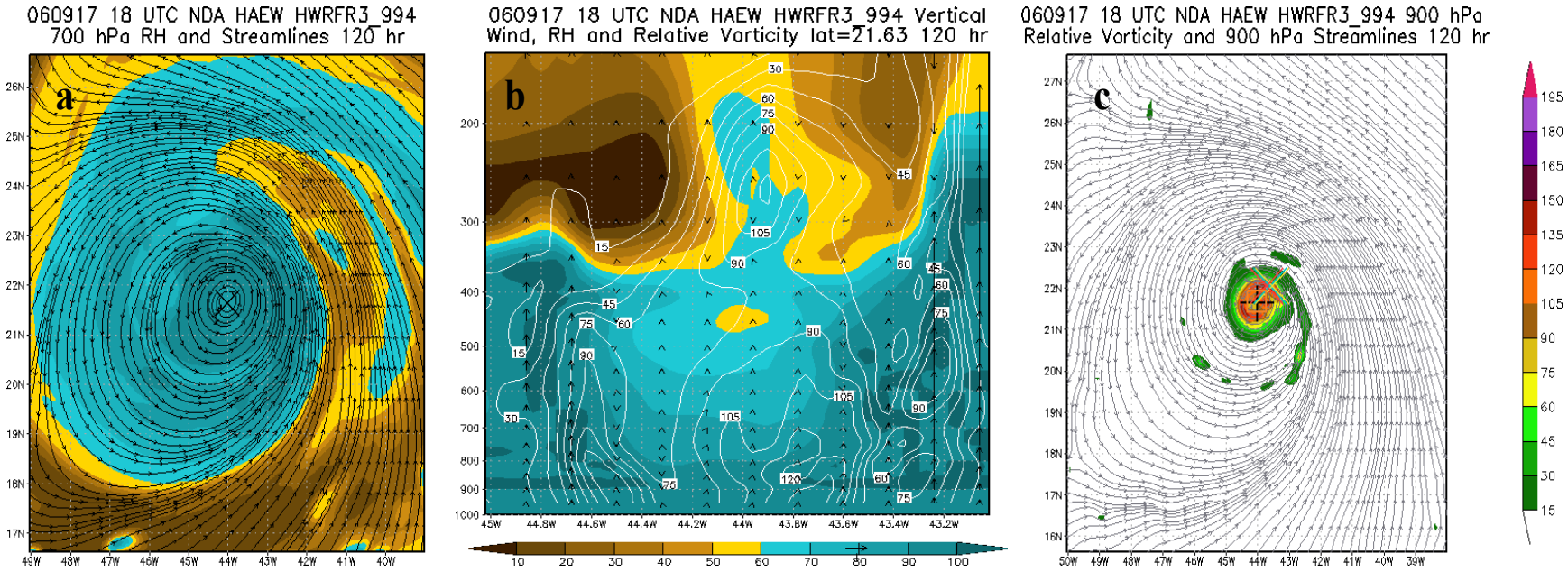

Figure 5.13 CNTRL Nested R3 994 structure of Helene at 120 h (continued): (a) 700-hPa RH and streamlines (b) east-west zonal VCS of RH (shaded), vertical wind (arrows) and RVORT (white contours) centered at the MLWSM, and (c) 900-hPa RVORT and streamlines.

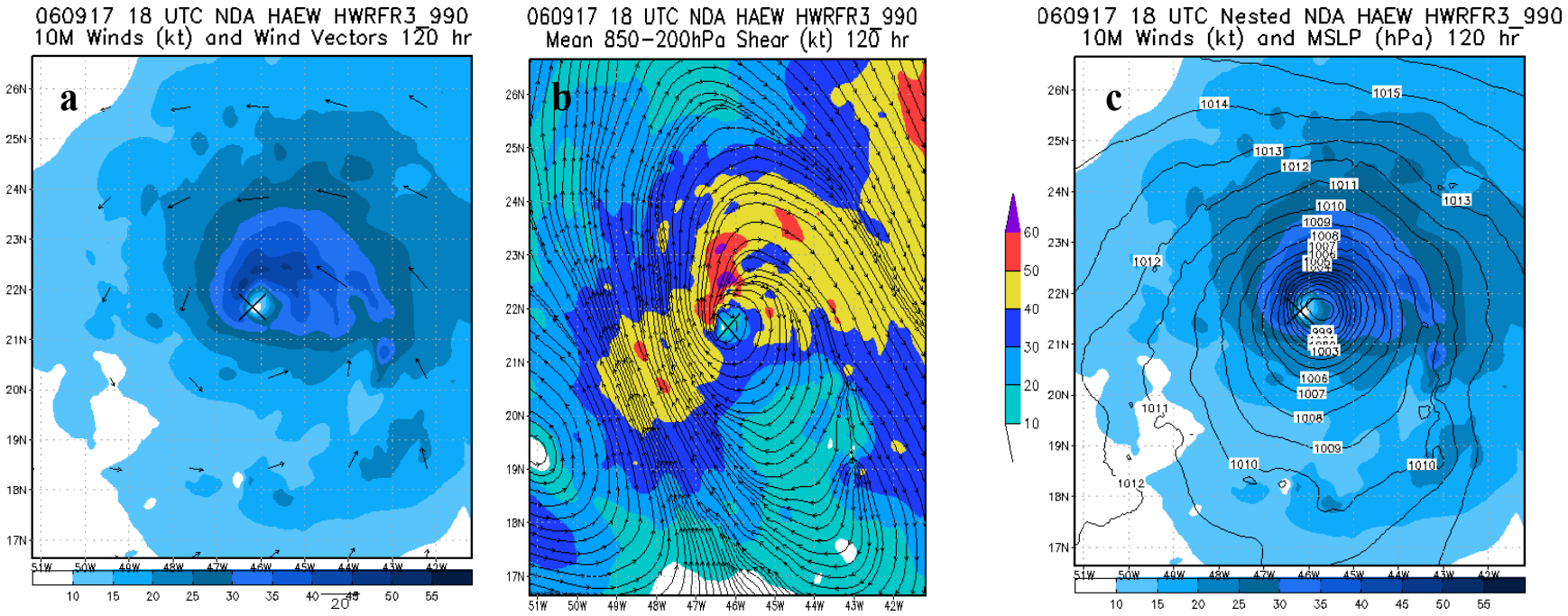

Figure 5.14 CNTRL Nested R3 990 structure of Helene at 120 h: (a) 10 m wind speed and vectors (b) deep layer environmental shear and (c) 10 m wind speed and MSLP. The MSW at this time was 46 kt and the minimum of MSLP was 998 hPa.

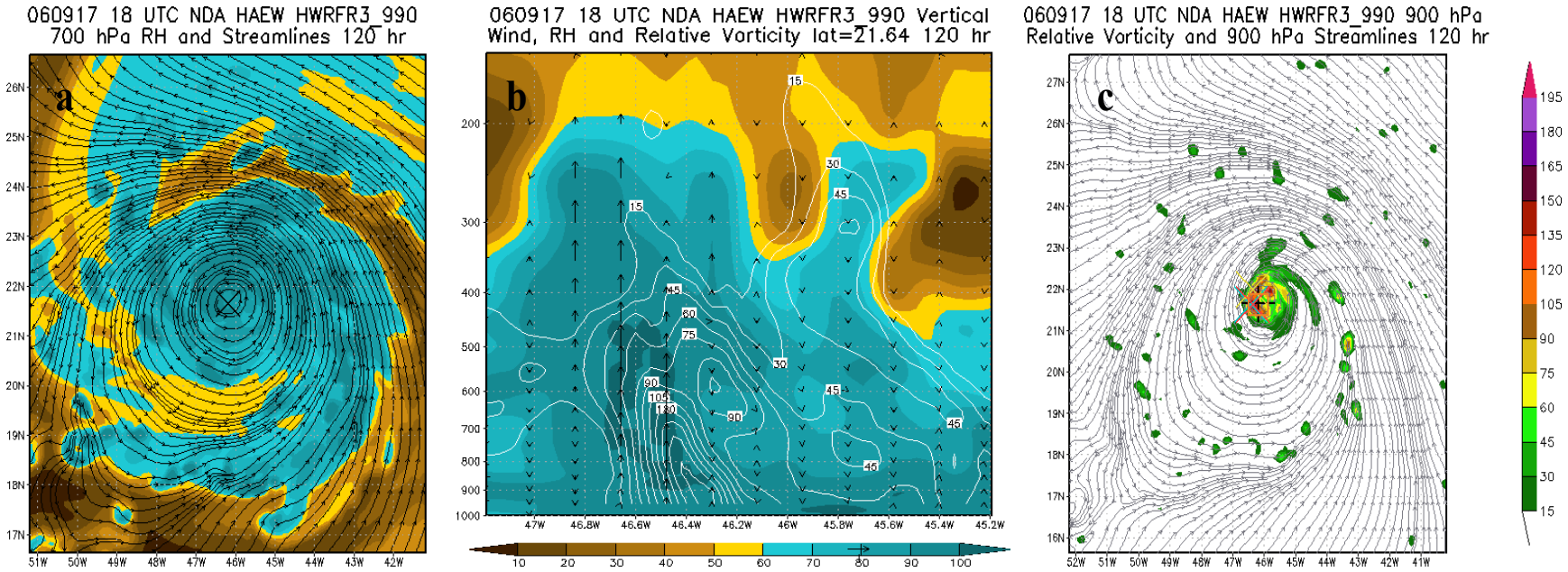

Figure 5.15 CNTRL Nested R3 990 structure of Helene at 120 h (continued): (a) 700-hPa RH and streamlines (b) east-west zonal VCS of RH (shaded), vertical wind (arrows) and RVORT (white contours) centered at the MLWSM, and (c) 900-hPa RVORT and streamlines.

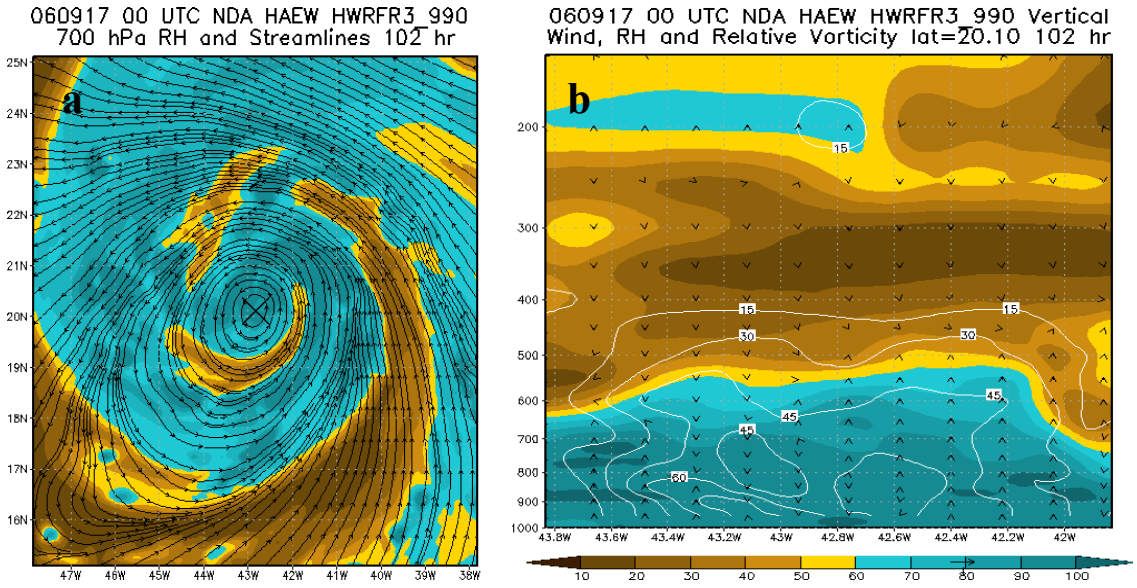

Figure 5.16 CNTRL Nested R3 990 structure of TS Helene at 102 h during a second period of dry air intrusion: (a) 700-hPa RH and streamlines (b) east-west zonal VCS of RH (shaded), vertical wind (arrows) and RVORT (white contours) centered at the MLWSM.

5.2 Nesting test

Operationally, the HWRF two-way interactive nesting capability in the 9- and 3-km resolution domains has demonstrated to produce a more realistic structure of the hurricanes when compared to observations (Gopalakrishnan et al. 2012). In this section, the HWRFx 3-km moving nest and high-resolution effect in the structure and intensity forecast of weak tropical systems are investigated. For each AEW under study, CNTRL nested (9:3 km) and un-nested (9 km) simulations were conducted. Based on the CUP sensitivity test results, the SAS was not applied to the 9-km parent domain of these simulations for the convection to be explicit. See Table 4.2 to refer to the details of the experiments settings.

5.2.1 NDAEW nesting sensitivity

The NDAEW nesting sensitivity results showed that the removal of the 3-km nest assisted in hindering the development of the wave. Both simulations depicted similar operational metrics from 0 h to approximately 93 h (Fig. 5.17). However, from approximately 96 h to the end of the simulation, the nested run predicted a stronger system. The MSW of the nested run forecast TS intensity starting at 96 h, which coincided with the time the NDAEW emerged from the dry air that was affecting the system in that run. It also concurred with the formation of a mid-to-upper levels anticyclone that started aligning to the MLWSM.

However as discussed in the CUP sensitivity test, TS cyclogenesis did not occur until 114 h (Figs. 5.4-5.8) when a well-defined center within the surface cyclonic circulation formed, and the mid-to-upper levels anticyclone developed a center aligned to the MLWSM and a RVORT core formed at the cyclone center. After TS genesis, the nested run maintained the TS intensity until the end of the simulation.

For the un-nested run, from 96 h to the end of the simulation, the intensity of the system fluctuated between TD and TS. Nevertheless, no development took place as shown by the structure and environment at 120 h (Figs. 5.18-5.19). By the end of the un-nested simulation, no surface well-defined cyclonic circulation center (Fig. 5.18a) and no core of RVORT formed (Fig. 5.19c). Reasons that prevented the development of the NDAEW included the model inability to maintain MSLP closed contours, periods of high environmental shear (equal or greater than 30 kt) near the MLWSM, a drier environment since early in the simulation (approximately 12 h), and dry air intrusion well in advance and for a longer period of time when compared to the nested run. Dry air intrusion to the core of the system occurred from 39 h to 120 h in the un-nested run whereas for the nested run it started at 63 h and ended approximately at 93 h. Figure 5.19a shows that at 120 h the NDAEW of the un-nested run started to emerge from the dry air that entrained to its environment. A weaker MSLP intensity and structure (Fig. 5.18c) inhibited moist convection and advanced convergence, which obstructed the generation of a RVORT core. Besides the dynamic constraints, the RVORT core formation was also hindered by the prolonged intrusion of very dry air to the wave environment, which caused subsidence of cooler dehumidified air.

Both the dynamic and thermodynamic factors avoided the merger of smaller centers of RVORT and its advection to upper levels in the troposphere (Fig. 5.19b).

Even though the un-nested run was able to hinder cyclogenesis, the model managed to maintain a cyclonic circulation at the lower levels centered around 10.5°N 44.5°W. The Hovmöller of Meteosat-8 IR imagery (Fig. 4.1) showed that on Sep 13 1130 UTC there were no cloud clusters associated with this wave. On the other hand, the model was able to capture the SAL dry air over that location (Fig. 5.20). In addition to the surface and lower-levels structure, other signs in the model that showed a weaker system were a broadened mid-to-upper levels anticyclone center aligned to the MLWSM and the outflow speed.

Results from this section demonstrated that the nesting in HWRFx does have a dynamic and thermodynamic impact on weak tropical systems. Inclusion of this capability developed the NDAEW while the removal of it resulted in hindering the wave intensification. Even though the two-way interactive nesting capability in the 9- and 3-km resolution domains of the operational HWRF has demonstrated to produce a more realistic structure for mature hurricanes (Gopalakrishnan et al. 2006), the effect on weaker systems it is unclear. To further understand the effect of nesting in the intensity forecast of weak disturbances, more case studies need to be investigated.

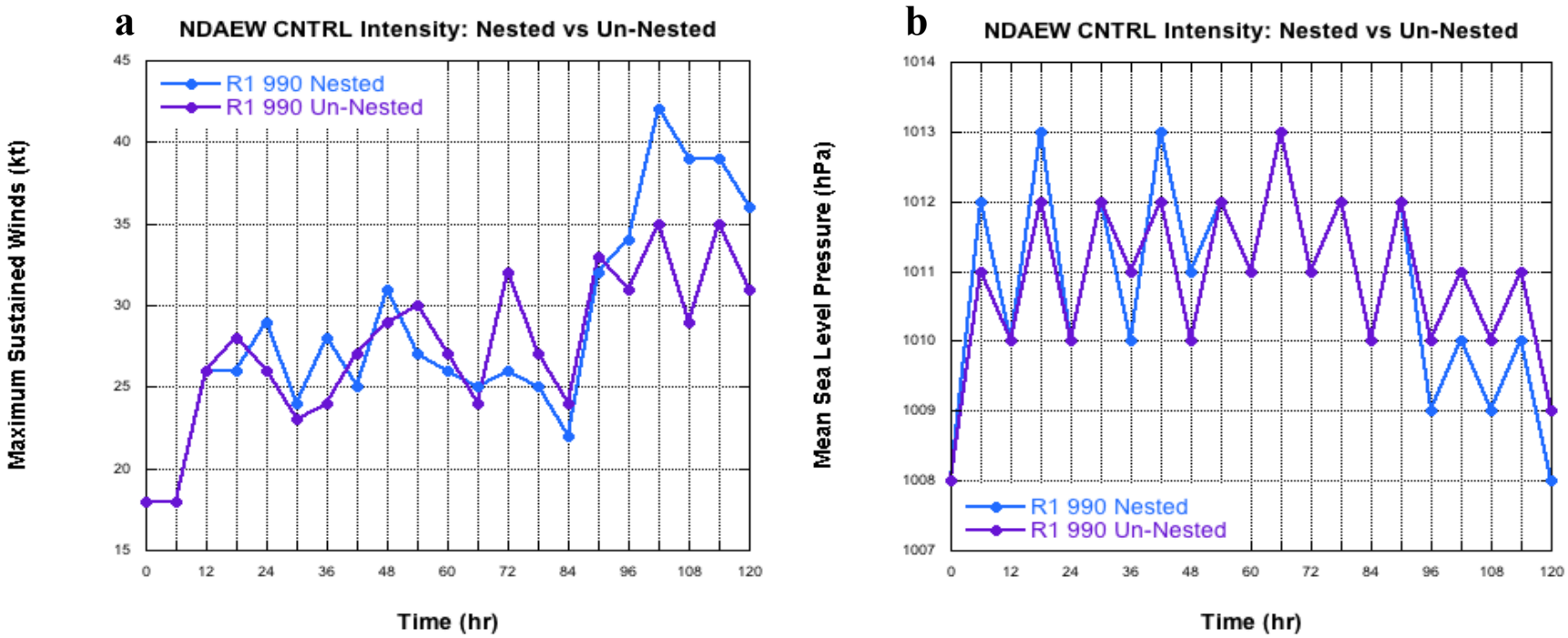

Figure 5.17 NDAEW surface intensity evolution from CNTRL Nesting sensitivity runs: (a) maximum sustained winds (kt) and (b) MSLP (hPa). The light blue and purple lines represent the nested and un-nested runs, respectively.

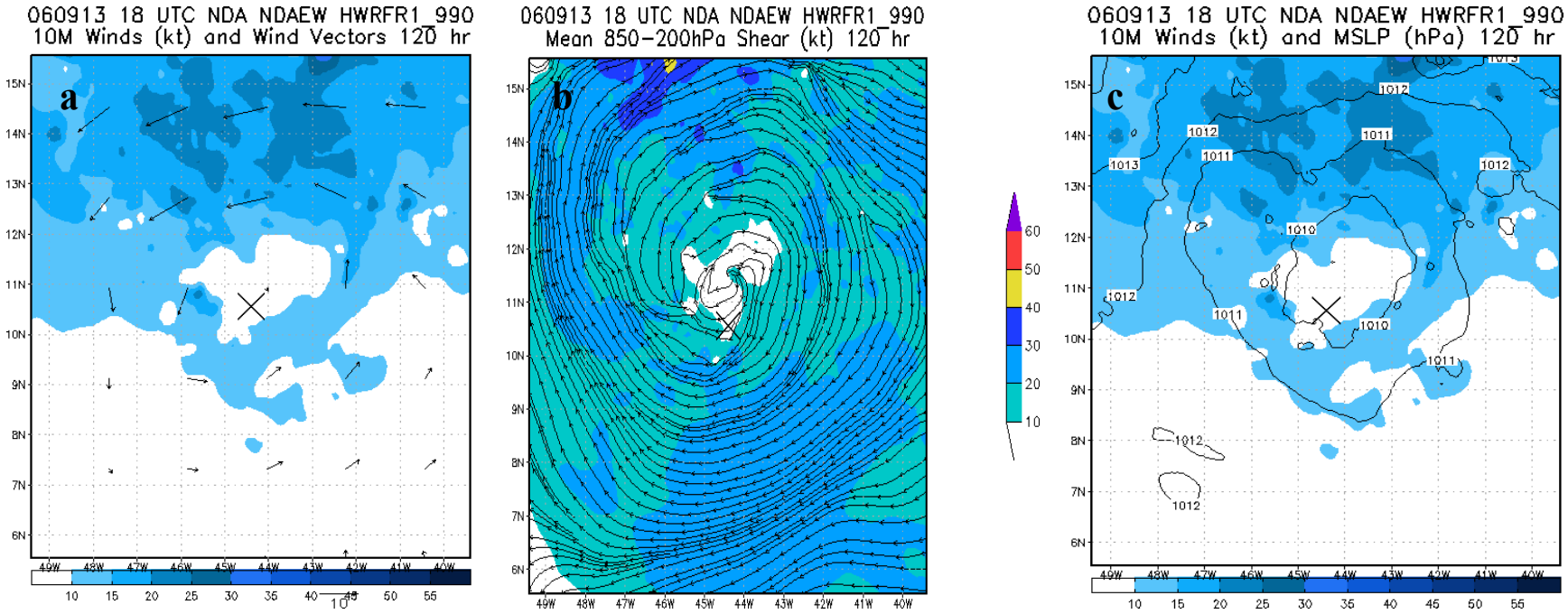

Figure 5.18 CNTRL Un-nested R1 990 structure of NDAEW at 120 h: (a) 10 m wind speed and vectors (b) deep layer environmental shear and (c) 10 m wind speed and MSLP. The MSW at this time was 32 kt and the minimum of MSLP was 1009 hPa.

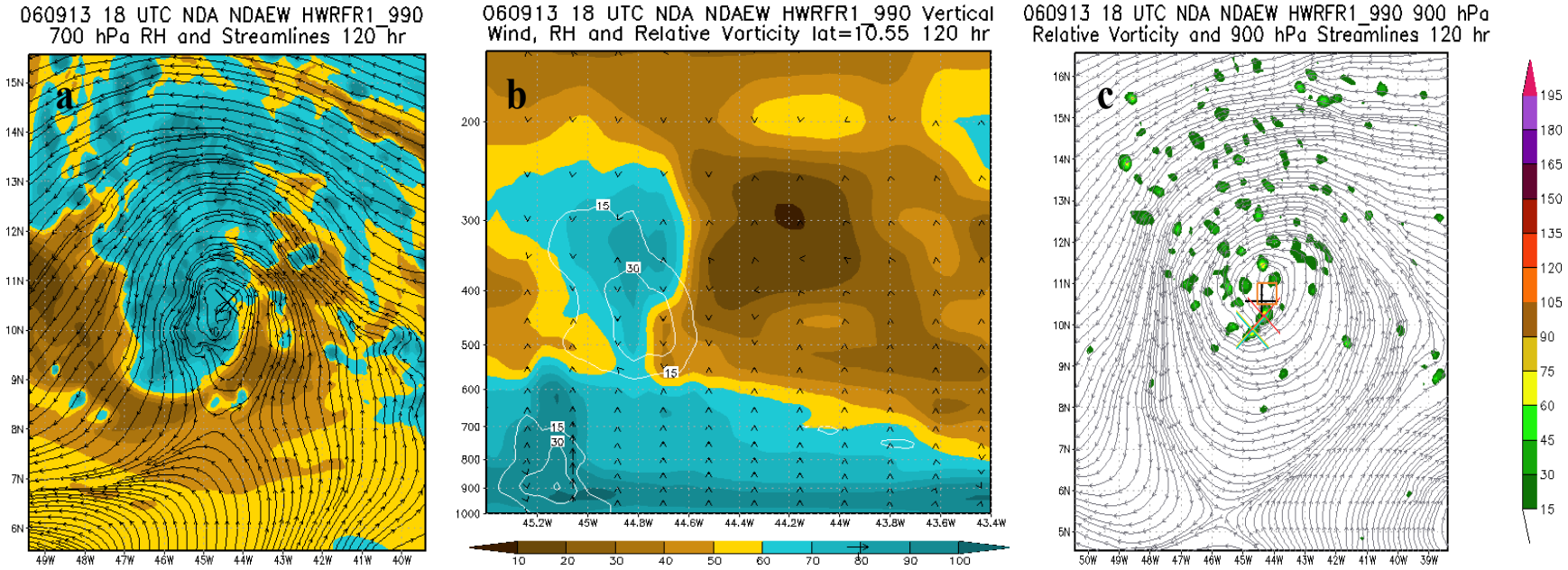

Figure 5.19 CNTRL Un-nested R1 990 structure of NDAEW at 120 h (continued): (a) 700-hPa RH and streamlines (b) east-west zonal VCS of RH (shaded), vertical wind (arrows) and RVORT (white contours) centered at the MLWSM, and (c) 900-hPa RVORT and streamlines.

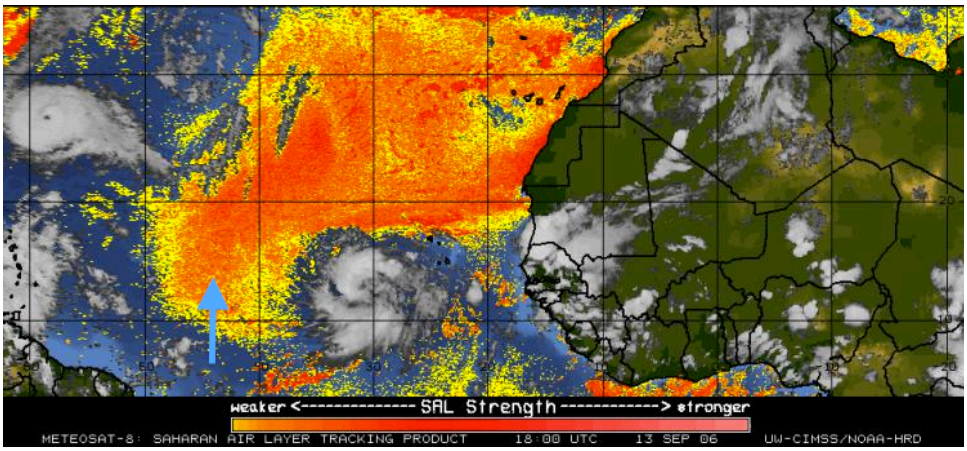

Figure 5.20 SAL tracking imagery on September 13 1800 UTC showing the NDAEW approximate position (blue arrow) according to the un-nested R1 990 HWRFx simulation.

5.2.2 HAEW nesting sensitivity

The nesting sensitivity results of the HAEW showed that the removal of the 3-km nest had a weakening effect similar to the NDAEW case. Besides predicting weaker TS, the exclusion of the 3-km nest further delayed the TS cyclogenesis when compared to the nested run and the NHC BT analyses. TS cyclogenesis was forecast earlier in both runs, yet the environment and structure of the waves determined that it occurred at 63 h (Figs. 5.10-5.11) and 90 h (Figs. 5.22-5.23) for the nested and un-nested runs, respectively. This represents thirty-three hours and sixty hours delay when compared to NHC (30 h). The nested and un-nested runs forecast the TD stage of Helene, though only during the first six hours of the simulations and weaker than the NHC BT analyses. None of the simulations predicted strengthening to hurricane category one (90 h) or two (120 h). Alternatively, TS intensity was sustained until the end of the simulations after TS cyclogenesis. During the TS stage, the inclusion of the 3-km nest assisted in forecasting

a stronger storm shown equally in the operational metrics (Fig. 5.21) and the wave structure. Figures 5.14-5.15 and Figs. 5.24-5.25 show the nested and un-nested structure of TS Helene at 120 h, respectively.

In both runs, factors that weakened the system and delayed TS cyclogenesis included strong environmental shear associated with a mid-to-upper levels ridge, and frequent dry air intrusion to the wave environment at 700 hPa as well as into the MLWSM within 500 hPa and 700 hPa. However, both factors lasted for a longer period of time in the un-nested run. Particularly, multiple periods of dry air intrusion to the HAEW environment occurred in the un-nested run at 700 hPa. These periods consisted of 27 h-72 h, 90 h-96 h, and 114 h-117 h whereas for the nested run dry air intrusion only occurred two times from 30 h-60 h and 96 h-114 h. Moreover, much drier air affected the un-nested run MLWSM within 500 hPa and 700 hPa.

After TS cyclogenesis, the un-nested run had two main weakening periods that supported the less intense storm predicted by the MSW. The first weakening episode happened at 96 h. At this time, 50-59 % RH air at 700 hPa was observed near the TC center (Fig. 5.26a) and at the MLWSM air with less than 10 % RH expanded from 500 hPa to 350 hPa, which acted to dehumidify the troposphere from 600 hPa to 800 hPa (Fig. 5.26b). As a result, subsidence of very dry air deterred moist convection and debilitated the core of RVORT at 800 hPa (Fig. 5.26c). However, this episode did not affect either the structure of the mid-to-upper levels anticyclone and the cyclone at the surface (Fig. 5.27). By 99 h, with the slightly but continual MSLP decrease the convergence augmented, the moist convection at the MLWSM increased and a stronger RVORT core developed via merger and vertical advection (Figs. 5.28b-c). The vertical

advection of RVORT at the MLWSM acted to displace the dry air from 600 hPa to approximately 500 hPa (Fig. 5.28b), which restored the high humidity at the center of the system (Fig. 5.28a). Past 99 h, as the system continued intensifying at the surface, the RVORT core at the lower levels kept strengthening via merger and consolidated at the center of the storm. A second brief weakening period in the un-nested run occurred from 114 h-117 h when air with 40-59% RH entrained the MLWSM from 600 hPa to 700 hPa (Fig. 5.29) and the intensity of the RVORT core decreased. At 120 h, with a slight drop on MSLP (Fig. 5.21b) both convergence and moist convection augmented, which re-established a moister environment and strengthened the RVORT core at the MLWSM (Figs. 5.25a-b).

Like for the NDAEW case, results from this section demonstrated that the nesting in HWRFx does have a dynamic and thermodynamic impact on weak tropical systems. The addition of the nesting capability resulted in the forecast of a stronger Helene whereas the exclusion of it not only predicted a weaker system but also further delayed the TS cyclogenesis twenty-seven and sixty hours when compared to the nested run (63 h) and NHC (30 h), respectively. To further understand the nesting effect on the intensity forecast of weak tropical systems, more case studies need to be investigated. Since the two-way interactive nesting capability in the 9- and 3-km resolution domains of the operational HWRF has demonstrated to produce a more realistic structure for mature hurricanes (Gopalakrishnan et al. 2006), a study that compares the structures of a mature system versus a weaker storm would be ideal to try to better understand the nesting effect on weaker systems.

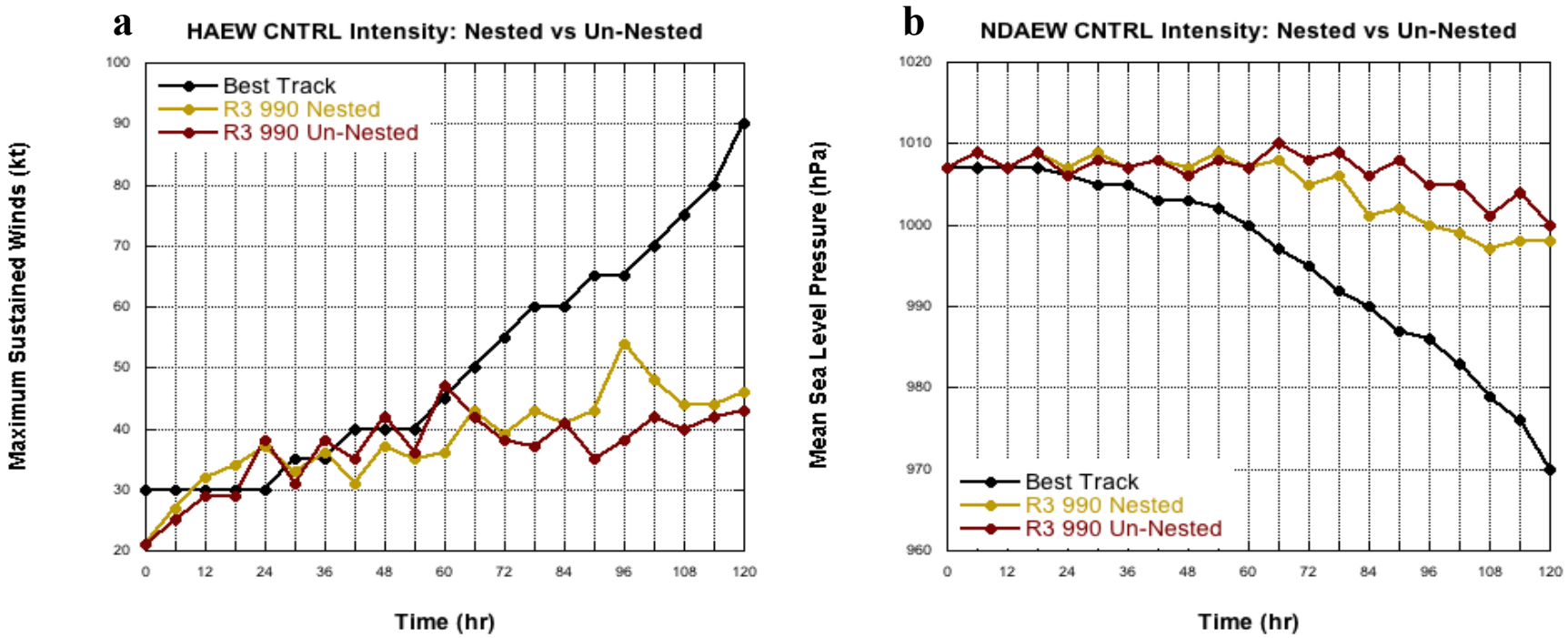

Figure 5.21 HAEW surface intensity evolution from CNTRL Nesting sensitivity runs: (a) maximum sustained winds (kt) and (b) MSLP (hPa). The yellow and red lines represent the nested and un-nested runs, respectively.

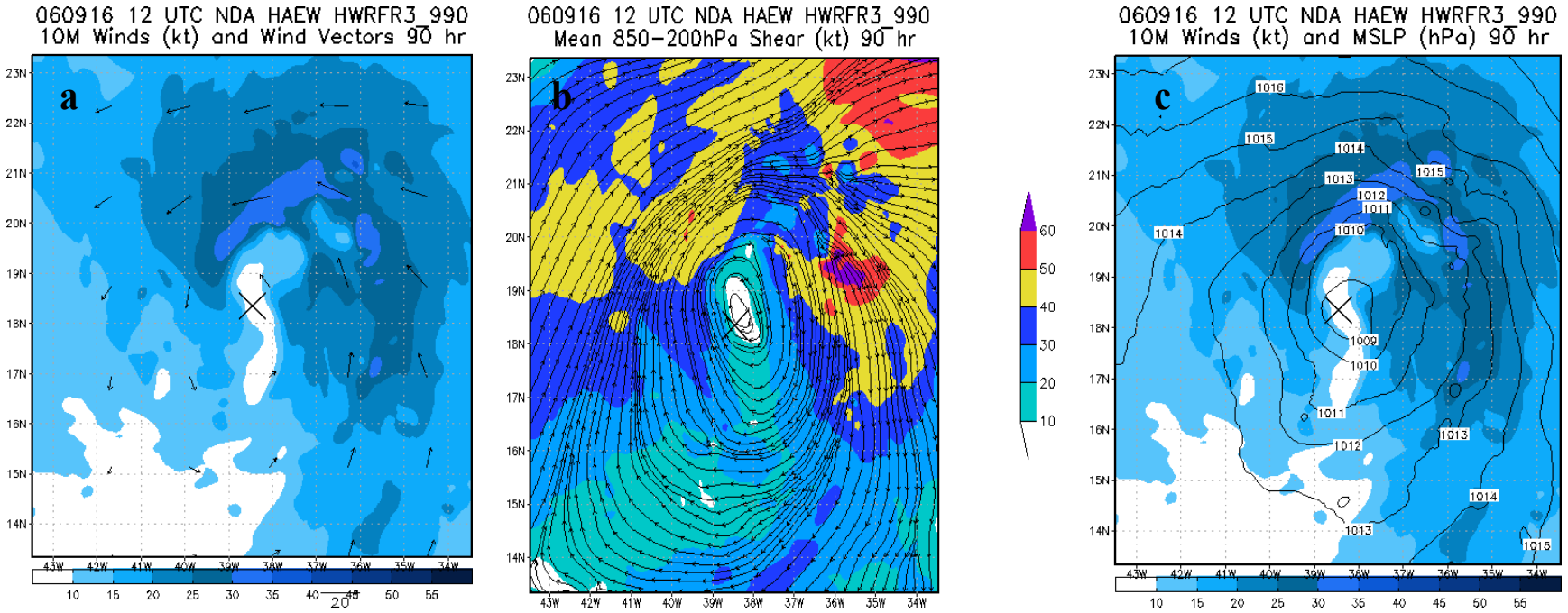

Figure 5.22 CNTRL Un-nested R3 990 structure of HAEW at time of TS cyclogenesis: (a) 10 m wind speed and vectors (b) deep layer environmental shear and (c) 10 m wind speed and MSLP. At 90 h, the MSW was 36 kt and the minimum of MSLP was 1008 hPa.

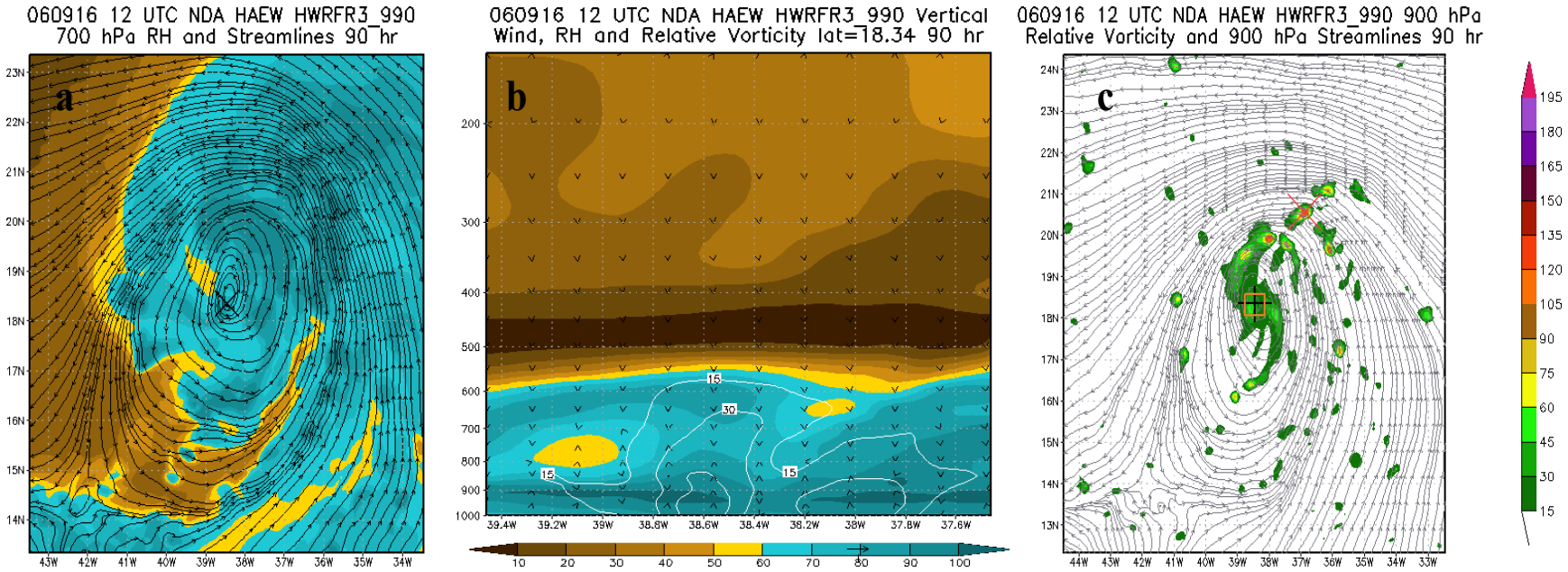

Figure 5.23 CNTRL Un-nested R3 990 structure of HAEW at time of TS cyclogenesis (continued): (a) 700-hPa RH and streamlines (b) east-west zonal VCS of RH (shaded), vertical wind (arrows) and RVORT (white contours) centered at the MLWSM, and (c) 900-hPa RVORT and streamlines.

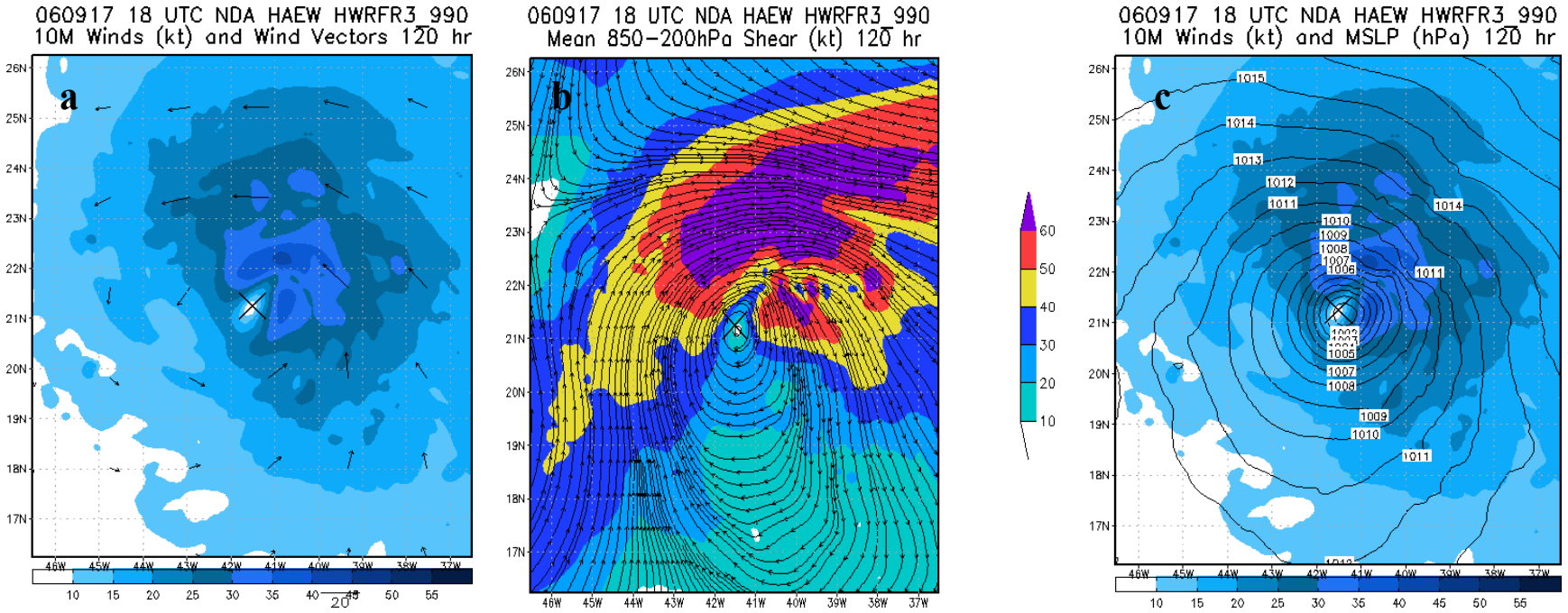

Figure 5.24 CNTRL Un-nested R3 990 structure of Helene at 120 h: (a) 10 m wind speed and vectors (b) deep layer environmental shear and (c) 10 m wind speed and MSLP. At 90 h, the MSW was 43 kt and the minimum of MSLP was 1000 hPa.

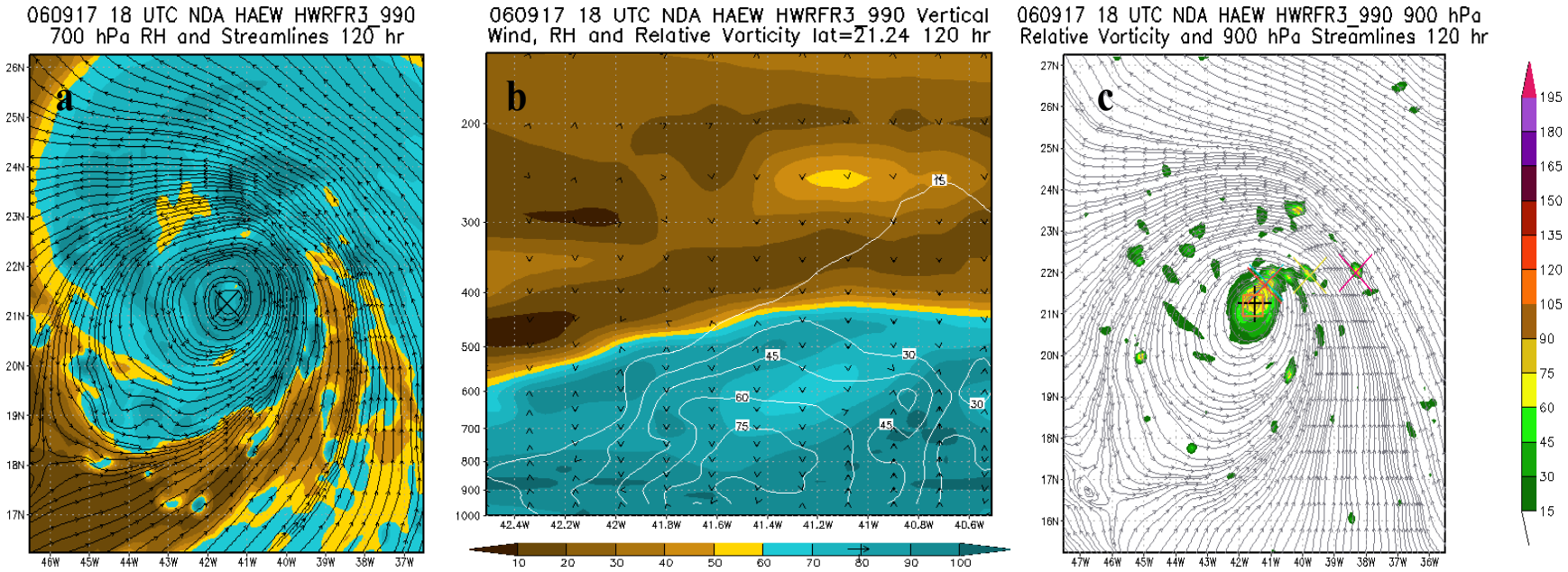

Figure 5.25 CNTRL Un-nested R3 990 structure of Helene at 120 h (continued): (a) 700-hPa RH and streamlines (b) east-west zonal VCS of RH (shaded), vertical wind (arrows) and RVORT (white contours) centered at the MLWSM, and (c) 900-hPa RVORT and streamlines.

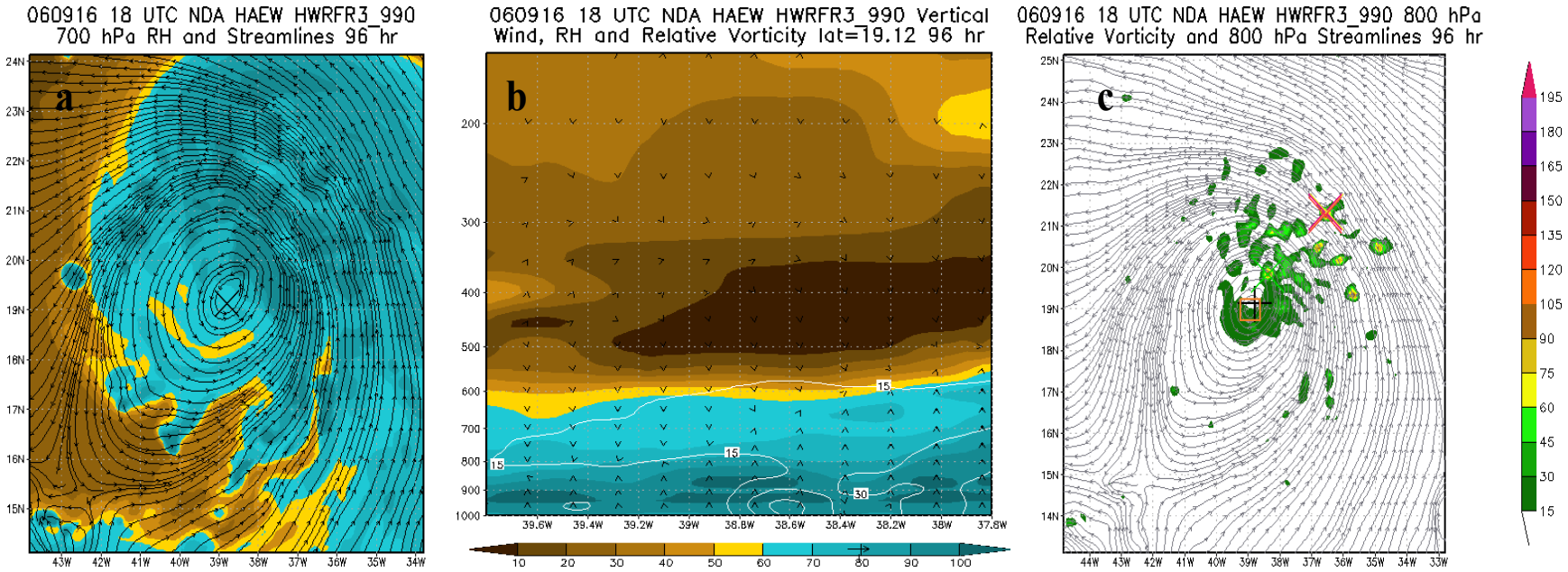

Figure 5.26 CNTRL Un-nested R3 990 structure of Helene at 96 h: (a) 700-hPa RH and streamlines (b) east-west zonal VCS of RH (shaded), vertical wind (arrows) and RVORT (white contours) centered at the MLWSM, and (c) 900-hPa RVORT and streamlines.

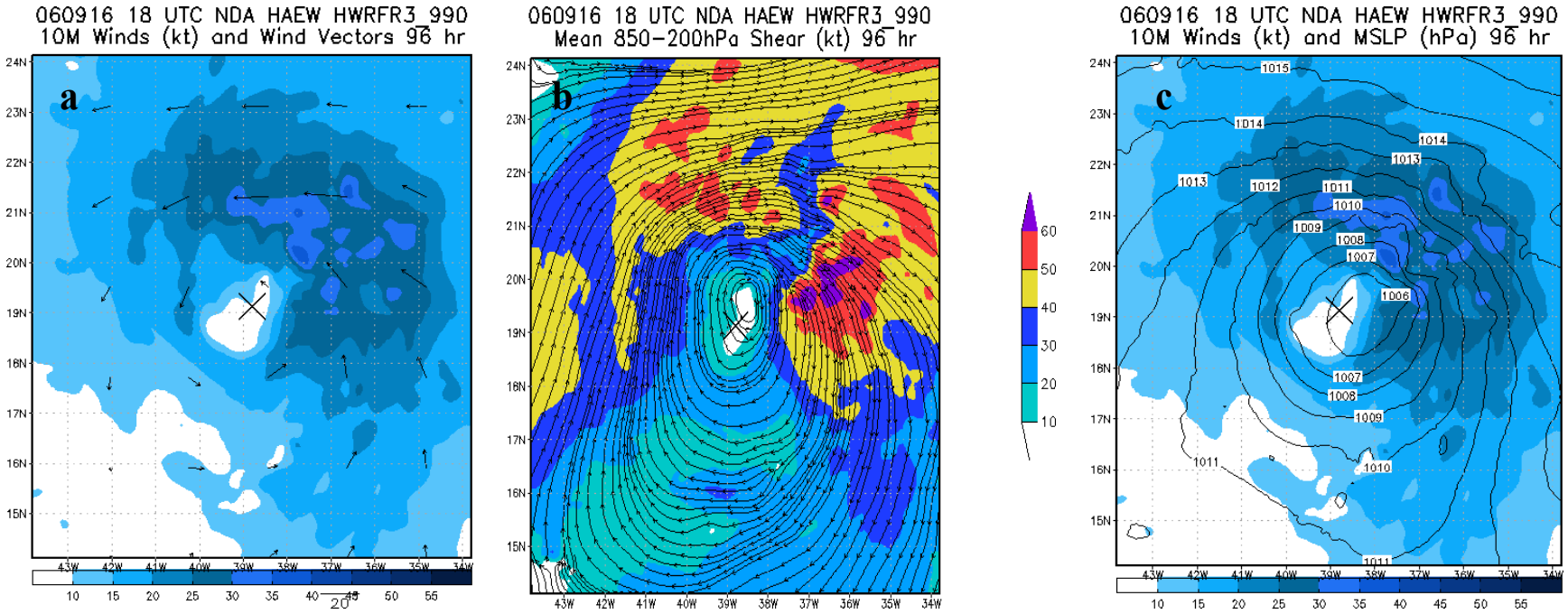

Figure 5.27 CNTRL Un-nested R3 990 structure of Helene at 96 h (continued): (a) 10 m wind speed and vectors (b) deep layer environmental shear and (c) 10 m wind speed and MSLP. At 96 h, the MSW was 38 kt and the minimum of MSLP was 1005 hPa.

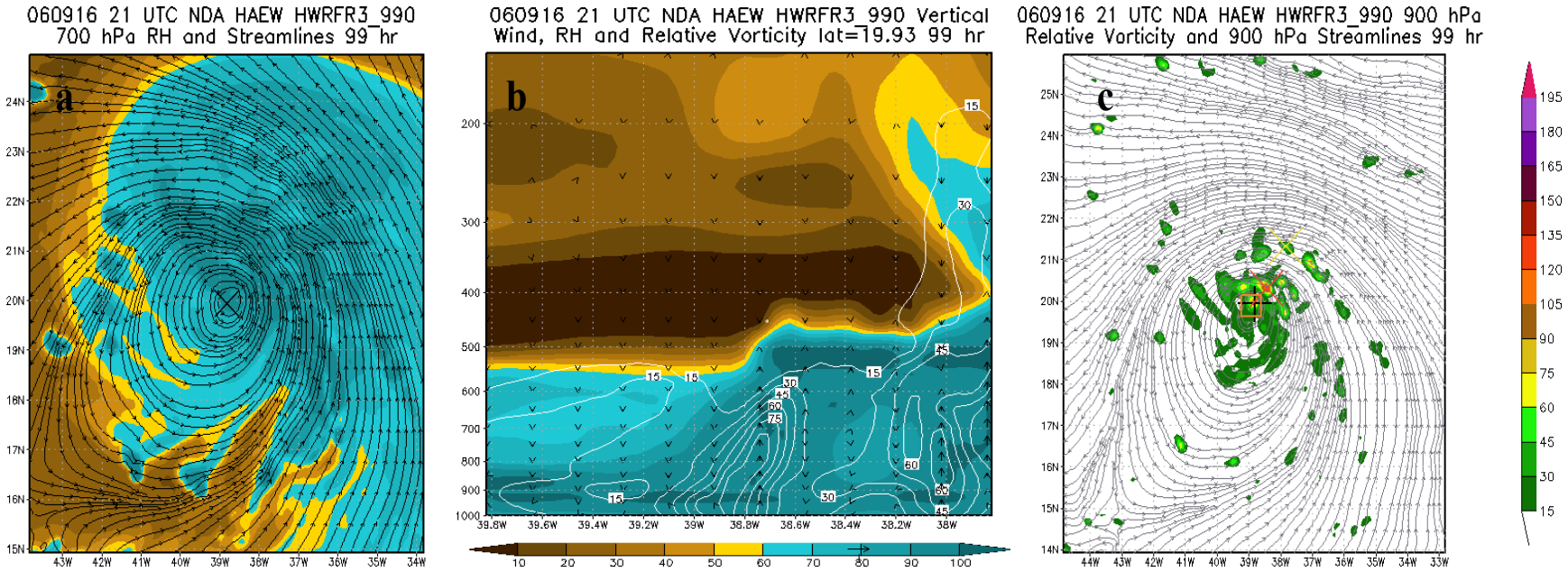

Figure 5.28 CNTRL Un-nested R3 990 structure of Helene at 99 h: (a) 700-hPa RH and streamlines (b) east-west zonal VCS of RH (shaded), vertical wind (arrows) and RVORT (white contours) centered at the MLWSM, and (c) 900-hPa RVORT and streamlines.

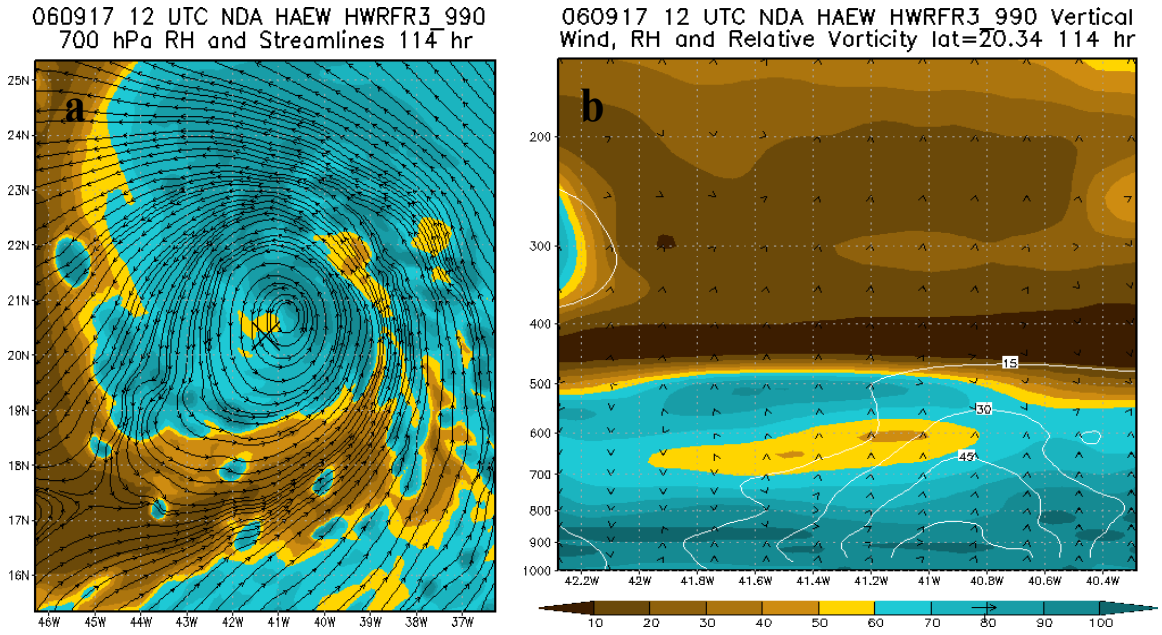

Figure 5.29 CNTRL Un-nested R3 990 structure of Helene at 114 h: (a) 700-hPa RH and streamlines (b) east-west zonal VCS of RH (shaded), vertical wind (arrows) and RVORT (white contours) centered at the MLWSM.

5.3 Initial conditions test

In this section, the HWRFx dynamic and thermodynamic initial conditions from CNTRL (NDA) and EXP (DA) runs were verified against the NAMMA dropwindsondes observations. The performance of HWRFx due to changes on ICs was also evaluated for each AEW under study. The purpose of this test was to investigate the impact of additional temperature, specific humidity and wind dropwindsonde data in the structure and intensity forecast of weak tropical systems. Both CNTRL and EXP runs in this section are un-nested and did not include the SAS CUP (see Table 4.2 to refer to the details of the experiments settings). As specified in chapter four, both the ICs and BCs of the CNTRL runs were from GFS final analyses. The BCs of the EXP runs were from the GFS final analyses, however the ICs were from the HEDAS mean final analysis, which utilized GEFS model data.

The AEWs wind dynamics and structure at the initial time of the CNTRL and EXP runs (see Table 4.3 for runs initialization times) were analyzed at mandatory levels 250 (only for HAEW), 300, 400, 500, 700, 850, 925, and 1000 hPa and compared to the NAMMA dropwindsonde wind observations. To get a clearer idea of the CNTRL and EXP analysis wind field near the actual observations, a blue dotted line was used to trace the flight track and dropwindsondes locations. To verify the CNTRL and EXP AEWs thermodynamic environment at the initial time of the runs, model skew-T diagrams at the actual dropwindsondes locations were compared to the NAMMA dropwindsondes vertical profiles. To ease the discussion, the letter D followed by a number was used to refer to each particular dropwindsonde.

5.3.1 NDAEW initial conditions

Results showed that the HWRFx CNTRL and EXP NDAEW wind structure were similar at the initial time, however different from the observations. The dropwindsondes sampled two cyclonic circulations, one north and another south of 13°N from 1000 hPa up to 500 hPa, however not completely closed (Figs. 5.30a-5.34a). The CNTRL and EXP analyses simulated only the northern cyclonic circulation but further west near 15°N 23°W and only at 1000 hPa (Figs. 5.30b-c). From 925 hPa to 500 hPa, this northern cyclonic circulation vanished, but a weak cyclonic circulation started being evident near 13°N 19.5°W, which increases in definition from 850 hPa to 700 hPa and in strength at 700 hPa (Figs. 5.31b-5.34b and 5.31c-5.34c). Since the model resolution is much higher (9 km) than the observations (200 km), it is possible that plotting more barbs could show a structure more alike to the observations.

At 400 hPa, the dropwindsondes showed mixed wind patterns where the northern cyclonic circulation prevailed, however below 13°N winds were anticyclonic west of 19°W but cyclonic eastward (Fig. 5.35a). On the other hand, for the CNTRL and EXP analyses wind started becoming anticyclonic for the most part west of 16°W (Figs. 5.35b-c). At 300 hPa, the dropwindsondes again showed mixed wind patterns but anticyclonic wind prevailed west of 19°W (Fig. 5.36a). In the CNTRL and EXP analyses anticyclonic wind predominated north of 10°N in the entire domain (Figs. 5.36b-c).

In terms of wind magnitude, both CNTRL and EXP analyses resulted comparable to the observations. For all of the mandatory levels, the difference in wind magnitude between the observations and the analyses was zero to 5 kt, except for the 400 hPa where there was a difference of 10 kt between the observations and the EXP analysis. The EXP

analysis matched the observations at 925, 850, and 500 hPa whereas the CNTRL did it at 500 and 300 hPa. The CNTRL and EXP wind magnitudes were equivalent at 1000, 700 and 500 hPa. The maximum wind speed from dropwindsondes observations, CNTRL and EXP analyses at each mandatory level is shown in Table 5.1.

Table 5.1

NDAEW maximum wind speed at mandatory levels from dropwindsondes and HWRFx CNTRL and EXP ICs

NDAEW	Maximum wind speed (kt) at mandatory levels (hPa)						
	1000	**925**	**850**	**700**	**500**	**400**	**300**
Dropsondes	15	20	15	35	25	30	20
CNTRL	20	15	20	30	25	25	20
EXP	20	20	15	30	25	20	25

The skew-T diagrams of the HWRFx EXP analysis best represented the thermodynamic structure and environment at the dropwindsondes locations (Figs. 5.37c-5.51c). The EXP thermodynamic ICs were able to capture the moister troposphere zones as well as the regions impacted by SAL dry air intrusion in D1 (Fig. 5.37c), D9-D10 (Figs. 5.45c-5.46c), and D13-15 (Figs. 5.49c-5.51c). Particularly, D13 (Fig. 5.49c) and D14 (Fig. 5.50c) almost replicated the dropwindsonde profiles structure (Figs. 5.49a and 5.50a). The EXP D2-D8 (Figs. 5.38c-5.44c) and D11-D12 (Figs. 5.47c-5.48c) verified the quasi-saturated to saturated environment at the dropwindsonde location (Figs. 5.38a-5.44a and Figs. 5.47a-5.48a), which was supported by none to minimal signal of brown haze associated with Saharan dust in the Meteosat-8 true color imagery (Fig. 4.12).

Conversely, the thermodynamic profiles in the HWRFx CNTRL analysis of the NDAEW were not able to represent most of the changes in the vertical structure at the

different dropwindsonde locations. Particularly, D2 to D7 (Figs. 5.38b-5.43b) and D11 to D12 (Figs. 5.47b-5.48b) CNTRL profiles vertical structure showed to be similar to each other. Besides sharing almost the same shape, these vertical profiles depicted a quasi-saturated to saturated atmosphere within approximately 450 hPa to 600 hPa, which was not necessarily the case when compared to the dropwindsonde profiles (Figs. 5.38a-5.43a and 5.47a-5.48a). The CNTRL D1 (Fig. 5.37b), D9-D10 (Figs. 5.45b-5.46b) and D13-D15 (Figs. 5.49b-5.51b) captured some of the drying effect of the SAL, however most of the times in a lesser extent when compared to the EXP profiles. In general, the CNTRL ICs showed a moister environment when it was drier and vice versa. Therefore, the ICs were less accurate since increased instability (stability) was depicted in regions that were stable (unstable).

Satellite imagery enhancements such as the Meteosat-8 true color and SAL tracking product are good tools to detect the dry air and its interaction with tropical systems. However, it is the dropwindsonde that actually can measure it and provide the data that once ingested in the forecasting models might help to better predict the fate of weak tropical disturbances, thus improving the forecast of cyclogenesis. To verify this assumption, the initial dynamic and thermodynamic structure of both HWRFx CNTRL and EXP simulations was further analyzed in section 5.3.3 in order to determine its effect on the NDAEW forecast.

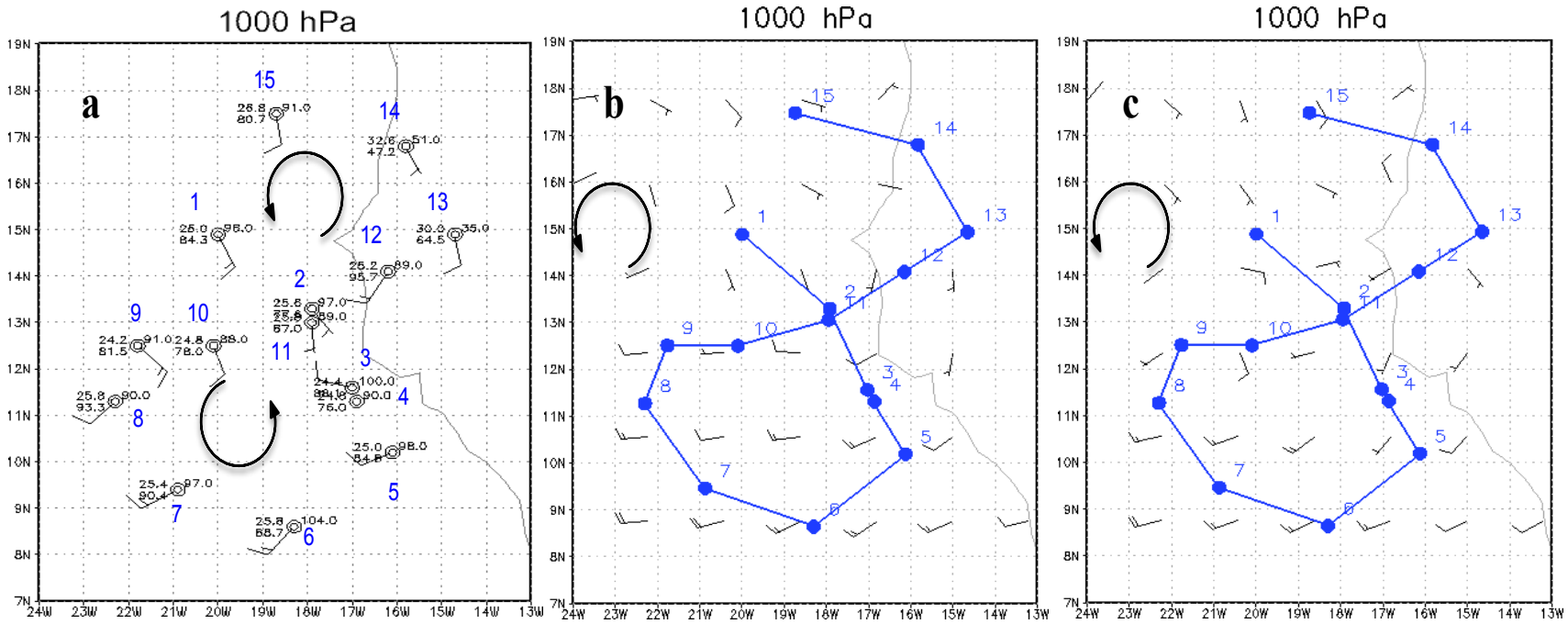

Figure 5.30 NDAEW wind dynamics at 1000 hPa from: (a) dropwindsondes (b) HWRFx CNTRL ICs and (c) HWRFx EXP ICs. The blue numbers identify the fifteen dropwindsondes used to sample the NDAEW. The blue dotted line traces the flight track and locations where the dropwindsondes were released.

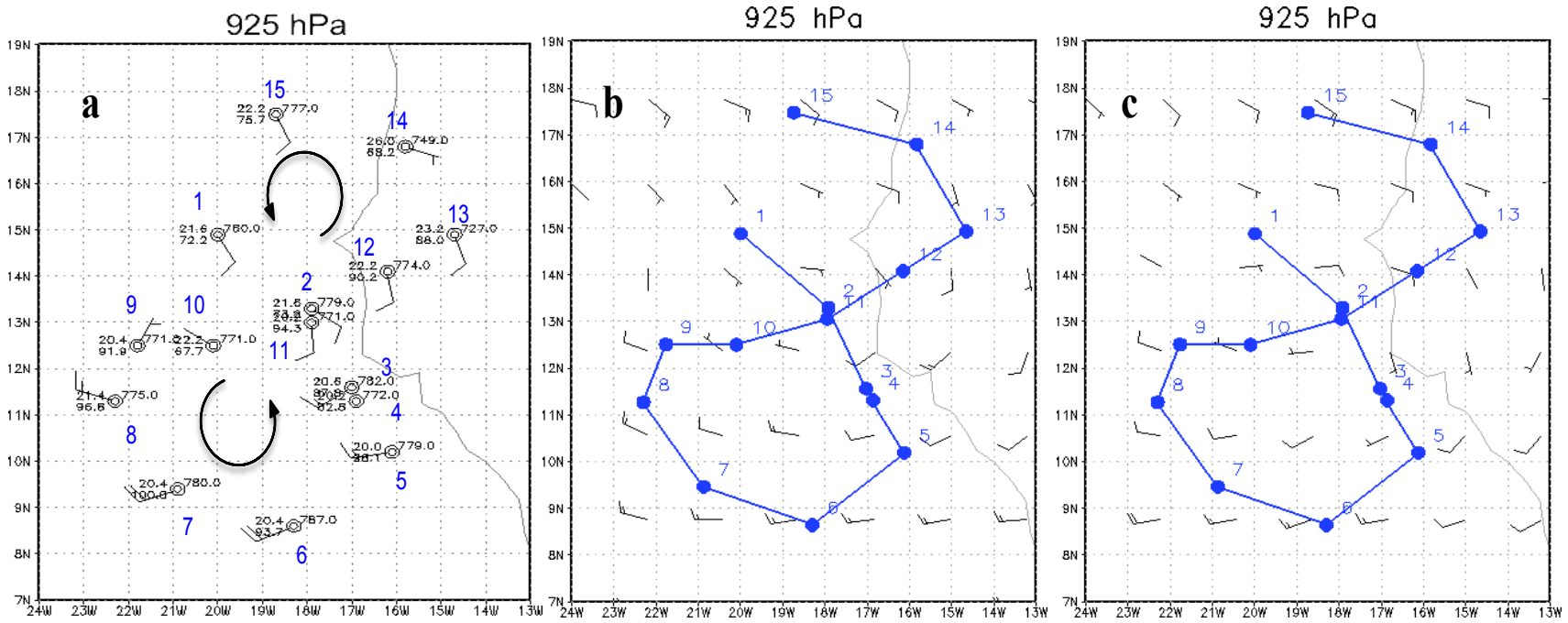

Figure 5.31 NDAEW wind dynamics at 925 hPa from: (a) dropwindsondes (b) HWRFx CNTRL ICs and (c) HWRFx EXP ICs. The blue numbers identify the fifteen dropwindsondes used to sample the NDAEW. The blue dotted line traces the flight track and locations where the dropwindsondes were released.

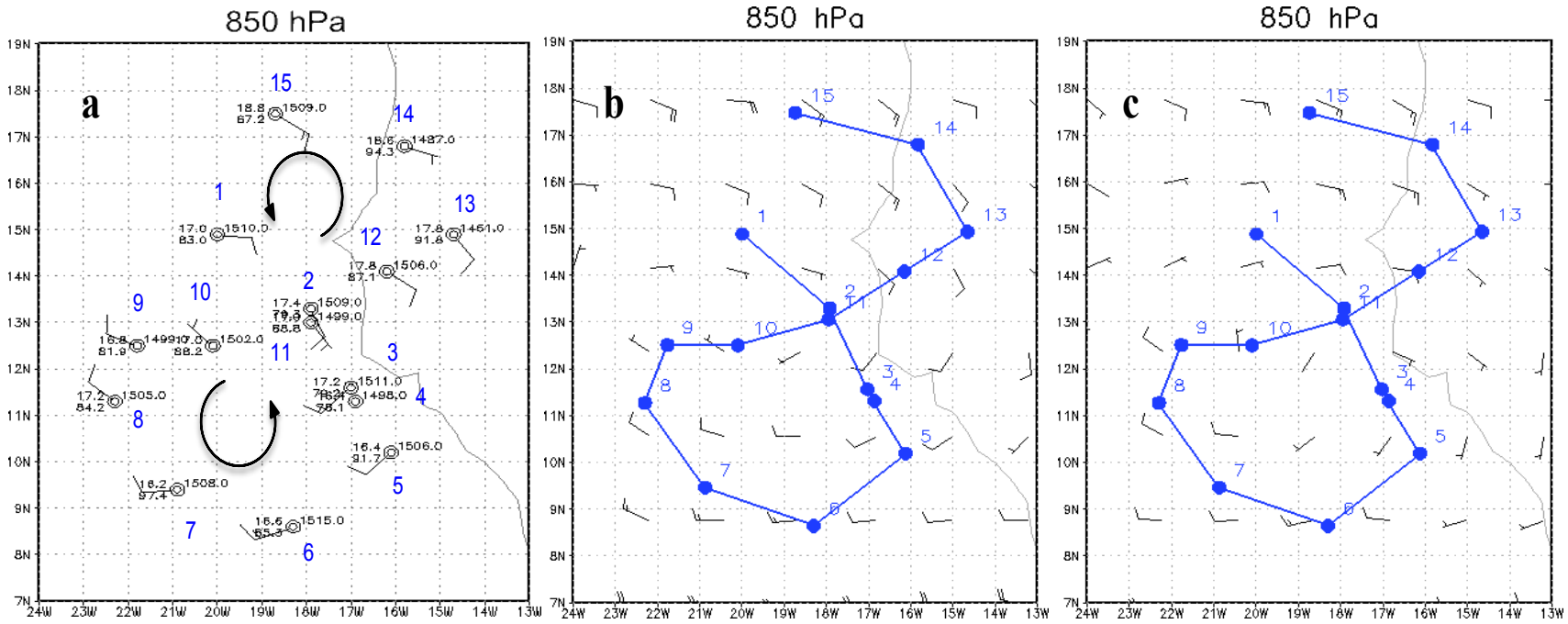

Figure 5.32 NDAEW wind dynamics at 850 hPa from: (a) dropwindsondes (b) HWRFx CNTRL ICs and (c) HWRFx EXP ICs. The blue numbers identify the fifteen dropwindsondes used to sample the NDAEW. The blue dotted line traces the flight track and locations where the dropwindsondes were released.

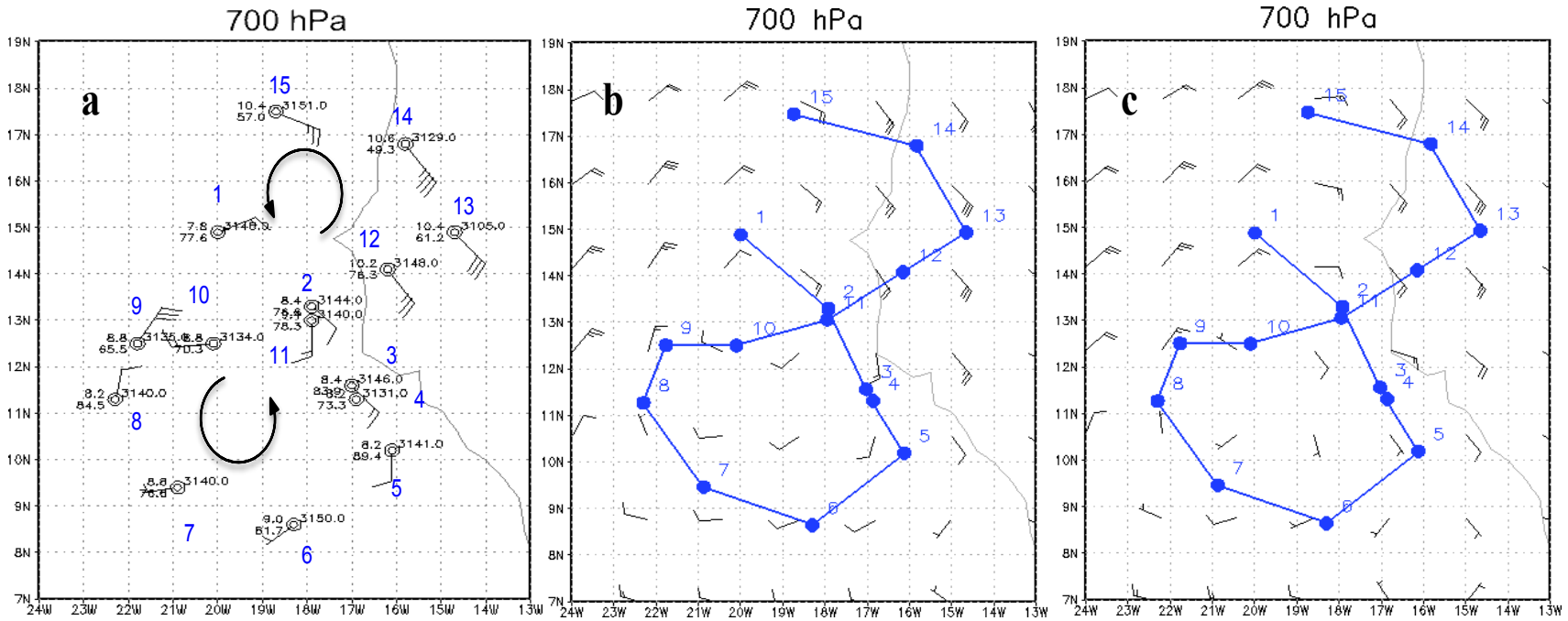

Figure 5.33 NDAEW wind dynamics at 700 hPa from: (a) dropwindsondes (b) HWRFx CNTRL ICs and (c) HWRFx EXP ICs. The blue numbers identify the fifteen dropwindsondes used to sample the NDAEW. The blue dotted line traces the flight track and locations where the dropwindsondes were released.

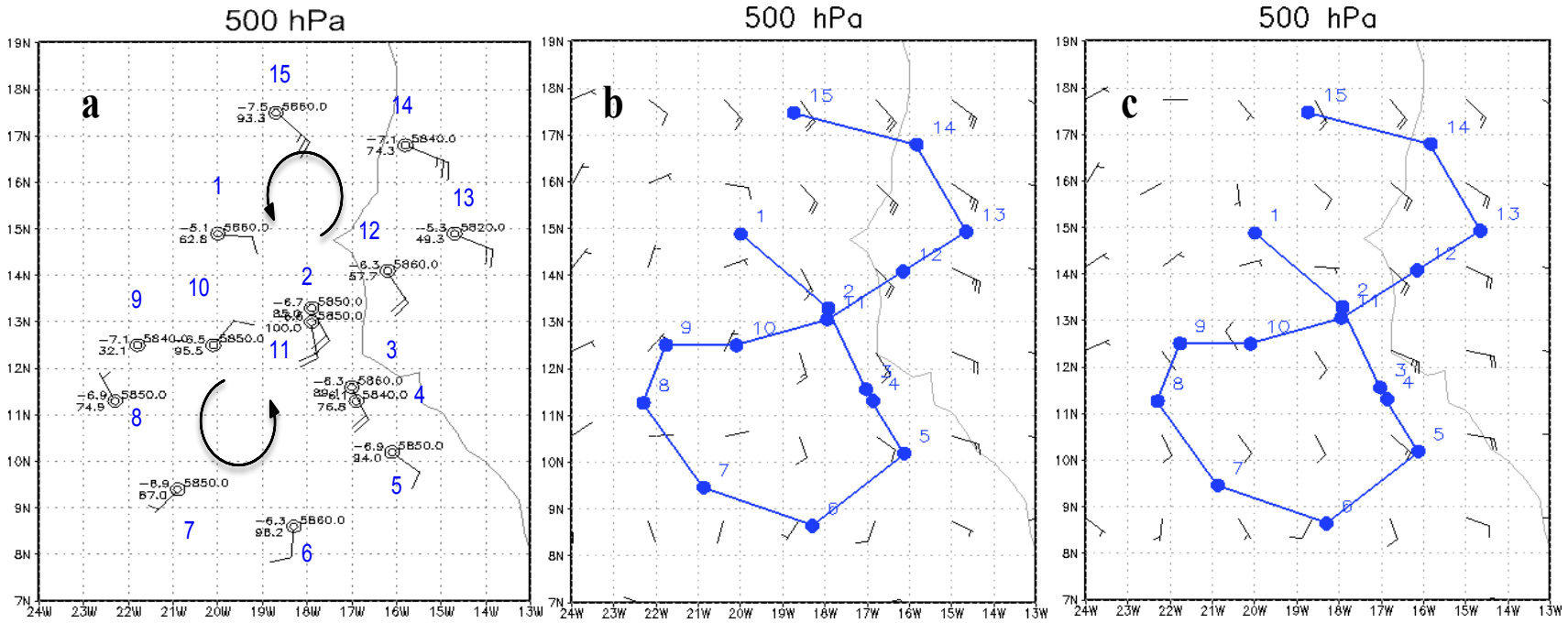

Figure 5.34 NDAEW wind dynamics at 500 hPa from: (a) dropwindsondes (b) HWRFx CNTRL ICs and (c) HWRFx EXP ICs. The blue numbers identify the fifteen dropwindsondes used to sample the NDAEW. The blue dotted line traces the flight track and locations where the dropwindsondes were released.

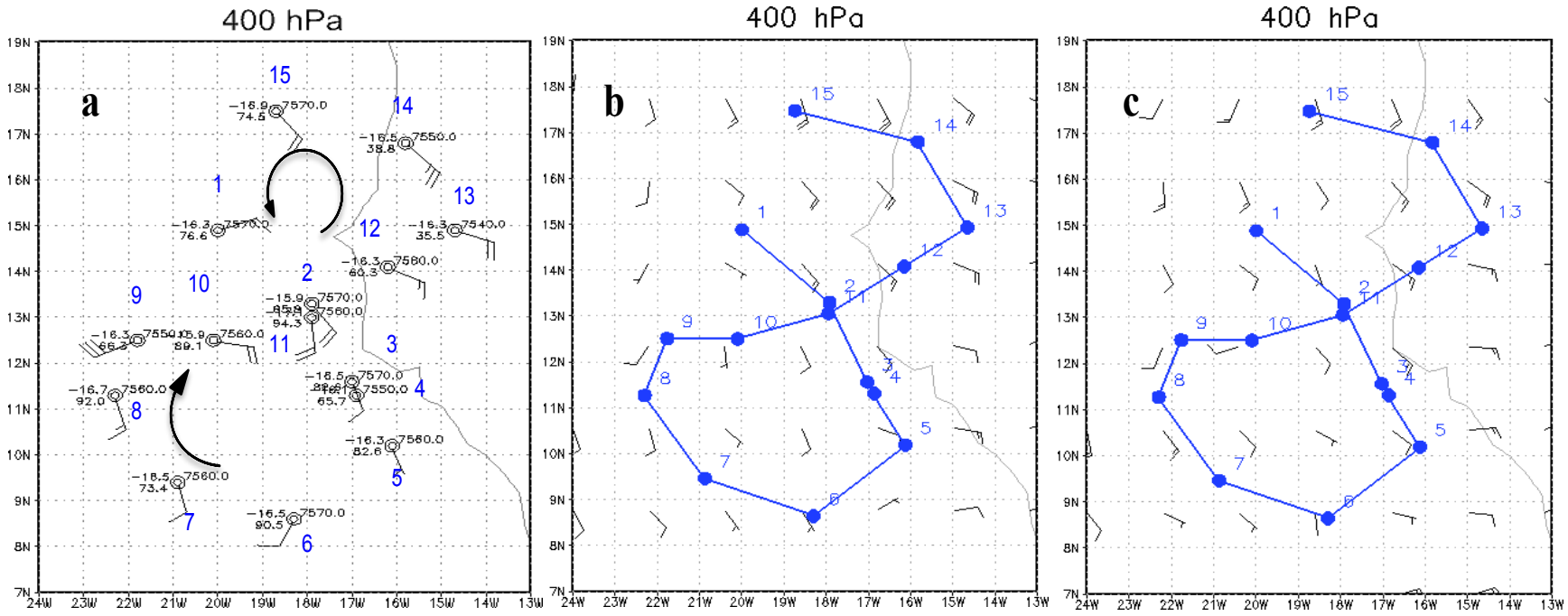

Figure 5.35 NDAEW wind dynamics at 400 hPa from: (a) dropwindsondes (b) HWRFx CNTRL ICs and (c) HWRFx EXP ICs. The blue numbers identify the fifteen dropwindsondes used to sample the NDAEW. The blue dotted line traces the flight track and locations where the dropwindsondes were released.

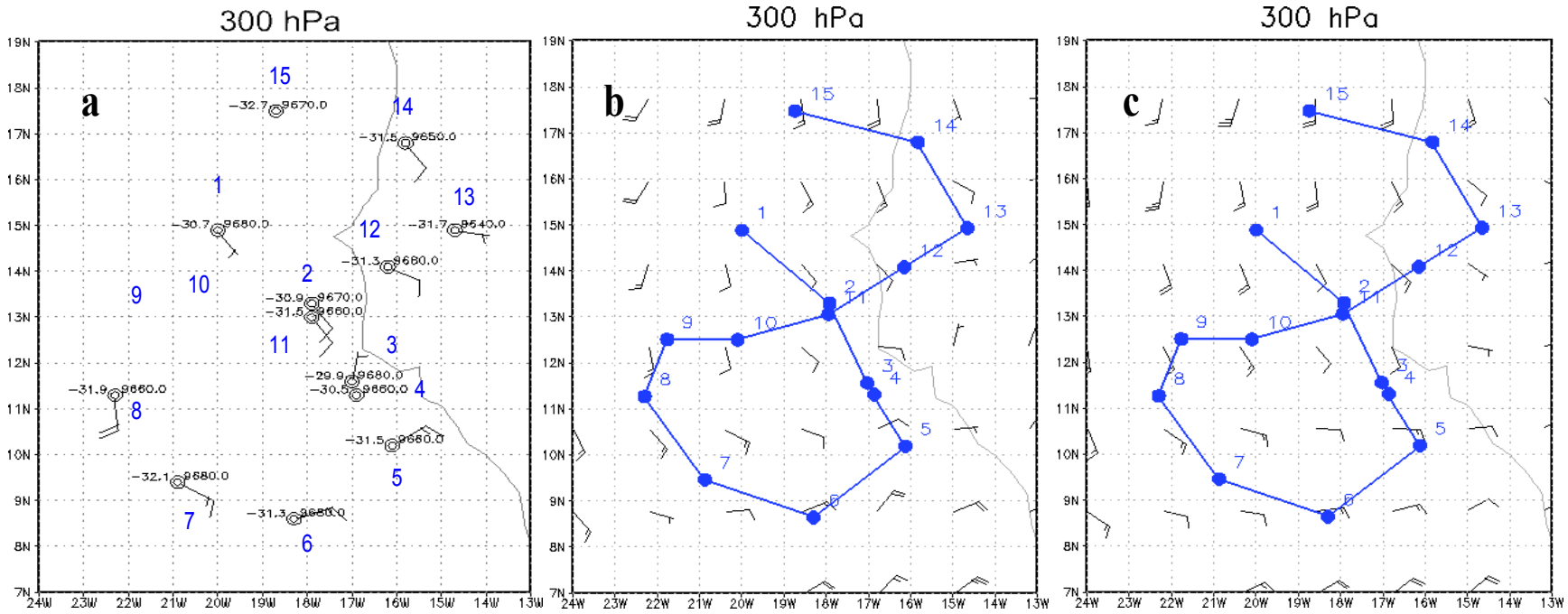

Figure 5.36 NDAEW wind dynamics at 300 hPa from: (a) dropwindsondes (b) HWRFx CNTRL ICs and (c) HWRFx EXP ICs. The blue numbers identify the fifteen dropwindsondes used to sample the NDAEW. The blue dotted line traces the flight track and locations where the dropwindsondes were released.

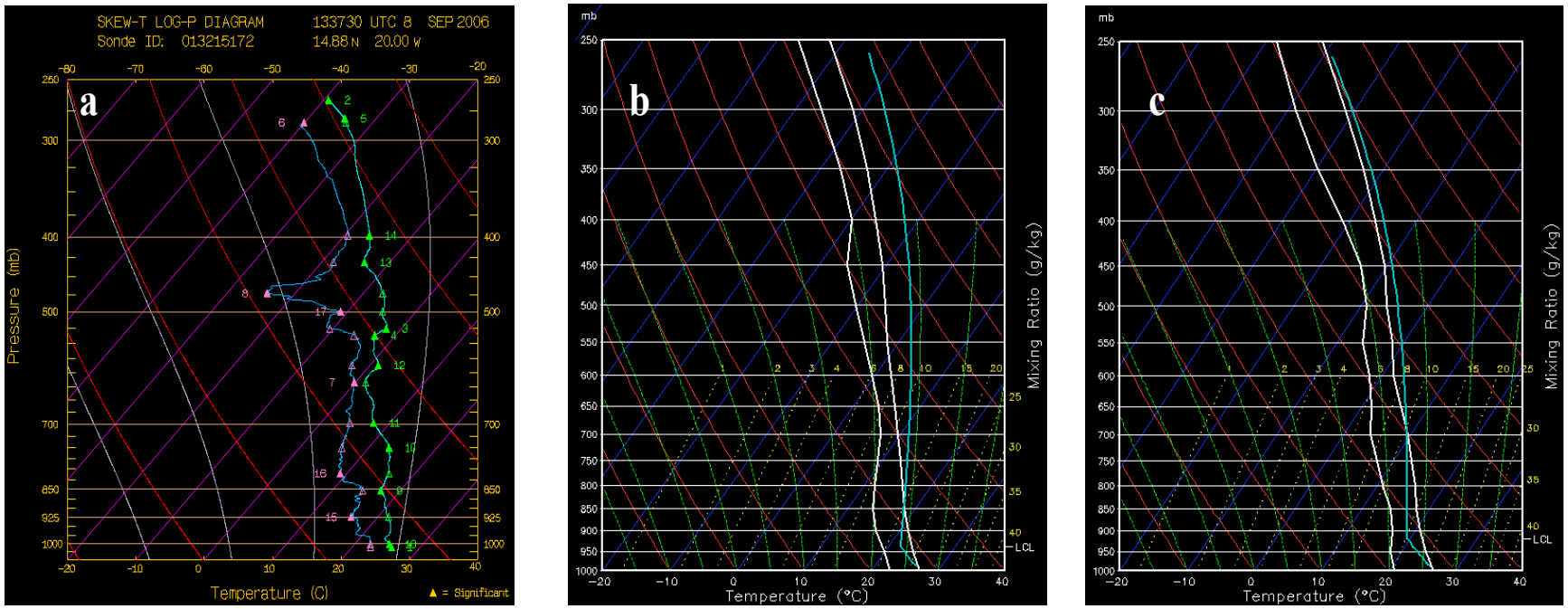

Figure 5.37 NDAEW skew-T thermodynamic profile from D1: (a) dropwindsonde (b) HWRFx CNTRL and (c) HWRFx EXP.

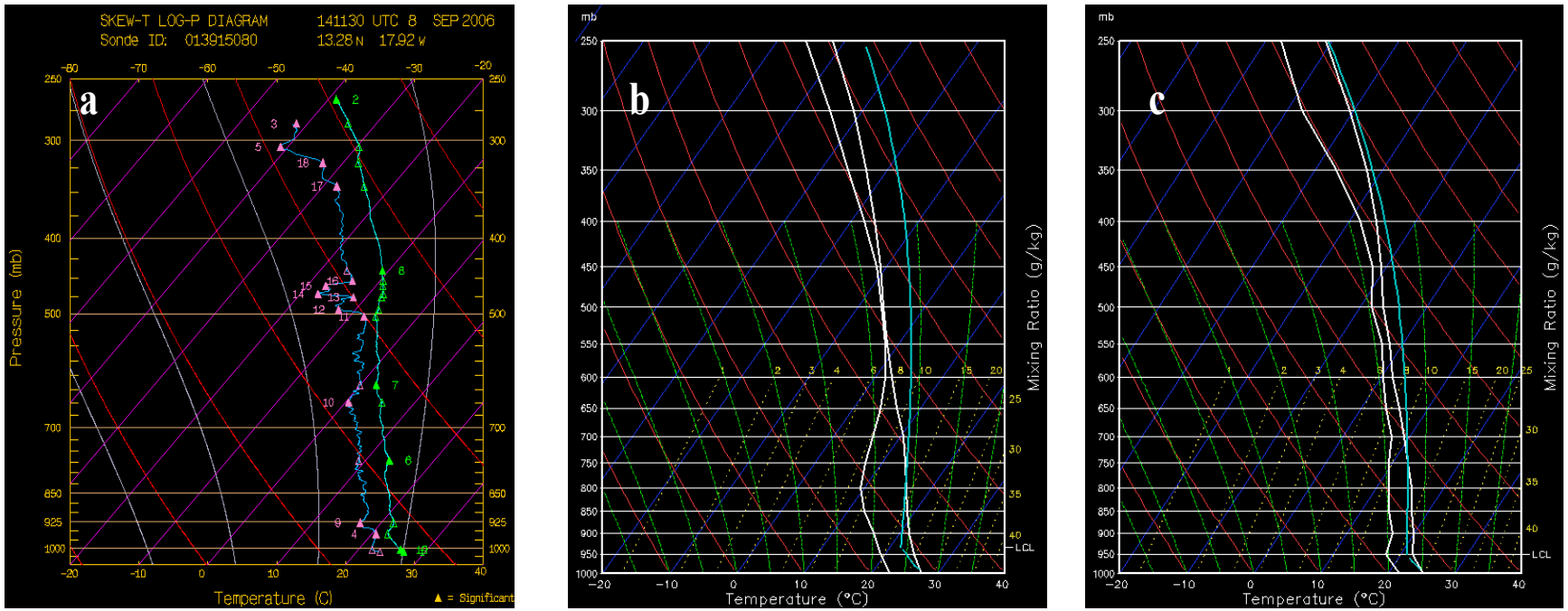

Figure 5.38 NDAEW skew-T thermodynamic profile from D2: (a) dropwindsonde (b) HWRFx CNTRL and (c) HWRFx EXP.

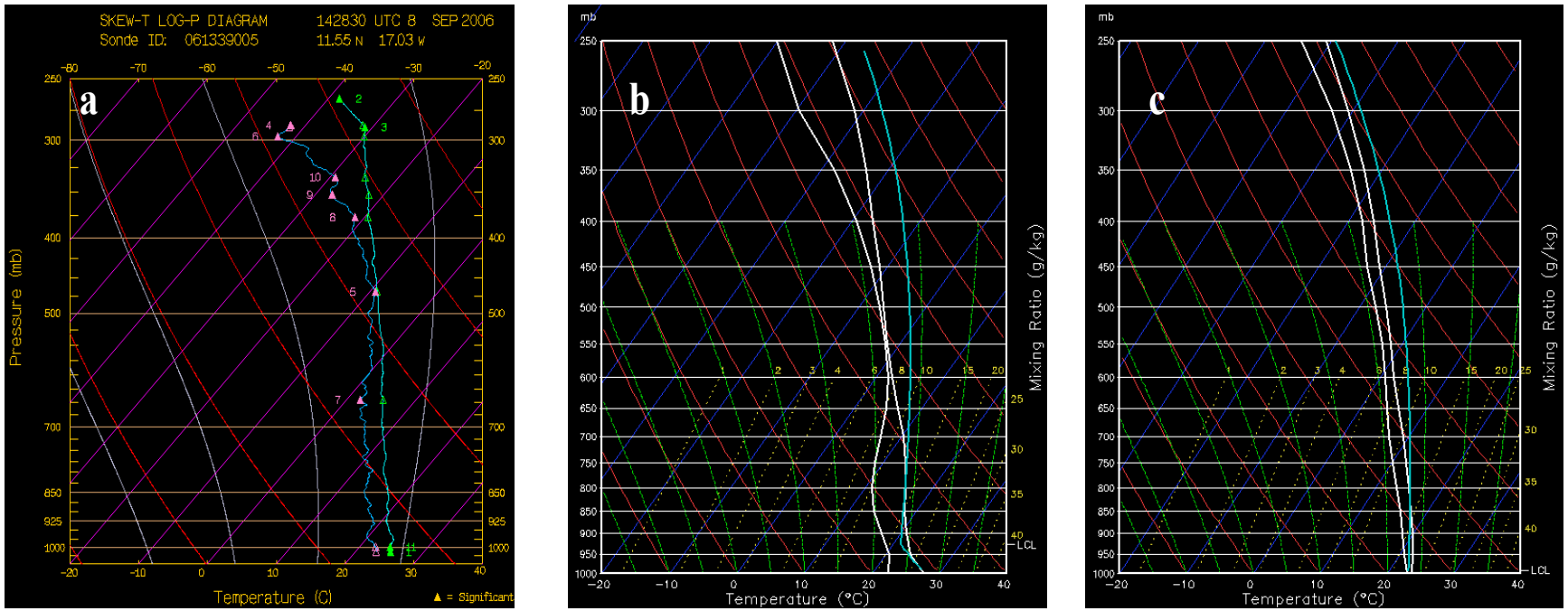

Figure 5.39 NDAEW skew-T thermodynamic profile from D3: (a) dropwindsonde (b) HWRFx CNTRL and (c) HWRFx EXP.

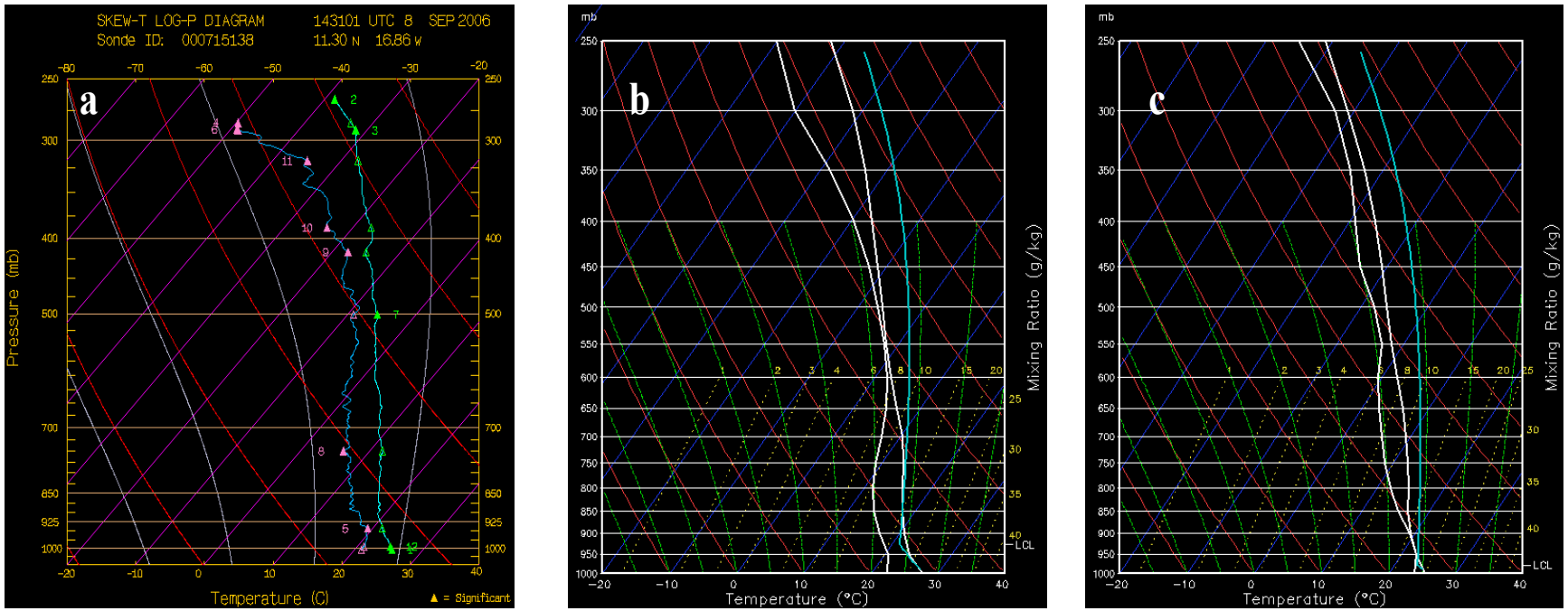

Figure 5.40 NDAEW skew-T thermodynamic profile from D4: (a) dropwindsonde (b) HWRFx CNTRL and (c) HWRFx EXP.

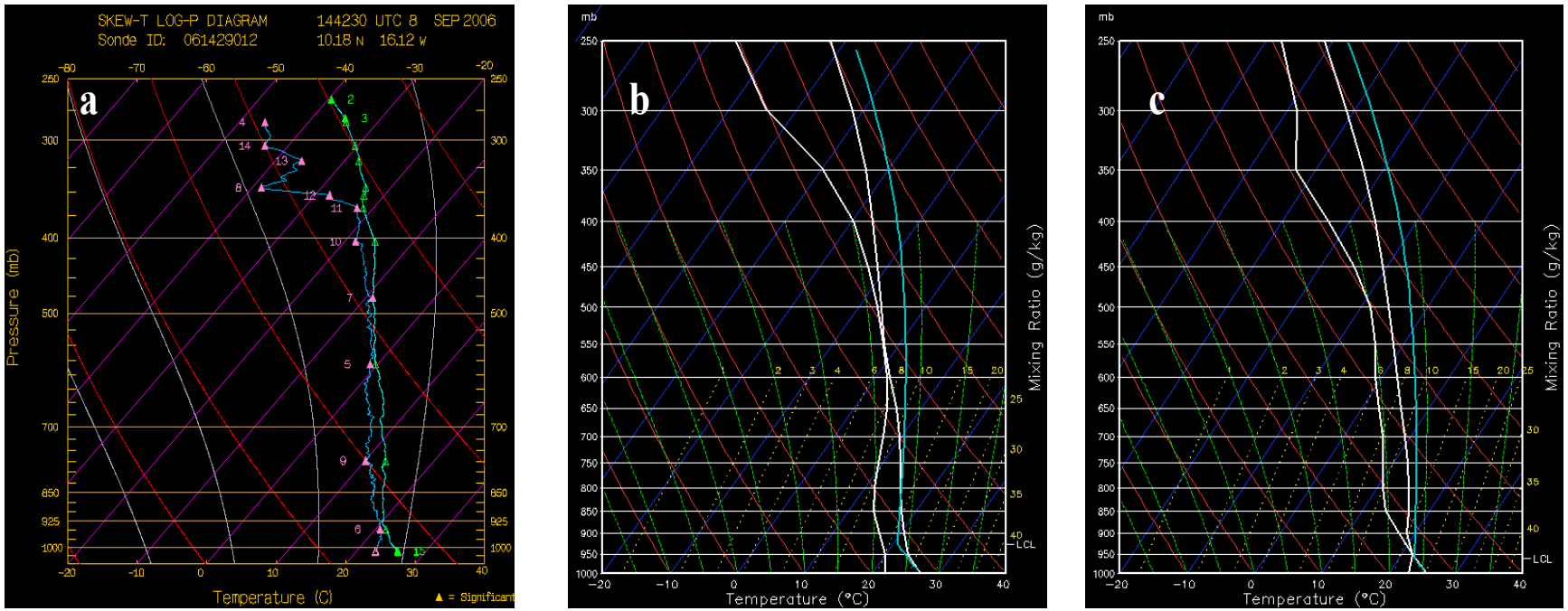

Figure 5.41 NDAEW skew-T thermodynamic profile from D5: (a) dropwindsonde (b) HWRFx CNTRL and (c) HWRFx EXP.

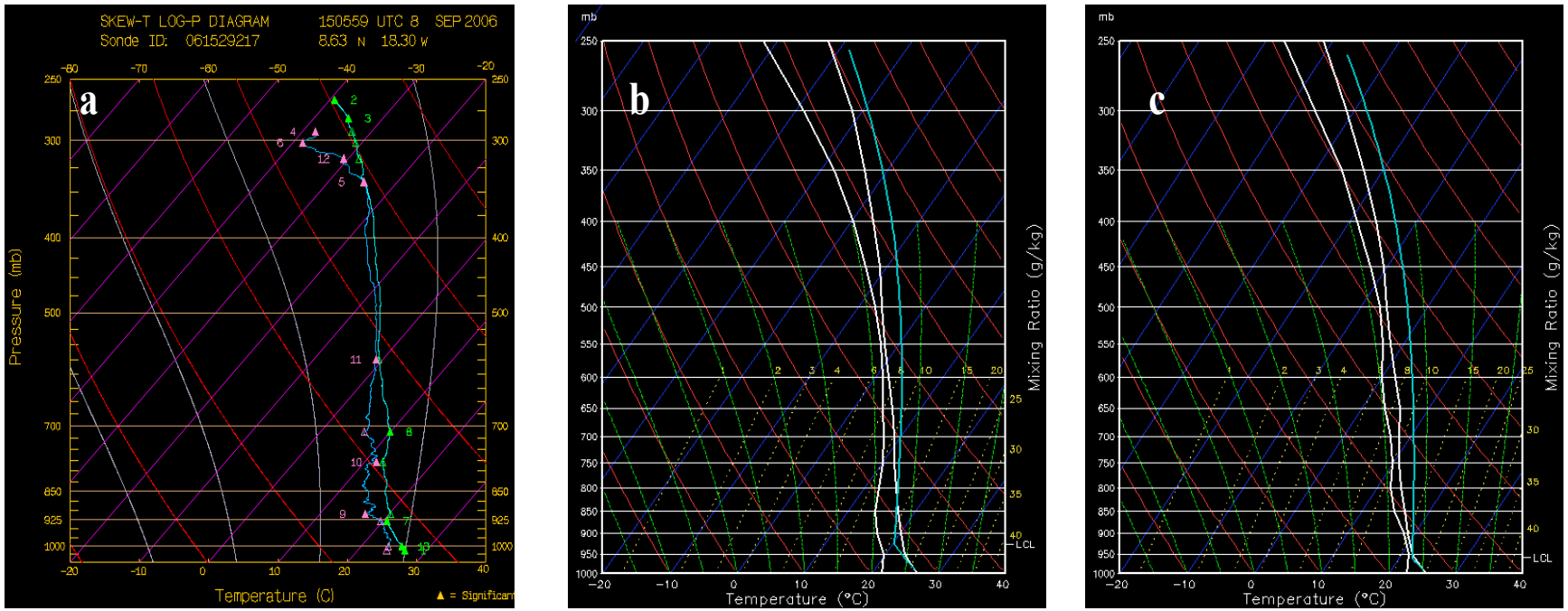

Figure 5.42 NDAEW skew-T thermodynamic profile from D6: (a) dropwindsonde (b) HWRFx CNTRL and (c) HWRFx EXP.

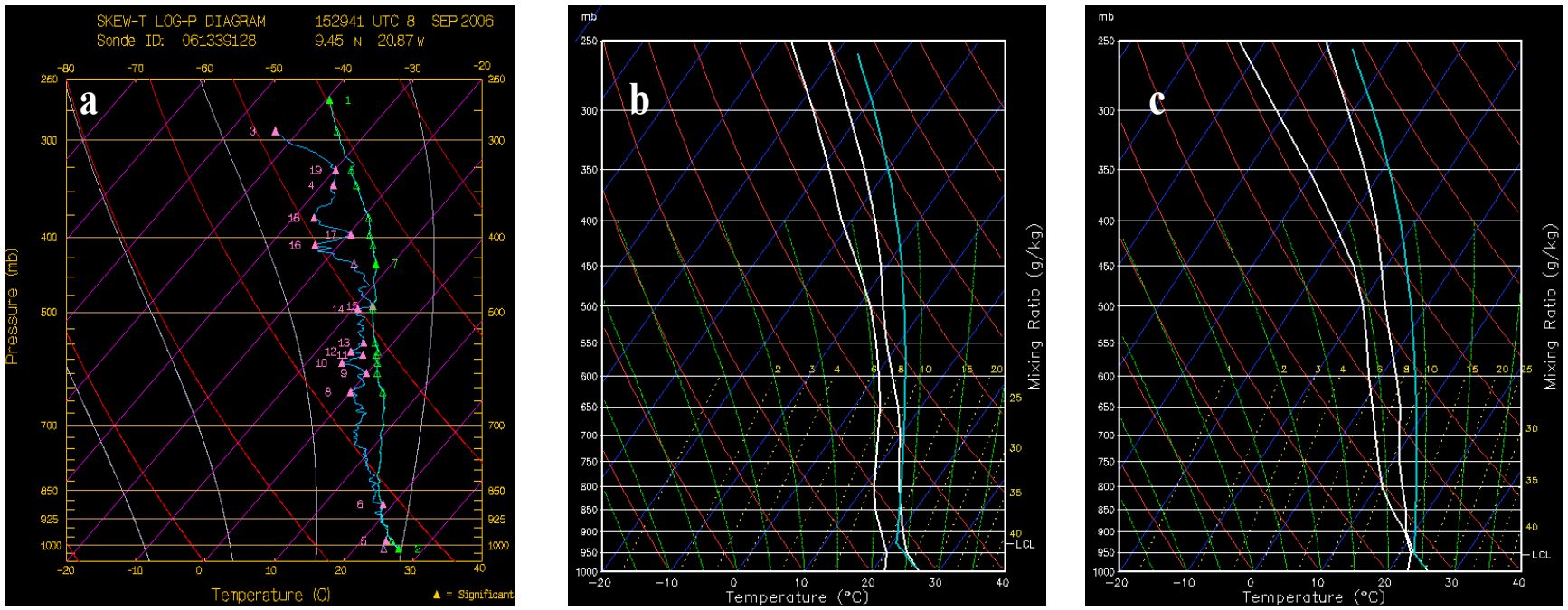

Figure 5.43 NDAEW skew-T thermodynamic profile from D7: (a) dropwindsonde (b) HWRFx CNTRL and (c) HWRFx EXP.

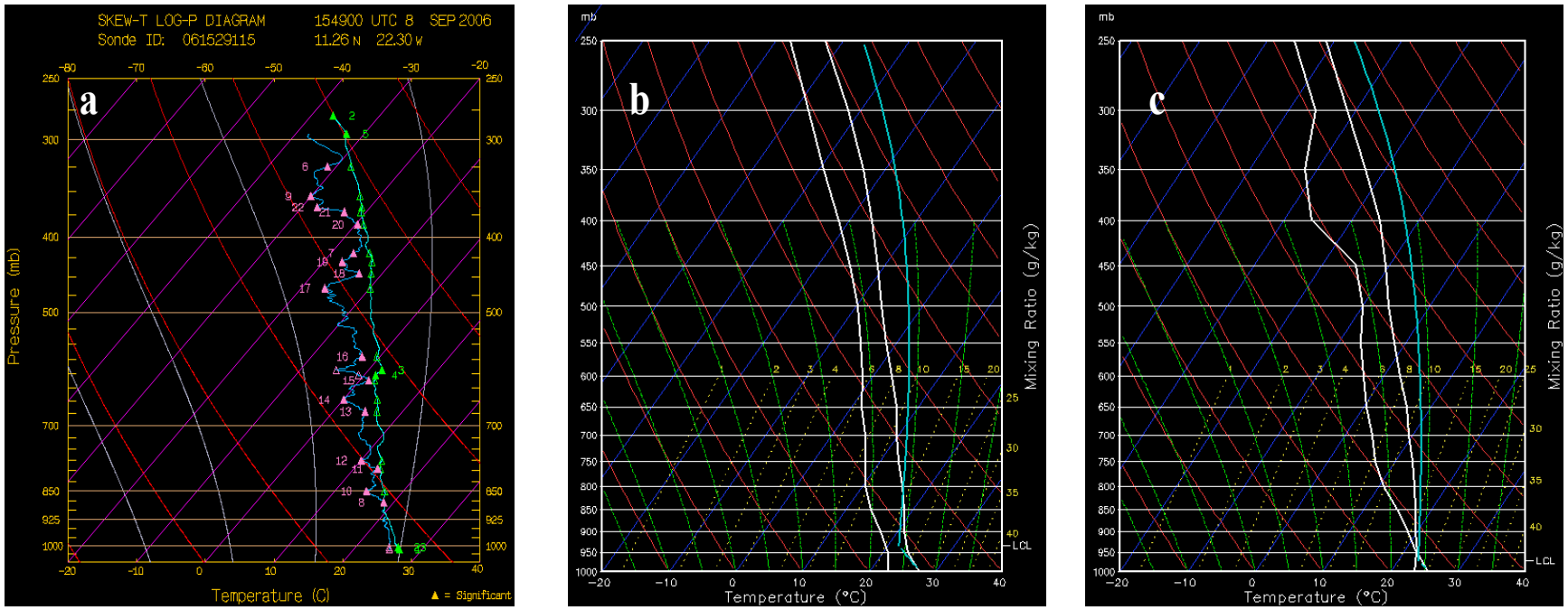

Figure 5.44 NDAEW skew-T thermodynamic profile from D8: (a) dropwindsonde (b) HWRFx CNTRL and (c) HWRFx EXP.

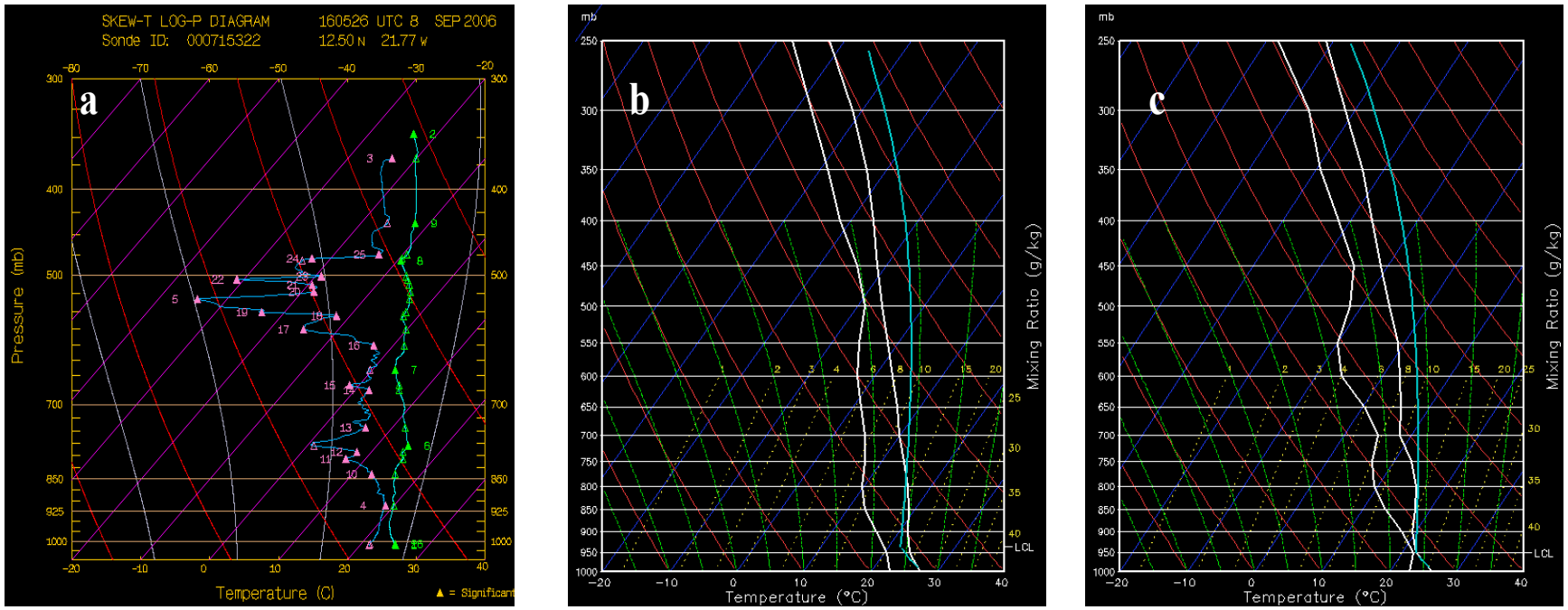

Figure 5.45 NDAEW skew-T thermodynamic profile from D9: (a) dropwindsonde (b) HWRFx CNTRL and (c) HWRFx EXP.

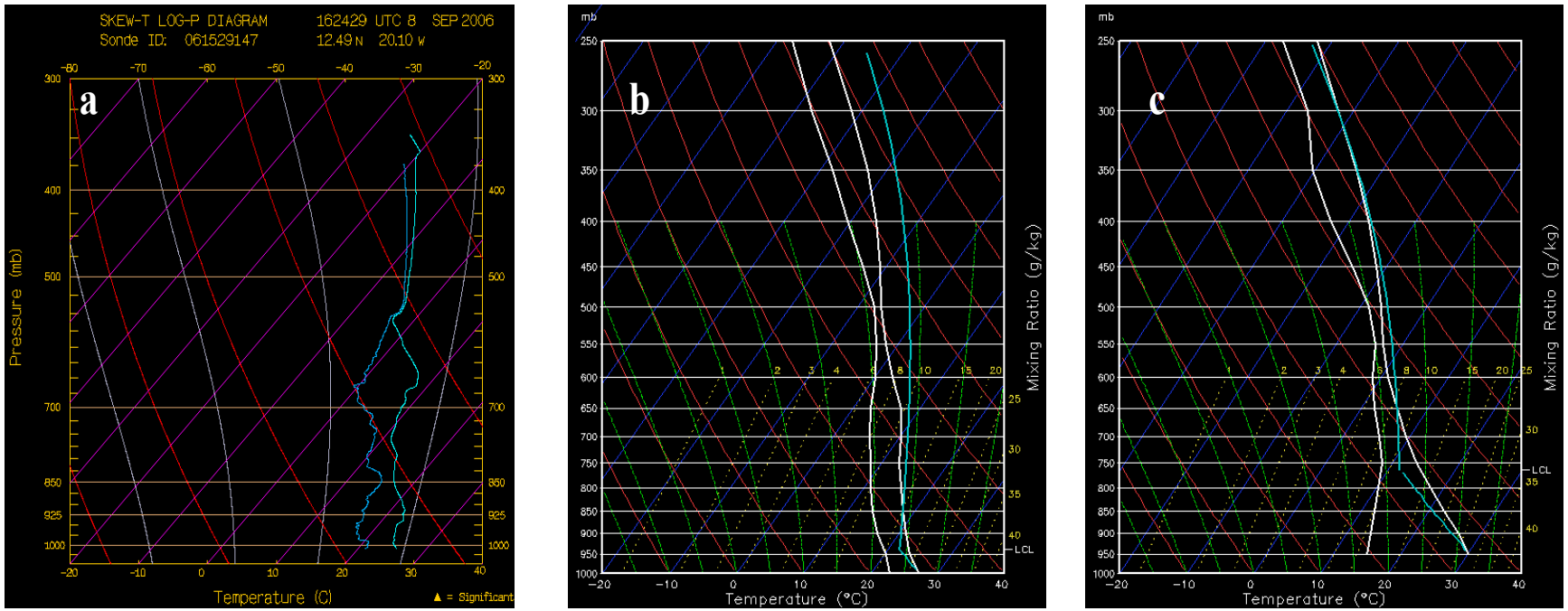

Figure 5.46 NDAEW skew-T thermodynamic profile from D10: (a) dropwindsonde (b) HWRFx CNTRL and (c) HWRFx EXP.

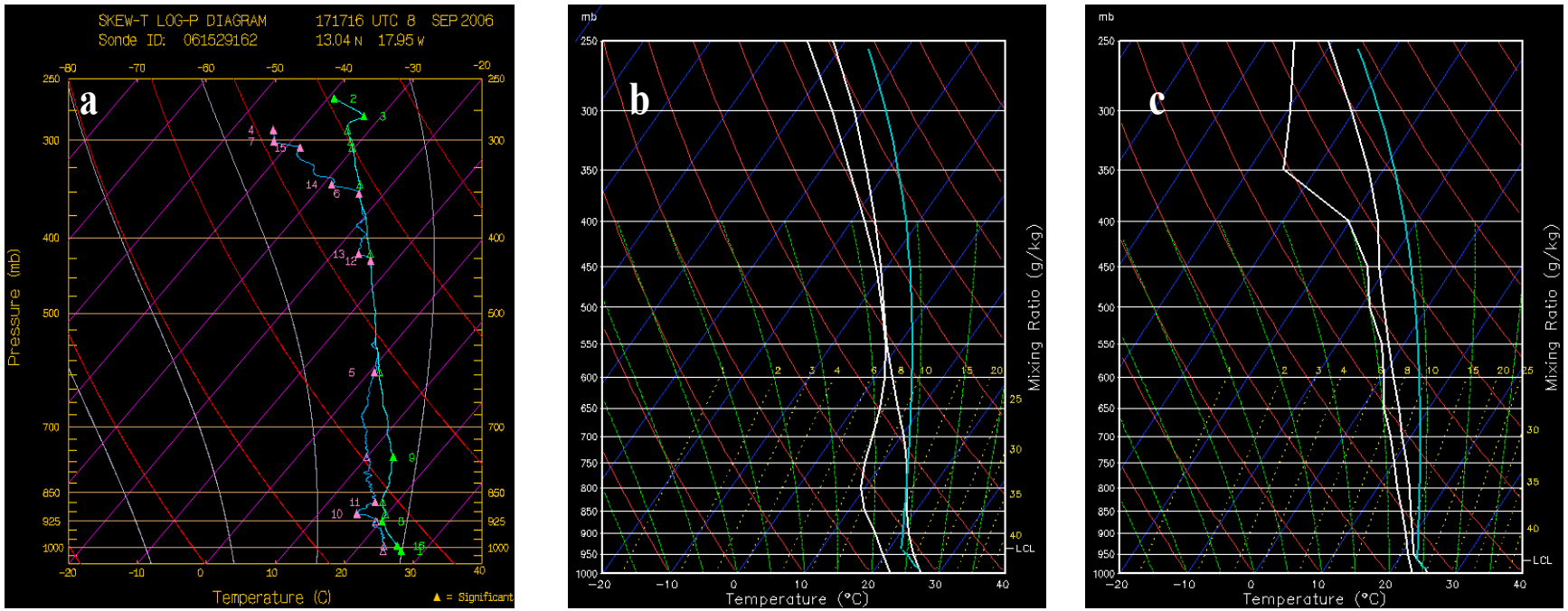

Figure 5.47 NDAEW skew-T thermodynamic profile from D11: (a) dropwindsonde (b) HWRFx CNTRL and (c) HWRFx EXP.

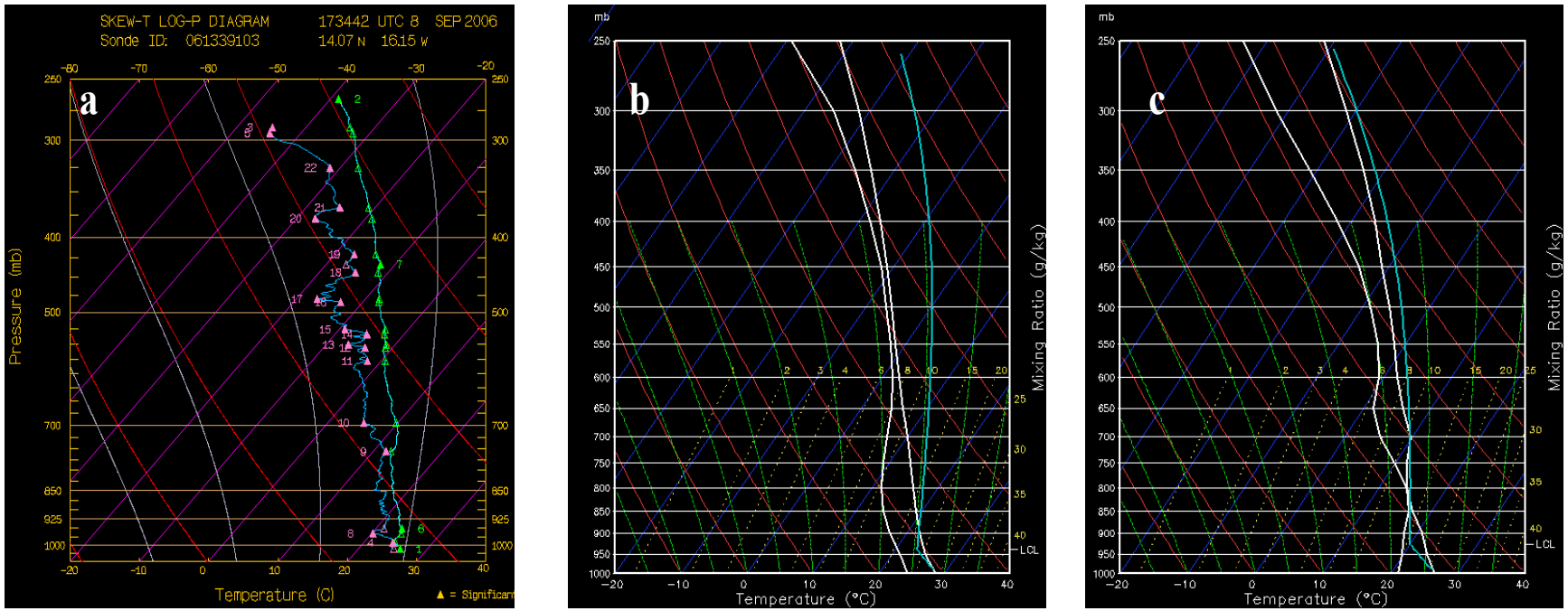

Figure 5.48 NDAEW skew-T thermodynamic profile from D12: (a) dropwindsonde (b) HWRFx CNTRL and (c) HWRFx EXP.

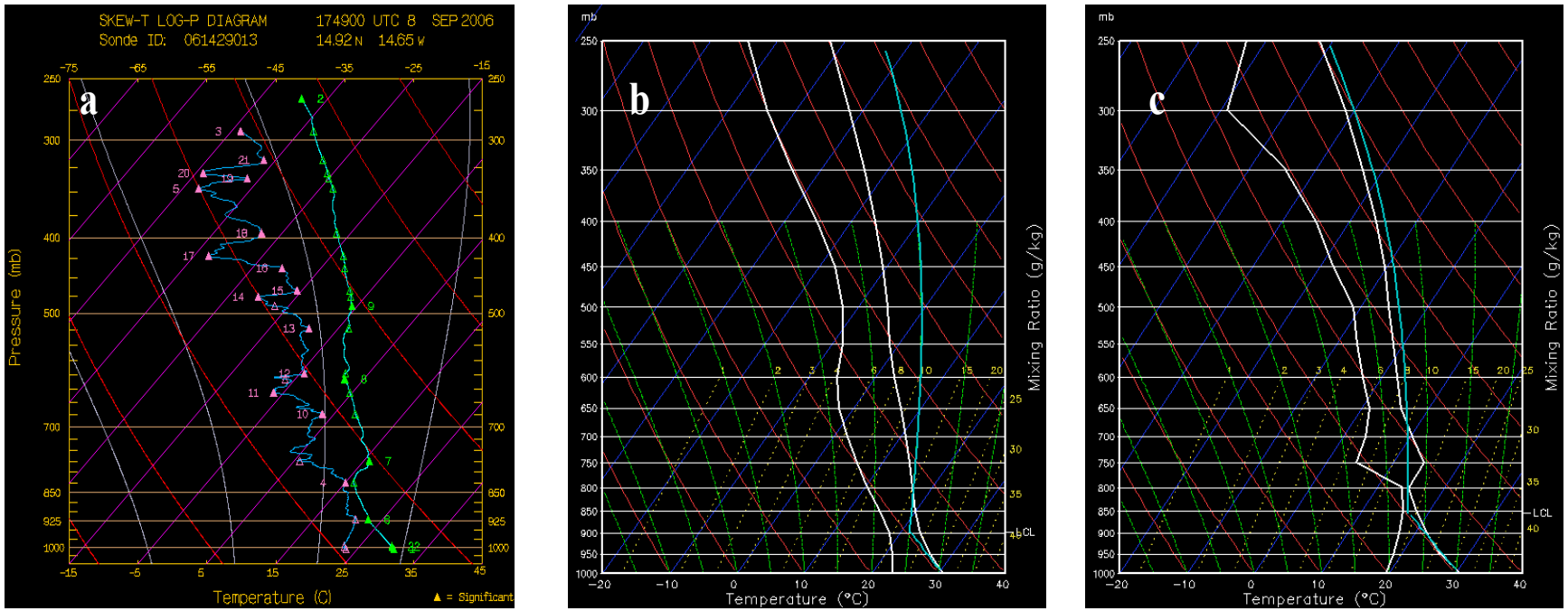

Figure 5.49 NDAEW skew-T thermodynamic profile from D13: (a) dropwindsonde (b) HWRFx CNTRL and (c) HWRFx EXP.

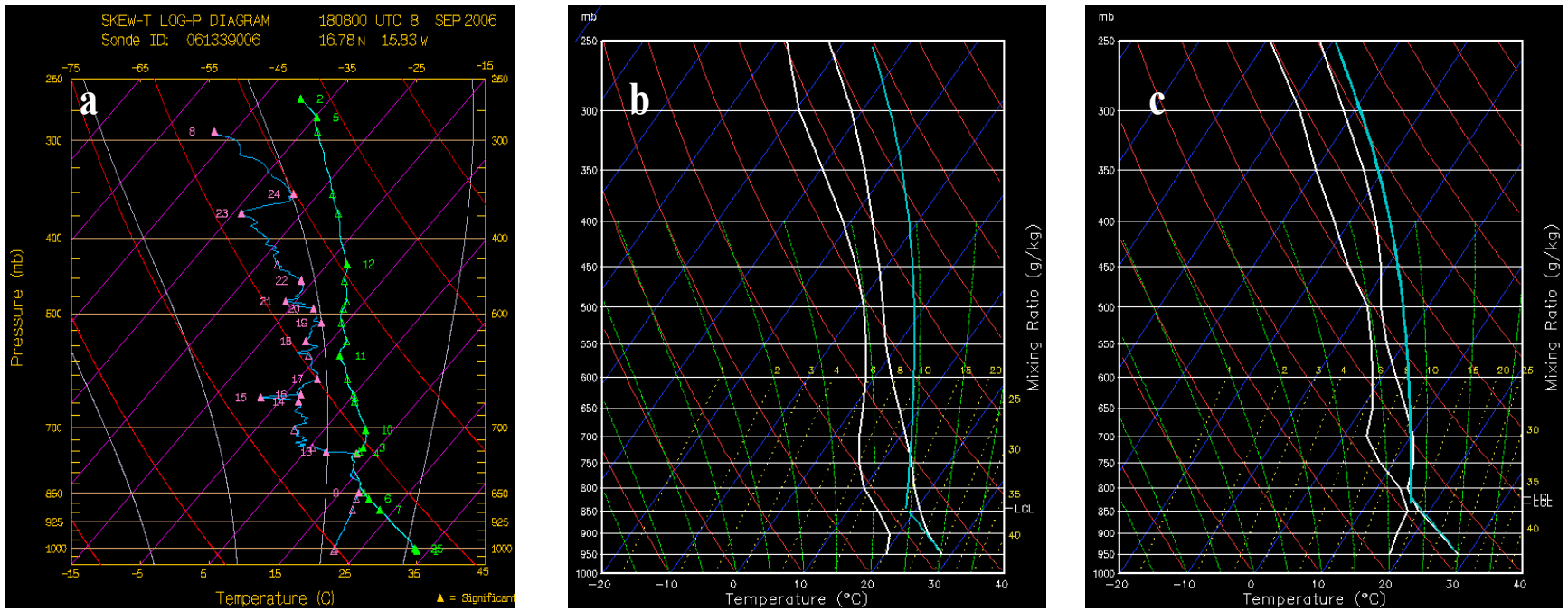

Figure 5.50 NDAEW skew-T thermodynamic profile from D14: (a) dropwindsonde (b) HWRFx CNTRL and (c) HWRFx EXP.

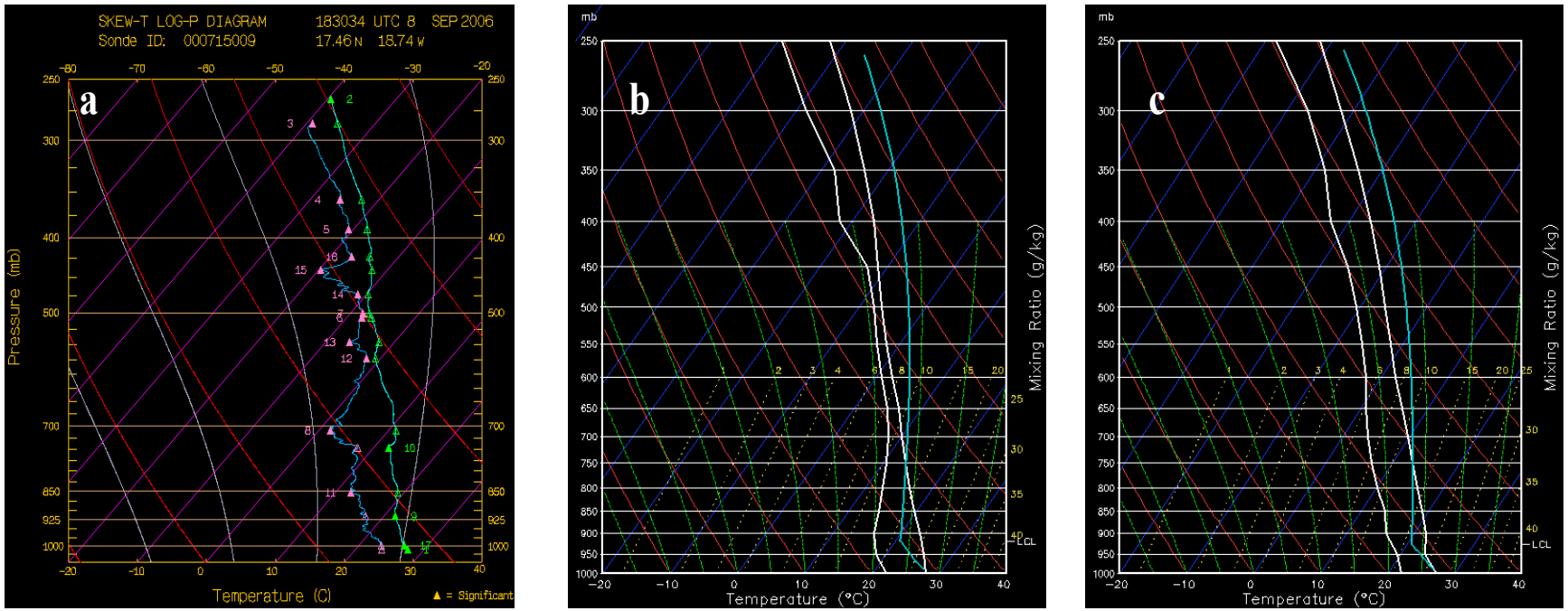

Figure 5.51 NDAEW skew-T thermodynamic profile from D15: (a) dropwindsonde (b) HWRFx CNTRL and (c) HWRFx EXP.

5.3.2 HAEW initial conditions

The HWRFx CNTRL analysis for the case of the HAEW best represented the wind structure at the ICs when compared to the drowindsondes observations (Figs. 5.52a-5.59a). A cyclonic circulation with center located near the NHC BT position (11.9°N 23.2°W) was depicted in the CNTRL analysis from 1000 hPa to 400 hPa (Figs. 5.52b-5.57b). The EXP analysis was able to depict the cyclonic circulation as well, however just up to 700 hPa and with the center shifted eastward near 11.5°N 21.8°W (Figs. 5.52c-5.55c). Particularly, the center of the circulation at 700 hPa shifted close to the NHC position. At 500 hPa and 400 hPa, the EXP analysis depicted an open cyclonic circulation, thus portraying a weaker system when compared to both the CNTRL analysis and the observations (Figs. 5.56c-5.57c). Conversely, at the upper-levels 300 hPa and 250 hPa where the observations sampled anticyclonic winds westward from 24°W and 23°W, respectively and cyclonic winds eastward, the analyses showed different wind patterns. Both CNTRL and EXP analyses portrayed cyclonic winds near D4 and D5 at both upper levels, however the rest of the domains depicted mostly easterly winds with some regions showing anticyclonic winds (Figs. 5.58b-5.59b and 5.58c-5.59c).

In terms of wind magnitude, both CNTRL and EXP analyses maximum wind speed was comparable to the observations within the specified domain. For all of the mandatory levels, the difference in wind magnitude between the observations and the analyses was none to 5 kt. Both the EXP and CNTRL analyses matched the observations at 850, 700, 400, and 250 hPa. In addition, the EXP and CNTRL analyses matched the observations at 1000, and 925 hPa, respectively. The EXP analysis was weaker by 5 kt at 925 hPa when compared to both the CNTRL and the observations. On the other hand,

the EXP and CNTRL wind magnitudes were equivalent but stronger than the observations by 5 kt at 500 and 300 hPa. The CNTRL analysis also showed to be stronger than the observations by 5 kt at 1000 hPa. However, both the dropwindsondes and the analyses underestimated the NHC BT intensity of 30 kt during September 12 1800 UTC. The HAEW maximum wind speed at each mandatory level from the dropwindsondes, CNTRL and EXP analyses is shown in Table 5.2.

It is worthwhile to point out that while the maximum wind speed within the analyses domain at the lower levels was similar to the dropwindsondes observations, it was not necessarily located near the TD center where winds should be higher due to stronger convergence and RVORT. Winds near the dropwindsondes that were surrounding the TD center (D3-D5 and D7) were sometimes weaker for both analyses, especially for the EXP analysis.

Table 5.2

HAEW maximum wind speed at mandatory levels from dropwindsondes and HWRFx CNTRL and EXP ICs

HAEW	Maximum wind speed (kt) at mandatory levels (hPa)							
	1000	**925**	**850**	**700**	**500**	**400**	**300**	**250**
Dropsondes	20	30	30	50	35	40	20	20
CNTRL	25	30	30	50	40	40	25	20
EXP	20	25	30	50	40	40	25	20

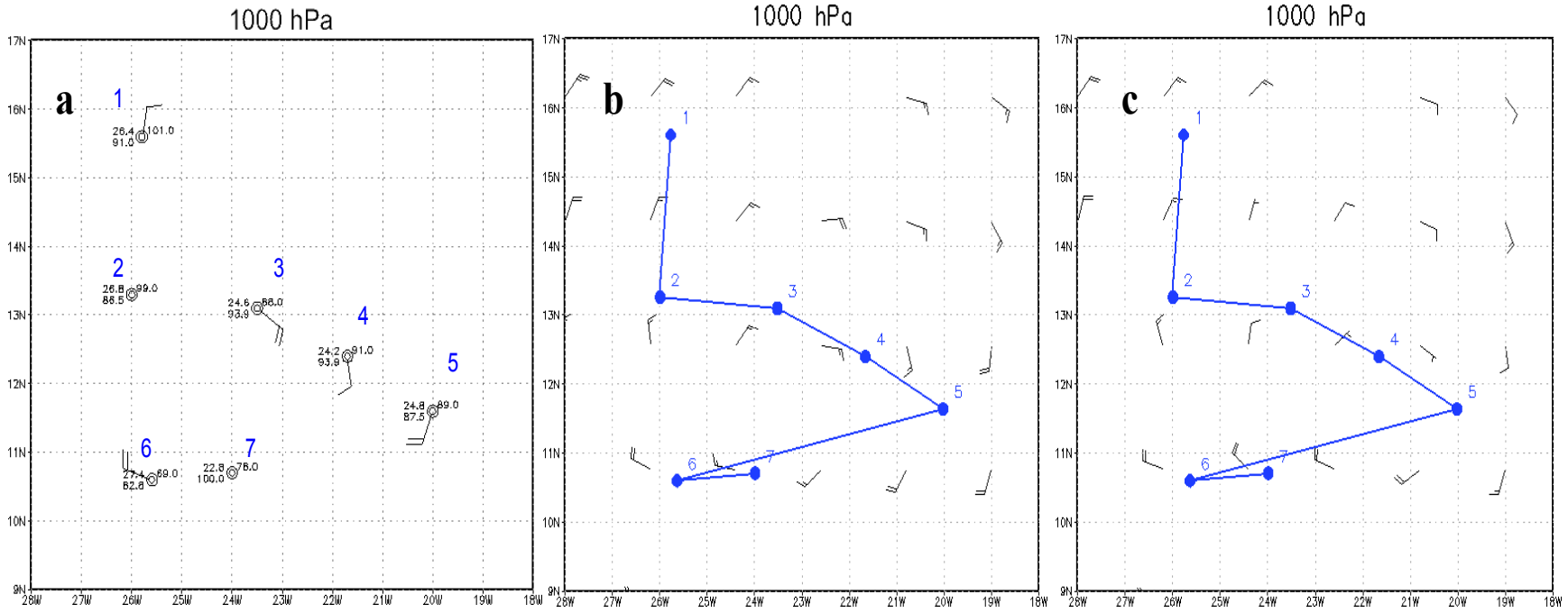

Figure 5.52 HAEW wind dynamics at 1000 hPa from: (a) dropwindsondes (b) HWRFx CNTRL ICs and (c) HWRFx EXP ICs. The blue numbers identify the seven dropwindsondes used to sample the HAEW. The blue dotted line traces the flight track and locations where the dropwindsondes were released.

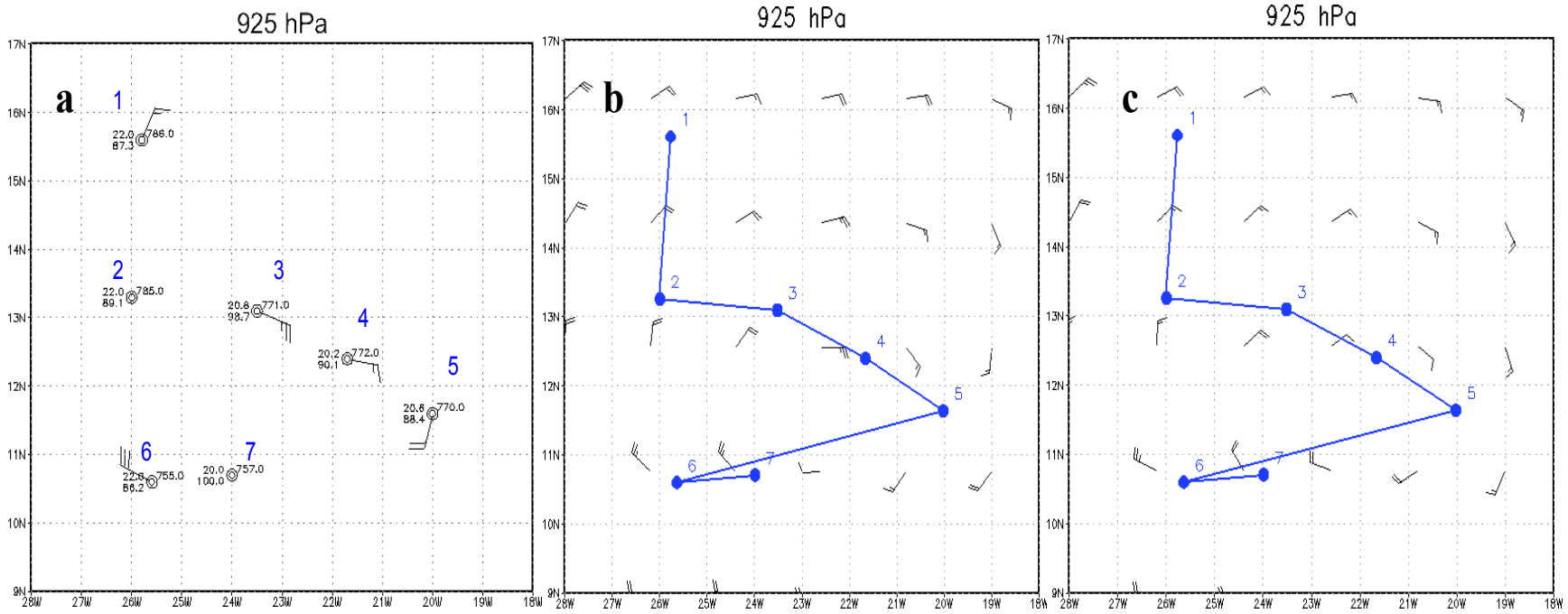

Figure 5.53 HAEW wind dynamics at 925 hPa from: (a) dropwindsondes (b) HWRFx CNTRL ICs and (c) HWRFx EXP ICs. The blue numbers identify the seven dropwindsondes used to sample the HAEW. The blue dotted line traces the flight track and locations where the dropwindsondes were released.

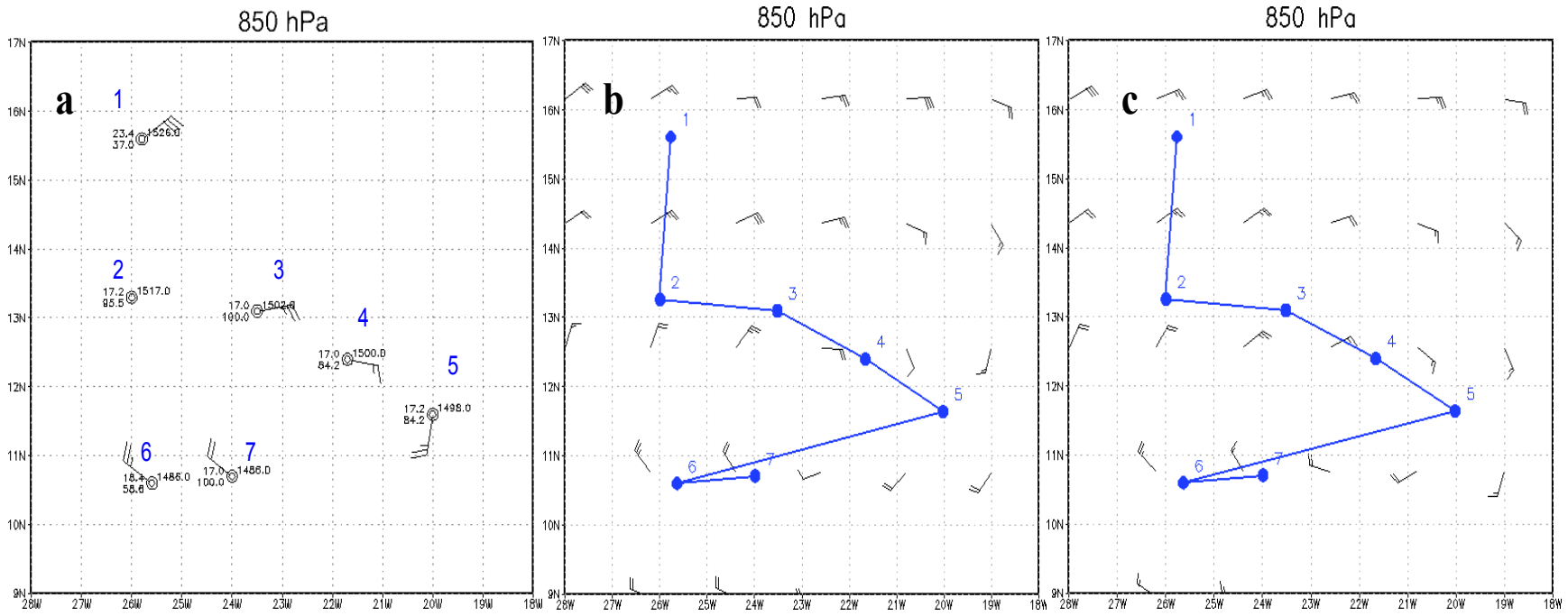

Figure 5.54 HAEW wind dynamics at 850 hPa from: (a) dropwindsondes (b) HWRFx CNTRL ICs and (c) HWRFx EXP ICs. The blue numbers identify the seven dropwindsondes used to sample the HAEW. The blue dotted line traces the flight track and locations where the dropwindsondes were released.

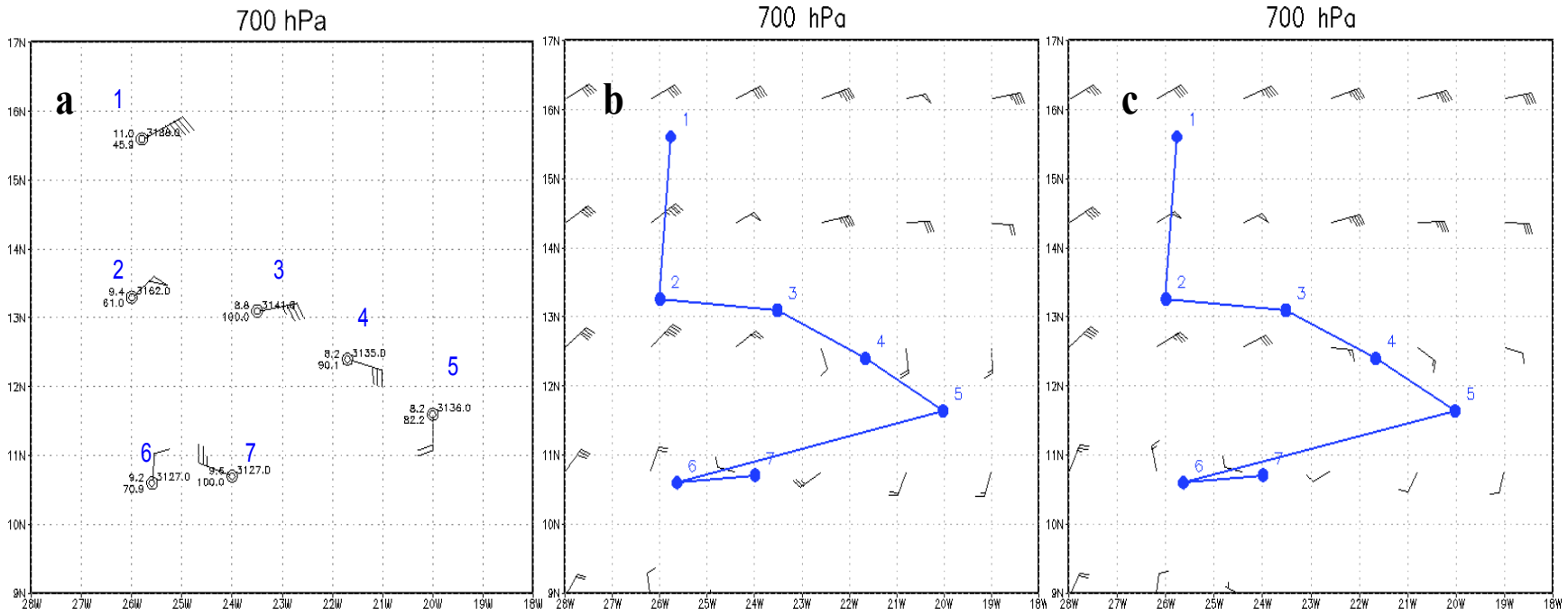

Figure 5.55 HAEW wind dynamics at 700 hPa from: (a) dropwindsondes (b) HWRFx CNTRL ICs and (c) HWRFx EXP ICs. The blue numbers identify the seven dropwindsondes used to sample the HAEW. The blue dotted line traces the flight track and locations where the dropwindsondes were released.

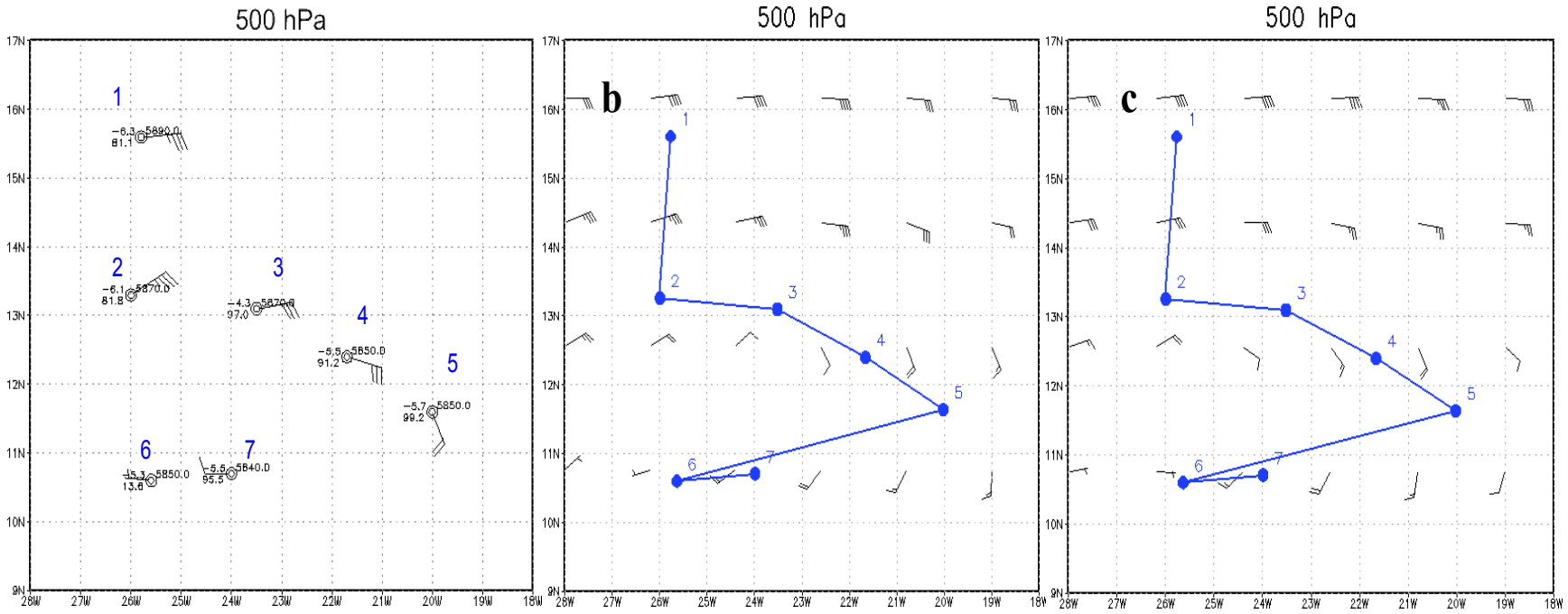

Figure 5.56 HAEW wind dynamics at 500 hPa from: (a) dropwindsondes (b) HWRFx CNTRL ICs and (c) HWRFx EXP ICs. The blue numbers identify the seven dropwindsondes used to sample the HAEW. The blue dotted line traces the flight track and locations where the dropwindsondes were released.

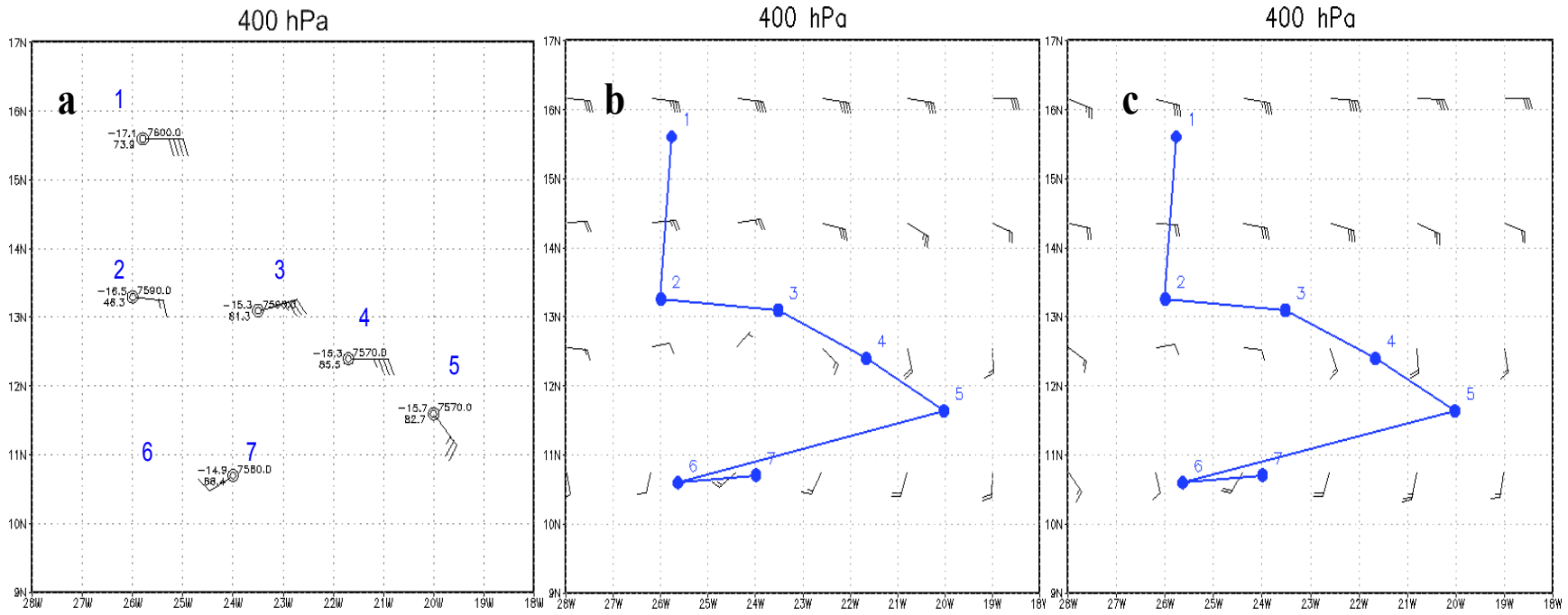

Figure 5.57 HAEW wind dynamics at 400 hPa from: (a) dropwindsondes (b) HWRFx CNTRL ICs and (c) HWRFx EXP ICs. The blue numbers identify the seven dropwindsondes used to sample the HAEW. The blue dotted line traces the flight track and locations where the dropwindsondes were released.

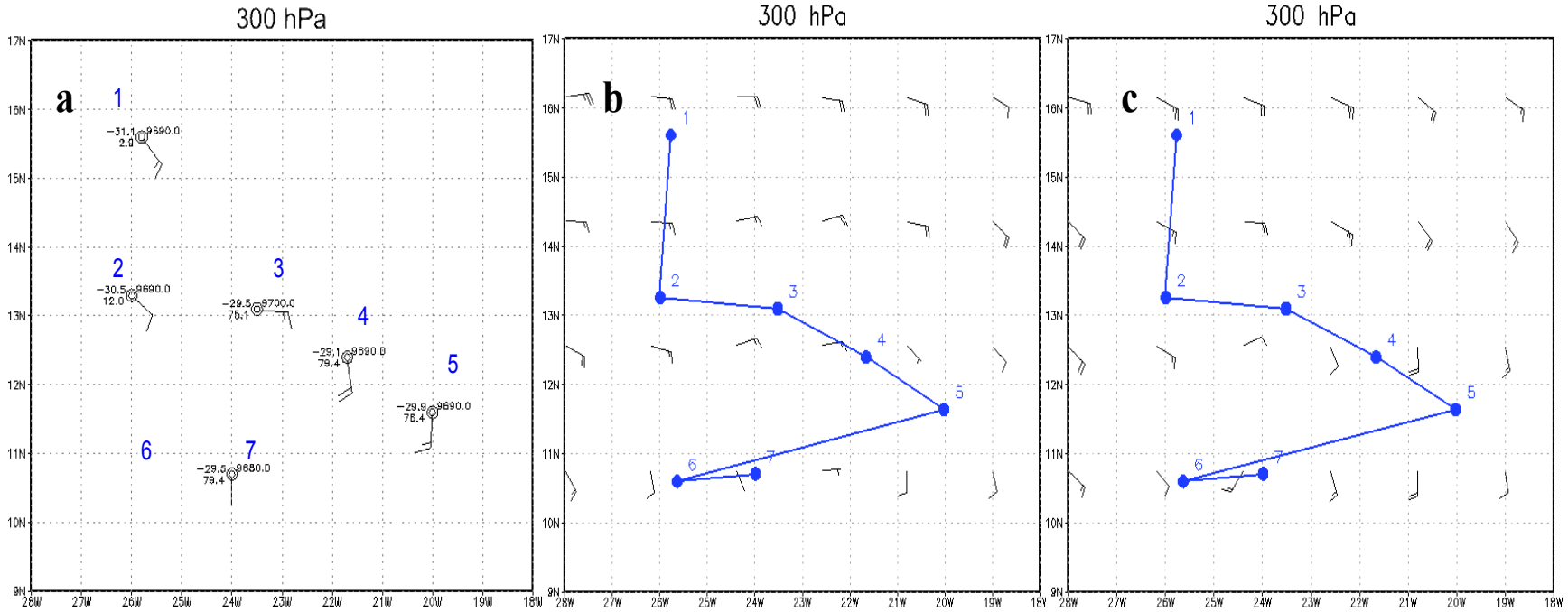

Figure 5.58 HAEW wind dynamics at 300 hPa from: (a) dropwindsondes (b) HWRFx CNTRL ICs and (c) HWRFx EXP ICs. The blue numbers identify the seven dropwindsondes used to sample the HAEW. The blue dotted line traces the flight track and locations where the dropwindsondes were released.

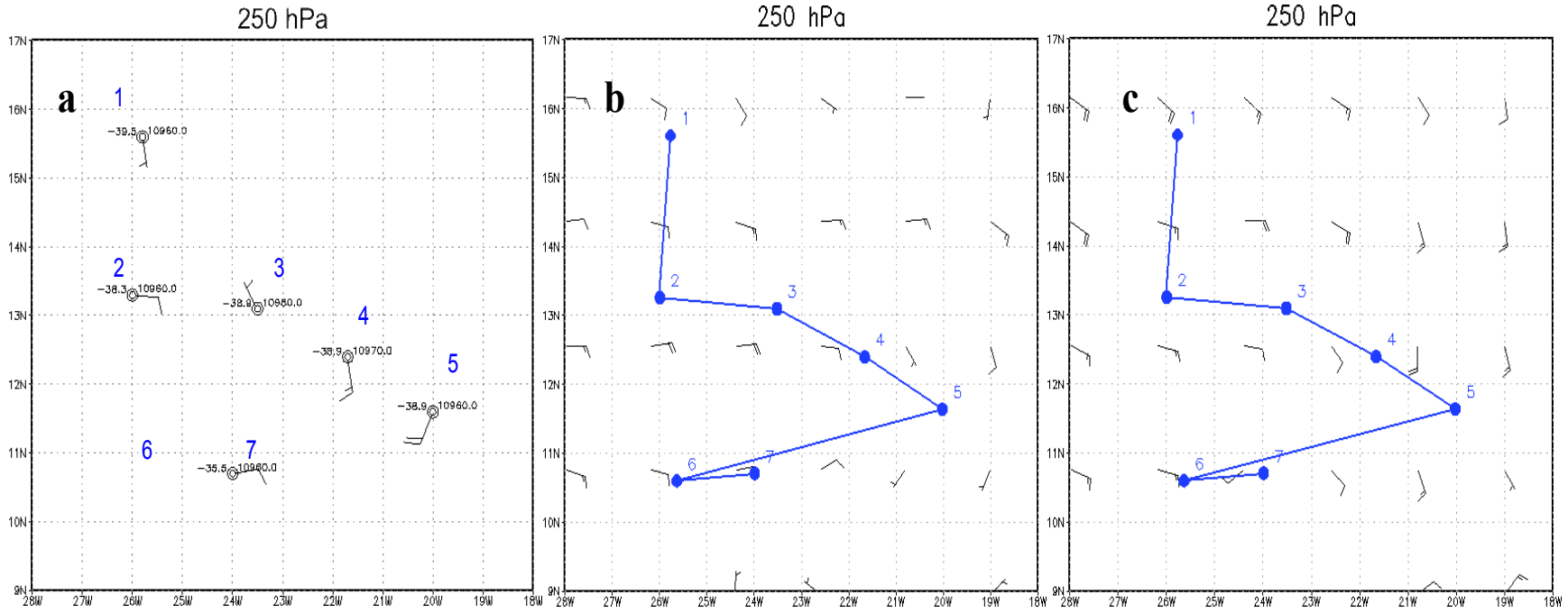

Figure 5.59 HAEW wind dynamics at 250 hPa from: (a) dropwindsondes (b) HWRFx CNTRL ICs and (c) HWRFx EXP ICs. The blue numbers identify the seven dropwindsondes used to sample the HAEW. The blue dotted line traces the flight track and locations where the dropwindsondes were released.

The skew-T diagrams from the HAEW CNTRL and EXP analyses showed mixed results when compared to the observations. In general, both analyses depicted the observed SAL drying effect west of the TD center at D1, D2 and D6 (Figs. 5.60-5.61 and 5.65) as well as the much moister environment at D3-D5 and D7 (Figs. 5.62-5.64 and 5.66). Particularly, except from D6 and D7 both analyses shared very similar vertical profiles. At D1, the CNTRL analysis best represented the SAL dehumidifying effect within 925 hPa to 600 hPa (Fig. 5.60b), however none of the analyses represented the saturation below 925 hPa. The CNTRL analysis was also best representing the vertical profiles of D3-D5 (Figs. 5.62b-5.64b). Even though it did not depict the observed saturated regions of the troposphere, the CNTRL analysis portrayed a moister environment than the EXP analysis (Figs. 5.62c-5.64c). However, the EXP analysis best represented the observations at D2, D6 and D7. At D2 and D6, the EXP analysis could represent the regions in the troposphere impacted by the SAL as well as the moistening at the lower levels (Figs. 5.61c and 5.65c). Conversely, D7 better depicted the deep moisture layer observed even that saturation was not achieved below 500 hPa (Fig. 5.66c).

In summary, the EXP analysis best represented the atmospheric structure and environment at D2, D6 and D7, however it portrayed a slightly moister environment at D1 and drier conditions at D3-D5. The impact of the initial dynamic and thermodynamic conditions on the forecast of the HAEW was further analyzed in section 5.3.4 for both the HWRFx CNTRL and EXP runs.

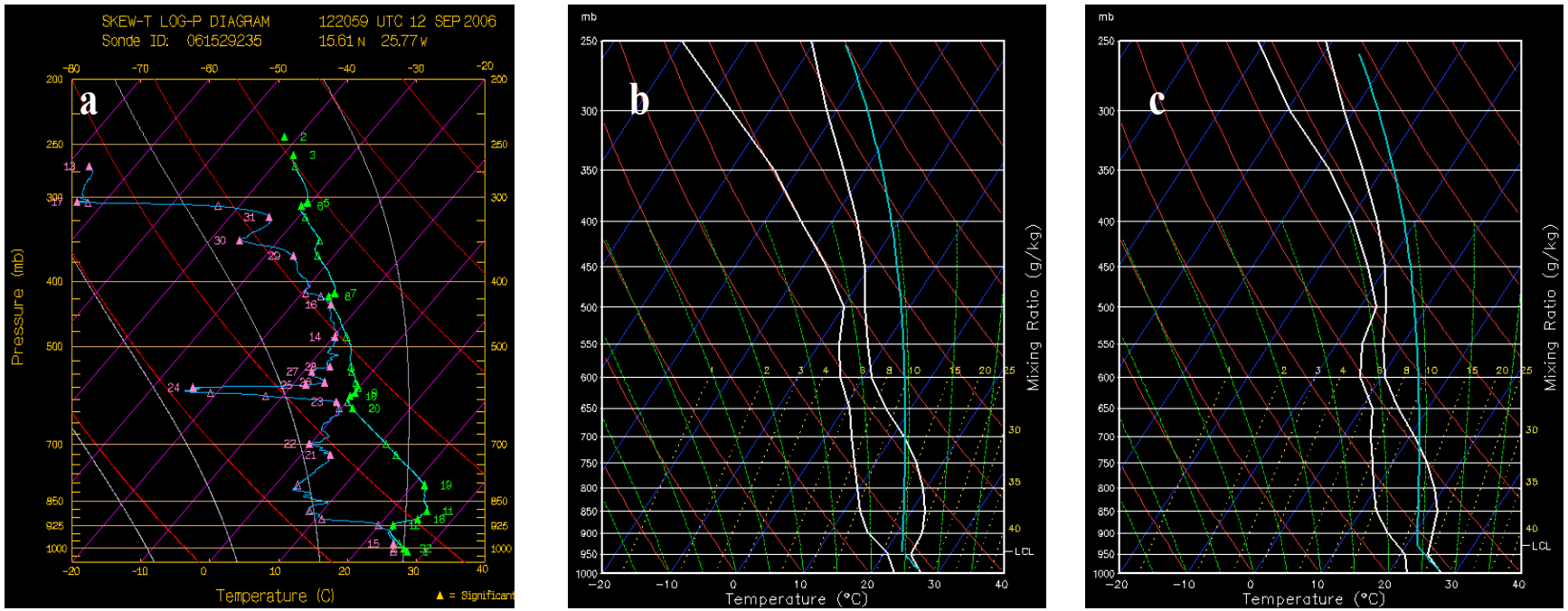

Figure 5.60 HAEW skew-T thermodynamic profile from D1: (a) dropwindsonde (b) HWRFx CNTRL and (c) HWRFx EXP.

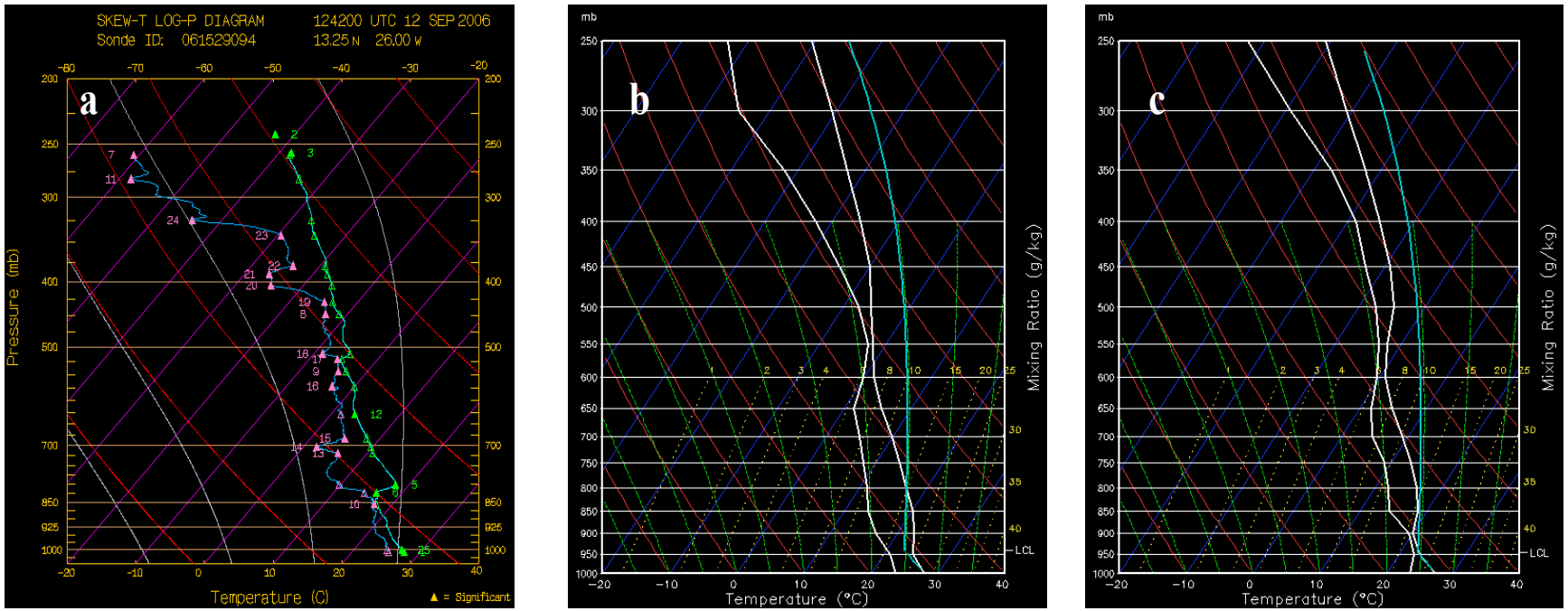

Figure 5.61 HAEW skew-T thermodynamic profile from D2: (a) dropwindsonde (b) HWRFx CNTRL and (c) HWRFx EXP.

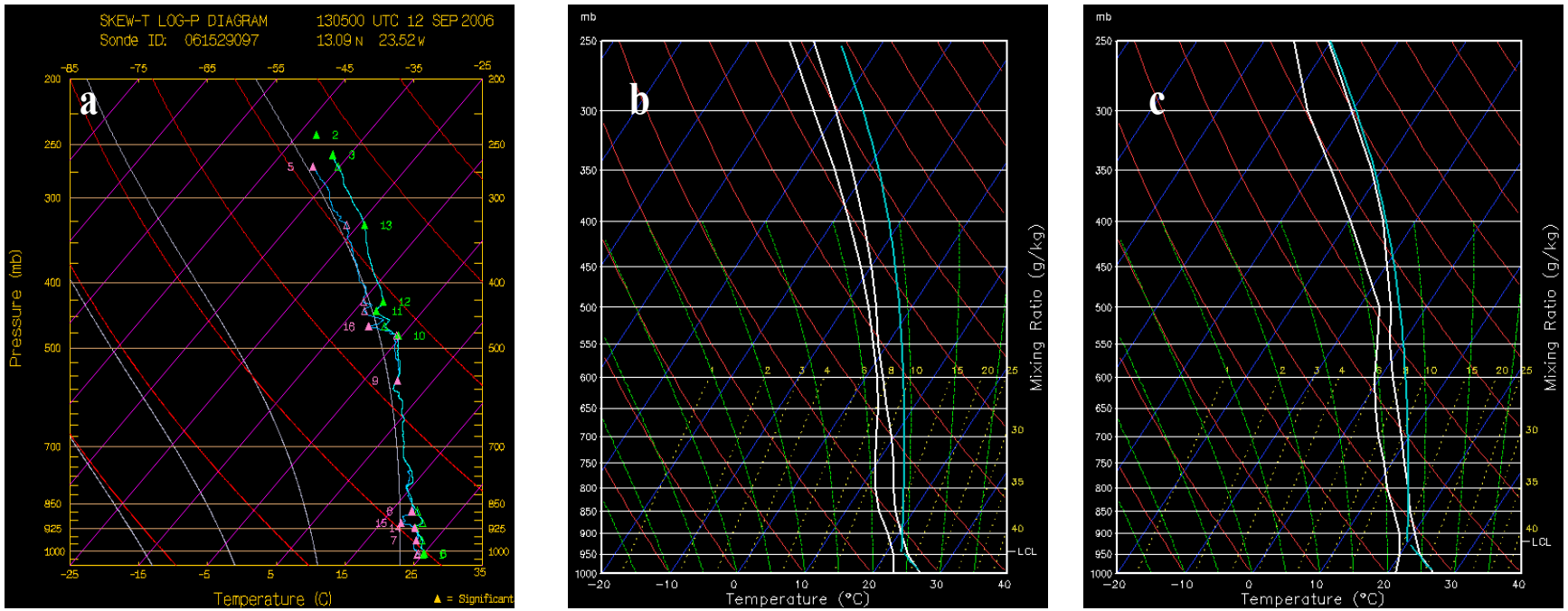

Figure 5.62 HAEW skew-T thermodynamic profile from D3: (a) dropwindsonde (b) HWRFx CNTRL and (c) HWRFx EXP.

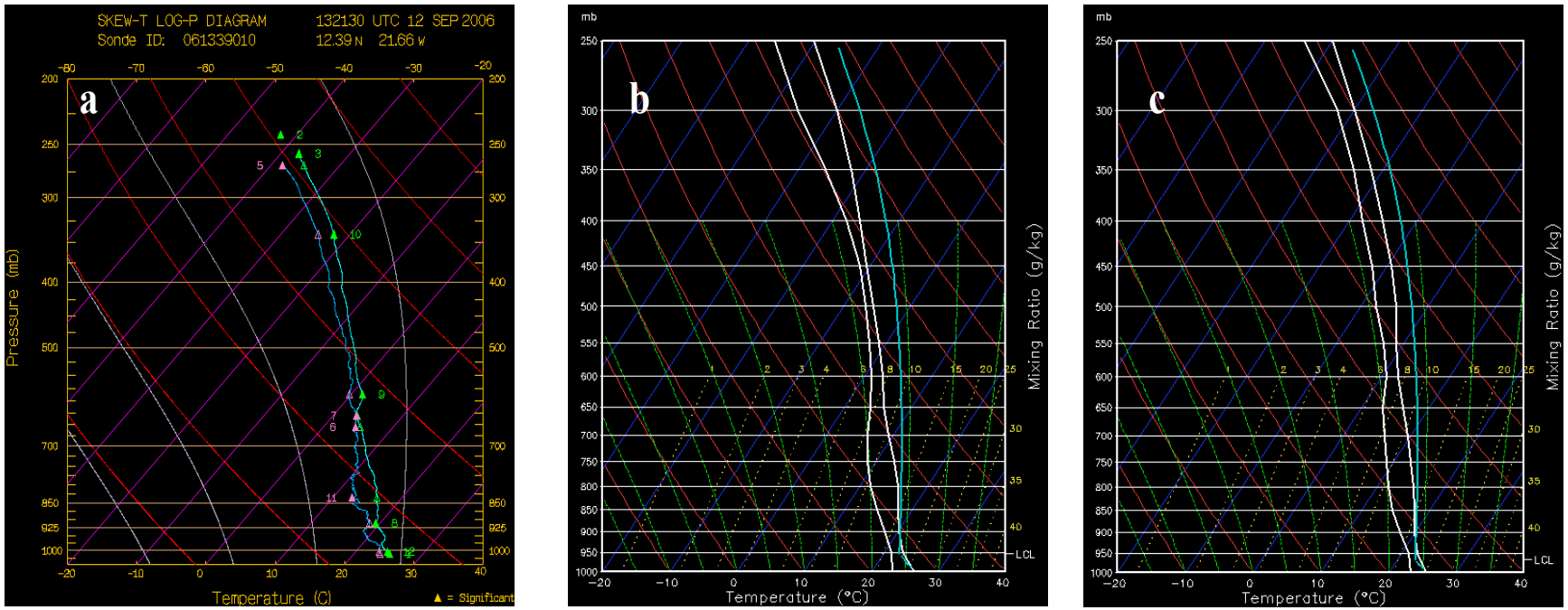

Figure 5.63 HAEW skew-T thermodynamic profile from D4: (a) dropwindsonde (b) HWRFx CNTRL and (c) HWRFx EXP.

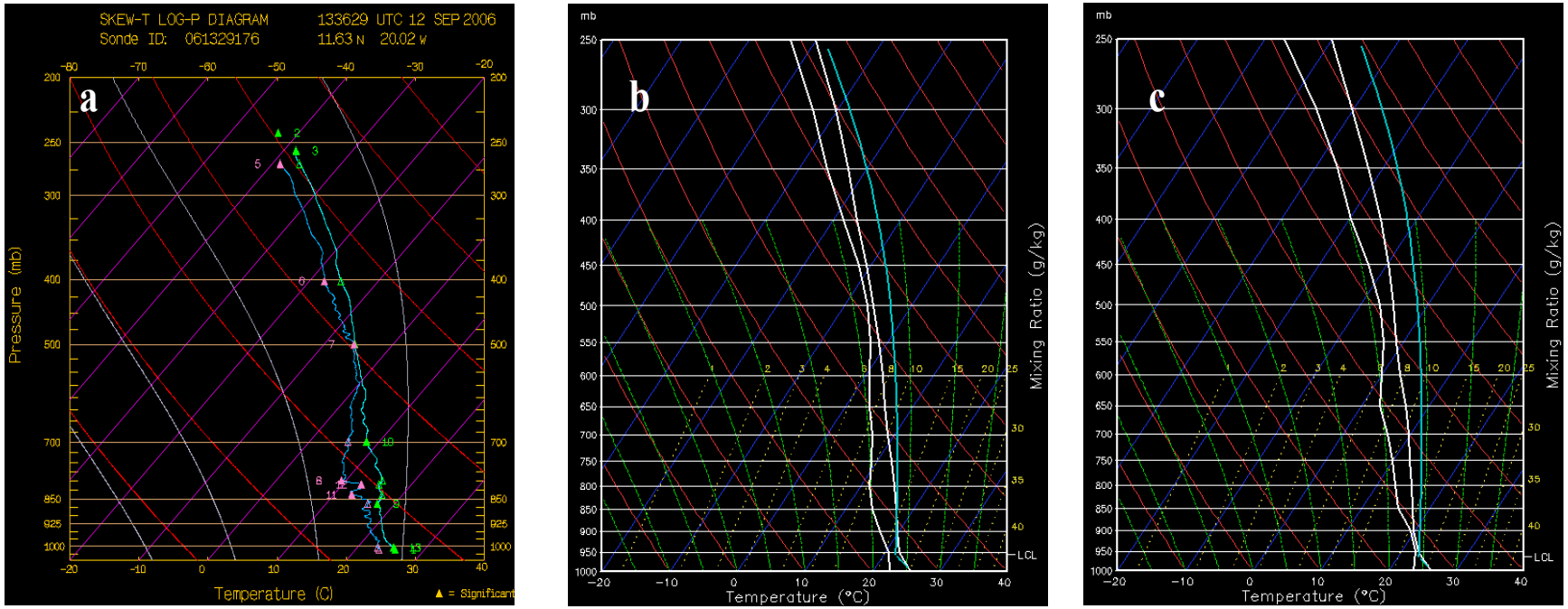

Figure 5.64 HAEW skew-T thermodynamic profile from D5: (a) dropwindsonde (b) HWRFx CNTRL and (c) HWRFx EXP.

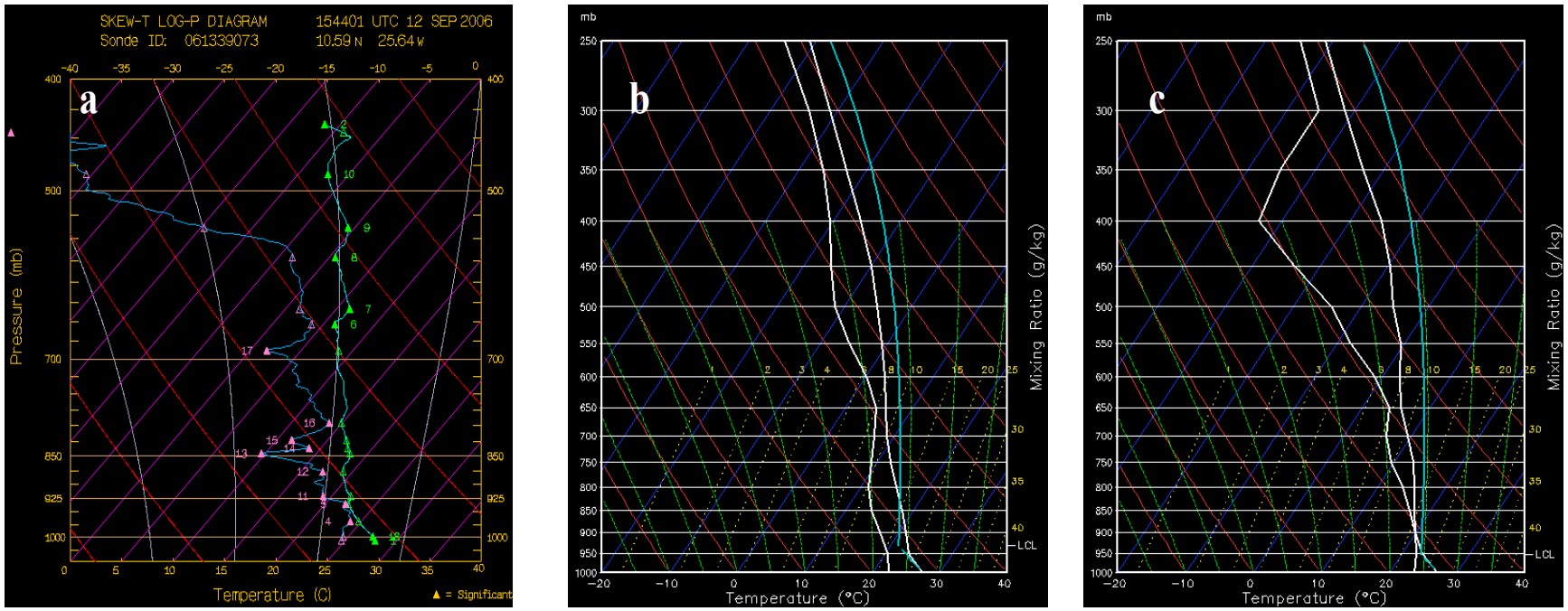

Figure 5.65 HAEW skew-T thermodynamic profile from D6: (a) dropwindsonde (b) HWRFx CNTRL and (c) HWRFx EXP.

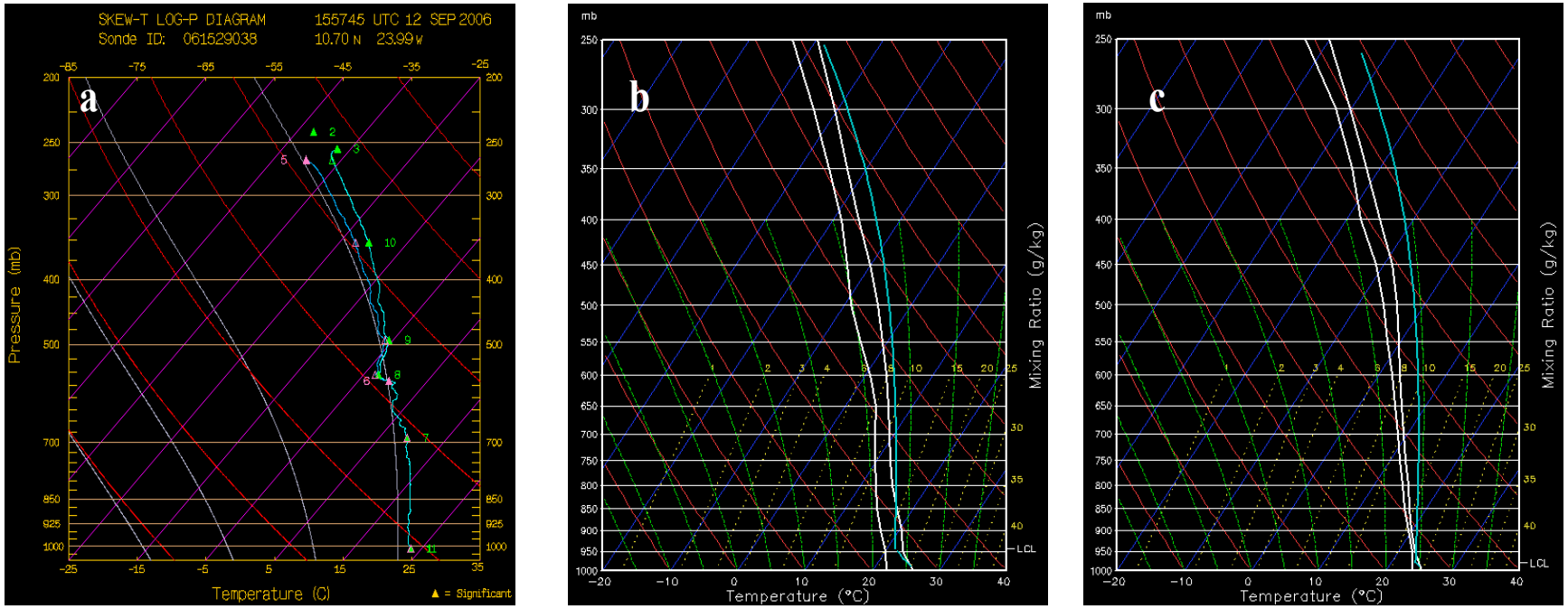

Figure 5.66 HAEW skew-T thermodynamic profile from D7: (a) dropwindsonde (b) HWRFx CNTRL and (c) HWRFx EXP.

5.3.3 NDAEW forecast sensitivity to initial conditions

The ICs sensitivity results showed that both the CNTRL and EXP simulations were successful in hindering the development of the NDAEW. However, the EXP simulation best represented the actual dynamic and thermodynamic structure of the AEW. Furthermore, the EXP run operational metrics best represented the weakening trend of the NDAEW structure, particularly after 66 h in the simulations.

During the period of 0 h to 66 h, the operational metrics values of both the CNTRL and EXP runs were similar for the most part (Fig. 5.67). However, beyond 66 h the simulations surface intensity greatly diverged. Past 66 h, the NDAEW CNTRL run forecast intensification whereas the EXP run forecast weakening. Particularly, for the period of 90 h to 120 h, the CNTRL run intensity of the NDAEW fluctuated between TS and TD status. Nevertheless, as was indicated in section 5.2.1, the structure and environment of the NDAEW demonstrated that no development took place by 120 h of the CNTRL simulation (Figs. 5.18-5.19).

Even though the surface intensity from 0 h to 66 h was comparable between the runs, the structure of the waves were different. Starting at 0 h, the CNTRL analysis showed a stronger AEW represented by a closed cyclonic circulation with a well-defined center at 700 hPa (Fig. 5.68a). Conversely, the EXP analysis showed a cyclonic circulation but not completely closed (Fig. 5.68b), which better resembled the dropwindsondes wind structure at 700 hPa (Fig. 5.33a) and the Meteosat-8 low-level wind field (Fig. 5.68c). Thermodynamically, at 700 hPa the CNTRL analysis showed a moister environment where the EXP analysis showed drier regions and vice versa. Particularly, at the center of the system or the MLWSM, the CNTRL analysis depicted

drier conditions whereas the EXP analysis showed a moister environment. As was discussed in section 5.3.1, the skew-T diagrams of the NDAEW HWRFx EXP analysis best represented the thermodynamic structure and environment at the dropwindsondes locations at the initial time. The EXP thermodynamic ICs were able to capture both the NDAEW moister regions as well as the zones that were impacted by SAL dry air intrusion, which was confirmed with the Meteosat-8 true color imagery. A RH data impact graph at 0 h (Fig. 5.69b), verified that the assimilation of the additional fifteen NAMMA dropwindsondes data reproduced more accurately the actual thermodynamic ICs. At 700 hPa and when compared to the Meteosat-8 true color imagery (Fig. 5.69a), this graph verified the drier regions sampled by D1, D12, and D14-D15 as well as the moist regions from D2-D3, D6 and D11, which were less impacted by the brown haze associated with the Saharan dust. However, at this particular level D4-D5 and D7-D8 showed to be drier, but D9-D10 and D13 moister.

Besides the ICs, the EXP run continued predicting a weaker NDAEW structure, which was verified against Meteosat-8 satellite imagery-derived information on derived winds and representation of SAL dry air. On September 10 1200 UTC when the NDAEW signal started to fade in the Hovmöller of Meteosat-8 IR imagery (Fig. 4.1), both runs were able to depict the SAL dry air that was affecting the wave (Figs. 5.70a-b), however the EXP run best represented the wind structure. While the CNTRL run sustained a closed cyclonic but weaker circulation (Fig. 5.70a), the EXP run predicted an open wave (Fig. 5.70b) similar to the Meteosat-8 IR imagery low-level winds (Fig. 5.70c). At 72 h, when the surface intensity of the simulations diverged, the NDAEW continued being impacted by dry air in both runs (Figs. 5.71a-b). The Meteosat-8 true

color imagery on September 11 at 1800 UTC confirmed the presence of SAL dry air in the eastern and central Atlantic (Fig. 5.72). Conversely, the wind structure of the waves showed to be different. The EXP run forecasts a much weaker open wave that starts to vanish (Fig. 5.71b), which was supported by the Meteosat-8 low-level winds (Fig. 5.71c). On the other hand, the closed cyclonic circulation of the CNTRL run intensified (Fig. 5.71a).

Past 72 h until the end of the simulations, the NDAEW remained affected by dry air intrusion to its environment (Figs. 5.19a-b and 5.74a-b). The EXP run open wave gradually continued to weaken losing almost its complete signal by the end of the simulation (Figs. 5.73a, 5.74a and 5.74c). Nevertheless, the CNTRL run lower-levels cyclonic circulation further intensified (Figs. 5.18a, 5.19a and 5.19c) as the MSLP steadily deepened (Fig. 5.67b), sustaining closed contours around the MLWSM (Fig. 5.18c) and consequently increasing the wind convergence. Another indication of the further organization of the system in the CNTRL run was the formation of a mid-to-upper levels anticyclone centered at the lower-level MLWSM (Fig. 5.18b), which was observed to occur prior to cyclogenesis in the earlier tests.

Results from the ICs sensitivity test for the NDAEW case demonstrated that the assimilation of additional dropwindsondes data into HWRFx greatly improved the initial state of the model (both dynamically and thermodynamically), thus producing a more accurate forecast.

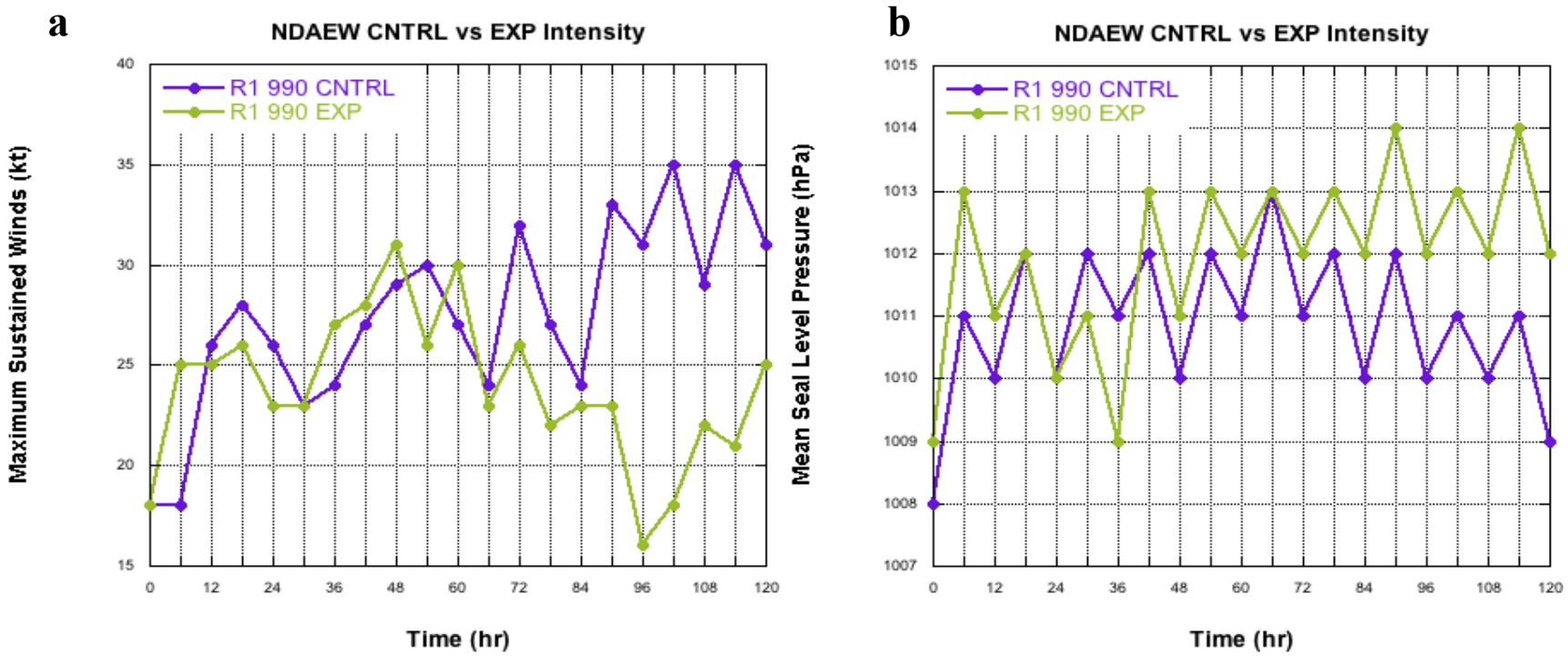

Figure 5.67 NDAEW surface intensity evolution from ICs sensitivity runs: (a) maximum sustained winds (kt) and (b) MSLP (hPa). The purple and light green lines represent the CNTRL (NDA) and EXP (DA) runs, respectively.

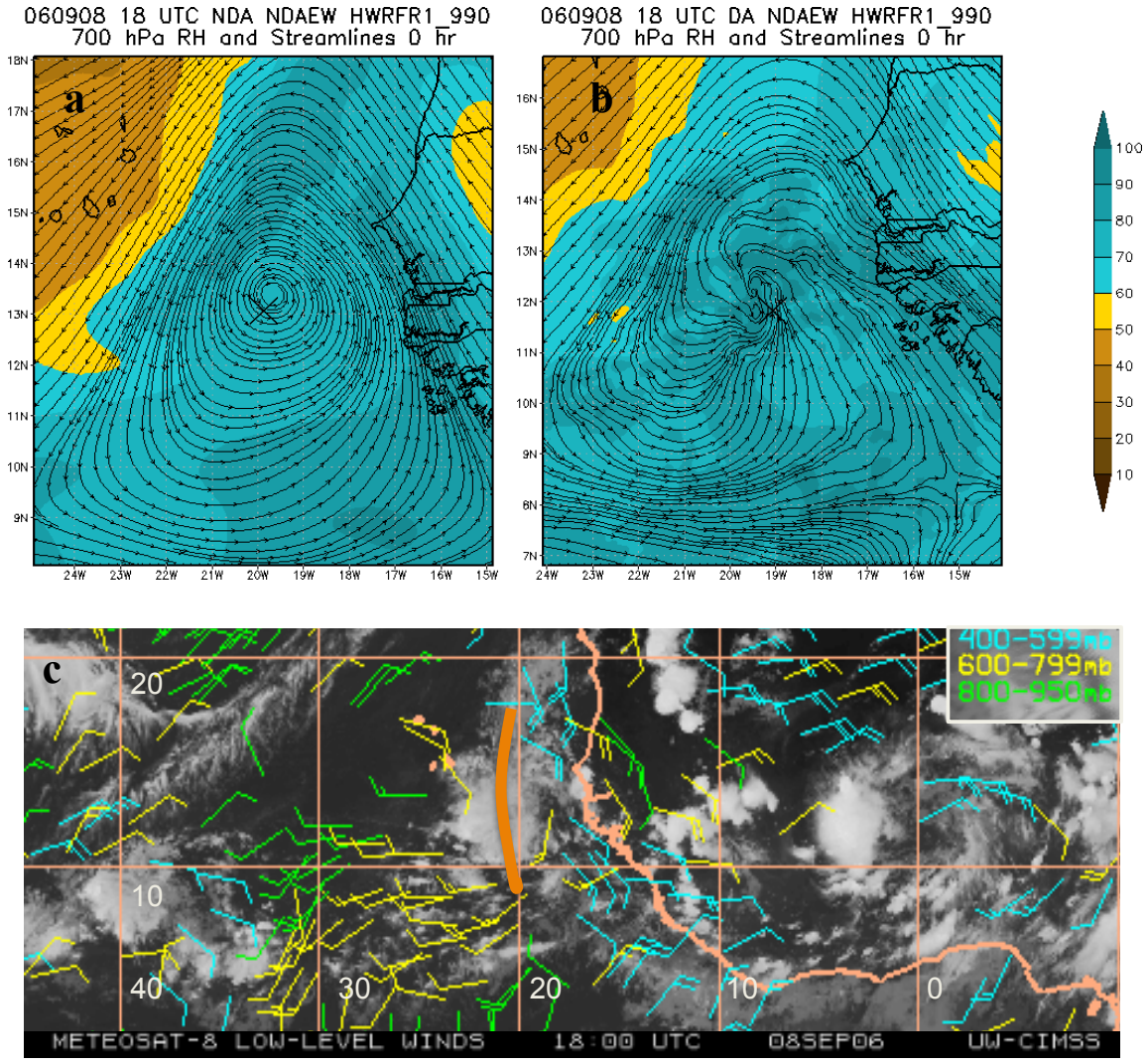

Figure 5.68 Dynamic and thermodynamic ICs from NDAEW (a) CNTRL and (b) EXP runs and (c) Meteosat-8 IR imagery depicting the NDAEW low-level wind field during September 8 1800 UTC. Dynamic and thermodynamic ICs refer to the 700-hPa streamlines and RH at 0 h in the runs.

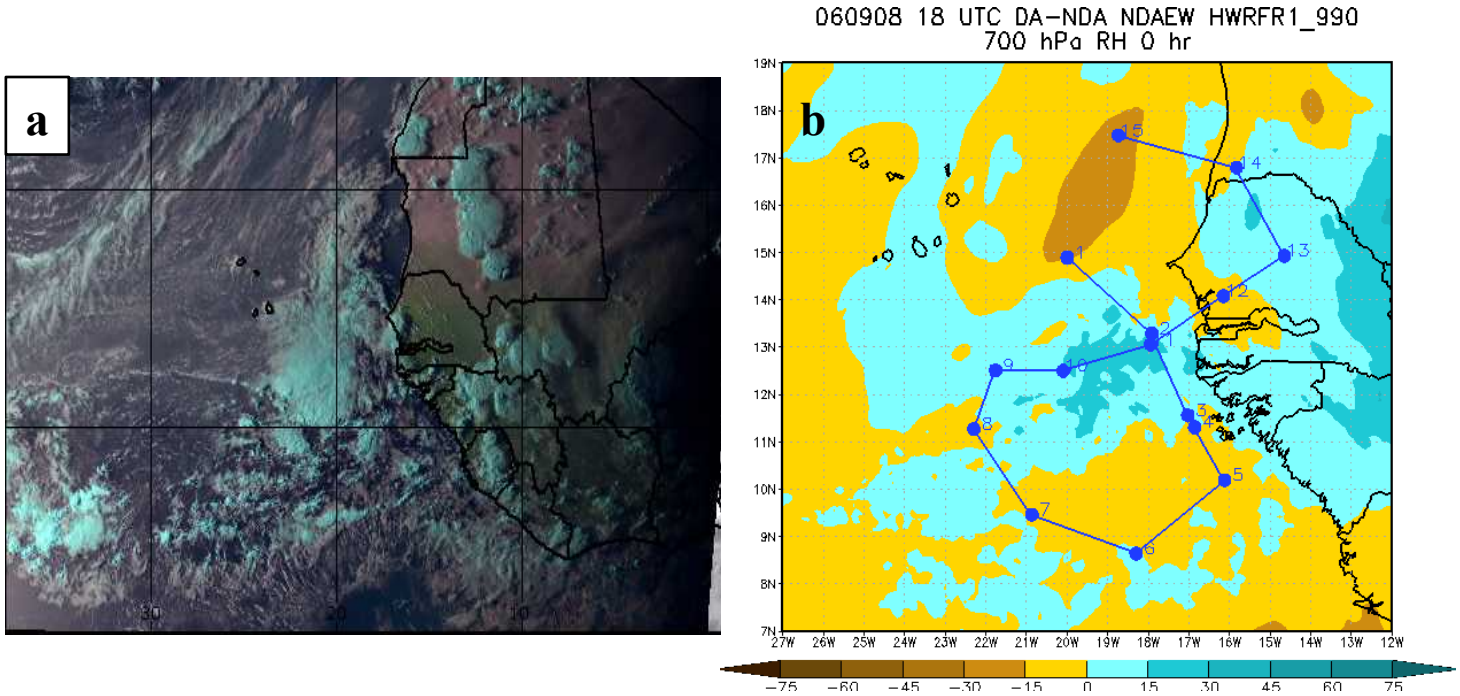

Figure 5.69 RH data impact graph at 0 h (b) verified that assimilation of additional NAMMA dropwindsondes data reproduced more accurately the real thermodynamic ICs when compared to the (a) Meteosat-8 true color imagery on September 8 1800 UTC. East of the Cape Verde islands, the dry air associated with the SAL dust (brown haze) as well as the moist regions sampled by the dropwindsondes were well represented by the HWRFx EXP analysis.

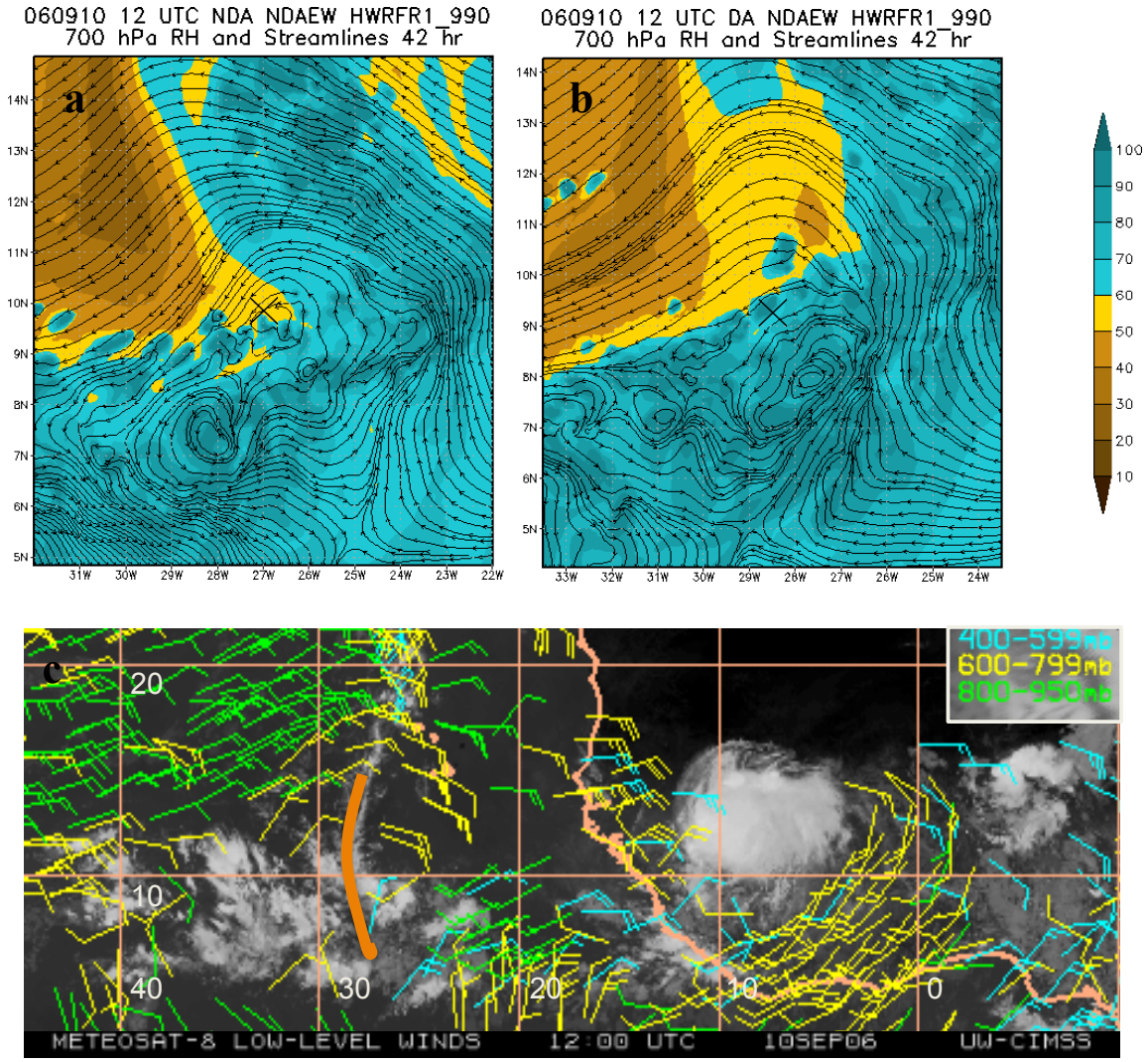

Figure 5.70 NDAEW 700-hPa streamlines and RH at 42 h from (a) CNTRL and (b) EXP runs and (c) Meteosat-8 IR imagery depicting the NDAEW low-level wind field during September 10 1200 UTC.

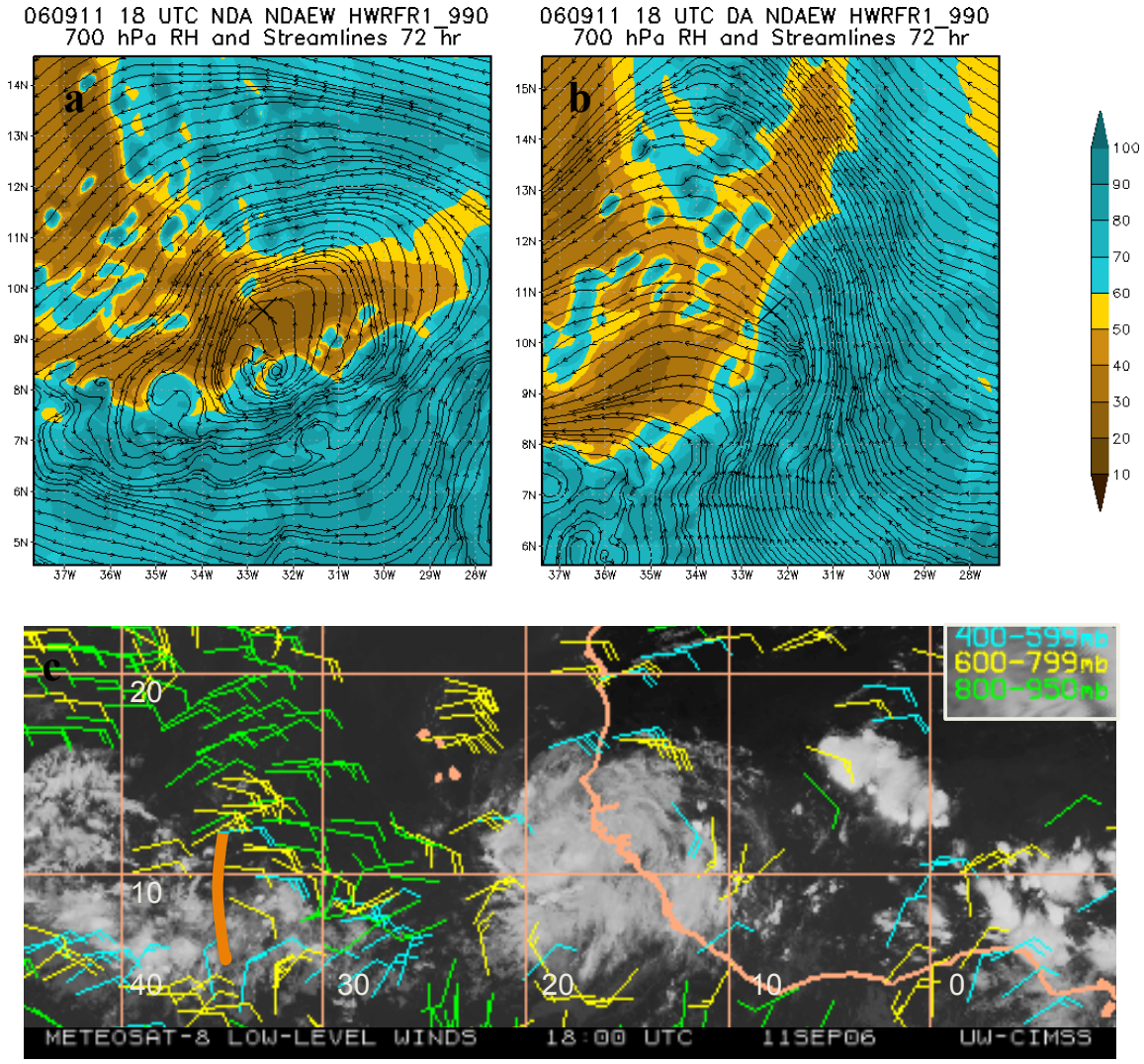

Figure 5.71 NDAEW 700-hPa streamlines and RH at 72 h from (a) CNTRL and (b) EXP runs and (c) Meteosat-8 IR imagery depicting the NDAEW low-level wind field during September 11 1800 UTC.

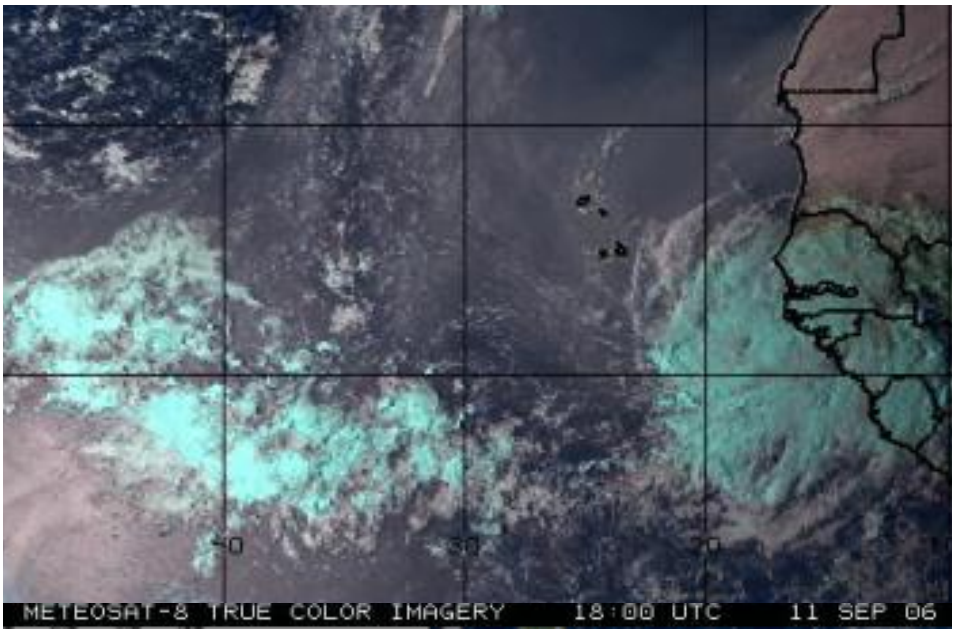

Figure 5.72 Meteosat-8 true color imagery on September 11 at 1800 UTC confirming the presence of SAL dry air in the eastern and central Atlantic.

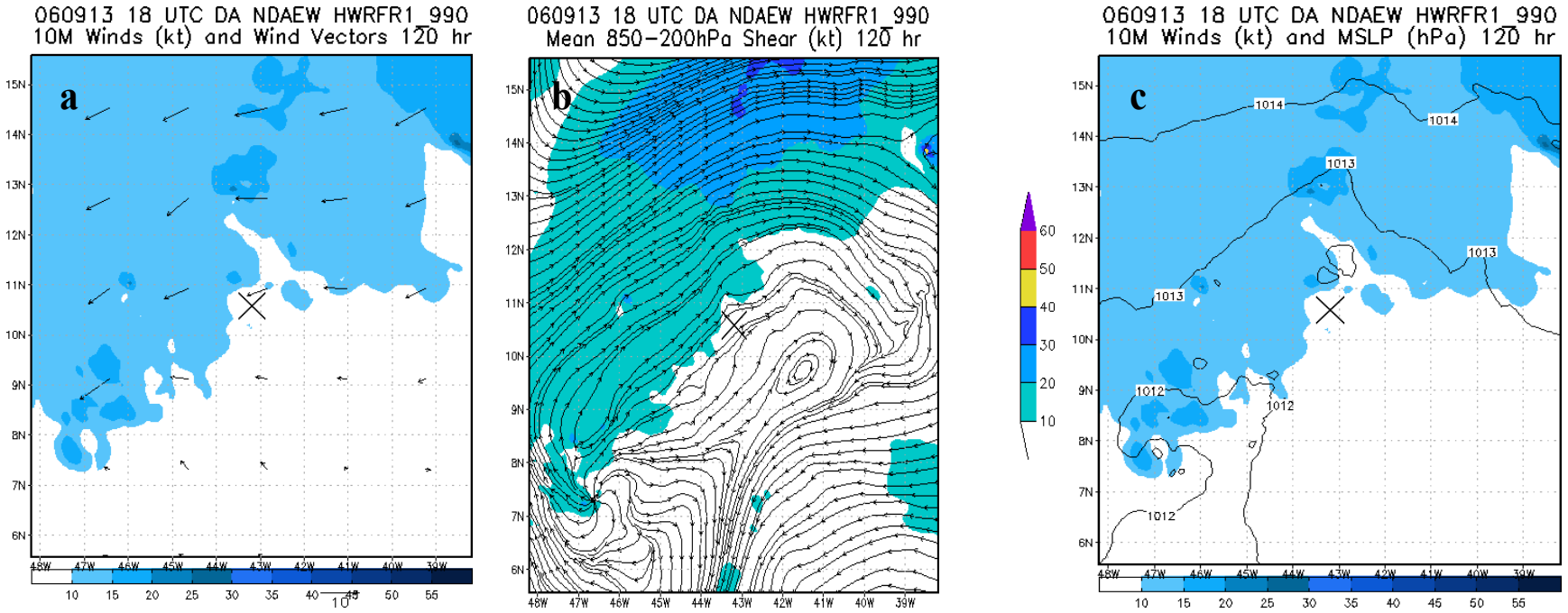

Figure 5.73 NDAEW EXP run structure at 120 h: (a) 10 m wind speed and vectors (b) deep layer environmental shear and (c) 10 m wind speed and MSLP. The MSW and MSLP at this time were 25 kt and 1012 hPa, respectively.

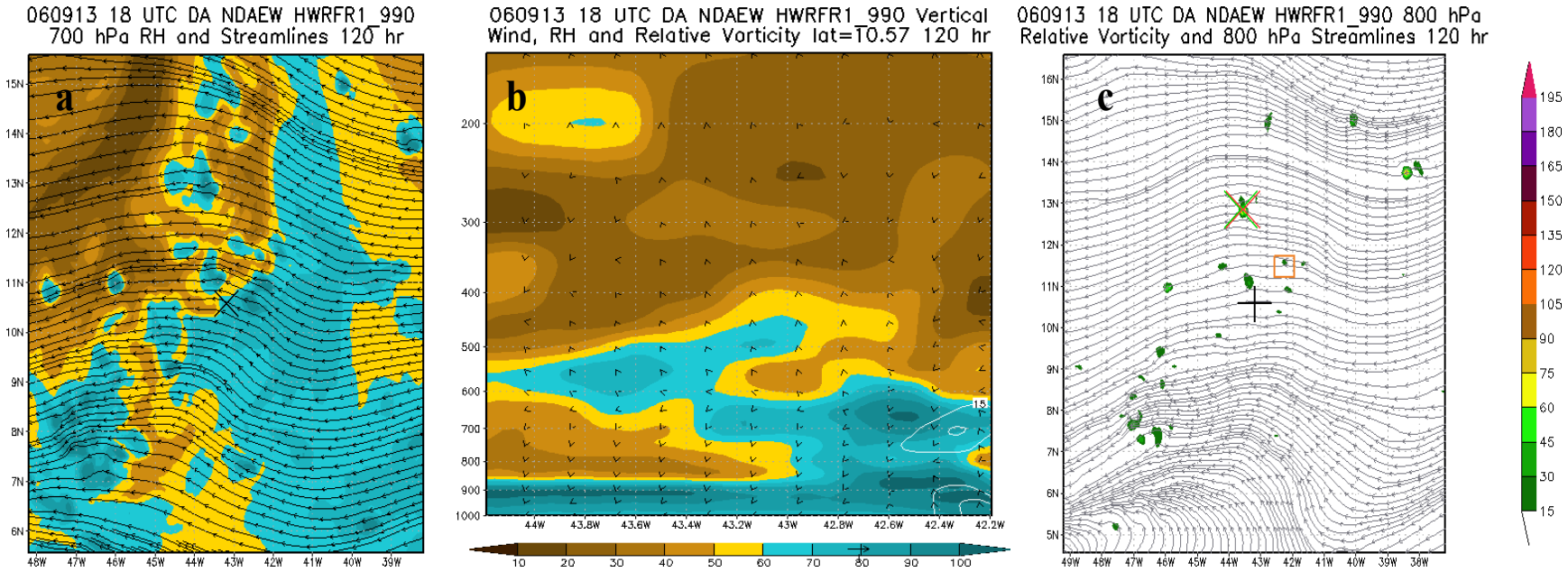

Figure 5.74 NDAEW EXP run structure at 120 h (continued): (a) 700-hPa RH and streamlines (b) east-west zonal VCS of RH (shaded), vertical wind (arrows) and RVORT (white contours) centered at the MLWSM, and (c) 800-hPa RVORT and streamlines.

5.3.4 HAEW forecast sensitivity to initial conditions

The HAEW ICs sensitivity results showed that the assimilation of additional dropwindsonde data did not improve the intensity forecast when compared to the CNTRL run. TS cyclogenesis in both runs occurred at 90 h, which represents sixty hours delay when compared to NHC (30 h). None of the simulations predicted strengthening to hurricane category one (90 h) or two (120 h). Instead, TS intensity was sustained until the end of the simulations. Conversely, unlike the CNTRL run TD stage was not forecast during the initial hours of the EXP simulation. Furthermore, the EXP run predicted a weaker TS as shown in both the operational metrics and structure.

The operational metrics for both runs at the initial time were comparable (Figs. 5.75a-b), yet the structure of the waves was different. At 0 h, the CNTRL analysis showed a stronger system represented by a closed cyclonic circulation with a well-defined center at both 700 hPa (Fig. 5.76a) and the surface (Fig. 5.76c). Conversely, the EXP analysis portrayed a weaker cyclonic circulation with an ill-defined center at 700 hPa (Fig. 5.76b) and at the surface, a cyclonic circulation but not completely closed (Fig. 5.76d). Thermodynamically, a moister environment at and near the center of the cyclonic circulation at 700 hPa supported a more intense system in the CNTRL analysis. As it was discussed in section 5.3.2, the HAEW CNTRL analysis best represented the ICs dynamic structure from 1000 hPa to 400 hPa when compared to the dropwindsondes observations whereas the EXP analysis resulted weaker. However, thermodynamically the skew-T diagrams showed mixed results when compared to the dropwindsondes vertical profiles. The 700-hPa RH data impact-graph at 0 h summarized these results (Fig. 5.77b). The EXP analysis was best representing the dropwindsondes moister

environment at D2 and D7 as well as the drier environment at D6. Conversely, the EXP analysis portrayed a moister environment at D1 where the dropwindsondes sampled dry air associated with a SAL outbreak and drier conditions at D3-D5 where the dropwindsondes sampled a moist atmosphere consistent with the dust brownish haze in the Meteosat-8 true color imagery (Fig. 5.77a).

Inaccurate ICs in both runs caused the model to forecast high environmental shear associated with a mid-to-upper levels ridge as well as frequent dry air entrainment to the wave environment at 700 hPa and at the MLWSM within 500 hPa and 800 hPa. Together, these two factors inhibited moist convection, which weakened the system structure and delayed TS cyclogenesis. Particularly, dry air intrusion to the wave environment at 700 hPa started eighteen hours earlier in the EXP run and continued affecting the system until 81 h in the simulation, which maintained a weaker system structure when compared to the CNTRL run. Moreover, stronger environmental shear affecting more frequently the MLWSM of the EXP run delayed the formation of a closed surface cyclonic circulation to 78 h.

During the 72 h of the EXP run and 78 h of the CNTRL run, a mid-to-upper levels anticyclone formed centered around the MLWSM (not shown), which reduced the environmental shear in that location to less than 20 kt giving space for moist convection to develop. Consequently, past 78 h in both simulations the MSLP started to drop (Fig. 5.75b), thus enhancing the convergence at the lower levels as well as the merger and vertical advection of RVORT. By 84 h in the EXP run and 90 h in the CNTRL run, a core of RVORT formed at the MLWSM. For the CNTRL run, the formation of the RVORT core at the MLWSM was the missing criterion for TS cyclogenesis to occur at

90 h (Figs. 5.22-5.23). TS cyclogenesis was achieved by the EXP run six hours after the RVORT core formation when the surface cyclonic circulation developed a well-defined center (Figs. 5.78-5.79). After 90 h, the outward extension of surface winds greater than 20 kt from the center of the storm, stronger RVORT core and outflow as well as stronger surface intensity determined more intense TS in the CNTRL run. Figures 5.24-5.25 and 5.80-5.81 show the CNTRL and EXP runs structure of TS Helene at 120 h, respectively.

The delay in tropical cyclogenesis and the hindrance of further intensification was attributed to the weaker wind structure and the misrepresented thermodynamic ICs in both runs. Even though the CNTRL and EXP runs best represented particular dropwindsondes profiles, none forecast the regions in the atmosphere were saturation occurred. Conversely, although the HAEW EXP run did not improve the timing of tropical cyclogenesis and the intensity forecast, it better predicted the track when compared to the BT of NHC (Fig. 5.82).

The HAEW case demonstrated that assimilation of additional data sometimes results in intensity forecast degradation, however improvements on track still can be achieved. In addition to possible errors in the initialization and BCs, other factors that could have contributed to the obtained results for this case include model errors (i.e. from horizontal, vertical and time-differencing schemes) and errors arising from the physics parameterizations. The amount of dropwindsondes available to assimilate as well as the sampling flight pattern might have influenced the results too. For the NDAEW case, the amount of dropwindsondes was little more than double the amount available for the HAEW case and the coverage of the sampling flight pattern around the wave was greater.

In order to better assess the impact of dropwindsonde data on the intensity forecast of weak tropical systems such as AEWs and TDs, more case studies need to be evaluated.

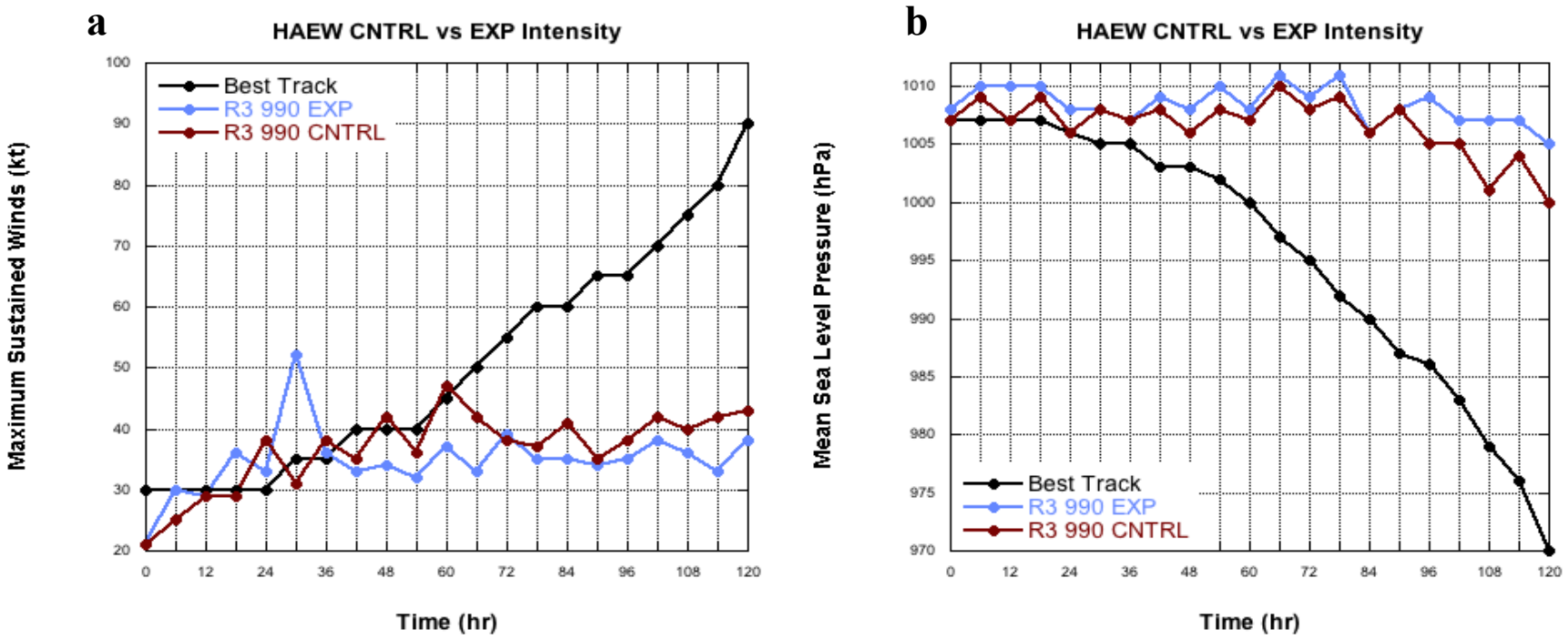

Figure 5.75 HAEW surface intensity evolution from ICs sensitivity runs: (a) maximum sustained winds (kt) and (b) MSLP (hPa). The red and blue lines represent the CNTRL (NDA) and EXP (DA) runs, respectively.

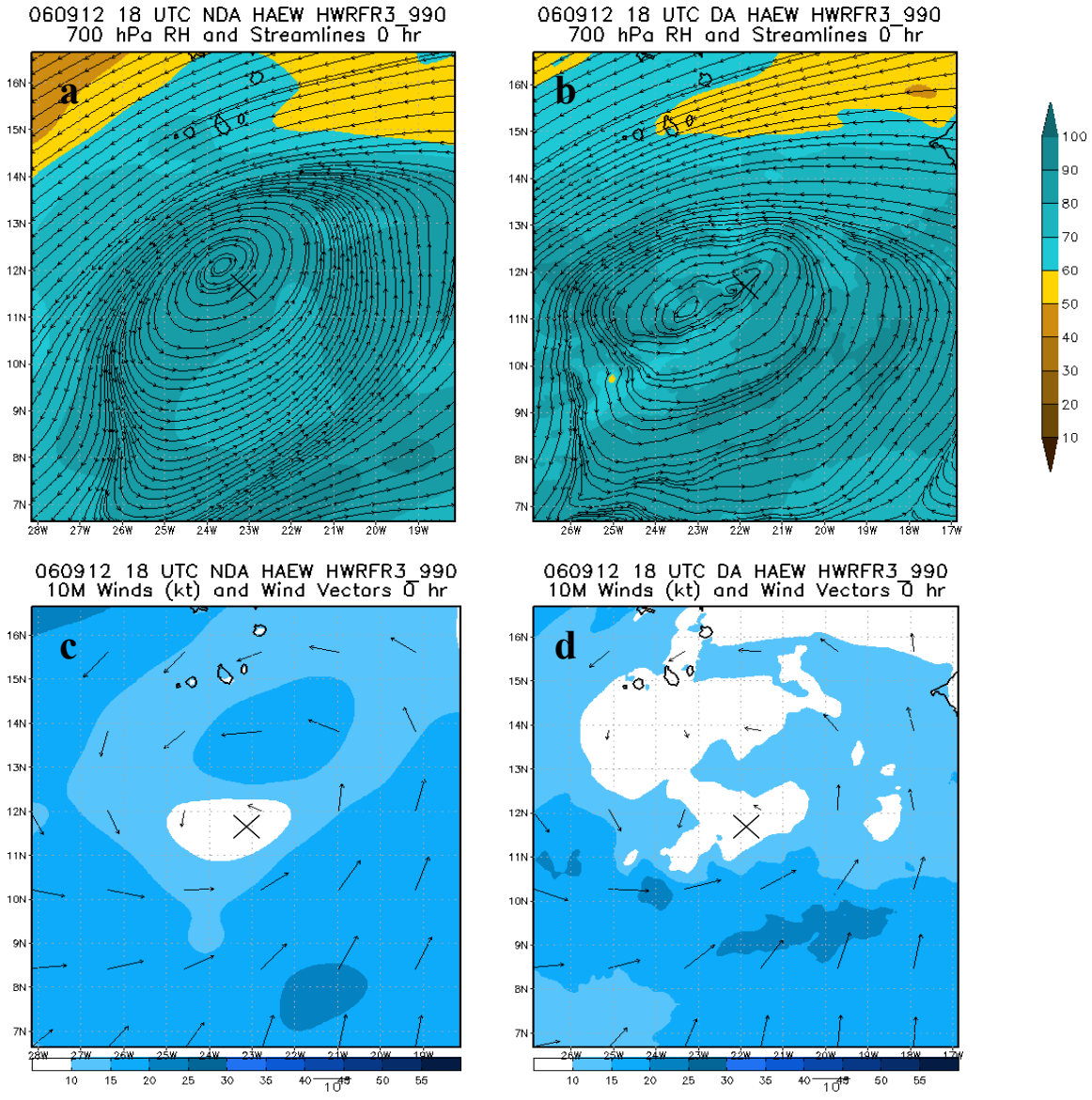

Figure 5.76 HAEW dynamic and thermodynamic ICs from CNTRL and EXP runs. The graphs in the first row are the 700-hPa streamlines and RH from the (a) CNTRL and (b) EXP runs. Plots in the second row represent the magnitude and vectors of the 10 m winds in the (c) CNTRL and (d) EXP runs.

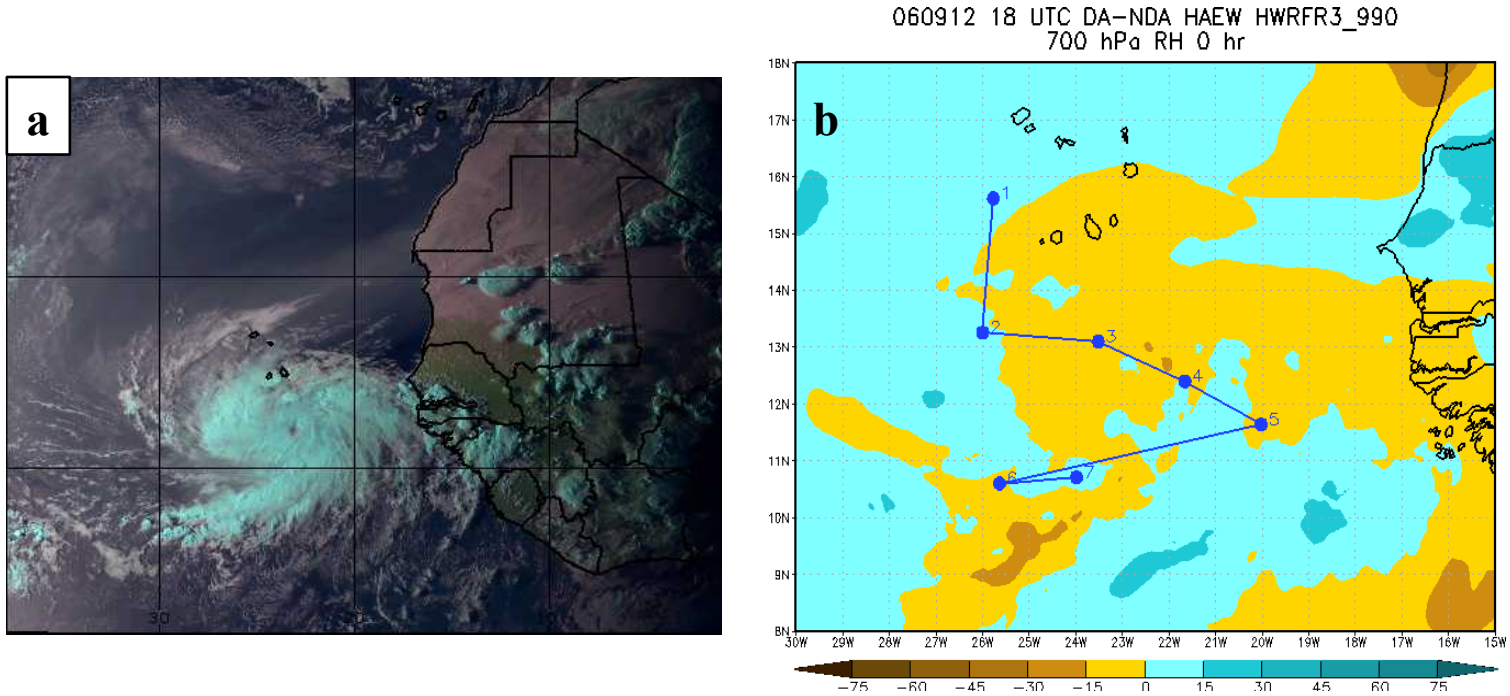

Figure 5.77 (a) Saharan dust outbreak spread over the TD associated with 2006 Hurricane Helene on September 12 1800 UTC. (b) HAEW ICs RH data impact at 700 hPa showed that the EXP analysis best represented the moister environment sampled by D2 and D7 as well as the drier environment at D6. This graph also depicted that the EXP analysis had a moister environment at D1 where the dropwindsondes sampled dry air associated with the SAL outbreak and drier conditions at D3-D5 where the dropwindsondes sampled a moist atmosphere confirmed by a less dense dust brownish haze in the Meteosat-8 true color imagery.

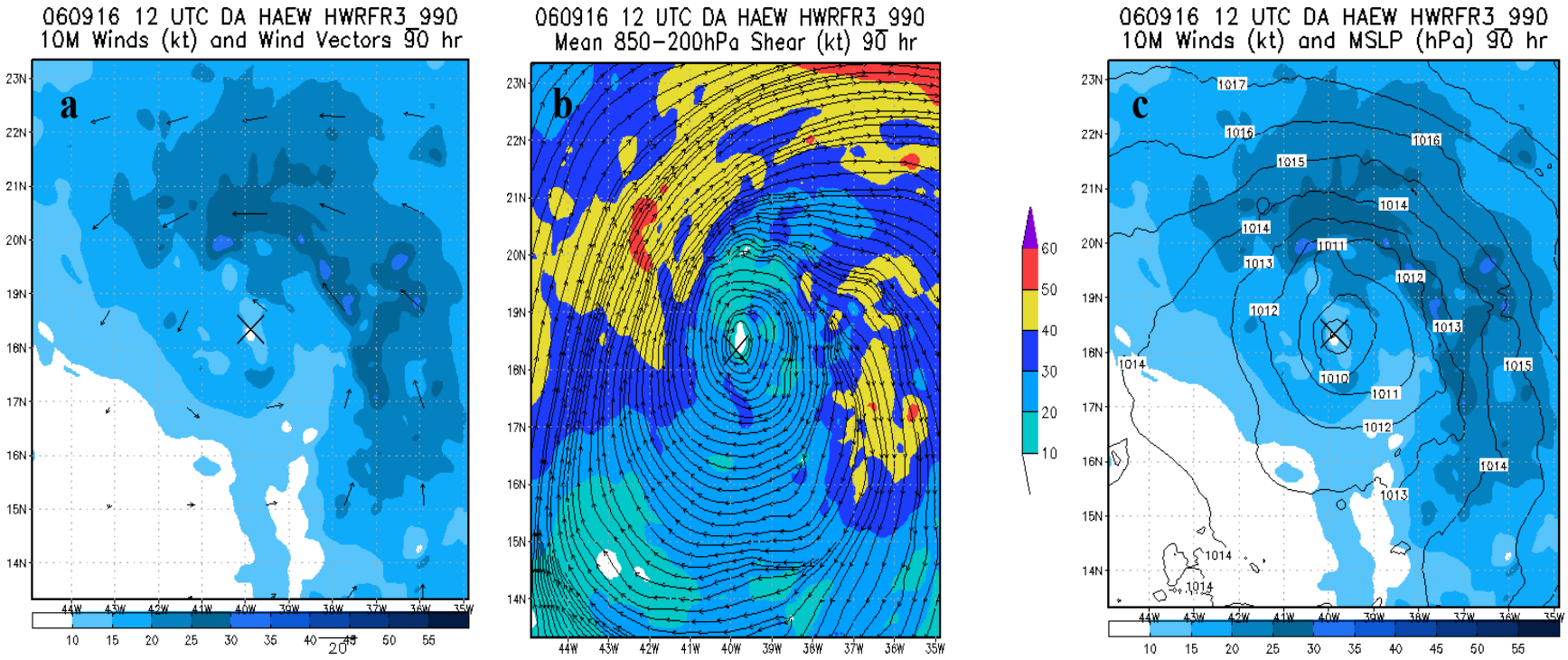

Figure 5.78 HAEW EXP run structure at time of TS cyclogenesis: (a) 10 m wind speed and vectors (b) deep layer environmental shear and (c) 10 m wind speed and MSLP. At 90 h, the MSW was 34 kt and the minimum of MSLP was 1008 hPa.

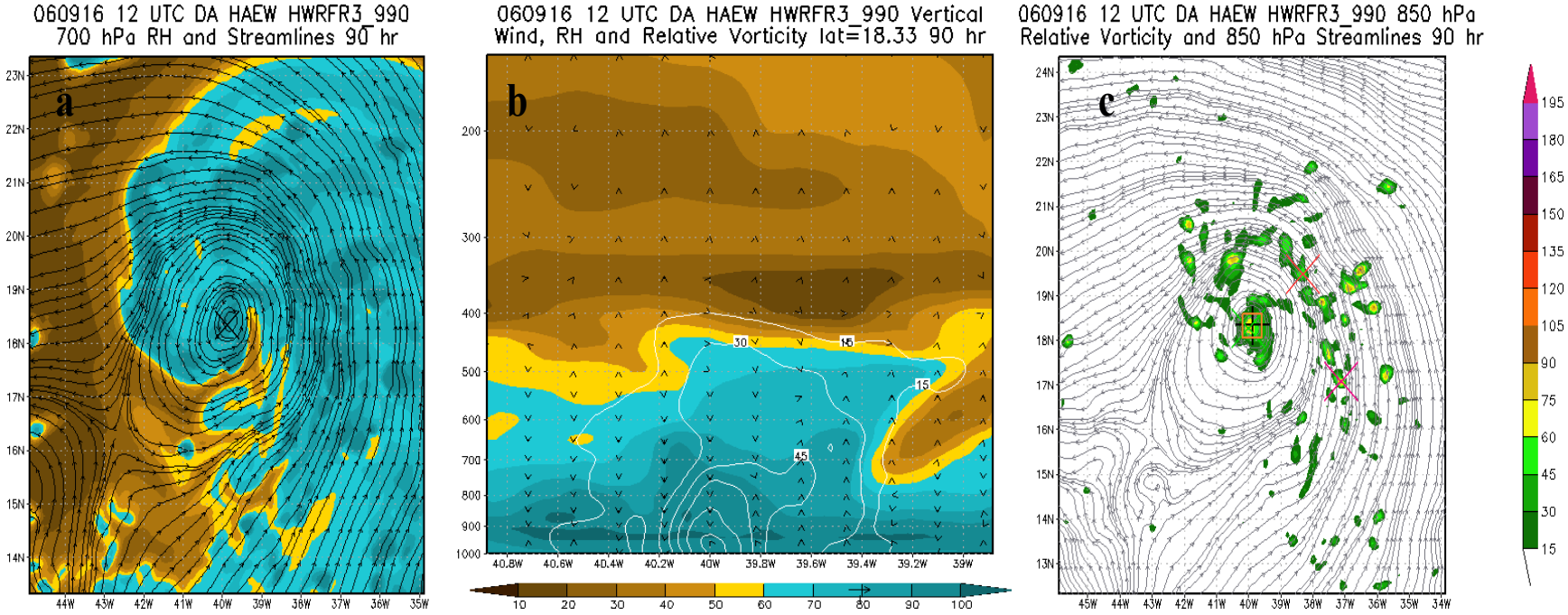

Figure 5.79 HAEW EXP run structure at time of TS cyclogenesis (continued): (a) 700-hPa RH and streamlines (b) east-west zonal VCS of RH (shaded), vertical wind (arrows) and RVORT (white contours) centered at the MLWSM, and (c) 850-hPa RVORT and streamlines.

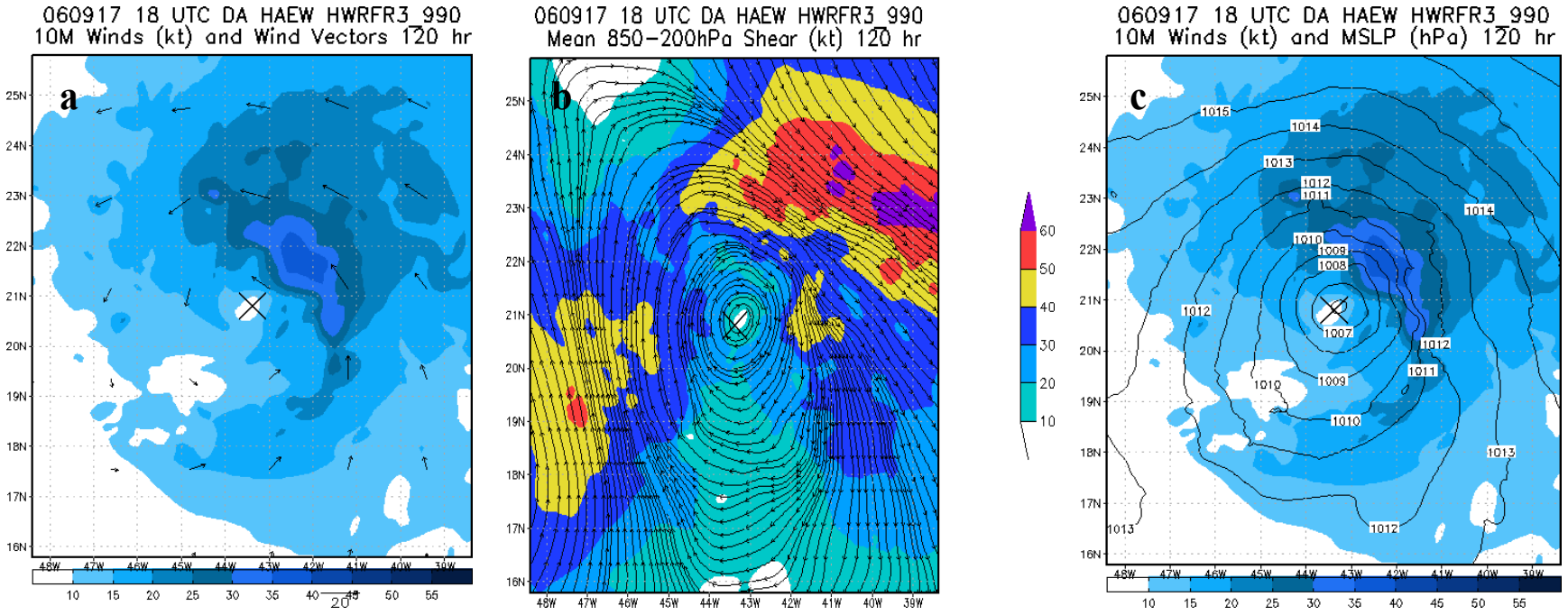

Figure 5.80 HAEW EXP run structure at 120 h: (a) 10 m wind speed and vectors (b) deep layer environmental shear and (c) 10 m wind speed and MSLP. The MSW and MSLP at the end of the simulation were 38 kt and 1005 hPa, respectively.

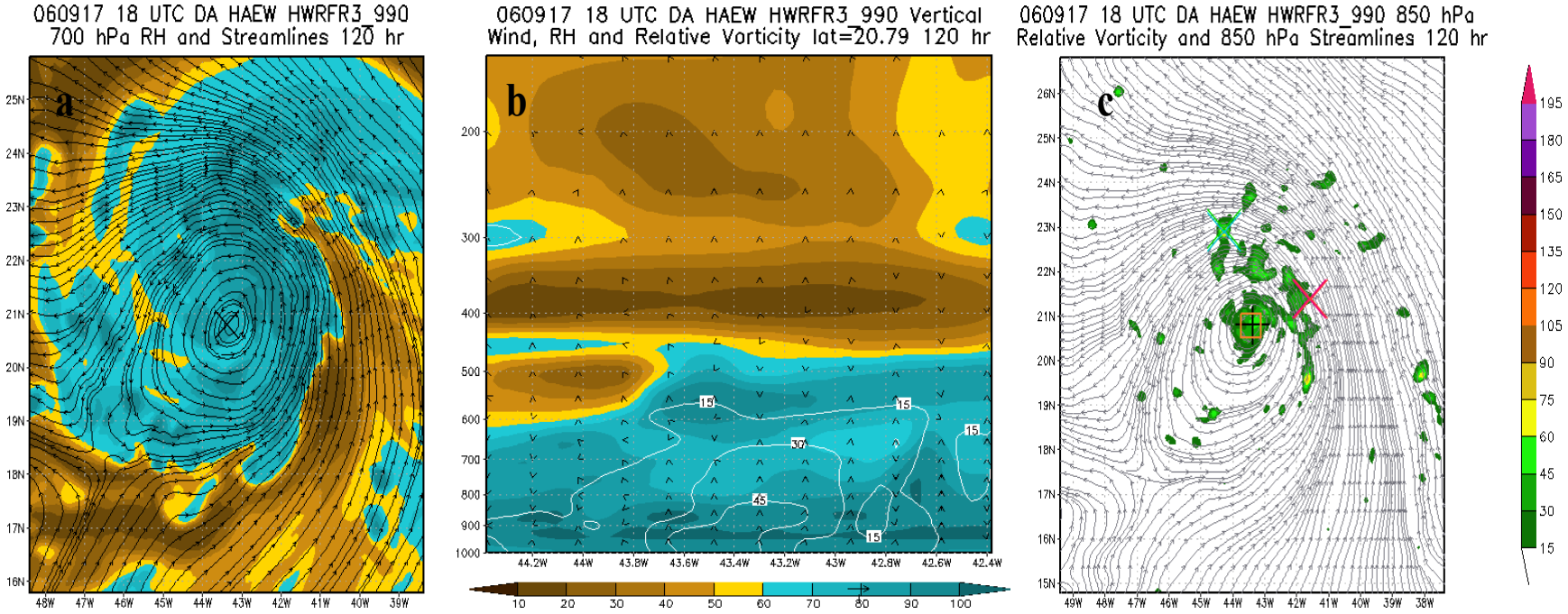

Figure 5.81 HAEW EXP run structure at 120 h (continued): (a) 700-hPa RH and streamlines (b) east-west zonal VCS of RH (shaded), vertical wind (arrows) and RVORT (white contours) centered at the MLWSM, and (c) 850-hPa RVORT and streamlines.

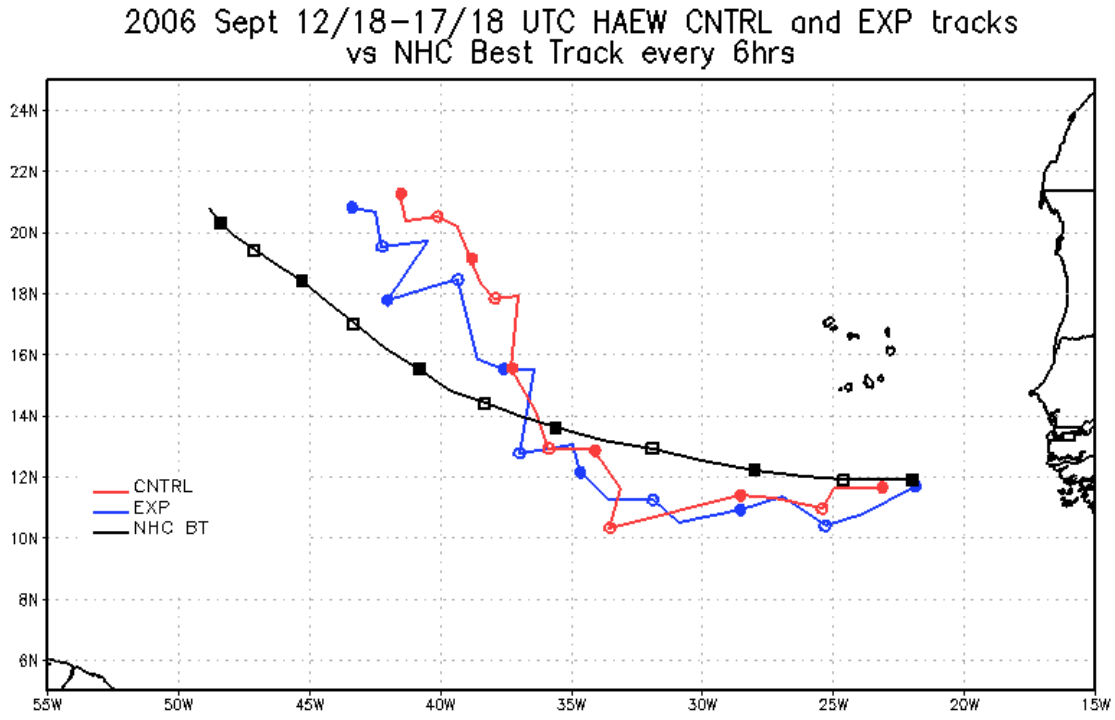

Figure 5.82 HAEW track from HWRFx CNTRL (red) and EXP (blue) runs versus the NHC BT (black) of Helene.

5.4 Developing versus non-developing AEWs

The environment and structure of the HAEW and NDAEW EXP runs were compared to determine the factors that were conducive to tropical cyclogenesis versus the ones that hindered intensification. The operational metrics from these two cases depicted a weaker intensity for the NDAEW since the beginning until the end of the simulation (Figs. 5.83a-b). However, a constant weakening or intensification trend of the waves was not observed until approximately 66 h of the simulations.

Although the HAEW showed an intensification trend in the MSW starting at 66 h (Fig. 5.83a), it is not until 90 h that TS cyclogenesis occurred after the MSLP significantly dropped (Fig. 5.83b). As it was indicated in section 5.3.4 for the HAEW

case as well as in previous sections, the environment and structure of the waves are the main determinants for tropical cyclogenesis (Figs. 5.78-5.79). The MSW intensity establishes if either TD or TS cyclogenesis take place. Environment and structure distinguishing factors at the time of tropical cyclogenesis in the HWRFx included: surface and lower-levels closed cyclonic circulation with a well-defined center, MSLP equal or less than 1010 hPa to sustain enough convergence and moist convection at the TC center, environmental shear less than 30 kt at the TC center by the establishment of a mid-to-upper levels anticyclone center near or at the MLWSM to support moist convection, organization of a quasi-saturated, saturated or super-saturated column of air (RH ≥ 90%) at the TC center extending up to at least 850 hPa as well as moist air within the cyclonic circulation, and the formation of a RVORT core at the TC center extending from the surface to at least 850 hPa. On the other hand, even though a weakening trend in the MSW of the NDAEW started at 66 h (Fig. 5.83a), a weaker system with low chances to survive a hostile environment was observed since the initial time of the simulation. At 0 h, the 700-hPa RH showed that at and near the MLWSM immediate surroundings the NDAEW had a moister environment (Fig. 5.84a) than the HAEW (Fig. 5.84b). However, dynamically the ICs of the NDAEW exhibited a weaker structure at both 700 hPa and the surface (Figs. 5.84a and 5.84c). At 700 hPa, the NDAEW analysis portrayed a cyclonic circulation yet not completely closed (Fig. 5.84a) whereas the HAEW analysis showed a stronger system represented by a closed cyclonic circulation (Fig. 5.84b), though with an ill-defined center. At the surface, the NDAEW wind field presented no signs of the existence of an AEW (Fig. 5.84c) while the HAEW analysis portrayed a weak cyclonic circulation not completely closed (Fig. 5.84d).

After the initial time, the model forecasts a high shear environment associated with a mid-to-upper levels ridge as well as frequent dry air entrainment from approximately 500 hPa to 800 hPa at the MLWSM for both AEWs. The fate of this AEW was determined by the combination of extensive and continual dry air intrusion to the NDAEW environment at 700 hPa since 30 h until the end of the simulation. The dry air reached down to 900 hPa at the MLWSM. Weaker MSLP with no consistency on the maintenance of closed isobars around the MLWSM was also a factor. The weaker MSLP intensity and structure restrained low-level convergence, which in turn prevented moist convection at the MLWSM. In addition, moisture accumulation at the MLWSM was not achieved due to constant dry air subsidence, which in turn hindered the formation of a RVORT core through merger and vertical advection. All these factors together caused the wave to progressively vanish toward the end of the simulation (Figs. 5.73-5.74).

HAEW results from this and prior sections show that global models outperformed the HWRFx regional model in forecasting the timing of cyclogenesis. As indicated by Brown (2006) in the Helene tropical cyclone report, many of the global models predicted the TD cyclogenesis of Helene twenty-four hours in advance. Moreover, data from the GFS final analyses showed that the NDAEW did not develop, which support at least the GFS model ability on determining the fate of the AEWs.

Although the HWRFx could not improve the HAEW cyclogenesis prediction and its further intensification, the regional model provided clues on where in the atmosphere tropical cyclogenesis takes place. TC formation occurs from approximately 700 hPa to the surface. This indicates that both dynamic and thermodynamic processes within 700 hPa down to the surface must be considered in order to accurately predict tropical

cyclogenesis. This information could be of advantage for the creation of new or improved methods to approach the cyclogenesis prediction problem. Consequently, this would reduce the uncertainty on less predictable cases at early stages of development and provide higher confidence on the cyclogenesis forecast.

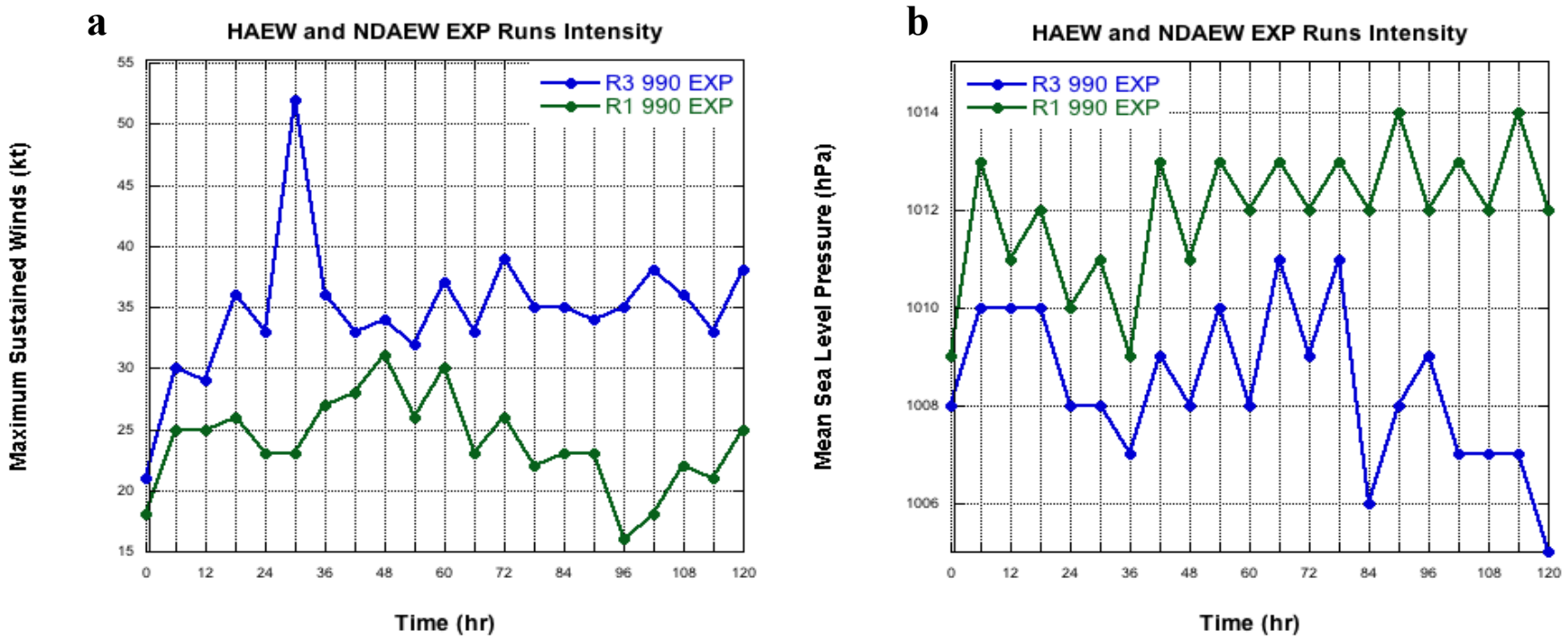

Figure 5.83 HAEW and NDAEW EXP runs surface intensity evolution: (a) maximum sustained winds (kt) and (b) MSLP (hPa). The blue and green lines represent the HAEW and the NDAEW, respectively.

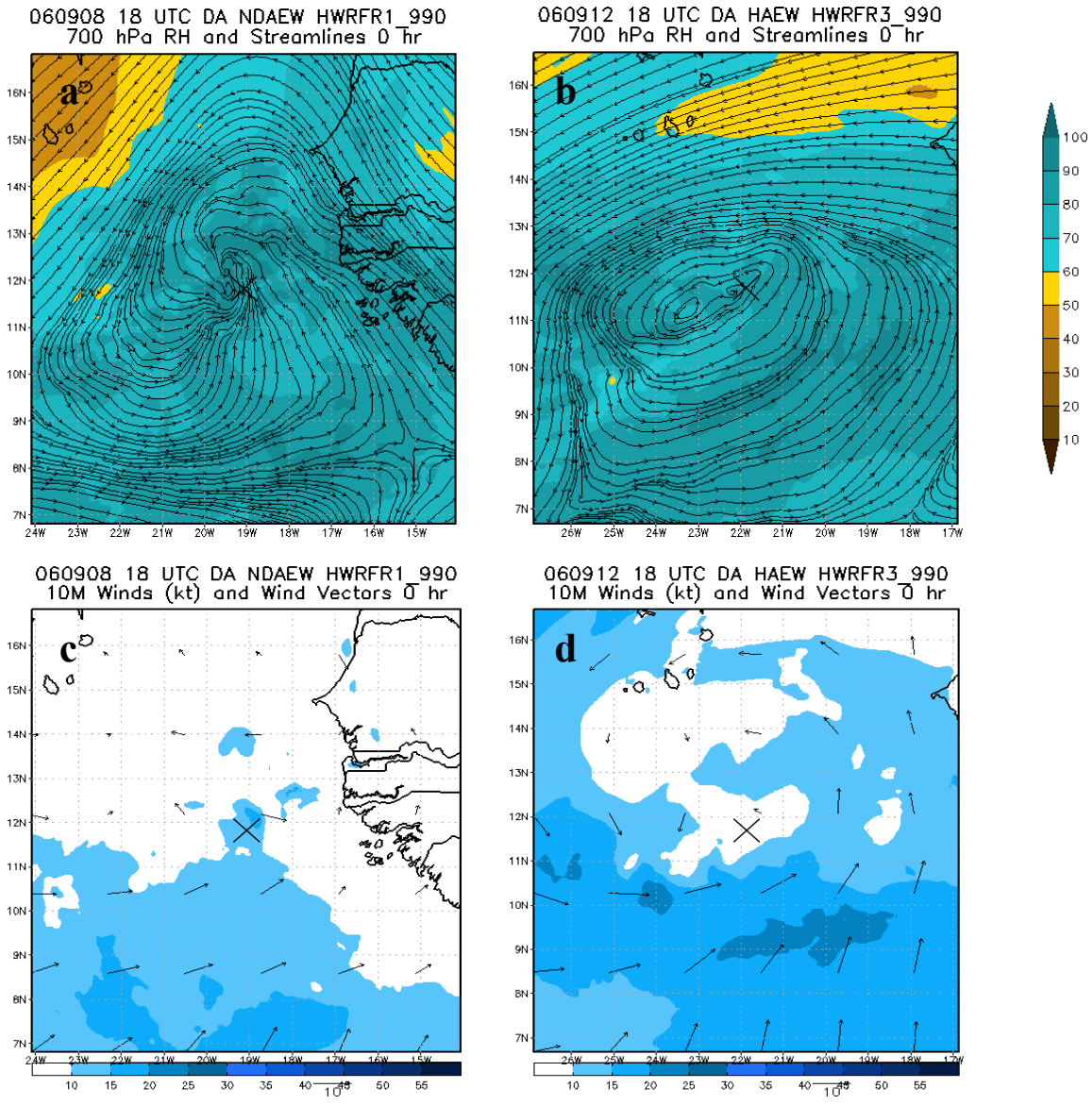

Figure 5.84 NDAEW and HAEW EXP dynamic and thermodynamic ICs. The graphs in the first row depict the 700-hPa streamlines and RH of the (a) NDAEW and the (b) HAEW. Plots in the second row represent the magnitude and vectors of the 10 m winds from the (c) NDAEW and the (d) HAEW.

6. DISCUSSION AND CONCLUSIONS

A modeling and data impact study was performed using the NOAA/AOML/HRD HWRFx high-resolution regional model with the aim to find distinguishing factors that discriminate between developing and non-developing AEWs. Two AEWs sampled with dropwindsondes during NAMMA were selected for this investigation. One AEW was the precursor of Hurricane Helene (HAEW), with its cyclogenesis was reasonably well anticipated about 24-h prior to TC formation by many of the global forecast models (Brown 2006). The second AEW preceded the HAEW, however it did not develop into a TC (NDAEW).

During the first phase of the investigation, CNTRL simulations were performed to examine the effect of CUP and nesting in the forecast of the two systems. Phase two consisted of a data impact analysis where deterministic EXP simulations were generated having new ICs produced by HEDAS. Unlike the CNTRL simulations, these assimilated the airborne data gathered in NAMMA not ingested into NOAA/NCEP models in real time. The added assimilation included dropwindsonde data of temperature, specific humidity as well as wind from the flight level down to the surface. This additional dataset was used to investigate if its assimilation improves the physical interpretation of the AEWs as well as the predictability of tropical cyclogenesis and to validate HWRFx ICs dynamic-thermodynamic structure.

CNTRL nested simulations had a static parent domain with grid spacing of 9 km and higher resolution-moving nest of 3 km. The CNTRL and EXP un-nested simulations were run only with the 9-km static parent domain. The physics options applied to the model were semi-operational or aligned as close as possible to the operational HWRF.

These options included the NCEP GFS surface and PBL, Ferrier microphysics, SAS CUP scheme (only for the CUP sensitivity test and 9-km domain), and GFDL land-surface and radiation physics. The NCEP 6-hourly GFS final operational analyses on 1.0 x 1.0 degree grids were used to provide ICs and BCs for the CNTRL nested and un-nested runs as well as the BCs of the EXP runs. The ICs for the HWRFx EXP runs were generated by HEDAS using as first guess GEFS data.

CUP sensitivity results showed that employment of the SAS implicit convection in the 9-km domain had a strengthening effect on the AEWs. On the other hand, setting the convection to be explicit had a weakening effect on the systems. For the NDAEW case, HWRFx predicted TS intensification with and without the inclusion of the SAS. However, the wave developed earlier and stronger when the SAS CUP was utilized. Regarding the intensification timing, the removal of the SAS CUP assisted delaying the cyclogenesis by 39 hours. With respect to the HAEW, inclusion of the SAS assisted in predicting stronger and fifteen hours earlier TS than with CUP removed. Even though both simulations predicted Helene TS cyclogenesis, it was later than in the NHC BT analyses. The TD stage of Helene was forecast by both runs, but only during the first six hours of the simulations and weaker than in the NHC BT. Strengthening of hurricane Helene to category one or two was missed, but TS intensity was sustained until the end of the simulations. Stronger systems due to the utilization of the SAS CUP were attributed to more intense operational metrics as well as structures and environments more favorable for TC development.

In the NDAEW case, the addition of the SAS CUP to the model supported the early generation and further intensification of minimum MSLP closed contours that

enhanced moist convection, resulting in greater surface convergence. Conversely, the removal of the SAS CUP predicted a drier environment due to prolonged periods of major multi-level dry air intrusion to the core of the system. Both factors hindered moist convection, which delayed the intensification of the wave in the model. For the HAEW case, the removal of the SAS CUP prolonged strong environmental shear and predicted a period of dry air intrusion that deterred the earlier organization and intensification of this wave in both runs. Results from this test confirmed the cyclogenesis dynamic-thermodynamic nature and suggested that besides the removal of implicit convection, there were other factors in the model that influenced the intensification of the systems.

The HWRFx nesting capability in the 3-km domain demonstrated to be one factor in the model influencing the structure and intensity of the AEWs. Improved horizontal resolution by means of transferring meteorological information from a fine to a coarser mesh and vice versa (over the region of coinciding grid points) resulted in a strengthening effect on the AEWs. The NDAEW nesting sensitivity results showed that the removal of the 3-km nest assisted in hindering the development of the wave whereas inclusion of it developed the wave late in the simulation. Reasons that prevented the development of the NDAEW in the un-nested run included the model inability to maintain minimum MSLP closed contours, periods of high environmental shear (equal or greater than 30 kt) near the MLWSM, a drier environment since early in the simulation, and dry air intrusion to the wave core well in advance and for a longer period of time when compared to the nested run. A weaker MSLP intensity and structure inhibited moist convection and advanced convergence, thus obstructing the generation of a RVORT core that has been considered as a necessary condition for cyclogenesis to happen (Tory el al. 2006).

Besides the dynamic constraints, the RVORT core formation was also hindered by the prolonged intrusion of very dry air to the wave environment, which caused subsidence of cooler dehumidified air. Both dynamic and thermodynamic factors prevented the merger of smaller centers of RVORT and its subsequent advection to upper levels in the troposphere. Similar to the NDAEW case, results of the HAEW runs demonstrated that the removal of the 3-km nest had a weakening effect. Addition of the nesting capability resulted in the forecast of a stronger Helene whereas the exclusion of it not only predicted a weaker system but also further delayed the TS cyclogenesis when compared to the nested run and NHC BT analyses. The TD stage of Helene was forecast by both runs, but only during the first six hours of the simulations and weaker than the NHC. Like in the CUP sensitivity test, none of the simulations predicted strengthening to hurricane category one or two, but sustained TS status until the end of the runs. Factors that weakened the TD and delayed TS cyclogenesis in both runs included strong environmental shear associated with a mid-to-upper levels ridge, and frequent dry air intrusion to the wave environment at 700 hPa as well as into the MLWSM within 500 hPa and 700 hPa. Besides the forecast of much drier air both factors lasted for a longer period of time in the un-nested run. Results from this sensitivity test suggest that to further understand the effect of nesting on weak disturbances, more case studies need to be investigated. These results also implied that besides the resolution, there were other factors in the model affecting the systems intensity forecast.

Evaluation of the HWRFx forecast performance due to changes on ICs provided mixed results. For the NDAEW case, the ICs sensitivity results showed that both the CNTRL and EXP simulations hindered the development of the NDAEW. However, the

EXP simulation best represented the actual dynamic and thermodynamic structure of the AEW at the initial time as well as its weakening trend towards the end of the forecast. The CNTRL run operational metrics suggested intensification of the wave near the end of the simulation possibly due to the forecast of a more favorable wind structure for development since the initial time of the run. At 0 h, the CNTRL analysis depicted a stronger AEW represented by a closed cyclonic circulation with a well-defined center at 700 hPa while the EXP analysis showed a cyclonic circulation not completely closed that better resembled the dropwindsondes wind structure at 700 hPa and the Meteosat-8 low-level wind field. A RH data-impact graph at 0 h verified that the assimilation of the additional fifteen NAMMA dropwindsondes data reproduced more accurately the actual thermodynamic ICs. The EXP ICs represented both the NDAEW moister regions in the southern side of the system as well as the zones that were impacted by the SAL dry air in the northern side of the wave, which were confirmed with the Meteosat-8 true color imagery. The HWRFx CNTRL thermodynamic profiles of the NDAEW did not represent the majority of the vertical structure changes at the different dropwindsondes locations. For the most part, the CNTRL profiles shared similar vertical structures and depicted quasi-saturated to saturated atmospheric regions not represented in the dropwindsonde profiles making these ICs and subsequent forecast less accurate.

For the HAEW case, the assimilation of the additional seven NAMMA dropwindsondes data did not optimize the ICs and the subsequent intensity forecast when compared to the CNTRL run. Both the CNTRL and EXP simulations predicted TS cyclogenesis, however sixty hours later than in NHC BT analyses. Like in the previous sensitivity tests, no hurricane was forecast and instead, TS force was sustained through

the end of the simulations. Unlike the CNTRL run, the EXP simulation did not forecast the initial TD stage of Helene and predicted weaker TS shown equally by the operational metrics and structure. A weaker system in the EXP run was attributed to misrepresented ICs. An assessment of the ICs for this case determined that, dynamically, the CNTRL analysis had a stronger system than the EXP run. The CNTRL analysis showed a closed cyclonic circulation with a well-defined center at both 700 hPa and the surface while the EXP analysis showed a weaker cyclonic circulation with an ill-defined center at 700 hPa and an open cyclonic circulation at the surface. When compared to the dropwindsondes, the HAEW CNTRL analysis best represented the ICs dynamic structure. The CNTRL analysis depicted the cyclonic circulation observed from 1000 hPa to 400 hPa whereas the EXP had a weaker structure showing this circulation only up to 700 hPa. Different to the CNTRL analysis, the EXP analysis portrayed a cyclonic circulation at both 500 and 400 hPa, however not definitively closed. At the upper levels both analyses resulted weaker by depicting for the most part easterly winds where the dropwindsondes sampled anticyclonic winds. Thermodynamically, the model ICs showed mixed results when compared to the dropwindsondes vertical profiles. In general and as was depicted in the RH data impact graph at 0 h, the EXP analysis best represented the SAL dry air west of the TD center whereas the CNTRL analysis best represented the much moister environment north of the TC center. Even when none of the analyses represented the observed saturated regions in the troposphere at the various dropwindsondes locations, the CNTRL analysis showed to have a moister environment than the EXP analysis, which resulted in the prediction of stronger TS. The delay in tropical cyclogenesis and the hindrance of further intensification was attributed to inaccurate dynamic and

thermodynamic ICs in both runs. Although the NAMMA supplemental data did not improve the timing of tropical cyclogenesis and the intensity forecast, it better assisted in predicting the storm track when compared to the BT of NHC.

In theory, the more accurate the estimate of the ICs, the better the quality of the forecast. However, as the results from both AEW cases indicated this is not always the case since models usually contain many errors arising from horizontal, vertical and time-differencing schemes, parameterized processes as well as errors in the initialization and BCs and the incorporation of inadequate terrain (Krishnamurti et al. 1980). While the NDAEW case demonstrated that the assimilation of additional dropwindsondes data into HWRFx greatly improved the initial state of the model (both dynamically and thermodynamically) and produced a more accurate forecast, the HAEW case showed that additional data sometimes could result in intensity forecast degradation, though improvements on track still can be achieved. Since the EXP ICs or HEDAS mean final analysis is dominated by the information contained in the observations, two factors that could influence the HAEW results were deficiency of observational data (seven dropwindsondes versus fifteen for the NDAEW) and possibly a less optimal observing strategy (the coverage of the sampling flight pattern around the NDAEW was greater). In order to determine if the early sampling of weak tropical systems (such as AEWs and TDs) has the potential to improve the forecast of cyclogenesis, more surveillance missions on these systems are needed and other cases with available observational data have to be investigated.

Besides the individual findings of each HWRFx sensitivity test performed, the model provided distinguishing factors about how TCs form. In addition to the forecast of

more intense operational metrics, the environment and structure of a developing AEW at the time of tropical cyclogenesis included: surface and lower-levels (700 hPa to 1000 hPa) closed cyclonic circulation with a well-defined center, MSLP equal or less than 1010 hPa to sustain enough convergence and moist convection at the TC center, environmental shear less than 30 kt at the TC center by the establishment of a mid-to-upper levels anticyclone center near or at the MLWSM to support moist convection, organization of a quasi-saturated, saturated or super-saturated column of air (RH ≥ 90%) at the TC center extending up to at least 850 hPa as well as moist air within the cyclonic circulation, and the formation of a RVORT core at the TC center extending from the surface to at least 850 hPa.

An AEW with low chances of development exhibited a weaker dynamic structure at both 700 hPa and the surface. This structure refers to a cyclonic circulation not completely closed (or an open system). The study showed that with an open AEW unable to protect the inner core of the system, the likelihood for development once it encounters a hostile environment such as high environmental shear and dry air is low. These results support in part the "wave pouch" theory in Wang et al. (2010). A weaker MSLP intensity and structure (model inability to maintain closed contours) added to the factors that deter the intensification of AEWs. This last factor restrained low-level convergence, which prevented moist convection at the MLWSM. Another factor that inhibited moisture accumulation at the MLWSM was the constant air subsidence due to dry air intrusion, which in turn acted to hinder the formation of a RVORT core.

In addition to favorable and un-favorable conditions for TC development, HWRFx provided clues on where in the atmosphere tropical cyclogenesis takes place.

The investigation determined that TC formation occurs from approximately 700 hPa to the surface or the lower troposphere. A distinctive signal for a developing system consisted on the formation of a RVORT core at the MLWSM extending from the surface to at least 850 hPa coinciding with the establishment of a saturated to super-saturated column of air extending to the same level. The core of RVORT did not correspond to the location of the RVORT maximum during cyclogenesis. This emphasizes the importance of evaluating the RVORT structure horizontally and vertically in order to accurately predict cyclogenesis.

A lot remains to be done in order to increase models accuracy and reliability in the forecast of tropical cyclogenesis. Current advancements in DA techniques and improved model resolution combined with the availability of more observations to produce more accurate ICs are tools that can be used for this purpose. However, more work on resolving the uncertainties in the models physics parameterizations for weak tropical systems is essential. In order to evaluate accurately the quality of a numerical model's prediction using observations, a better understanding of the atmospheric processes at smaller scale is needed so that model physics could be improved. With progress in this area, studies that test the sensitivity to variations in model physics would be required to reach a consensus on the operational physics parameterizations more suitable for weak tropical systems such as the AEWs.

REFERENCES

Aberson, S. D., Black, M. L., Black, R. A., Burpee, R. W., Cione, J. J., Landsea, C. W., and F. D. Marks, 2006: Thirty years of tropical cyclone research with the NOAA P-3 aircraft. *Bull. Amer. Meteor. Soc.*, 87, 1039–1055.

_____, and M. DeMaria, 1994: Verification of a nested barotropic hurricane track prediction model. *Mon. Wea. Rev.*, 122, 2804-2515.

_____, 2003: Targeted Observations to Improve Operational Tropical Cyclone Track Forecast Guidance. *Mon. Wea. Rev.,* 131, 1613–1628.

_____, 2009: 10 Years of Hurricane Synoptic Surveillance (1997–2006) *Mon. Wea. Rev.*, vol. 138, issue 5, pp. 1536-1549.

Aksoy, A., K. J. Sellwood, P. Leighton, T. Vukicevic, S. D. Aberson, and F. Zhang, 2010: Development of the ensemble Kalman filter system for hurricane data assimilation at NOAA/AOML/HRD: Preliminary evaluation using environmental and vortex-scale dropwindsonde data. Preprints, *14th Symposium on Integrated Observing and Assimilation Systems for the Atmosphere, Oceans, and Land Surface*, Tucson, AZ, Amer. Meteor. Soc., 6B.2.

Aiyyer, A., and J. Molinari, 2008: MJO and Tropical Cyclogenesis in the Gulf of Mexico and Eastern Pacific: Case Study and Idealized Numerical Modeling. *J. Atmos. Sci.,* **65**, 2691–2704.

Albignat, J. P., and R. J. Reed, 1980: The origin of African wave disturbances during Phase III of GATE. *Mon. Wea. Rev*., 108, 1827–1839.

Arakawa, A., and W. H., Schubert, 1974: Interaction of a Cumulus Cloud Ensemble with the Large-Scale Environment, Part I. *J. Atmos. Sci.,* 31, 674-701.

_____, 2004: The Cumulus Parameterization Problem: Past, Present, and Future. *J. Climate,* 17, 2493-2525.

Avila, L. A., and R. J. Pasch, 1992: Atlantic tropical systems of 1991. *Mon. Wea. Rev,* 120, 2688–2696.

Bao, J.-W., Gopalakrishnan, S. G., Michelson, S. A., Marks, F. D., and Michael T.Montgomery, 2012: Impact of Physics Representations in the HWRFX Model on Simulated Hurricane Structure and Wind-Pressure Relationships. *Mon. Wea. Rev*., 140, 3278-3299.

Bell, G., Blake E., Landsea C., Chelliah, M., Pasch, R., Mo, K., and S. Goldenberg, cited 2009: The 2006 North Atlantic Hurricane Season a Climate Perspective [http://www.cpc.noaa.gov/products/expert_assessment/hurrsummary_2006.pdf]

Bengtsson, L., H. Böttger, and M. Kanamitsu, 1982: Simulation of hurricane-like vortices in a general circulation model. *Tellus*, 34, 440-457.

Berry, G. J., and C. Thorncroft, 2005: Case Study of an Intense African Easterly Wave. *Mon. Wea. Rev.*, 133, 752-766.

_____, C. Thorncroft, and T. Hewson, 2007: African Easterly Waves during 2004 – Analysis using objective techniques. *Mon. Wea. Rev.,* 1-50.

Bister, M., and K. A. Emanuel, 1997: The genesis of Hurricane Guillermo: TEXMEX analyses and modeling study. *Mon. Wea. Rev*., 125, 2662-2682.

Bracken, W. E., and L. F. Bosart, 2000: The Role of Synoptic-Scale Flow during Tropical Cyclogenesis over the North Atlantic Ocean. *Mon. Wea. Rev.,* 128, 353–376.

Brown, D. P., 2006: Hurricane Helene (AL082006). NOAA/NHC Tropical Cyclone Rep., 12 pp.

Burpee, R. W., 1972: The origin and structure of easterly waves in the lower troposphere of North Africa. *J. Atmos. Sci.,* 29**,** 77–90

_____, 1974: Characteristics of the North African easterly waves during the Summers of 1968 and 1969. *J. Atmos. Sci*., 31, 1556-1570.

Carlson, T. N., 1969a: Synoptic histories of three African disturbances that developed into Atlantic hurricanes. *Mon. Wea. Rev*, 97, 256-276.

_____, 1969b: Some remarks on African disturbances and their progress over the tropical Atlantic. *Mon. Wea. Rev*, 97, 716-726.

_____, and J. M. Prospero, 1972: The large-scale movement of Saharan air outbreaks over the northern equatorial Atlantic. *J. Appl. Meteor.,* 11**,** 283–297.

Ceselski, B. F., 1974: Cumulus Convection in Weak and Strong Tropical Disturbances. *J. Atmos. Sci.,* 31, 1241-1255.

Chen, T.-C., 2006: Characteristics of African Easterly Waves Depicted by ECMWF Reanalyses for 1991–2000. *Mon. Wea. Rev*, 134, 3539-3566.

Colon, J. A., and W. Nightingale, 1963: Development of tropical cyclones in relation to circulation patterns at the 200-millibar level. *Mon. Wea. Rev.,* 91, 329-336.

DeMaria, M., 1996: The effect of vertical shear on tropical cyclone intensity change. *J. Atmos.Sci.,* **53,** 2076–2087.

_____, M., Knaff, J. A., and B. H. Connell, 2001: A Tropical Cyclone Genesis Parameter for the Tropical Atlantic. *Wea. Forecasting*, 16, 219–233.

Dunion, J. P., and C. S. Velden, 2004: The Impact of the Saharan Air Layer on Atlantic Tropical Cyclone Activity. *Bull. Amer. Meteor. Soc*., 85, pp. 353–365.

Duvel, J. P., 1990: Convection over tropical Africa and the Atlantic Ocean during northern summer. Part II: Modulation by easterly waves. *Mon. Wea. Rev.*, 118, 1855–1868.

Eastin, M. D., Gray, W. M., and P. G. Black, 2005: Buoyancy of Convective Vertical Motions in the Inner Core of Intense Hurricanes. Part I: General Statistics. *Mon. Wea. Rev.*, 133, 188-208.

_____, 2005: Buoyancy of Convective Vertical Motions in the Inner Core of Intense Hurricanes. Part II: Case Studies. *Mon. Wea. Rev.*, 133, 209-227.

Emanuel, K., 2003: Tropical Cyclones. *Annu. Rev. Earth Planet. Sci*., 31, 75–104.

Erickson, C. O., 1963: An Incipient Hurricane near the West African Coast. *Mon. Wea. Rev.,* 91, 61-68.

Evensen, G., 1994: Sequential data assimilation with a nonlinear quasigeostrophic model using Monte Carlo methods to forecast error statistics. *J. Geophys. Res.*, 99, 10143–10162.

_____, 2003: The Ensemble Kalman filter: theoretical formulation and practical implementation. *Ocean Dyn*. 53, 343–367.

Fink, A. H., D. G. Vincent, P. M. Reiner, and P. Speth, 2004: Mean State and Wave Disturbances during Phases I, II, and III of GATE Based on ERA-40. *Mon. Wea. Rev*, 132, 1661-1683.

Frank, N. L., 1969: The ―inverted V‖ cloud pattern—An easterly wave? *Mon. Wea. Rev*, 97, 130-140.

Frank, W. M., 1983: The Cumulus Parameterization Problem. *Mon. Wea. Rev.,* 111, 1859-1871.

Frank, W. M., 1987: Tropical cyclone formation. *A Global View of tropical Cyclones.* ONR Marine Meteorology Program, 185.

Franklin, J. L., Black, M. L., and K. Valde, 2003: GPS Dropwindsonde Wind Profiles in Hurricanes and Their Operational Implications. *Wea. Forecasting,* 18, 32-44.

Fyfe, J. C., 1999: Climate simulations of African easterly waves. *J. Climate*, 12, 1747–1769.

Gaunce, M., 2006: NASA African Monsoon Multidisciplinary Analyses (NAMMA) Mission. NASA Ames Research Center Tech. Rep., 1 pp.

Gray, W. M., 1968: Global view of the origin of tropical disturbances and storms. *Mon. Wea. Rev.,* 96, 669–700.

Goerss, J.S. and R.A. Jeffries, 1994: Assimilation of synthetic tropical cyclone observations into the Navy Operational Global Atmospheric Prediction System. *Wea. Forecasting,* 9, 557-576.

Gopalakrishnan, S. G., Goldenberg, S., Quirino, T., Zhang, X., Marks Jr., F., Yeh, K.-S., Atlas, R., and V. Tallapragada, 2012: Toward Improving High-Resolution Numerical Hurricane Forecasting: Influence of Model Horizontal Grid Resolution, Initialization, and Physics. *Wea. Forecasting*, 27, 647-666.

_____, F. Marks, X. Zhang, J.-W. Bao, K.-S. Yeh, and R. Atlas, 2010: The Experimental HWRF system: A study on the influence of horizontal resolution on the structure and intensity changes in tropical cyclones using an idealized framework. *Mon. Wea. Rev.*, 139, 1762-1784.

_____, N. Surgi, R. Tuleya, and Z. Janjic, 2006: NCEP's two-way-interactive-moving-nest NMM-WRF modeling system for hurricane forecasting. Preprints, *27th Conference on Hurricanes and Tropical Meteorology*, Monterey, CA, Amer. Meteor. Soc., Ar. 7A.3.

_____, David P. Bacon, Nash'at N. Ahmad, Zafer Boybeyi, Thomas J. Dunn, Mary S. Hall, Yi Jin, Pius C. S. Lee, Rangaro V. Madala, R.Ananthakrishna Sarma, Mark D. Turner, and Tim Wait, 2002: An Operational Multi-Scale Atmospheric Model with Grid Adaptivity for Hurricane Forecasting. *Mon. Wea. Rev*, Vol. 130, No. 7, pp. 1830-1847.

Grell, G. A., 1993: Prognostic evaluation of assumption used by cumulus parameterization. *Mon. Wea. Rev.*, 121, 764–787.

Halverson, J. B., Simpson, J., Heymsfield, G., Pierce, H., Hock, T., and L. Ritchie, 2006: Warm Core Structure of Hurricane Erin Diagnosed from High Altitude Dropsondes during CAMEX-4. *J. Atmos. Sci.*, 63, 309-324.

Han, J., and H.-L. Pan, 2011: Revision of Convection and Vertical Diffusion Schemes in the NCEP Global Forecast System. *Wea. Forecasting,* 26, 520-533.

Hausman, S. A., 2001: Formulation and sensitivity analysis of a nonhydrostatic, axisymmetric tropical cyclone model. Atmospheric Science Paper 701, Dept. of Atmospheric Science, Colorado State University, 210 pp.

Hennon, C. C., and J. S. Hobgood, 2003: Forecasting tropical cyclogenesis over the Atlantic basin using large-scale data. *Mon. Wea. Rev*, 131, 2927-2940.

Hock, T. F., and J. L. Franklin, 1999: The NCAR GPS Dropwindsonde. *Bull. Amer. Metor. Soc.,* 80, 407-420.

Holton, J. R., 1971: A Diagnostic Model for Equatorial Wave Disturbances: The Role of Vertical Shear of the Mean Zonal Wind. *J. Atmos. Sci.,* 28, 55-64.

Hong, S.-Y. and H-L. Pan, 1996: Nonlocal boundary layer vertical diffusion in a medium-range forecast model. *Mon. Wea. Rev.*, 124**,** 2322-2339.

_____, and _____, 1998: Convective trigger function for a mass-flux cumulus parametrization scheme. *Mon. Wea. Rev.*, 126**,** 2599–2620

Hopsch, S. B., C. D. Thorncroft, K. Hodges, and A. Aiyyer, 2007: West African storm tracks and their relationship to Atlantic tropical cyclones. *J. Climate*, 20, 2468-2483.

Hou, Y-T, K. A. Campana and S-K Yang, 1996: Shortwave radiation calculations in the NCEP's global model. *International Radiation Symposium, IRS-96*, August 19-24, Fairbanks, AL.

_____, S. Moorthi,. K. Campana, 2002: Parameterization of solar radiation transfer in the NCEP models. *NCEP Office Note, 441*. http://www.emc.ncep.noaa.gov/officenotes/FullTOC.html#2000

Houze Jr., R. A., Lee, W., and M. M. Bell, 2009: Convective Contribution to the Genesis of Hurricane Ophelia (2005). Mon. Wea. Rev., 137, 2778-2800.

_____, Cetrone, J., Rita Brodzik, S., Chen, S. S., Zhao, W., Lee, W., Moore, J. A., Stossmeister, G. J., Bell, M. M., and R. F. Rogers, 2006: The Hurricane Rainband and Intensity Change Experiment: Observations and Modeling of Hurricanes Katrina, Ophelia, and Rita. *Bull. Amer. Meteor. Soc.*, 87, 1503-1521.

Kalnay, E., M. Kanamitsu, and W. E. Baker, 1990: Global numerical weather prediction at the National Meteorological Center. *Bull. Amer. Meteor. Soc*., 71, 1410-1428.

_____, and Coauthors, 1996: The NCEP/NCAR 40-Year reanalysis project. *Bull. Amer. Meteor. Soc.*, 77, 437-471.

_____, 2003: *Atmospheric modeling, data assimilation and predictability*. Cambridge Univ. Press, 341 pp.

Kanamitsu, M., 1989: Description of the NCEP global data assimilation and forecast system. *Wea. and Forecasting*, 4, 334-342.

Kepert, J. D., 2006: Observed Boundary Layer Wind Structure and Balance in the Hurricane Core. Part I: Hurricane Georges. *J. Atmos. Sci.*, 63, 2169-2193.

_____, 2006: Observed Boundary Layer Wind Structure and Balance in the Hurricane Core. Part II: Hurricane Mitch. *J. Atmos. Sci.,* 63, 2194-2211.

Kerns, B., K. Greene, and E. Zipser, 2008: Four Years of Tropical ERA-40 Vorticity Maxima Tracks. Part I: Climatology and Vertical Vorticity Structure. *Mon. Wea. Rev*, 136, 4301-4319.

Kim, Y-J and A. Arakawa, 1995: Improvement of orographic gravity wave parameterization using a mesoscale gravity wave model. *J. Atmos. Sci.*, 52, 11, 1875-1902.

Kistler, R., E. and Coauthors, 2001: The NCEP-NCAR 50-Year Reanalysis: Monthly Means CD-ROM and Documentation. *Bull. Amer. Meteor. Soc.*, 82, No. 2, 247-268.

Krishnamurti, T. N., Ramanathan, Y., Pan, H., Pasch, R. J., and J. Molinari, 1980: Cumulus Parameterization and Rainfall Rates I. *Mon. Wea. Rev.,* 108, 465-472.

Kurihara, Y., and R. E. Tuleya, 1981: A Numerical Simulation Study on the Genesis of a Tropical Storm. *Mon. Wea. Rev.*, 109, 1629-1653.

Martin, D. W., and D. N. Sikdar, 1979: A Case Study of West Atlantic Cloud Clusters: Part 2. Dynamic Structure and Environment. *Mon. Wea. Rev*, 107, 1343-1369.

McTaggart-Cowan, R., Deane, G., Bosart, L., Davis, C., and T. Galarneau, 2008: Climatology of Tropical Cyclogenesis in the North Atlantic (1948–2004). *Mon. Wea. Rev.,* **136**, 1284–1304.

Montgomery, M. T., Davis, C., Dunkerton, T., Wang, Z., Velden, C., Torn, R., Majumdar, S. J., Zhang, F., Smith, R. K., Bosart, L., Bell, M. M., Haase, J. S., Heymsfield, A., Jensen, J., Campos, T., and M. A. Boothe, 2012: The Pre-Depression Investigation of Cloud-Systems in the Tropics (PREDICT) Experiment: Scientific Basis, New Analysis Tools, and Some First Results. *Bull. Amer. Meteor. Soc.*, 93, 153-172.

_____, Farrell, B. F., 1993: Tropical Cyclone Formation. *J. Atmos. Sci.,* 50, 285-310.

_____, Bell, M. M., Aberson, S. D., and M. L. Black, 2006: Hurricane Isabel (2003): New Insights into the Physics of Intense Storms. Part I: Mean Vortex Structure and Maximum Intensity Estimates. *Bull. Amer. Meteor. Soc.*, 87, 1335-1347.

Moorthi, S., H.-L. Pan, P. Caplan, 2001: Changes to the 2001 NCEP operational MRF/AVN global analysis/forecast system. *NWS Technical Procedures Bulletin,* 484, pp14. [Available at http://www.nws.noaa.gov/om/tpb/484.htm]

Ooyama, K. V., 1982: Conceptual evolution of the theory and modeling of the tropical cyclone. *J. Met. Soc. Japan*, 60, 369-380.

Pattanayak, S., Mohanty, U. C., and K. K. Osuri, 2012: Impact of Parameterization of Physical Processes on Simulation of Track and Intensity of Tropical Cyclone Nargis (2008) with WRF-NMM Model. *The Scientific World Journal,* 2012, 1-18.

Payne, S. W., and M. M. McGarry, 1977: The relationship of satellite inferred convective activity to easterly waves over West Africa and the adjacent ocean during phase III of GATE. *Mon. Wea. Rev.,* 105, 413–420.

Powell, M. D., Vickery, P. J., and T. A. Reinhold, 2003: Reduced drag coefficients for high wind speeds in tropical cyclones. *Nature*, 422, 279–283.

Pratt, A., and J. Evans, 2009: Potential Impacts of the Saharan Air Layer on Numerical Model Forecasts of North Atlantic Tropical Cyclogenesis. *Wea. Forecasting*, 24, 420-435.

Ramos, N. A., 2007: 2004 Hurricane Danielle Tropical Cyclogenesis Forecasting Study Using the National Center for Atmospheric Research (NCAR) Advanced Research Weather Research and Forecasting (WRF) Model. Thesis, Atmospheric Sciences Program, Howard University, 110.

Redelsperger, J., C. D. Thorncroft, A. Diedhiou, T. Lebel, D. J. Parker, and J. Polcher, 2006: African Monsoon Multidisciplinary Analysis: An International Research Project and Field Campaign. *Bull. Amer. Meteor. Soc.*, 87, 1739–1746.

Reed, R. J., D. C. Norquist, and E. E. Recker, 1977: The structure and properties of African wave disturbances as observed during phase III of GATE. *Mon. Wea. Rev.,* 105, 17–33.

_____, A. Hollingsworth, W. A. Heckley, and F. Delsol, 1988: An Evaluation of the Performance of the ECMWF Operational System in Analyzing and Forecasting Easterly Wave Disturbances over Africa and the Tropical Atlantic. *Mon. Wea. Rev,* 116, pp. 824-865.

Riehl, H., 1948: On the formation of typhoons. *J. Meteorol.,* 5, 247–264.

Ritchie, E. A., Holland, GJ, 1993: On the interaction of tropical-cyclone scale vortices. II: Interacting vortex patches. *Q. J. R. Meteorol. Soc.,* 119, 1363–1397.

_____, J. Simpson, W. T. Liu, J. Halverson, C.S. Velden, K.F. Brueske and H. Pierce, 2002: Present Day Satellite Technology for Hurricane Research – A Closer Look at Formation and Intensification, *American Geophysical Union*, 249-289.

Schreck III, C., and J. Molinari, 2009: A Case Study of an Outbreak of Twin Tropical Cyclones. *Mon. Wea. Rev.*, 137, 863-875.

Schubert, W. H., Hack, J. J., Silvia Dias, P. L. and Fulton, S. R., 1980: Geostrophic adjustment in an axisymmetric vortex. *J. Atmos. Sci*., 37, 1464-1484.

Sela, J. G., 1980: Spectral modeling at the National Meteorological Center. *Mon. Wea. Rev*., 103, 246-257.

Serra, Y. L., G. N. Kiladis, and K. I. Hodges, 2010: Tracking and Mean Structure of Easterly Waves over the Intra-Americas Sea. *J. Climate*, 23, 4823-4840.

Shaman, J., Esbensen, S., and E. Maloney, 2009: The Dynamics of the ENSO-Atlantic Hurricane Teleconnection: ENSO-related changes to the North African-Asian Jet affect Atlantic Basin Tropical Cyclogenesis. *J. Climate*, 22, 2458-2482.

Shelton, K., 2011: Easterly Waves and Tropical Cyclogenesis in the Caribbean. Ph.D. dissertation, State University of New York at Albany, 233 pp.

Simpson, J., E. Ritchie, G. J. Holland, J. Halverson, and S. Stewart, 1997: Mesoscale Interactions in Tropical Cyclone Genesis. *Mon. Wea. Rev.*, 125, 2643-2661.

Sundqvist, H., E. Berge, and J. E. Kristjansson, 1989: Condensation and cloud studies with mesoscale numerical weather prediction model. *Mon. Wea. Rev.*, 117, 1641-1757.

Talagrand, O., 1997: Assimilation of observations, an introduction. *J. Met. Soc*. *Japan*, 75, 191-209.

Thompson, R. M. Jr., Payne, S. W., Recker E. E and Reed, R. J., 1979: Structure and Properties of Synoptic-Scale Wave Disturbances in the Intertropical Convergence Zone of the Eastern Atlantic. *J. Atmos. Sci.* 36, 53–72.

Thorncroft, C., Hodges, K., 2001: African Easterly Wave Variability and Its Relationship to Atlantic Tropical Cyclone Activity. *J. Climate*, Vol. 14, No. 6, 1166–1179.

Tory, K. J., Montgomery, M. T., and N. E. Davidson, 2006: Prediction and Diagnosis of Tropical Cyclone Formation in a NWP System. Part I: The Critical Role of Vortex Enhancement in Deep Convection. *J. Atmos. Sci.,* 63, 3077-3090.

_____, M. T. Montgomery, N. E. Davidson, and J. D. Kepert, 2006: Prediction and Diagnosis of Tropical Cyclone Formation in an NWP System. Part II: A Diagnosis of Tropical Cyclone Chris Formation. *J. Atmos. Sci.*, 63, 3091-3113.

_____, N. E. Davidson, and M. T. Montgomery, 2007: Prediction and Diagnosis of Tropical Cyclone Formation in an NWP System. Part III: Diagnosis of Developing and Nondeveloping Storms. *J. Atmos. Sci.*, 64, 3195-3213.

Uhlhorn, E.W., and P. G. Black, 2003: Verification of remotely sensed sea surface winds in hurricanes. *J. Atmos. Oceanic. Tech.,* 20, 99-116.

Vukicevic, T., 2010: Introduction to data assimilation. 24 pp.

Wang, Z., M. T. Montgomery, and T. J. Dunkerton, 2008: A dynamically based method for forecasting tropical cyclogenesis location in the Atlantic sector using global model products. *Geophys. Res. Lett.,* 36.

_____, M. T. Montgomery, and T. J. Dunkerton, 2010: Genesis of Pre–Hurricane Felix (2007). Part II: Warm Core Formation, Precipitation Evolution, and Predictability. *J. Atmos. Sci.*, 67, 1730-1744.

Yeh, K., X. Zhang, S.G. Gopalakrishnan, S. Aberson, R. Rogers, F. Marks and R. Atlas, 2011: Performance of the experimental HWRF in the 2008 Hurricane Season. *Nat. Hazards*, 1-11.

Zhao, Q. Y., and F. H. Carr, 1997: A prognostic cloud scheme for operational NWP models. *Mon. Wea. Rev.*, 125, 1931-1953.

Zhang, X., K. Yeh, T.S. Quirino, S.G. Gopalakrishnan, F.D Marks, S.B. Goldenberg and S. Aberson, 2010: HWRFx: Improving Hurricane Forecasts with High-Resolution Modeling. *Computing in Science & Engineering*, 13, 13-21.

Zipser, E. J., C. H. Twohy, S. Tsay, K. L. Thornhill, S. Tanelli, R. Ross, T.N. Krishnamurti, Q. Ji, G. Jenkins, S. Ismail, N. C. Hsu, R. Hood, G. M. Heymsfield, A. Heymsfield, J. Halverson, H. M. Goodman, R. Ferrare, J. P. Dunion, M. Douglas, R. Cifelli, G. Chen, E. V. Browell, and B. Anderson, 2009: The Saharan Air Layer and the Fate of African Easterly Waves NASA's AMMA 2006 Field Program to Study Tropical Cyclogenesis: NAMMA. *Bull. Amer. Meteor. Soc*., 90, 1137-1156.